Mapping Mercury's Debussy Quadrangle and Exploration of Volcanic Vents on a Shrinking World

Thesis

Mapping Mercury's Debussy Quadrangle and Exploration of Volcanic Vents on a Shrinking World

David Lawrence Pegg MSci (Hons)

April 2021

A thesis submitted to the Open University in the subject of Planetary Geology

for the degree of Doctor of Philosophy.

School of Physical Sciences

“It is good to have an end to journey toward; but it is the journey that matters, in the end.”
— Ursula K. Le Guin, The Left Hand of Darkness

Abstract

NASA's MESSENGER (Bacronym: MErcury Surface, Space Environment and Ranging) spacecraft was the first to orbit the planet Mercury and return images of the entire globe. This thesis uses data from this mission to build a better understanding of the planet, its volcanic, and tectonic nature.

I used image data to produce a 1:3 million scale geomorphological map of the H-14 "Debussy" Quadrangle, dividing the surface into crater materials and three generations of volcanic plains. I classified craters using two different morphological (degradation class) systems; a three-class and a five-class. I found the five-class system more useful. The Rembrandt impact basin and tectonic activity have also modified parts of this quadrangle.

Following on from mapping several explosive volcanic vents within the quadrangle, I undertook a global survey of volcanic vent sites to work out how many are compound volcanoes (comprised of multiple vents, and likely to have erupted multiple times). I found 71% of the vent sites with good image quality on Mercury are compound. Their repeated eruption requires either a continued supply of volatile-rich magma or assimilation of volatiles in the crust.

During my global vent survey, I identified a vent site that had exposed a fault scarp. This is the first direct observation of a fault scarp in three dimensions, and using shadow measurements, I measured the dip of the fault plane as 28° ±5°; this is within the range of those measured indirectly. If further measurements confirm this, then this would suggest that the higher end of estimates for Mercury's global contraction (caused by cooling) are probably correct.

Volcanism on Mercury has shaped the planet's surface and reflects its interior. Vent sites will be important targets for the BepiColombo mission, which launched during my research and is due to arrive in orbit around Mercury in 2025.

Acknowledgements

Thank you Dave, Matt, and Susan for being SUPER-visors trying to understand what on Mercury I was on about and correcting my abuse of the English language and sensibilities. Jack, Chris, and Ben, my fellow Mercury mappers; thanks for the camaraderie and wild speculation in the face of insufficient image resolution. Thanks to all those in the Planetary Environments Group for all the cups of tea and the Z101 lunch crew for not banishing me for my puns. Alex, Lawrie, Chris, and Stacy as some of my most supportive friends; I could not have done it without you. My parents instilled curiosity and an appreciation of the wonder of the universe that I will forever be thankful. Finally, my thanks must go to all those on the MESSENGER team for getting a mission to this often overlooked world.

Table of Contents

List of Figures

List of Tables

List of Abbreviations

Abbreviation	Meaning
BDR	Bulk Data Record
BELA	BepiColombo Laser Altimeter
DEM	Digital Elevation Model
EBV	Enterprise-Belgica Valley
ESA	European Space Agency
GIS	Geographical Information System
HIE	High Incidence East
HIW	High Incidence West
IAU	International Astronomical Union
ICP	Intercrater plains
IMP	Intermediate Plains
ISA	Italian Spring Accelerometer
ISIS3	Integrated Software for Imagers and Spectrometers Version 3
JAXA	Japan Aerospace Exploration Agency
LIDAR	Laser Imaging, Detection, and Ranging
LOI	Low Incidence Angle
LRM	Low Refelctance Material
MASCS	Mercury Atmospheric and Surface Composition Spectrometer
MDIS	Mercury Dual Imaging System
MERTIS	Mercury Radiometer and Thermal Infrared Spectrometer
MESSENGER	MErcury Surface, Space ENvironment, GEochemistry, and Ranging
MGNS	Mercury Gamma-ray and Neutron Spectrometer
MIXS	Mercury Imaging X-ray Spectrometer
MLA	Mercury Lazer Altimeter
MORE	Mercury Orbiter Radio-science Experiment
NAC	Narrow-Angle-Camera
NASA	National Aeronautics and Space Administration
NS	Neutron Spectrometer
PDS	Planitary Data System
PHEBUS	Probing of Hermean Exosphere by Ultraviolet Spectroscopy
SERENA	Search for Exosphere Refilling and Emitted Neutral Abundances
SIMBIO-SYS	Spectrometers and Imagers for MPO BepiColombo Integrated Observatory System
SIXS	Solar Intensity X-ray and Particle Spectrometer
SP	Smooth Plains

USGS	United States Geological Survey
WAC	Wide-Angle Camera
XRS	X-Ray Spectrometer

List of Appendices

1 Introduction

In 2008, the National Aeronautics and Space Administration's (NASA) MESSENGER (backronym: MErcury Surface, Space ENvironment, GEochemistry, and Ranging) mission to the planet Mercury imaged parts of the planet never before observed in detail. The mission provided the first-ever global data sets enabling the study of the entire planet.

1.1 Thesis Overview

This thesis presents a geological map of the H-14 (Debussy) quadrangle and the science-inspired during the creation of the map. The map is part of an international group of effort to produce a map of the planet at a scale of 1:3 million before the joint European Space Agency (ESA) - Japan Aerospace Exploration Agency (JAXA) mission BepiColombo arrives at Mercury in 2025. Besides mapping a portion of a planet, I researched two topics initiated by the process of systematic mapping. Following the identification of several explosive volcanic vent sites within the mapped quadrangle, I undertook a global study of explosive volcanic vents to understand their eruptive history and look at the implications for explosive volcanism over the history of the planet. The second is the first direct measurement of the dip of a tectonic fault on the planet's surface based on my discovery during my global survey of a fault scarp exposed by an explosive volcanic site.

1.1 Methodology

To construct the geomorphological map and to study volcanic vents, my research relied on the image data and related data products from MESSENGER. I produced the map using a range of mosaic basemaps with a minimum resolution of either 166 m/pixel or 250m/pixel. I interpreted the basemaps using a geographical information system (GIS), dividing them into different morphological units and categorising them based on their texture. My map is an interpretation of the complex processes that formed and modified part of the planet's surface; this process is subjective and sometimes tricky (especially with areas of low-quality image data). The history told by the map and its implications are based on my interpretation. Working within a team to map the entire planet reduces some of these biases. Adherence to similar mapping standards enables me to deduce the history of the quadrangle based on the global understanding, and I can place my quadrangle in a global context while still having the freedom to innovate and define new morphological units where needed.

To study the explosive vents, I compiled the pre-existing lists of vents as well as adding new ones that I found during the mapping and global survey process. I studied each vent using MDIS' (Mercury dual imaging system) NAC (narrow-angle camera) and WAC (wide-angle cameras) images to classify each vent site as either compound (multiple vent sites) or not. It was while undertaking this study I discovered the fault surface exposed by a volcanic vent. I constructed a stereo digital elevation model of this vent site, but I found

I could not use this approach due to tilts and distortions caused by pointing uncertainties, and I relied on shadow measurements from nadir images to generate the measurements of dip for the fault system. BepiColombo provides an opportunity to revisit many of these vent sites and collect more data to check my conclusions and build on them.

1.2 Thesis Structure

I have divided my thesis into eight chapters:

1. This introduction
2. A background chapter overviewing the current status of the relevant Mercury research and the current open research questions to be explored in this thesis.
3. The methodology chapter, where I explain how I created the map and the criteria to identify the different morphological units. It will form the basis of a Journal of Maps paper, where I hope to publish my map. The map referred to in this chapter (and chapter 4) is provided as a separate PDF file to accompany the thesis.
4. A chapter discussing the geological map (appendix 1) a derived geological history of the mapped area, which I place into a global context.
5. A global study of the explosive volcanic vent sites on Mercury identifying which are compound and which are not, demonstrating that compound vents are very common, and examining the implications of this for Mercury's history. I have submitted a paper closely related to this chapter to *Icarus* and under review at the time of submission.
6. The measurement of a fault plane in three dimensions, identified during the study of volcanic vents, placing that in the context of previous indirect measurements of fault dip. This chapter has been submitted as a paper to *Planetary and Space Sciences* and currently under revision for resubmission.
7. A synthesis drawing together the outcomes of the above chapters and suggestions for future work.
8. A brief conclusion to summarise the results of this thesis.

The research for each chapter was undertaken primarily by me. I completed this work in collaboration with my supervisors Professor David Rothery, Professor Matthew Balme, and Dr Susan Conway, who provided me with expertise and guidance in completing the research. The geomorphology mapping process (Chapter 3) draws on that of Valentina Galluzzi, Jack Wright, and Christopher Mallband so that my map can be integrated with the other 1:3 million scale maps in the future. I completed the mapping myself and modified the process to the unique features and circumstances that come with mapping a new area. I wrote the first drafts of all the papers, and my supervisors provided editorial input afterwards.

2 Background

The planet Mercury has been known about since ancient times and is represented in many classical pantheons: Hermes, Mercury [W]oden, Set (or Seth) and Thoth, Nabu, बुध [Budha graha], 黑帝［Hedi], Zorya.

As the innermost planet in the solar system and the smallest of the planets according to the current definition (International Astronomical Union 2006), Mercury presents a world of extremes with features both strikingly familiar and oddly alien. To the planetary geologist, it provides an exciting opportunity to understand the processes that shape rocky planets without the additions of oceans and atmospheres.

2.1 Exploration

Mercury's location, so close to the Sun, means it was poorly studied before the advent of space exploration, and even then it is difficult, with only two missions having visited the planet and one currently on its way.

2.1.1 Ground-Based Study

Early astronomers could predict when Mercury would be seen in the sky, though often confused it as two separate bodies, one observed in the morning sky and another in the evening. It took until 1965 for radio astronomers to determine the rotation of the planet was 58.7 Earth days, and not the same length as its orbit of the Sun; 88 Earth days (Pettengill and Dyce 1965) See Section 2.2.

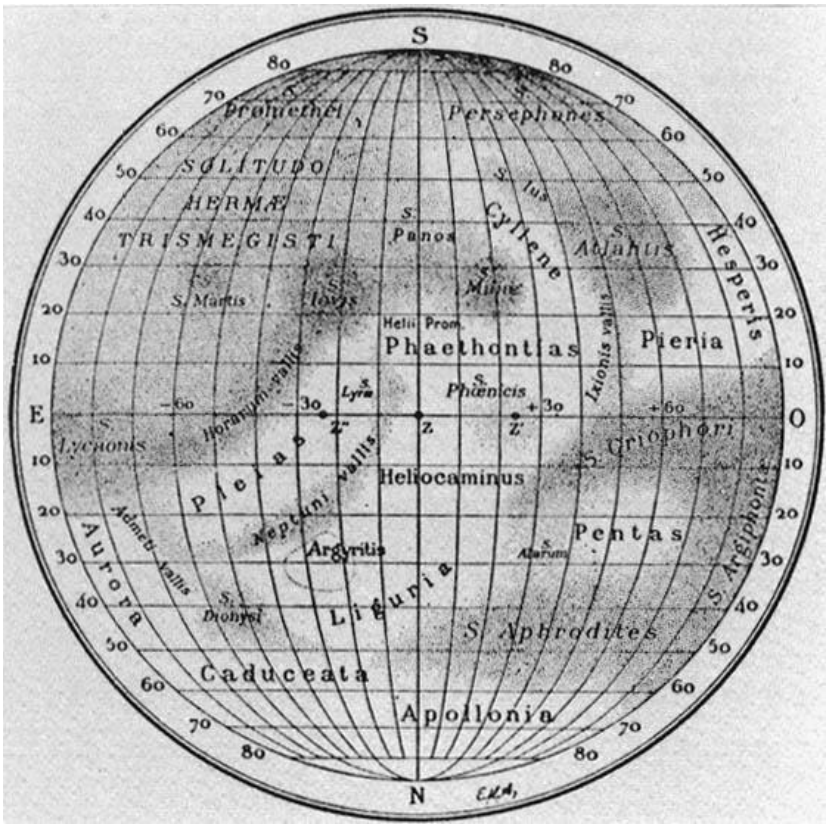

Figure 2.1 Map of Mercury's albedo features made before its rotation was understood (Antoniadi, 1933).

Astronomers had made some observations of the planet's surface by identifying possible albedo patches (Figure 2.1, Antoniadi, 1933) and were misled by these into the assumption that Mercury was tidally locked to the Sun. However, some of these features remained and kept their name after Mariner 10 collected its flyby data (Dollfus *et al* 1978). Since then, astronomers have studied the planet's interactions with the solar wind and used radio astronomy to study Mercury's poles (Slade *et al* 1992, Chabot *et al* 2018).

2.1.2 Mariner 10

The first mission, Mariner 10, was launched by the US's National Aeronautics and Space Administration (NASA) in 1973. It was the first mission to undertake a gravitational assist, using a flyby of Venus to adjust its course to pass Mercury in a 2:1 resonant orbit with the planet, a trajectory designed by Giuseppe Colombo. This allowed Mariner 10 to make three flybys of the planet (one in 1974 and two in 1975). Instruments on board included: television photography, UV spectrometer, infrared radiometer, magnetometer, plasma and charged particle detectors (Figure 2.2). Mariner 10 provided the first images and insights into the planet's surface and environment. All three of the flybys occurred while the same side of the planet was facing the Sun, so no imaging was possible of the other hemisphere.

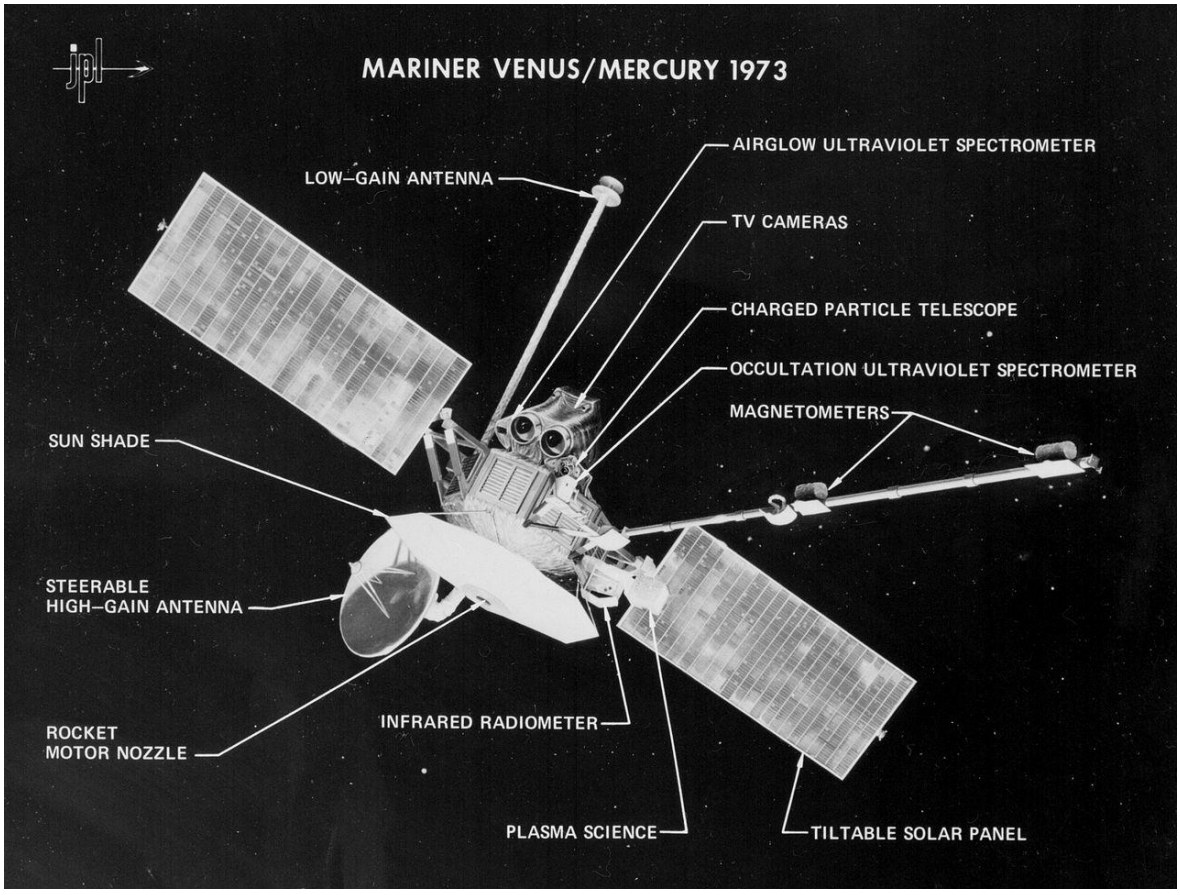

Figure 2.2 Schematic of Mariner 10 with instruments labelled (Image Credit: NASA/ Jet Propulsion Laboratory).

2.1.3 MESSENGER

The next mission to visit the planet was NASA's MESSENGER (whose backronym is MErcury Surface Space ENvironment GEochemistry and Ranging). This was a "Discovery" class mission, the lowest cost category in NASA planetary exploration. MESSENGER carried multiple scientific instruments (Section 2.1.3.2). Launching in 2004, it undertook two flybys of Venus and three of Mercury before becoming the first probe to orbit the planet in 2011; it carried on operating around Mercury until crashing into the surface in April 2015. I use MESSENGER data throughout this thesis.

2.1.3.1 Orbit

On the way to Mercury MESSENGER undertook three flybys of Mercury with the closest approach ranging from 199 km to 228 km before entering orbit around the planet. The orbit was highly elliptical due to fuel and thermal reasons. During its primary mission, MESSENGER's orbit had a periapsis (the closest point in an orbit to the planet) of 200 – 500 km above the northern hemisphere (Figure 2.3), its apoapsis was 15,200 km. The initial orbital period was 12 hours. During the extended mission (post-2012), the apoapsis was lowered to reduce the orbital period to 8 hours, and periapsis drifted lower over time (though boosted by occasional thruster burns) until it impacted the surface in 2015, ending the mission.

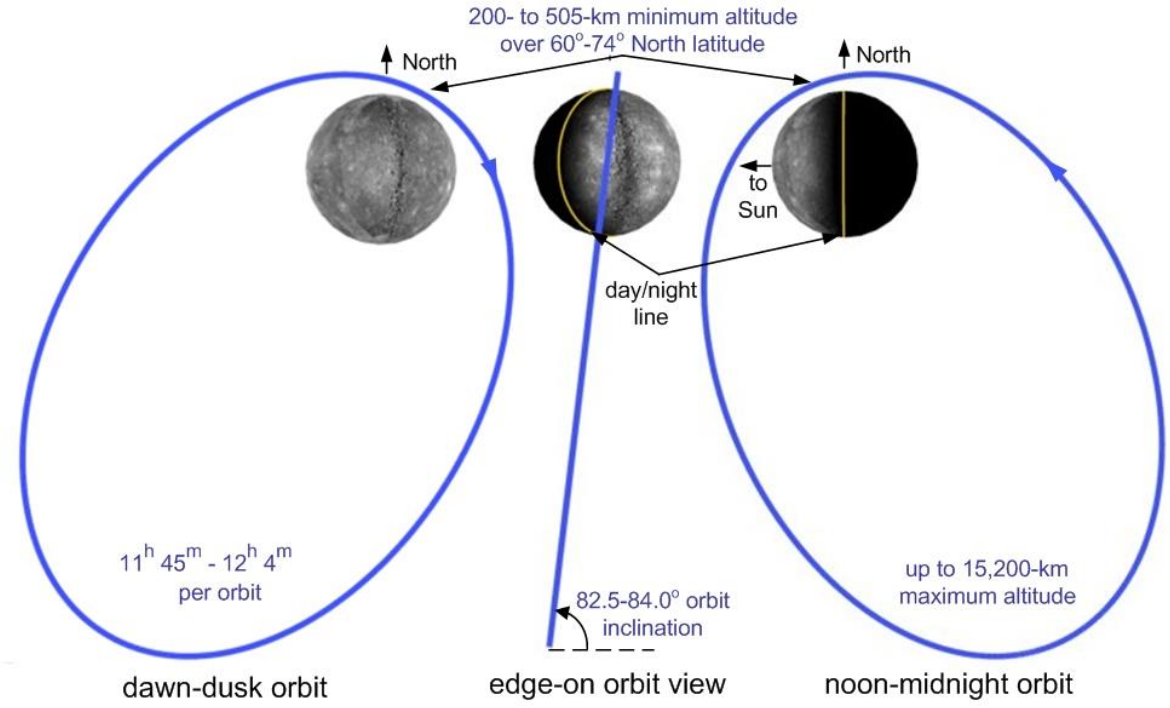

Figure 2.3 Schematic of MESSENGER's orbit during the primary mission phase (Image: NASA/ John Hopkins University Applied Physics Laboratory/Carnegie Institue of Washington).

2.1.3.2 Instruments

The mission had nine scientific Instruments onboard (Figure 2.4). The data were downloaded to Earth and stored in the Planetary Data System (https://pds-geosciences.wustl.edu/). I now give a brief overview of each instrument:

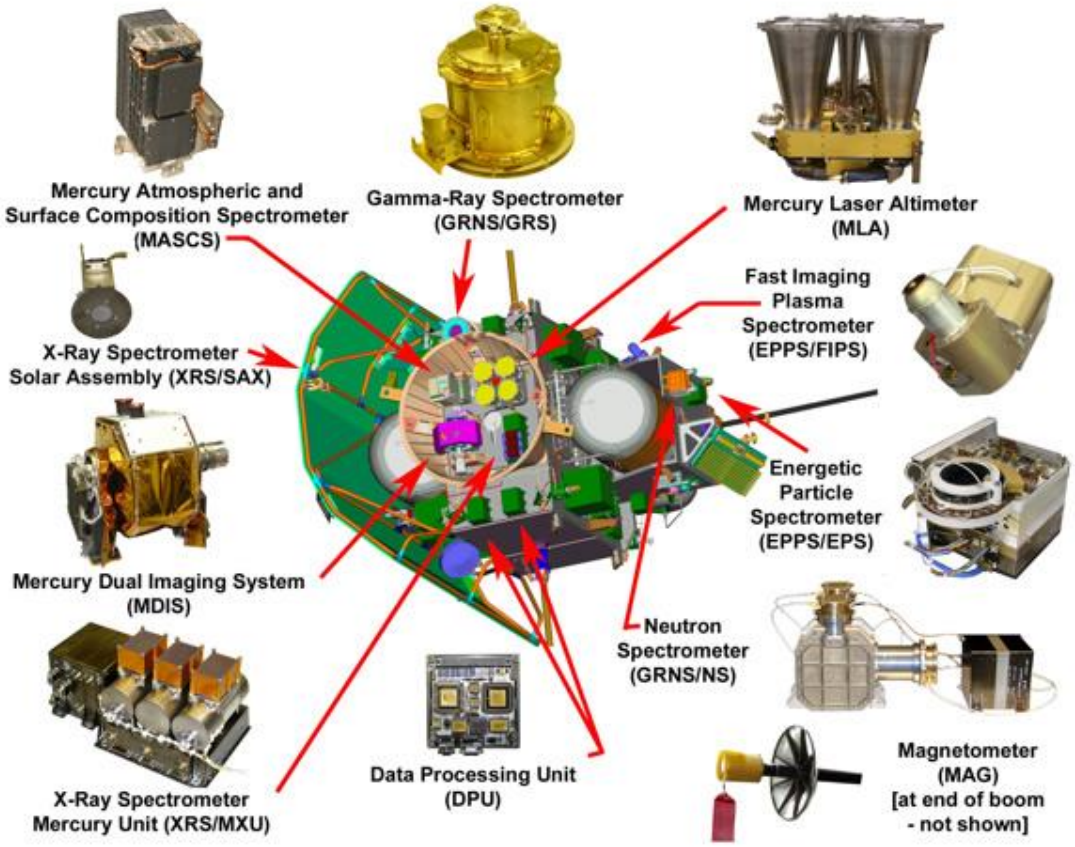

Figure 2.4 Schematic of MESSENGER showing the location of each instrument. (Image: NASA/ John Hopkins University Applied Physics Laboratory/Carnegie Institue of Washington).

2.1.3.3 Mercury Dual Imaging System (MDIS)

The Mercury dual imaging system (MDIS) consisted of two cameras: a narrow-angle camera (NAC) with a single filter for taking images of the surface with a field of view of 1.5°, and the Wide-angle camera (WAC) with a 10.5° field of view and 12-filters on a wheel. Both the NAC and WAC had a 1024 x 1024 charge-coupled device detector, which means that the NAC camera gave much more detailed images compared to the more extensive areas covered by the WAC. I used MDIS data for my research, predominatly NAC images. The first global maps were created with data from this instrument.

2.1.3.4 Mercury Laser Altimeter (MLA)

This used the two way travel time of laser pulses from MESSENGER bouncing off the surface of the planet and then detected by sensors on MESSENGER. The instrument produced points along a transect that can be used to recreate topographic profiles across the planet. Due to the elliptical orbit, the range was too great for data to be collected in the southern hemisphere (Figure 2.5). The laser fired at a frequency of 8 Hz, so the spot spacing varies along the transect depending on the orbital velocity at the time.

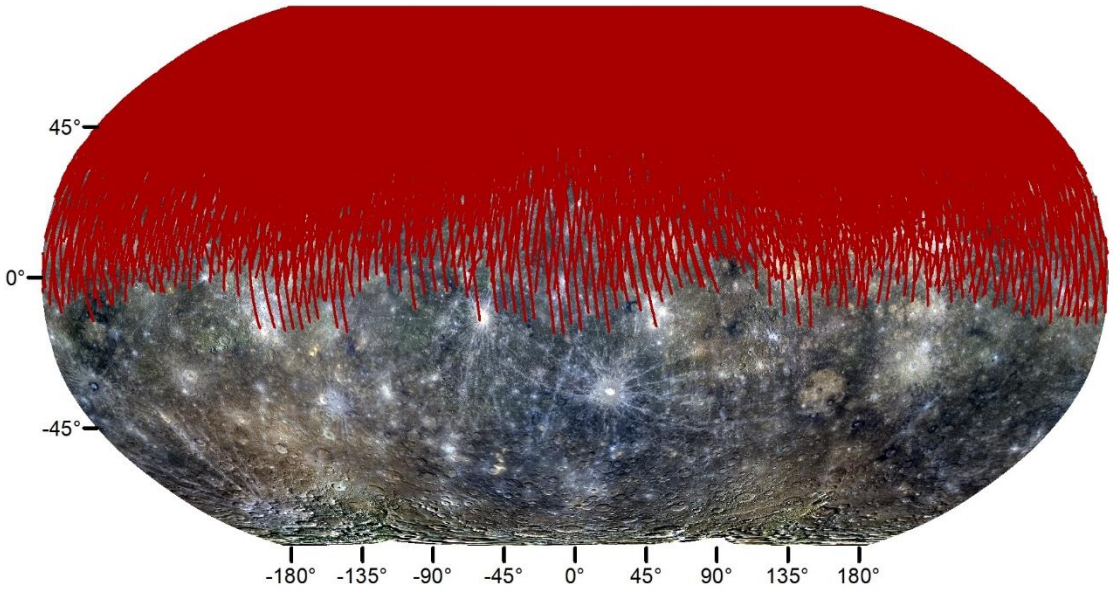

Figure 2.5 Map of MLA coverage (red) over Mercury, illustrating the northern bias in data collection. Basemap is global colour mosaic (Denevi *et al* 2018a).

2.1.3.5 Gamma-Ray Spectrometer

The Gamma-Ray spectrometer sensed gamma rays emitted in the top 0.1 m of regolith from radioactive decay (K, Th, U) or produced by the interaction of cosmic rays with O, S, Si, Fe, and H. It produced element maps of the planet's surface, but at very low spatial resolution.

2.1.3.6 Neutron Spectrometer (NS)

The Neutron spectrometer detected neutrons produced by cosmic rays interacting with hydrogen-rich material in the top 0.4 m of the planet's surface. It confirmed the presence of hydrogen, presumably in water-ice in permanently shadowed craters at high northern latitudes.

2.1.3.7 X-Ray Spectrometer (XRS)

This instrument detected X-rays fluoresced by the planet's surface to detect magnesium, aluminium, silicon, sulfur, calcium, titanium, and iron. The sensitivity of this instrument was highly dependant on the intensity of X-rays generated by the Sun. The XRS helped produce several major element maps of the surface of the planet (e.g. Nittler *et al*., 2020).

2.1.3.8 Magnetometer

This boom-mounted (to reduce the influence of the rest of the spacecraft) instrument measured the planet's magnetic field at a resolution of 0.047 nT.

2.1.3.9 Mercury Atmospheric and Surface Composition Spectrometer (MASCS)

Ultraviolet light emissions from Mercury's exosphere were detected by MASCS. It also detected UV-NIR light reflected from the surface, providing some insights into mineralogy, but it was a non-imaging instrument, collecting data only along the sub-spacecraft track (McClintock and Lankton 2007). MASCS has helped study the local composition of features on Mercury's surface as well as understand the planet's exosphere (e.g. Suzuki *et al.*, 2020).

2.1.3.10 Energetic Particle and Plasma Spectrometer

This device measured the composition and energy of charged particles in Mercury's magnetosphere.

2.1.3.11 Radio Science

This used changes in radio signals from the probe to measure changes in spacecraft velocity, from which the planet's gravitational field and core size could be constrained.

2.1.4 BepiColombo

BepiColombo is a joint ESA/JAXA mission (Benkhoff *et al* 2010), launched in October 2018 and on route to Mercury. It will arrive in orbit in 2025 and start its science campaign in 2026. The mission is comprised of two satellites: Bepi and Mio. Mio is the Japanese orbiter and will study the Mercury exosphere and environment with an orbit of 590 x 11,640 km. Bepi will orbit the planet at a lower and more circular orbit (480 x 1500 km) to study its surface and interior principally. The Mercury transfer module is used for propulsion during the cruise to the planet (Figure 2.6).

Figure 2.6 BepiColombo component spacecraft. From bottom to top these are the Mercury Transfer Module, 'Bepi', Sunshield and Interface Structure, and Mio. (Image: ESA)

Bepi's instruments for studying Mercury's surface include:

BepiColombo Laser Altimeter (BELA), Italian Spring Accelerometer (ISA), Mercury Magnetometer (MPO-MAG, MERMAG), Mercury Radiometer and Thermal Infrared Spectrometer (MERTIS), Mercury Gamma-ray and Neutron Spectrometer (MGNS), Mercury Imaging X-ray Spectrometer (MIXS), Mercury Orbiter Radio-science Experiment (MORE), Probing of Hermean Exosphere by Ultraviolet Spectroscopy (PHEBUS), Search for Exosphere Refilling and Emitted Neutral Abundances (SERENA): two neutral and two ionised particle analysers, Spectrometers and Imagers for MPO BepiColombo Integrated Observatory System (SIMBIO-SYS), high-resolution stereo cameras and a visual and near-infrared spectrometer, Solar Intensity X-ray and Particle Spectrometer (SIXS), see Figure 2.7.

SIMBIO-SYS will map the entire planet in stereo; with an average resolution of <110 m, a maximum stereo resolution of 50 m per pixel. Additionally, it will image the globe in three colours at a spatial resolution of <110 m. A high-resolution camera will provide images with a resolution of 5 m/pixel from an altitude of 400 km. It also has a hyperspectral imager to provide a global map of mineralogy. BELA will provide spot heights approximately 250 m apart along-track and with tracks every 25 km at the equator.

BepiColombo will build on the work of MESSENGER. To make sure that the most is made out of its capabilities, as much information as possible should be first extracted from MESSENGER data so that areas of special interest can be identified in advance.

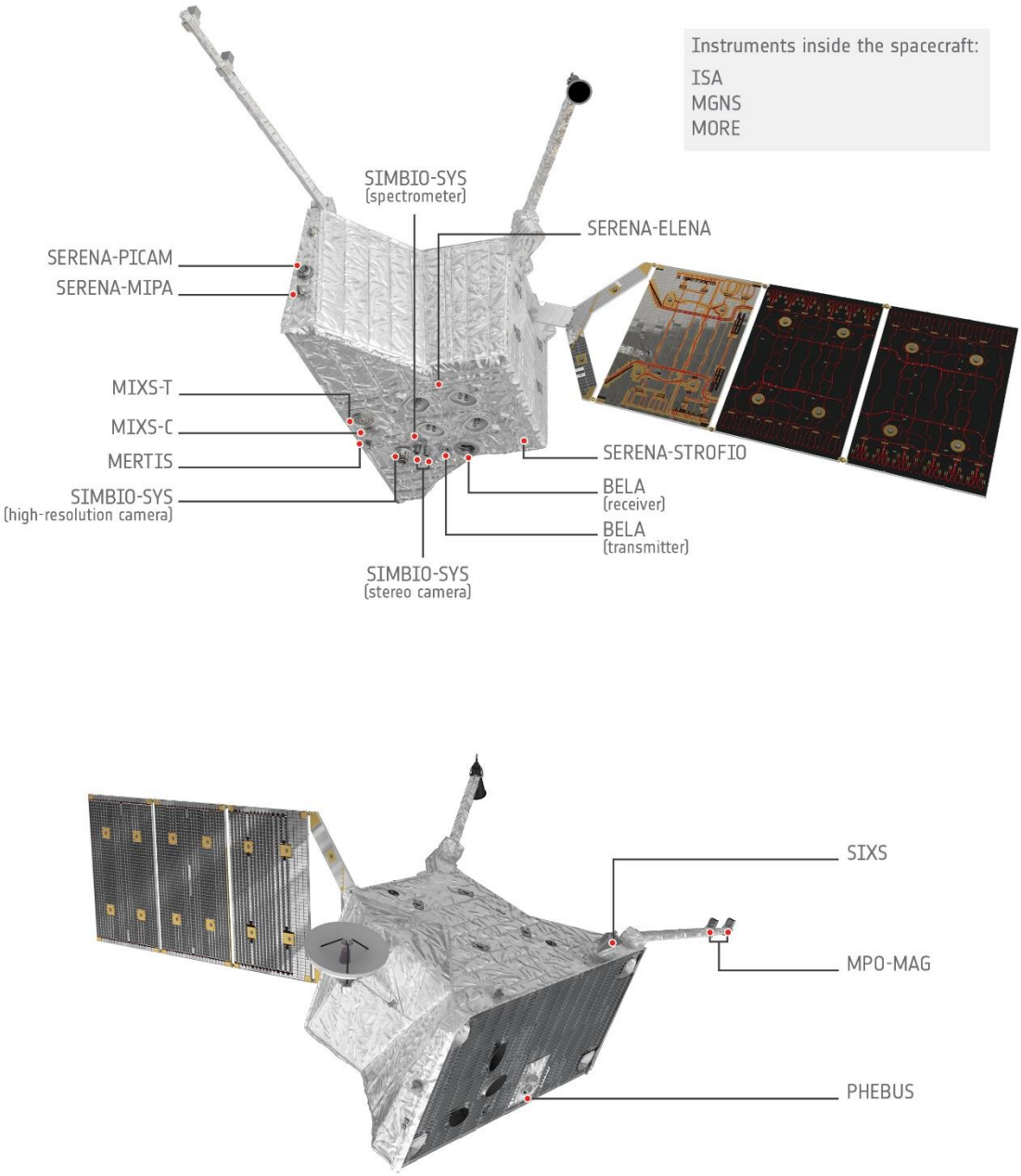

Figure 2.7 Schematic of 'Bepi' showing the location of instruments. (Image: ESA)

2.2 Size and Orbit

Mercury is the closest planet to the Sun. It has an elliptical orbit ranging between 0.31 and 0.47 AU (an eccentricity of 0.21, the largest of any planet), and its orbit is inclined 7° relative to the ecliptic. Mercury has the lowest axial tilt of any planet with an obliquity of only 0.03°.

The planet takes 87.969 days to orbit the Sun. Radar observations show that it takes 58.646 Earth days to spin once on its axis (Pettengill and Dyce 1965). The planet has a 3:2 resonance, with three rotations on its axis for every two orbits of the Sun (taking precisely 175.938 days); a consequence of this is a sidereal day (Sunrise to Sunrise at the same location) takes 175.938 days.

As the planet completes one orbit, it rotates one and a half times, resulting in the same point on the planet's equator facing the Sun at perihelion every other orbit, with the opposite side of the planet closest during the following perihelion. These two locations are called 'hot poles'. There are also two 'cold poles' which are the two points on the planet's equator that face the Sun at aphelion.

Over time a planet's perihelion will precess (rotate) around the Sun. Mercury's precession was slower than suggested by Newtonian Mechanics, and instead, is best explained by General Relativity (Einstein 1915).

Mercury's radius is 2439.36±0.02 km (Perry *et al* 2015). It does not have a significant equatorial bulge due to its slow rotation, and so its polar radius is only 1.65 km less than its equatorial radius. The planet has a surface area of approximately 7.5×10^7 km^2, equal to half the landmasses on Earth.

2.3 Magnetic Field and Exosphere

One of the most surprising outcomes from Mariner 10 was the discovery of Mercury's magnetic field (Ness *et al* 1974, 1975). The planet is the only terrestrial body, other than Earth, to generate a magnetic field. Its strength is 300 nT, approximately 1% of Earth's (Ness *et al* 1975). It is so weak that, during the largest solar storms, the solar wind can push the field back into the surface of the planet, exposing the dayside surface to the solar wind (Slavin *et al* 2019).

Mercury's atmosphere consists solely of an exosphere; where molecules are gravitationally bound, but the densities are too low to act like a gas, instead they move ballistically. The exosphere is composed of hydrogen, helium, oxygen, sodium, calcium, potassium, magnesium, aluminium, iron, and water vapour (Vervack *et al* 2016). These molecules either come from the surface of the planet, the solar wind (hydrogen, helium), and micrometeoroids. The solar wind pushes away the exosphere creating a tail behind Mercury. This tail has been observed from Earth (Figure 2.8, Baumgardner, Wilson and Mendillo, 2008) and also from Mercury by MESSENGER (Vervack *et al* 2016). The exosphere is then lost through ionisation by sunlight, reaching escape velocity, or adsorption onto the planet's surface.

The exosphere shows variation during its day-night cycle (the dayside increasing the number of Ca molecules, the night side decreasing it). Mercury has sessional cycles; caused by orbital eccentricity, with a higher density exosphere during aphelion, due to the lower intensity of solar wind (Suzuki *et al* 2020).

Changes in solar activity also modify the density of the exosphere (Potter *et al* 1999) though there is variation between how different elements change (McClintock *et al* 2018).

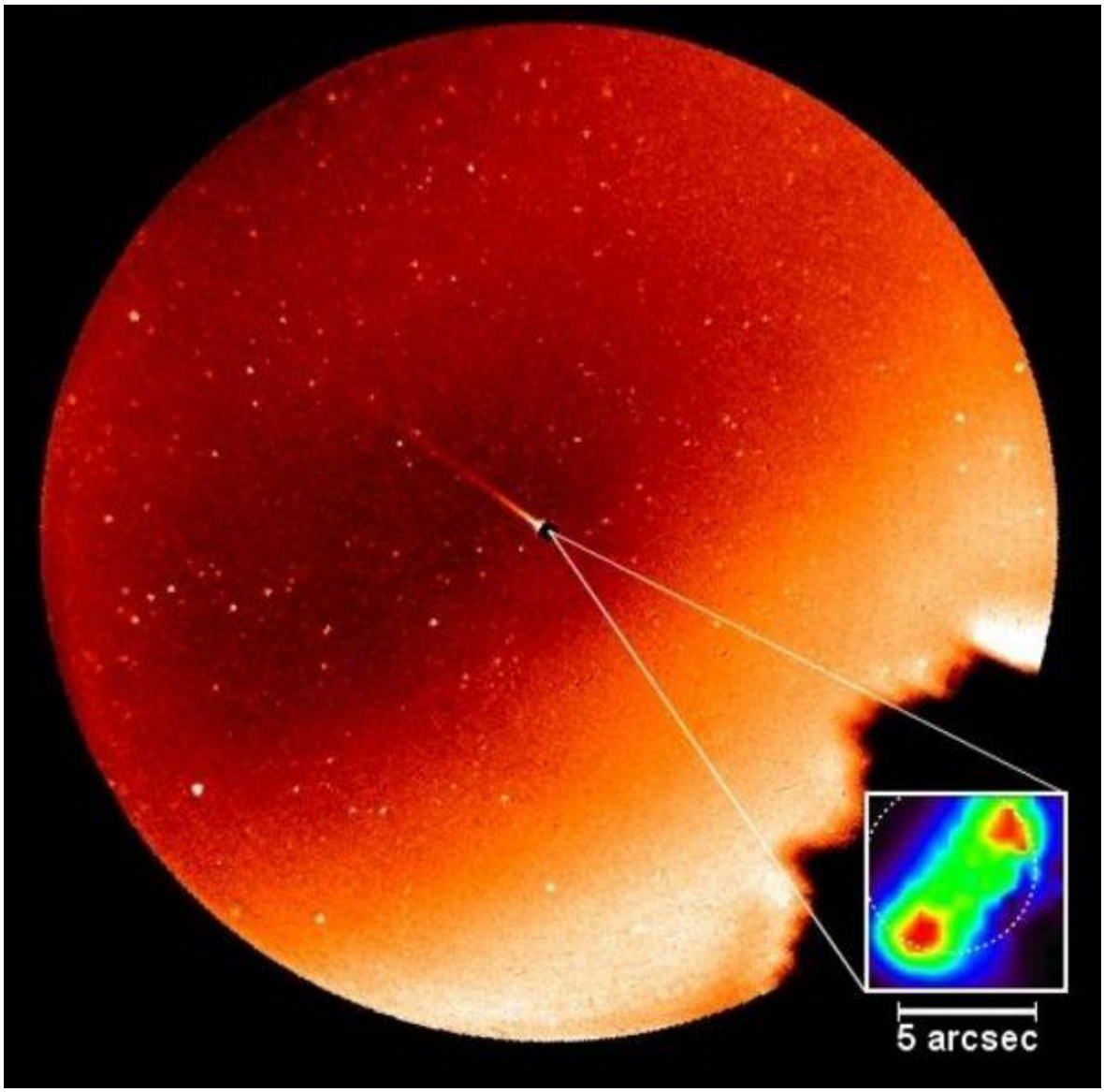

Figure 2.8 Mercury's sodium gas tail as viewed from the McDonald Observatory, Texas, USA, using a Sodium filter. Mercury is blacked out (centre of image) with a tail of sodium extending 2.5 million kilometres long towards the top left in the image. (Sun to the bottom right). Insert shows the origin of the sodium Ions on the planet's surface (Source: Center for Space Physics, Boston University).

2.4 Gravity and Interior

Perturbations in Venus' orbit, detected by radio astronomy, enabled the calculation of Mercury's density as 5.42 g/cm^3 (Ash *et al* 1971). This measurement was refined by Mariner 10 to 5.44 g/cm^3 (Howard *et al* 1974) and MESSENGER; 5.429 g/cm^3 (Smith *et al* 2012). Mercury's density is the second-highest in the solar system

after Earth (5.514 g.cm^3), as result of this, and the planet's small radius is that the surface gravity at Mercury is 0.37 m/s^2 compared to Mars 0.38 m/s^2. However, Earth's density is similar to Mercury's only because Earth greater mass has caused a great deal of self-compression. Mercury's uncompressed density is much greater than Earth's uncompressed density.

Mercury's high uncompressed density is due to its sizeable core with only a thin outer silicate layer. It has a metallic core of ~1860 km in radius (Figure 2.9), 76% of the planet's radius compared to 54% for Earth (Solomon 1976).

The active generation of the magnetic field is a sign of a (partially) liquid core with both a thermal and chemical gradient to induce convection. The weakness of Mercury's magnetic field possibly requires stable, stratified layers in the liquid core to dampen convection. (Christensen and Wicht 2008, Manglik *et al* 2010). A pure iron core would have already frozen, and so it needs some impurities to keep it molten. Silica is soluble under Hermian conditions and, along with sulfur, likely to help keep the core molten. (Namur *et al* 2016, Hauck *et al* 2013). Gravity models of the planet, in combination with studies of the variation in the spin axis of the planet relative to Mercury's orbital plane, suggest that Mercury probably has a solid inner core with a radius of 0.3-0.7 of the total core (Genova *et al* 2019).

The silicate layer outside the core divides into the crust (the outer part rich in Al, Si, Na, and Ca) and the mantle: the inner silicate layer rich in magnesium silicates. The crust is estimated to be 35 ± 18 km thick (Padovan *et al* 2015) and but may be as thin as 26 ± 11 km (Sori 2018). There are substantial regional variations and it may thin to <30 km near the North pole. The crust thickness may vary by 24 km between the hot and cold poles (Perry *et al* 2015, Padovan *et al* 2015). Mercury's mantle is 500-580 km thick, dominated by magnesium silicates. Mantle convection is likely to be either ongoing or ended within the last few 100 Ma (Hauck *et al* 2018).

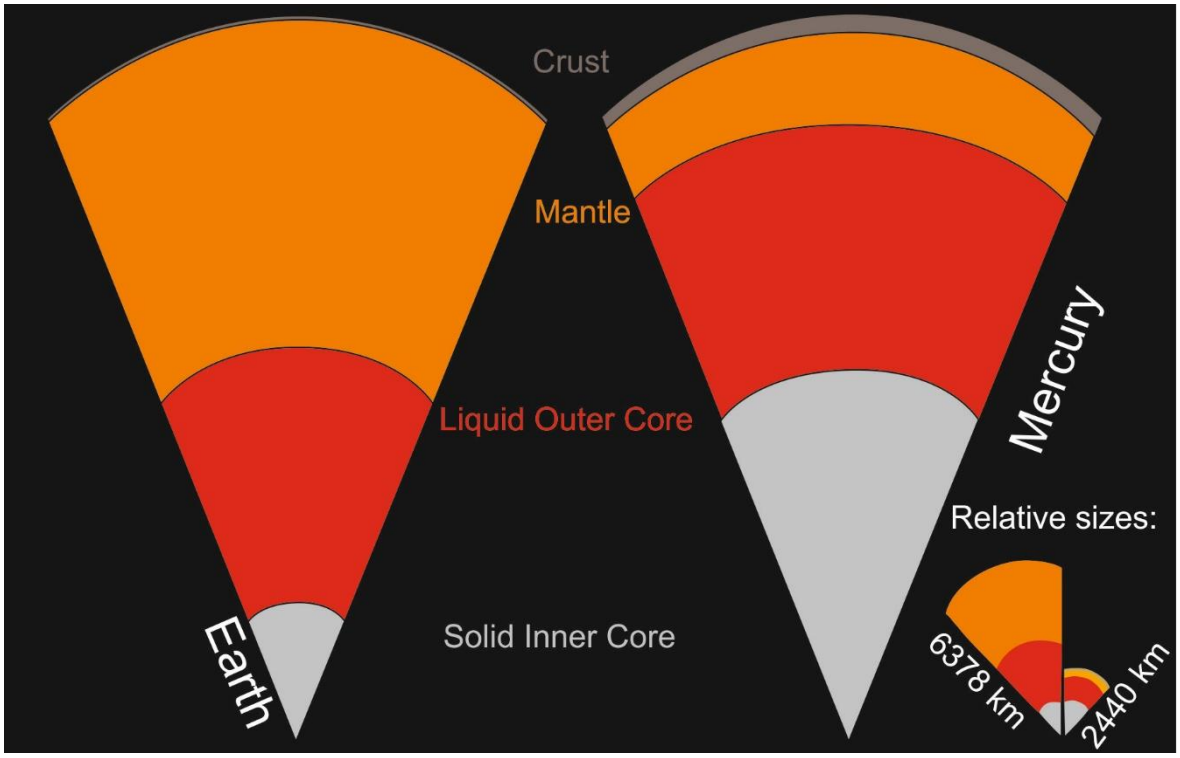

Figure 2.9 Schematic showing the relative sizes of the interior structures of Earth (left) and Mercury (right). The bottom right shows absolute sizes, modified from an image by NASA/Johns Hopkins University Applied Physics Laboratory/Carnegie Institution of Washington.

2.5 Mercury's Surface

Two main features dominate Mercury's surface: impact craters and the plains between them (Dzurisin 1978, Spudis and Guest 1988, Solomon *et al* 2008). They reflect the geological processes that formed and modified the planet's surface and guided the understanding of the planet's history.

2.5.1 Impact Cratering

Impact craters are the most dominant landform on the planet. Impact craters have a range of sizes, with morphologies changing as the crater size increases, depending on the mass and velocity of the bolide and the rheology of the planet surface (e.g. Melosh, 2011). A simple crater is a bowl-shaped depression in the ground. Complex craters have flat floors, terraced walls, and a central peak in the middle of the crater. In larger craters, the peak becomes a ring, and they become a peak-ring basin. Protobasins are an intermediary with a partial ring and small peak (Figure 2.10). Multi-ring basins are the largest sizes and can have multiple rings inside them (Melosh 2011). On Mercury, the transitions between crater morphologies occur at the following diameters: simple <1-10 km, complex 10-168 km, protobasin: 50 – 195 km, peak-ring basins 85-320 km and large basins >300 km. The majority of large basins on Mercury only have one ring rather than forming multi-ring basins as seen elsewhere in the solar system, probably due to a combination of volcanic resurfacing, lithospheric relaxation, or failure to form multi-ring structure (Fassett *et al* 2012).

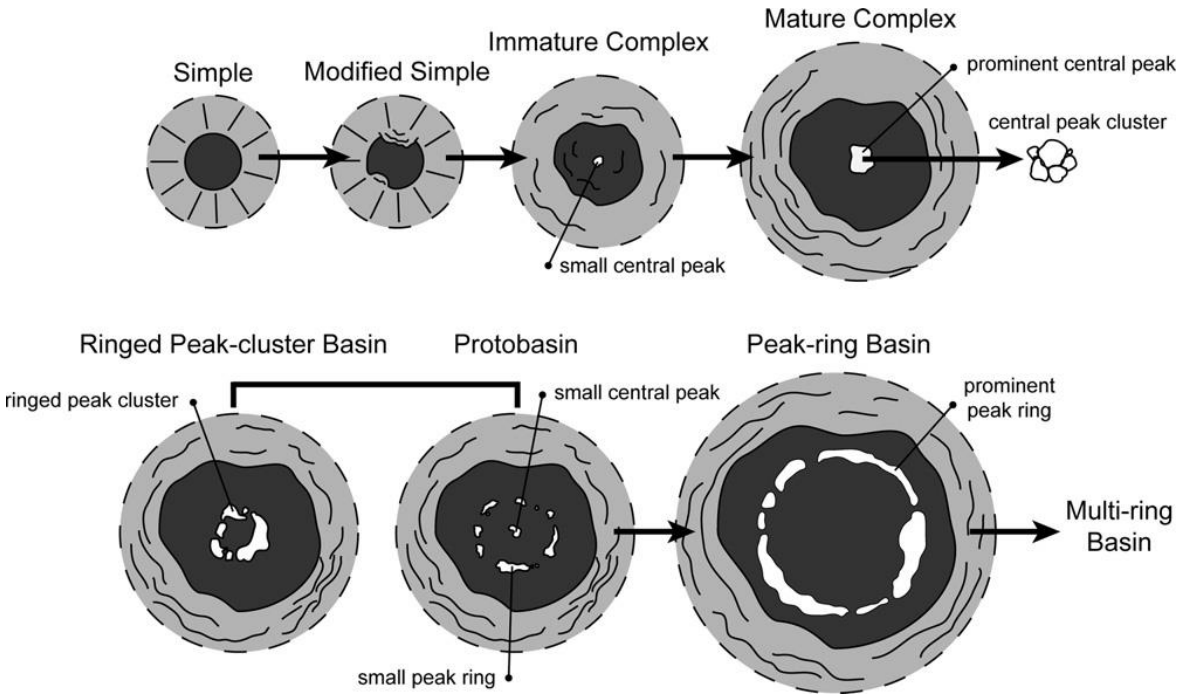

Figure 2.10 Schematic of the range of crater morphologies and intermediate stages showing that the morphologies are a continual evolution rather than discrete type. Image: Baker *et al.*, (2011).

Secondary craters are impact craters generated by material thrown out during the formation of impact craters (Roberts 1964). Secondary craters are found as clusters, chains or individual craters. Mercury's high gravity and the relatively high velocity of objects at this part of the solar system means that secondary craters can be up to 10 km in diameter (Strom *et al* 2008, 2011).

2.5.1.1 Caloris Impact Basin

Whilst 94 large impact basins (>300 km) have been identified on Mercury, many of them are poorly preserved and usually only identifiable in topography (Fassett *et al* 2012, Orgel *et al* 2020). The largest visible impact basin on the planet is the (informally named) Caloris impact basin (Figure 2.11), with a diameter of 1550 km (Ernst *et al* 2015, Fassett *et al* 2009).

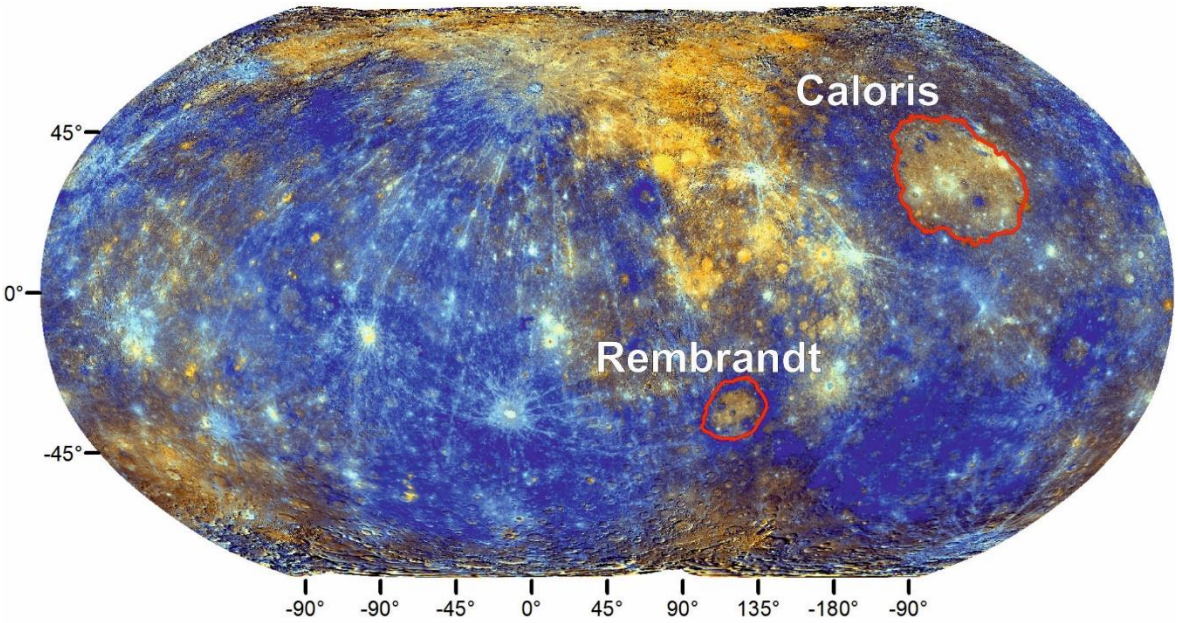

Figure 2.11 Map of Mercury showing the location of Caloris and Rembrandt impact basins on the enhanced data record basemap (Denevi *et al* 2016) *using a Robinson projection centred on 45°E.*

Just under half of Caloris was imaged by Mariner 10 and mapped. However, MESSENGER imaged the basin in its entirety, and several maps have been produced with this data, making it the best-studied impact basin on the planet. The ejecta around Caloris has been split into multiple units summarised in Table 2.1, one of the interpretations shown in Figure 2.12. One (partial) map of Caloris groups the Van Eyke, Caloris Montes and Nervo formations into a single Caloris Rough Ejecta unit (Mancinelli *et al* 2016).

Table 2.1 Caloris Morphological Mapping units.

Unit Name	**Description**	References and comments
Van Eyke Formation	Ejecta with linear features caused by secondaries scouring and ejecta rays	(Fassett *et al* 2009, Mccauley *et al* 1981, Schaber and McCauley 1980)
Odin Formation	Blocks of ejecta 'knobs' on plains mantled by impact melt or ejecta	(Fassett *et al* 2009, Mccauley *et al* 1981, Schaber and McCauley 1980)
Caloris Montes/Caloris rim	Large mountains formed from ejecta blocks forming the basin rim	(Fassett *et al* 2009, Mccauley *et al* 1981, Schaber and McCauley 1980)
Nervo Formation	Patches of hackly rolling plains draped over the underlying morphology	Variable usage: Fassett *et al.* (2009) do not identify it as a morphological unit, Schaber and McCauley (1980); Mccauley *et al.* (1981); & Goosmann *et al.* (2016) all do identify it.

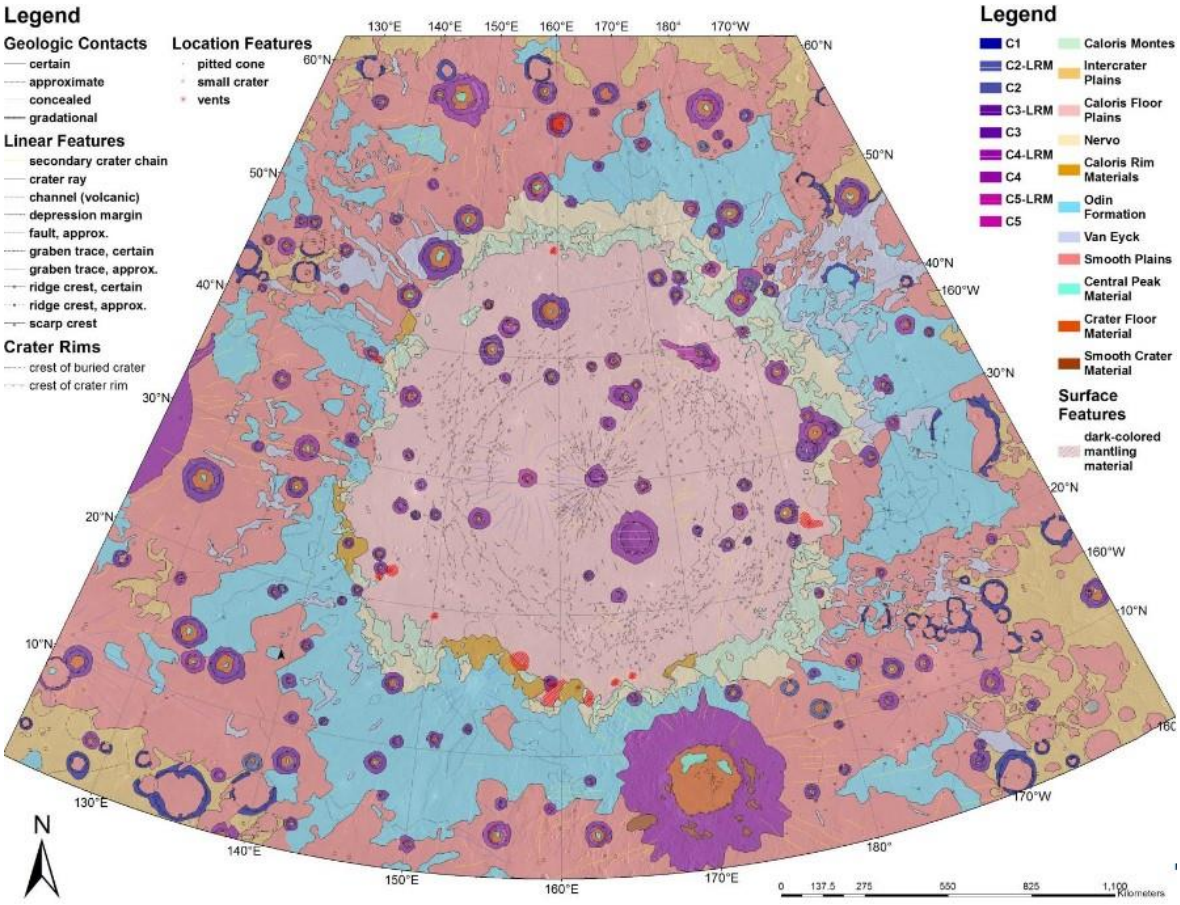

Figure 2.12 Geological map of Caloris from Goosmann *et al.* (2016) and Buczkowski *et al.* (2017).

2.5.1.2 Rembrandt Impact Basin

The second-largest, clearly visible impact basin is Rembrandt at 715 km diameter (Watters *et al* 2009a), part of which is within the quadrangle that I have mapped (see chapter 3). Its morphology is different to Caloris as part of its interior includes hummocky material, which may be the original crater floor, suggesting it was not entirely covered by lavas (Watters *et al* 2009a). Rembrandt is being mapped using morphology by Hynek *et al.* (2017, Figure 2.13). Similar to Caloris, there are a rim and a lineated unit, some of the plains have been divided by albedo, and there is the interior hummocky unit (Figure 2.13). Semenzato *et al.* (2020) created both a morphology map and an additional map which included interpretation of stratigraphic units as well as morphologies. They identified patches of the interior Smooth Plains, which may be the youngest Smooth Plains on Mercury (Section 2.5.2).

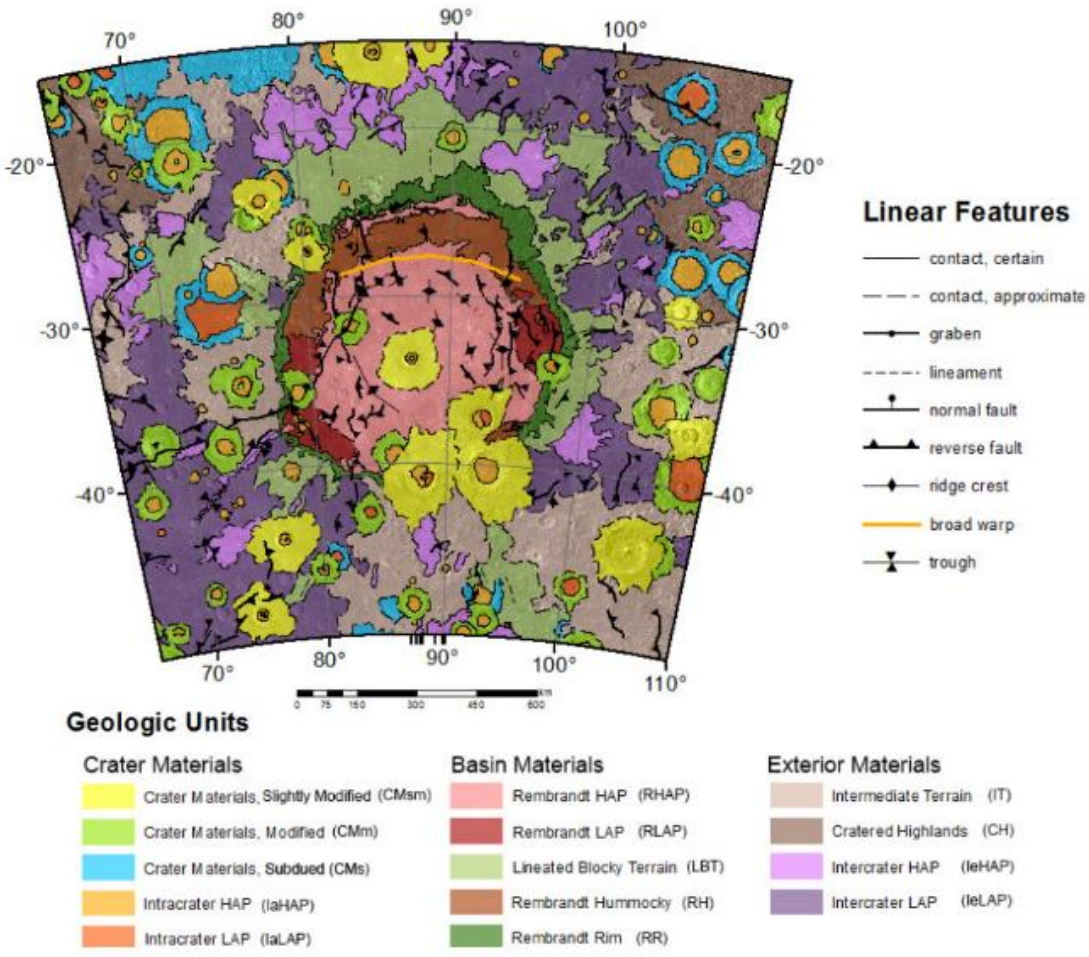

Figure 2.13 Preliminary geomorphic map of Rembrandt from Hynek et al. (2016).

2.5.2 Plains

Mercury's plains have been divided up by both morphologies and by spectral properties. I briefly examine both of these systems:

There are three different plain morphologies: Intercrater Plains, Smooth Plains and, variably, Intermediate Plains (Trask and Guest 1975, Murray *et al* 1975, Spudis and Guest 1988, Whitten *et al* 2014a, Strom *et al* 2011). I briefly describe them here; see chapter 3.7.2 for a more detailed description of their morphology.

Intercrater Plains have a high density of small and secondary impact craters; these plains cover the majority of the planet outside impact craters. The oldest areas are dated at 4.0-4.1 Ga (Marchi *et al*., 2013). Smooth Plains are flat and relatively uncratered and as considered the youngest plains on Mercury. Most are older than about 3.5 Ga (Byrne *et al* 2016). Intermediate Plains have an intermediate in roughness or crater density as compared to the Intercrater Plains and Smooth Plains. The Intermediate Plains are a controversial unit, with Whitten *et al*. (2014) suggesting they are small patches of Smooth Plains prematurely aged by nearby impact craters, or areas of intercrater plains that by chance have not been as heavily cratered. Mapping of the planet based on morphological plains has been completed at a scale of 1:15 million and is underway at a scale of 1:3 million (see chapter 3.1).

2.5.3 Spectral Characteristics

The first-order controls on albedo and colour contrast in multispectral images of Mercury are fresh crater materials (such as those from Hokusai). The rest of Mercury shows lower variations in reflectance compared to the Moon (Robinson *et al* 2008, Denevi *et al* 2009, Robinson and Lucey 1997). The Mercury Dual Imaging System (MDIS) spectral bands show a red slope which suggests a general lunar-like space weathering through time. Variations between units are little more than a change of steepness of the slope between bands (Denevi *et al* 2009).

The surface can be divided up into multiple units based on their reflectance (typically at 0.75 μm) and the 430-nm/1000-nm ratio (to determine if they are relatively more reflective in the blue or infrared parts of the spectrum). These spectral units include: Low-reflectance material (LRM), Low-reflectance blue plains, Intermediate Plains (which is separate to the morphological Intermediate Plains), High Reflectance Plains; additional less common units include: red spots (first identified by Rava & Hapke, (1987) and subsequently linked to explosive volcanism, section 2.6.2), bright hollows (section 2.9), and fresh crater materials (Murchie *et al.*, 2015). The spectral plains do not correspond to morphological plains. The High Reflectance Plains are found only in Smooth Plains but not all Smooth Plains are High Reflectance Plains. The lack of correlation is not yet understood (Robinson *et al* 2008, Domingue *et al* 2017, Prockter *et al* 2016).

The LRM has a reflectance up to 30% lower than the average surface and usually found impact ejecta from large craters (Robinson *et al* 2008, Murchie *et al* 2015, Thomas *et al* 2016, Denevi *et al* 2009). LRM contains up to 5% graphite (Murchie *et al* 2015, Klima *et al* 2018, Peplowski *et al* 2016). Spectral mapping has the advantage of showing that the crust has some heterogeneity, with some craters excavating low reflectance material from beneath areas of high reflectance materials (Denevi *et al*., 2009). The LRM is interpreted to be the remains of a flotation crust (Vander Kaaden and McCubbin 2015) that formed as a skin on the magma ocean and is the earliest remains of a surface. This layer was between 100 m and 10 km thick, depending on the amount of carbon in Mercury (Vander Kaaden and McCubbin 2015) but now covered over by lavas and heavily modified by impacts.

2.5.4 Composition

MESSENGER's XRS, MASCS and neutron spectrometer provided the first geochemical information about the planet's composition. MESSENGER's spectrometers (X-ray and Gamma) have enabled the development of a greater understanding of the composition of the planet. It was previously assumed, due to the planet's high density and the understanding of the Lunar crust, that Mercury has an iron-rich crust (Strom *et al* 1975). However, It has subsequently been discovered that the crust is highly depleted in iron with only 1-2 wt% (Weider *et al* 2015, 2016, McClintock *et al* 2008, Nittler *et al* 2011). Mercury's crust has an average Mg/Si ratio of 0.33-0.67; this composition is between basalt and komatiite (Nittler *et al* 2011); however, its MgO concentration and low TiO_2 is closer to boninite, which is a form of primitive andesite (Vander Kaaden *et al* 2017).

The crust has an average of 4 wt% sulfur and 1-2% carbon (Peplowski *et al* 2016). It has an O/Si ratio of 1.2 ± 0.1, which is markedly lower than in other rocky bodies of the solar system (McCubbin *et al* 2017). The low iron, oxygen and high sulfur content of Mercury surface suggest Mercury formed under highly reducing conditions, with nearly all the iron partitioning into the core, so making Mercury the most reduced terrestrial planet (Namur *et al* 2016). Mercury's K/Th ratio (Figure 2.14) suggests the abundance of more volatile elements (K) relative to the more refractory elements (Th) is similar to Mars', slightly higher than Venus and Earth, and well above that of the Moon (Peplowski *et al* 2012).

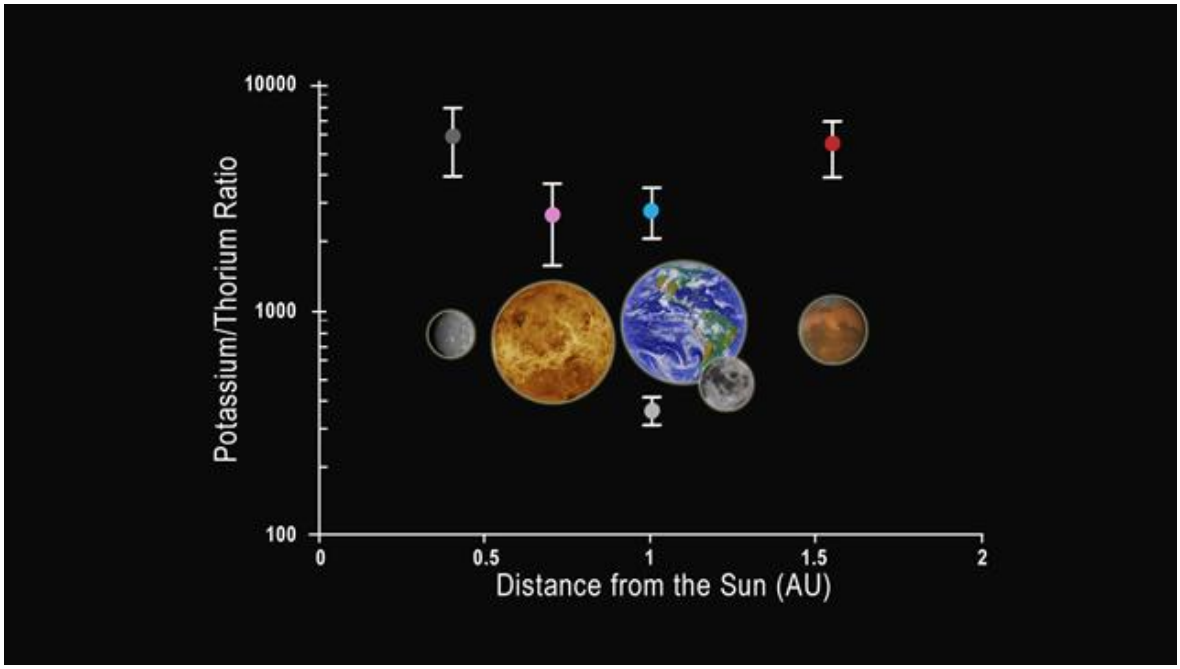

Figure 2.14 Potassium/Thorium ratios for the inner solar system Image credit: NASA/Johns Hopkins University Applied Physics Laboratory/Carnegie Institute of Washington.

Older terrains, in general, have higher Mg/Si and S/Si ratios and a lower Al/Si ratio than the Smooth Plains and so Mercury's Intercrater Plains is relatively more basic, and the Smooth Plains are of a more evolved composition (McClintock *et al* 2008, Weider *et al* 2012, Solomon *et al* 2008), with Mg/Si of 0.57 in the Intercrater Plains and 0.34 in the Northern Smooth Plains (Weider *et al* 2012). There are several discrete

geochemical regions in the northern hemisphere (Figure 2.15), but there is insufficient resolution in the southern hemisphere due to MESSENGER's orbit. The most striking is the High Magnesium Region, which is enriched in magnesium relative to the rest of the planet (Stockstill-Cahill *et al* 2012, Nittler *et al* 2020), but there is no spectral or morphological unit that correlates with this. The Smooth Plains within the Caloris impact basin are different from the Northern Smooth Plains, suggesting a chemically heterogeneous mantle (Weider *et al* 2015, Namur *et al* 2016).

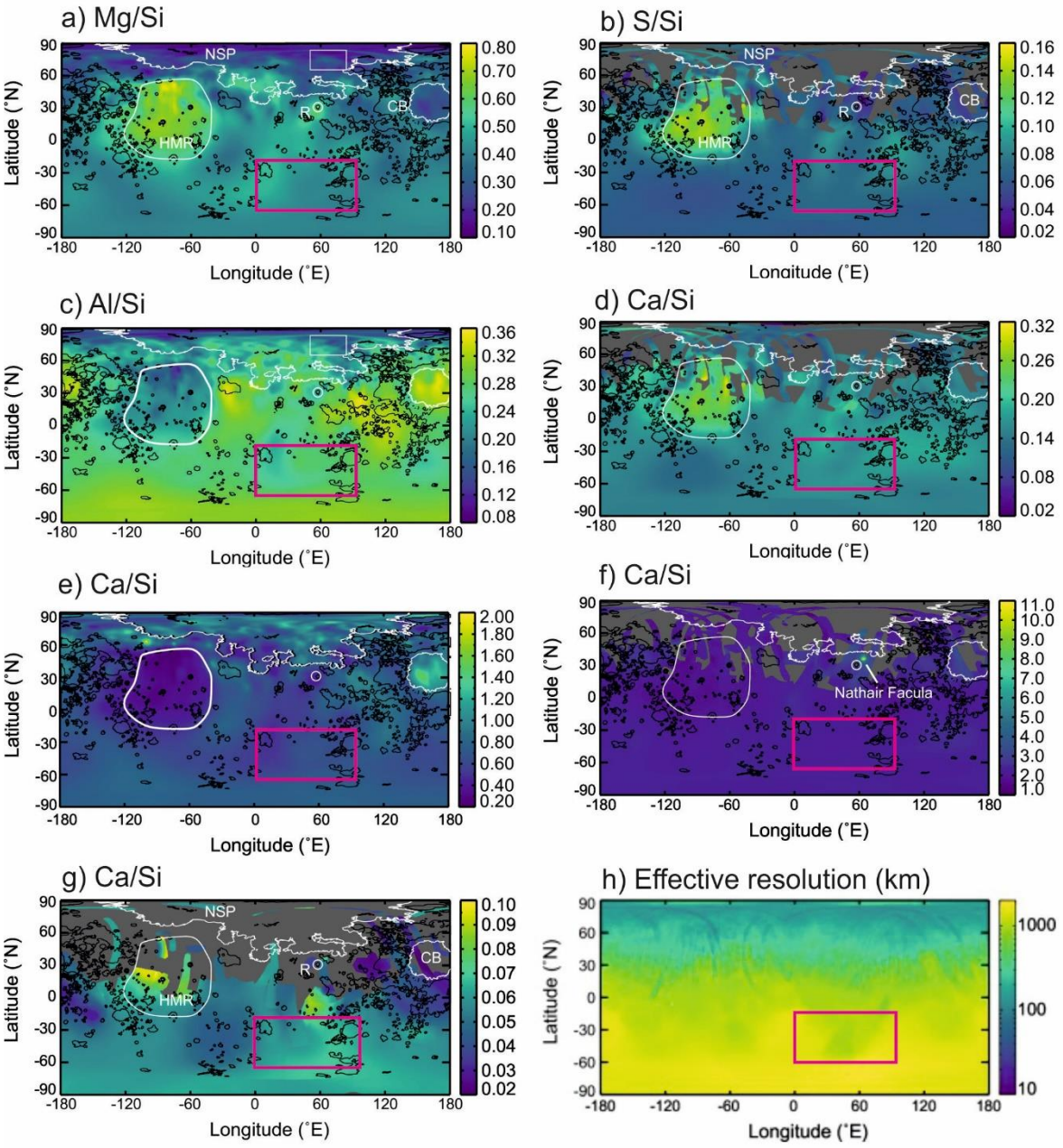

Figure 2.15 Element ratio maps of Mercury, with the location of H-14 overlayed. Modified from Nittler et al. (2020).

2.5.5 Chronostratigraphy

Mercury's geological history has been divided into five chronostratigraphic units to provide context to surface studies. This geological history is based on features seen on the surface of the planet, in the same manner as originally used for the Lunar time periods (Figure 2.16, Spudis and Guest, 1988).

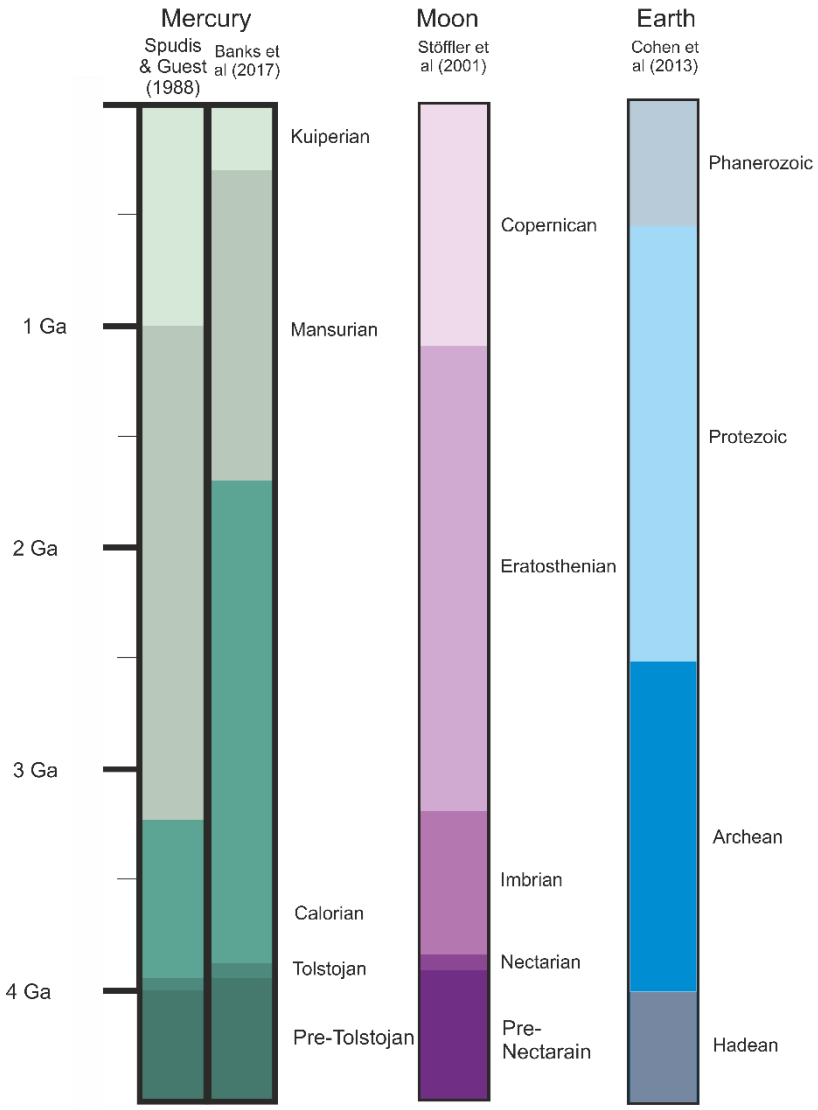

Figure 2.16 Geological time periods of Mercury compared to the Moon (Stoffler and Ryderm 2001) *and Earth* (Cohen *et al* 2013), *authors own schematic.*

The oldest period is the Pre-Tolstojan which relates to those features and surfaces generated before the Tolstoy impact basin formed (Spudis and Guest 1988). The base of the Tolstojan is marked by the Tolstoj basin impact. There are several basins, including Beethoven and some Smooth Plains may be emplaced during this interval (Spudis and Guest 1988, Whitten *et al* 2014a). The start of the Calorian system is marked by the Caloris impact event, which occurred towards the end of the late heavy bombardment (Oberst *et al.*, 2010; Strom *et al.*, 2011; Fassett, Head, Baker, *et al.*, 2012). The Mansurian is dominated by cratering and crater degradation rather than endogenic processes. Impact craters that show some signs of degradation but the

ejecta and rims are still intact are considered Mansurian (Spudis and Guest 1988). The craters in the Kuiperian system are distinguished by fresh rayed craters, named after the Kuiper crater (Spudis and Guest 1988).

There are several issues with using impact crater dating on Mercury for both absolute and relative dating. The impact flux is poorly understood; this leads to large error bars in the production rate on the surface and dramatically changes the age range. Banks *et al*. (2017) have suggested that the Mansurian may have begun as late as 1.9 Ga (+/- 0.3 Ma), and the Kuiperian as recently as 300 Ma (+/-40 Ma) depending on which impact flux model is used. Similarly, the weathering rates of rays and terraces are poorly constrained due to proximity to the Sun, the poorly understood cratering flux, and the effect of the magnetic field on weathering (Pokorný *et al* 2017), which will modify the Mansurian and Kuiperian crater ages. Additionally, it has yet to be quantified how quickly features of different scales are lost. Larger craters have bigger features such as ejecta and terracing and degrade more slowly than the same features on smaller craters. Thus, it is important to use crater degradation with a measure of scepticism.

2.6 Volcanic History

Past volcanic activity has occurred on all terrestrial planets in the solar system as well as several moons. Mercury is no exception to this, with examples of both effusive and explosive volcanism.

2.6.1 Effusive Volcanism

Mariner 10 showed that there are numerous Smooth Plains with a low abundance of impact craters on the surface of Mercury. There was a debate as to whether Mercury's plains are volcanic in origin (Murray *et al* 1975, Strom *et al* 1975, Trask and Guest 1975) or originated from impact melt. The latter was mooted because volcanism is difficult under global compression (Strom *et al* 1975) and because it fitted neatly with the relatively low albedo variation between the plains relative to those on the Moon (Wilhelms 1976).

MESSENGER data supported several lines of evidence for a volcanic origin to the majority of plains. Smooth Plains cover craters to a much greater depth than would be expected by the volumes of melt generated by impactors (Padovan *et al* 2016) and plains embay craters without draping over more elevated nearby topography, as would be expected by impact melt. Ghost craters, which are craters that are completely covered by lavas but outlined by cooling structures (e.g. Cruikshank, Hartmann and Wood, 1973; Watters *et al.*, 2012; Crane and Klimczak, 2019), are found within flooded crater floors showing time passed between the formation of the basin (when impact melts are deposited almost immediately after) and the emplacement of Smooth Plains (Murchie *et al* 2008). Widespread Smooth Plains emplacement is thought to have ended by 3.5 Ga (Byrne *et al* 2016, Byrne 2020). Smaller-scale, more recent occurrences include the inner ring of Rachmaninoff (Prockter 2010) and part of the floor within the Rembrandt impact basin (Semenzato *et al* 2020).

The origin of Intercrater Plains is less clear as no morphological indicators indicate their origin (Strom et al., 2011; Trask and Guest, 1975; Whitten *et al*., 2014). The youngest Intercrater Plains overlap in date with

the oldest Smooth Plain ages (Whitten *et al* 2014a), though Whitten does not include Intermediate Plains in this analysis. As they are not so old as the lunar highlands (Strom *et al* 1975, 2011, Fassett *et al* 2011), which formed as a flotation crust, it suggests they are not flotation crust (Walker and Hays 1977). Instead, Mercury's Intercrater Plains are likely to be older volcanic plains that have been heavily modified by impact cratering (Trask and Guest 1975, Whitten *et al* 2014a). Intermediate Plains, if they exist, are likely to be an intermediate stage of plains formation (Trask and Guest, 1975; Galluzzi *et al.*, 2016; Galluzzi and BC Geological Mapping Team, 2017).

The greatest extent of these lava Smooth Plains is in the Northern hemisphere, where the Northern Smooth Plains cover 7% of the planet's surface (Figure 2.17, Ostrach *et al.*, 2015). Overall, Smooth Plains cover 27% of the planet's surface (Denevi *et al.*, 2013). Smooth Plains cover the floor of the Caloris basin, where impact cratering shows the lavas are several kilometres thick (Denevi *et al* 2009, Prockter 2010).

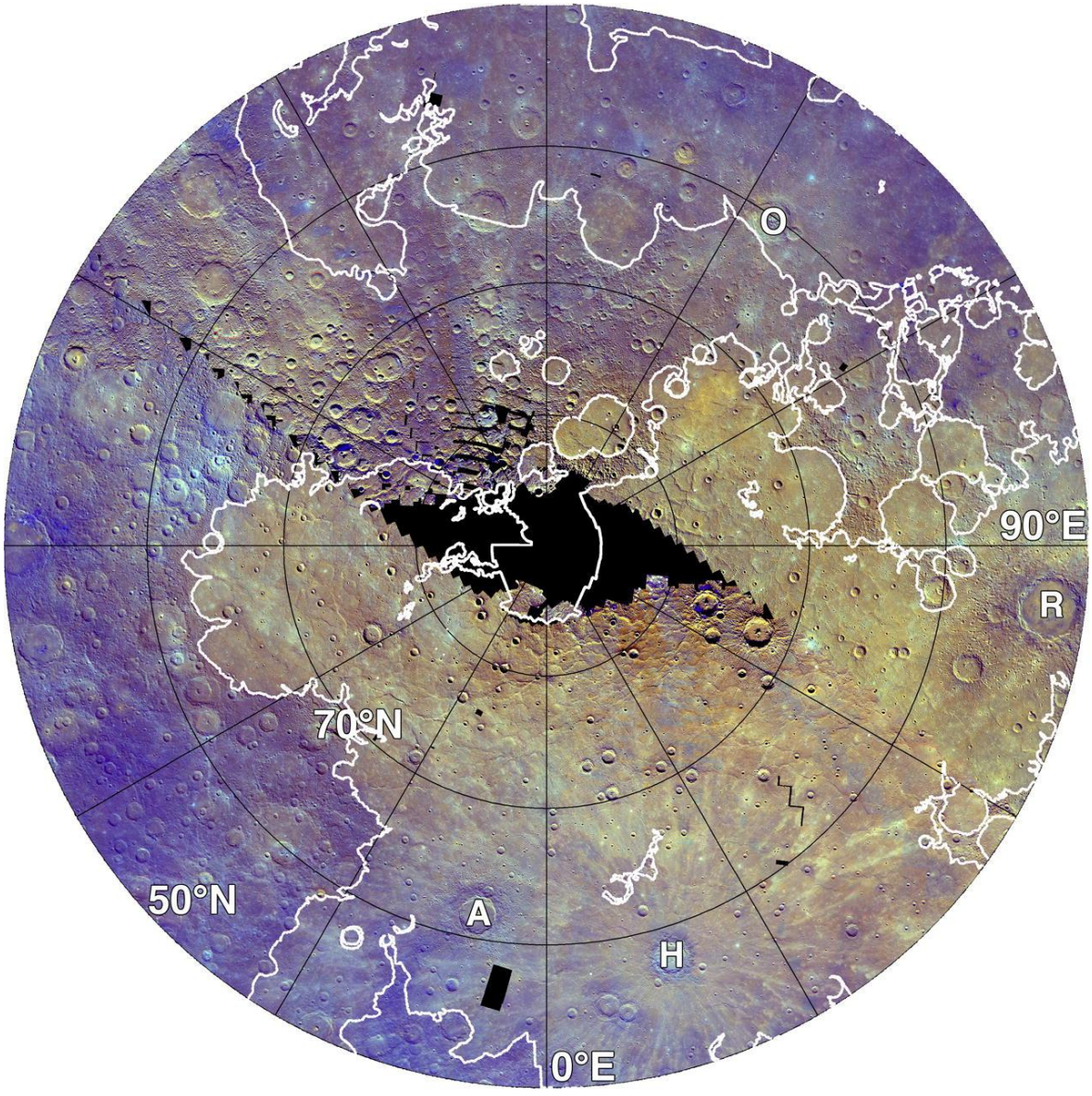

Figure 2.17 Mercury's Northern Smooth Plains (Borealis Planitia) outlined in white on the enhanced colour basemap (Denevi *et al* 2016). *Note that some of the plains are a reddish-orange colour, but other parts are blue-purple. Several*

impact craters are labelled: A, Abedin, H, Hokusai. Image is in polar stereographic projection, showing the region north of 50° N. Image from Ostrach *et al.* (2015).

Multiple flow features have been observed within Smooth Plains including; broad channels with eroded islands where Smooth Plains flowed over and carving into Intercrater Plains, as well as more sinuous channels. These features may exist in areas only before total inundation and so are only seen towards the edges of Smooth Plains where the Smooth Plains did not completely cover the floor of the basins they were erupting into (Byrne *et al* 2013).

Different spectral colours of flows are attributed to separate melt events being of a different composition (McClintock *et al* 2008, Rava and Hapke 1987, Weider *et al* 2012, Murchie *et al* 2008). However, Rothery *et al.* (2017) have shown that there is a connection between the interior and exterior plains of Caloris, where different spectral types likely interfinger each other.

The spatial association of Smooth Plains with impact basins can be linked to structural weakening and thinning of the crust, providing pathways for magma as well as impacts generating long-lasting thermal anomalies that may encourage magmatism (Padovan *et al* 2017, 2016). There is still insufficient understanding of the plumbing or control on Mercury's volcanism with no signs of sinuous rilles. This is surprising given rilles occur commonly on the Moon (Head and Wilson 1992), as well as in komatiites on Earth (Hill *et al* 1995). Other features seen on the surface include very rare possible shield volcanoes (Wright *et al* 2018).

2.6.2 Explosive Volcanism

Rava and Hapke (1987) identified faculae (previously referred to as red spots, Section 2.5.3) on the surface of Mercury in Mariner 10 data. Following superior images from MESSENGER, they are found to be diffuse patches (Figure 2.18), often with pits towards the centre of the facula (Gillis-Davis *et al* 2009, Head *et al* 2009, Blewett *et al* 2009). These diffuse patches are interpreted to be of pyroclastic origin (Blewett *et al* 2009, Kerber *et al* 2011, Jozwiak *et al* 2018, Weider *et al* 2016).

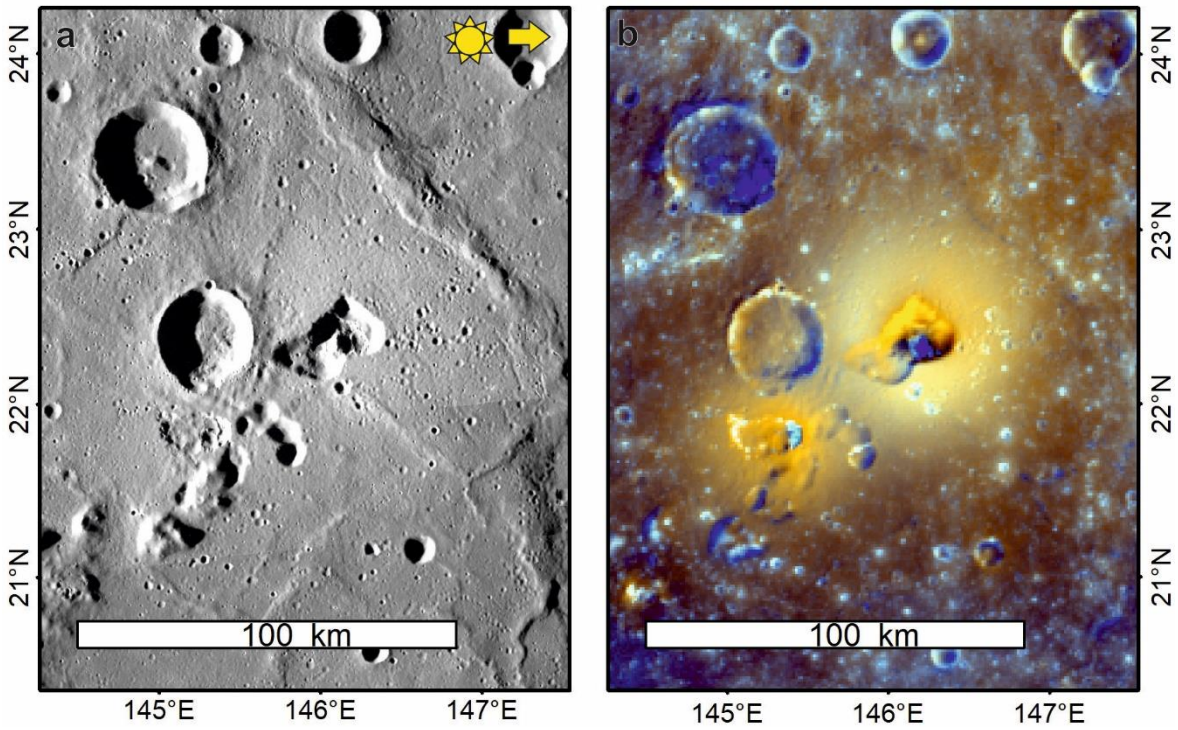

Figure 2.18 Agwo Facula and vent. An example of a volcanic vent and facula on Mercury. a. bulk data record 166 m/pixel images of vent site. b enhanced colour image 665 m/pixel showing the facula surrounding the vent site.

The faculae can be several hundred kilometres in diameter; the pits are 10s of kilometres across. The pits have an asymmetrical shape and no raised rim (Kerber *et al* 2011, Jozwiak *et al* 2018). Rothery, Thomas and Kerber (2014) describes the vent inside Agwo facula as being compound because its interior is divided up into multiple vents, potentially indicating multiple eruptions. I conducted a global survey to determine how often this applies to the other vents around Mercury (chapter 5).

Faculae are significantly larger than Lunar explosive deposits (Kerber *et al* 2011, Weider *et al* 2016), suggesting higher volatile fractions than on the Moon (especially given the greater gravitational pull the planet would have on ejecta). It is thought that the volatile gases driving the explosive eruptions are SO_2, CO, and CO_2 (Weider *et al* 2016). Faculae are widely dispersed, often well beyond the extent visible in MDIS images (Besse *et al* 2020). They do not form significant constructive edifices, with slopes <1° (Thomas *et al.* 2014b). The lack of constructive edifices is due to the low gravity and lack of atmosphere enabling wide dispersion of pyroclastic materials from these eruptions rather than constructing a volcanic edifice (Brož *et al* 2018).

Some faculae do not show any central pit. Instead, they contain a rough (over the kilometre scale), highly textured, surface is known as Pitted Ground (Thomas et al., 2014b).

Explosive volcanism peaked during Mercury's Calorian (3.9 to ~3.5–3.0 Ga) and Mansurian (~3.5–3.0 to ~1.0–0.28 Ga) but continued into the Kuiperian (Thomas et al., 2014b; Jozwiak, Head and Wilson, 2018), which may have begun as recently as 280 Ma (Banks *et al* 2017). As Mercury's lithosphere has cooled, it has thickened (Peplowski *et al* 2011), and contraction hinders volcanism by impeding magma ascent (Solomon 1978). The

formation of volcanic vents on Mercury, therefore, probably requires crustal weakness to aid the continued rising of the volatile-rich magmas (Klimczak *et al* 2018). Possible crustal weaknesses include impact craters or faulting. Faculae often occur on impact crater floors (Jozwiak *et al* 2018, Klimczak *et al* 2018). This may be due to the impact crater's structural weakening and thinning of the crust acting as a pathway for ascending magmas. There is no other known global association with other landforms (Thomas *et al* 2014b, Klimczak *et al* 2018). However, there is a noticeable paucity within Smooth Plains, probably caused by Smooth Plains acting as a barrier to ascent (Thomas *et al*., 2014). The relatively high density of contractional tectonic features, called lobate scarps (Section 2.7.1), on Mercury's surface, means that it is impossible to distinguish any relationship with tectonic features from random (Klimczak *et al* 2018).

2.6.3 Melt Generation

Both explosive and effusive volcanism on Mercury requires a melt source. The formation of both Intercrater and Smooth Plains dates to between 4.0 – 3.5 Ga, suggesting widespread volcanism was only active for 500 Ma (Byrne 2020); this is backed by thermal models which suggest that melts could only have been generated by partial melting of the mantle through the first half of Mercury's history (Tosi *et al* 2013). However, this does not explain the relatively recent explosive volcanism, or that subsequent younger plains likely cover over any older plains that may have existed pre 4.0 Ga.

Given the relatively thin mantle (Section 2.4), Mercury's crust represents 10% of all silicate material on the planet (Padovan *et al* 2015). The high Mg/Si and low Al/Si ratios suggest high amounts of partial melting (Nittler *et al* 2011). The variation in chemical provinces over Mercury's surface is evidence of various degrees of partial melting in a chemically heterogeneous mantle (Charlier *et al* 2013, Vander Kaaden and McCubbin 2016, Vander Kaaden *et al* 2017, Nittler *et al* 2020, Peplowski and Stockstill-Cahill 2019, McCoy *et al* 2018) and with different depth for melting to occur with Intercrater Plains forming at the core-mantle boundary (400 km depth) and the Northern Smooth Plains at 200 km depth. A partial melt generated anywhere in the mantle will remain buoyant throughout its upward transport (Vander Kaaden and McCubbin 2016).

In explosive volcanism, the volatiles that drive the eruptions are probably SO_2, CO, and CO_2 (Weider *et al* 2016, Besse *et al* 2020, Kerber *et al* 2009). The only facula with sufficient data to be analysed shows the erupted materials are depleted in sulfur and carbon, suggesting these were lost as volatile gas during the eruptive process (Weider *et al* 2016). There is at least one location where the size of the facula is such that it would need additional volatiles to make a facula that extensive and suggesting assimilation of volatile elements from the crust (Peplowski *et al* 2016, Weider *et al* 2016).

2.7 Tectonic Landforms

There are both compressional and extensional (graben) features on Mercury. In the past, the compressional structures on Mercury have been described as multiple separate morphological features; lobate scarps, wrinkle ridges, and high relief ridges (Watters *et al* 2009c, Watters and Nimmo 2010, Strom *et al* 1975). More recently, they have started to be grouped as a continuum of structures (Byrne *et al* 2014, Klimczak *et al* 2015, Crane 2020). I now go through each of these compressional structures then explain how they are linked.

2.7.1 Lobate Scarps

Lobate scarps (Figure 2.19) are asymmetrical topographic features characterised by a steep fore scarp and a gradual back scarp (Strom *et al* 1975). They can be linear or arcuate in plan (Rothery and Massironi 2010). They can be several kilometres high and 1000s of kilometres long. Lobate scarps are the surface manifestation of thrust faults (Strom *et al* 1975). Similar but smaller structures are seen on the Moon and Mars (Watters and Nimmo 2010, Watters 2006). They are compared to parts of Rocky Mountain foreland thrust in geometry (Watters *et al* 1998, Watters and Nimmo 2010); however, there is no apparent frontal wedge in these systems as seen on terrestrial analogues (Tavani *et al* 2015). Lobate scarps have a shorter fault displacement to length ratio than terrestrial faults, which is probably due to a lack of fluids to lubricate the faults (Watters and Nimmo 2010).

Scarp systems can be complex systems, with back thrusts and reversals in direction (Watters *et al* 2009c, Zuber *et al* 2010), making the single thrust plane model an oversimplification. Those scarps that are arcuate in plan view have transfer faults on the curved margins of the scarp (Rothery and Massironi 2010).

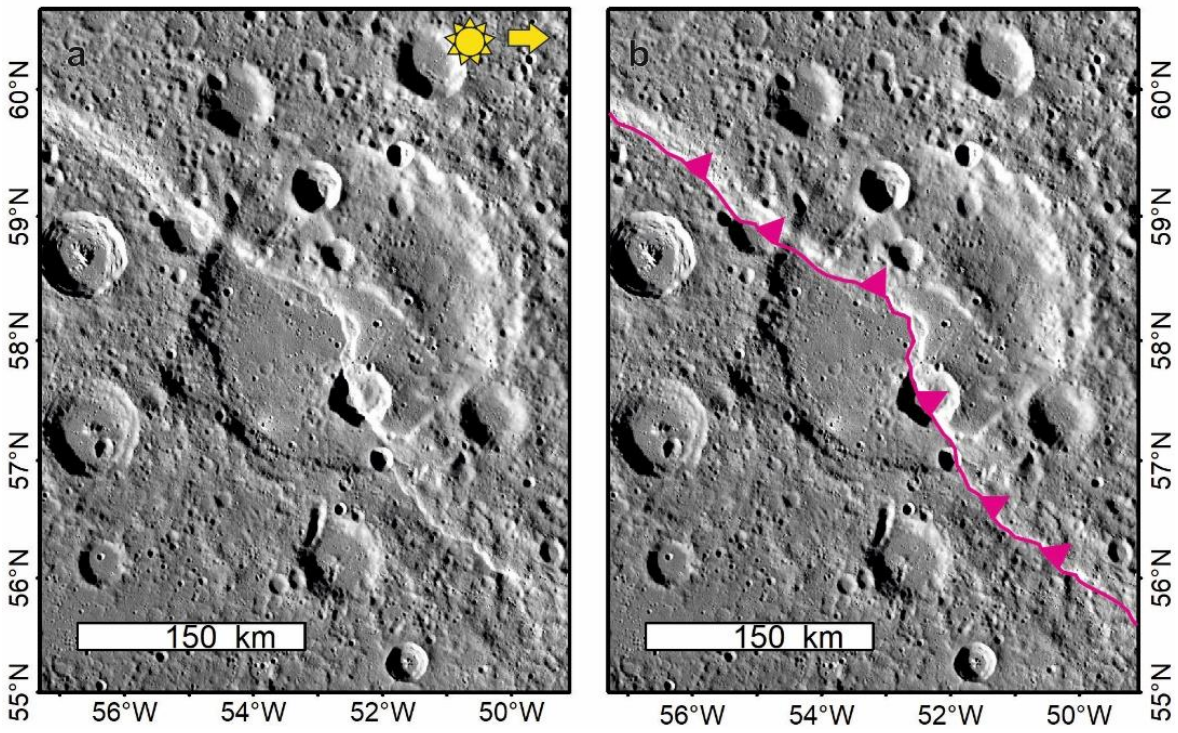

Figure 2.19 Carnegie Rupes as an example of a lobate scarp, a: lobate scarp from bulk data record (Denevi *et al* 2018a)*, sun and arrow symbol shows illumination direction, b: lobate scarp with a line showing break of the slope, ticks represent the down-dip direction of thrust.*

Fault planes beneath lobate scarps were assumed to have a dip of around 25-30° based on models and simulations (Byrne *et al* 2014, Kennedy *et al* 2008, Strom *et al* 1975, Watters *et al* 1998). Work using the horizontal and vertical offset in craters has shown a wider range of dips 7 – 57° (Galluzzi *et al* 2015, 2019). It is likely that, at least in some cases, they may flatten out to form decollements (Giacomini *et al* 2015, Rothery and Massironi 2010). I measure the fault geometry of a lobate scarp in chapter 6.

The timing of lobate scarp formation can be constrained by observing their relationships with surrounding features; they may cross-cut impact craters, extensional faults, and volcanic plains, as well as being overprinted by impact craters. In other locations, pre-existing features, such as impact craters, can influence the direction of the scarps (Ruiz *et al* 2012). Scarps both predate and postdate effusive volcanism (Byrne *et al* 2015, Solomon *et al* 2008), the relationship with explosive volcanism is unclear due to the diffuse nature of faculae. Lobate scarps cross-cut craters from the Pre-Tolstojan up to the Kuiperian and some are overprinted by Tolstojan or more recent craters (Banks *et al* 2015), showing that deformation across the planet has been long-lived. The number of active fault segments, as identified by overprinting by impact craters, seems to have declined over time (Banks *et al* 2015). It is not clear if this is a factor of how often individual fault segments are activated as the study did not look at the rates of displacement/shortening for different impact crater ages. Small scarps 10s of meters in scale suggest that the surface of Mercury is likely still currently active (Watters *et al* 2016a), which is confirmed by scarps cross-cutting over <3 km craters, which should be relatively young (Banks *et al* 2015).

2.7.2 High Relief Ridges

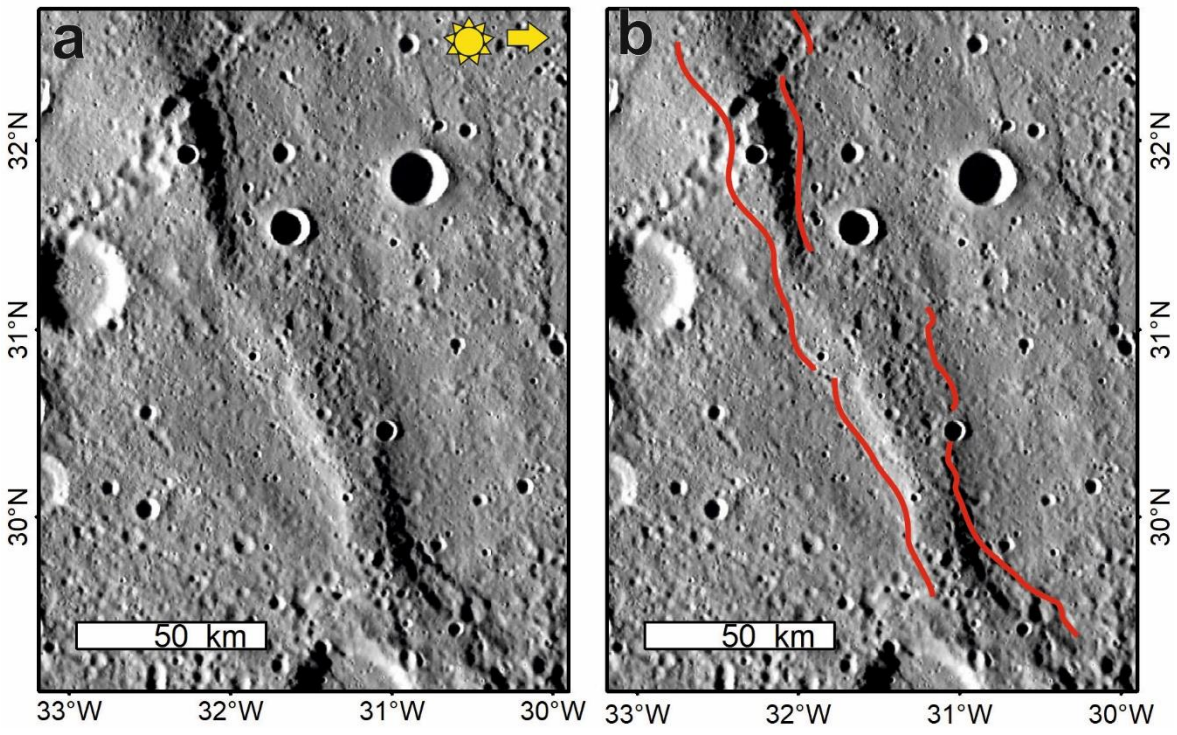

Figure 2.20 Antoniadi Dorsum an example of high relief ridge: a. bulk data record (Denevi *et al* 2018a) *b. red lines show the location of edges of high relief ridge.*

High relief ridges (Figure 2.20) are described as symmetrical with positive topographic relief on both sides (Dzurisin 1978), interpreted to be either two sets of high angle faults creating a ridge with dips of 45° (Watters and Nimmo 2010) or a shallower fault with a scarp and back scarp. They occur less frequently than other structures and are often found in proximity or along strike to lobate scarps (Watters and Nimmo 2010).

2.7.3 Wrinkle Ridges

These topographic features are found in Smooth Plains (Watters *et al* 2015, Watters and Nimmo 2010, Dzurisin 1978). They are morphologically broad low relief arches with superimposed ridges 100s meters wide and several 10s of kilometres long (Figure 2.21). They have a higher relief on Mercury than on the Moon (Watters and Nimmo 2010); the reason for this is not apparent.

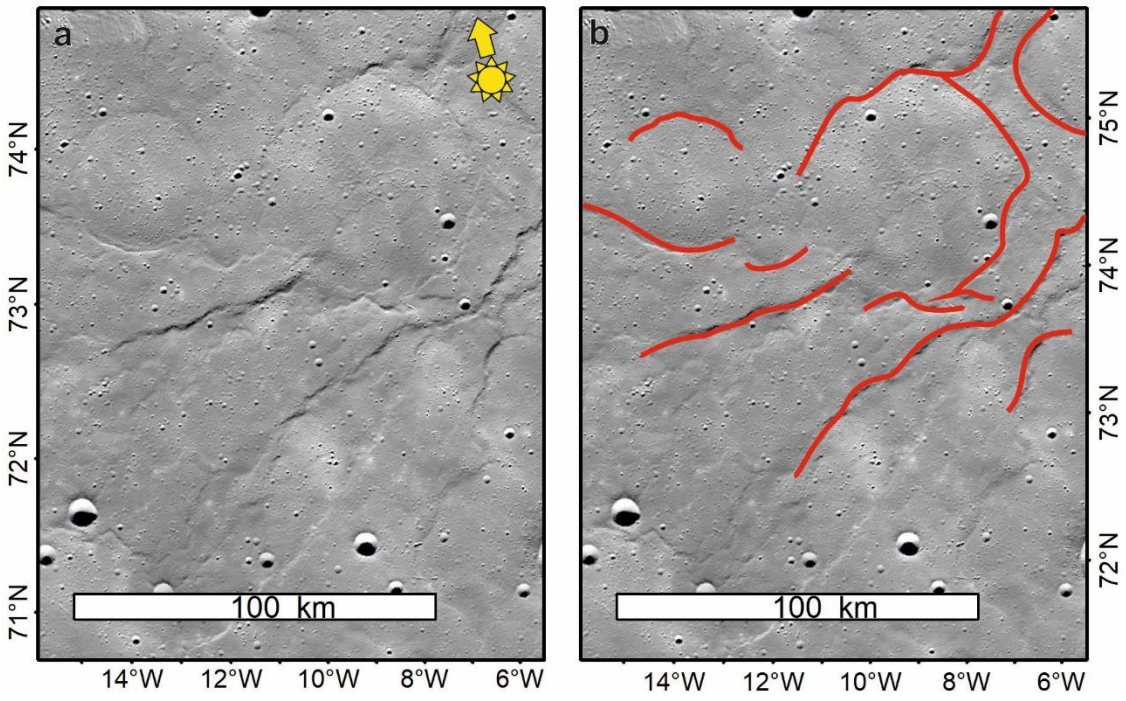

Figure 2.21 Example of Wrinkle ridges in the Northern Smooth Plain of Mercury using bulk data record (Denevi *et al* 2018a)*. a. example without annotation. b likes show locations of prominent wrinkle ridges.*

2.7.4 A Continuum of Compressional Structures

While lobate scarps have a shallower dip than high relief ridges, they often occur along strike on the same structure (Figure 2.22). Many structures do not fit neatly into one morphology or the other but have aspects of both suggesting that they are all reverse faults with different dips (Ruiz *et al* 2012, Watters and Nimmo 2010, Peterson *et al* 2018, Byrne *et al* 2014, Spudis and Guest 1988, Williams *et al* 2011). Similarly, but more rarely, wrinkle ridges occur along the same structures, often when they move into Smooth Plains (e.g. Ruiz *et al.*, 2012). These compressional structures now considered a continuum with varying dips that grade into each other and whose morphology reflects the local tectonic conditions (Byrne *et al* 2018a, Klimczak *et al* 2015, Peterson *et al* 2018, Byrne *et al* 2014).

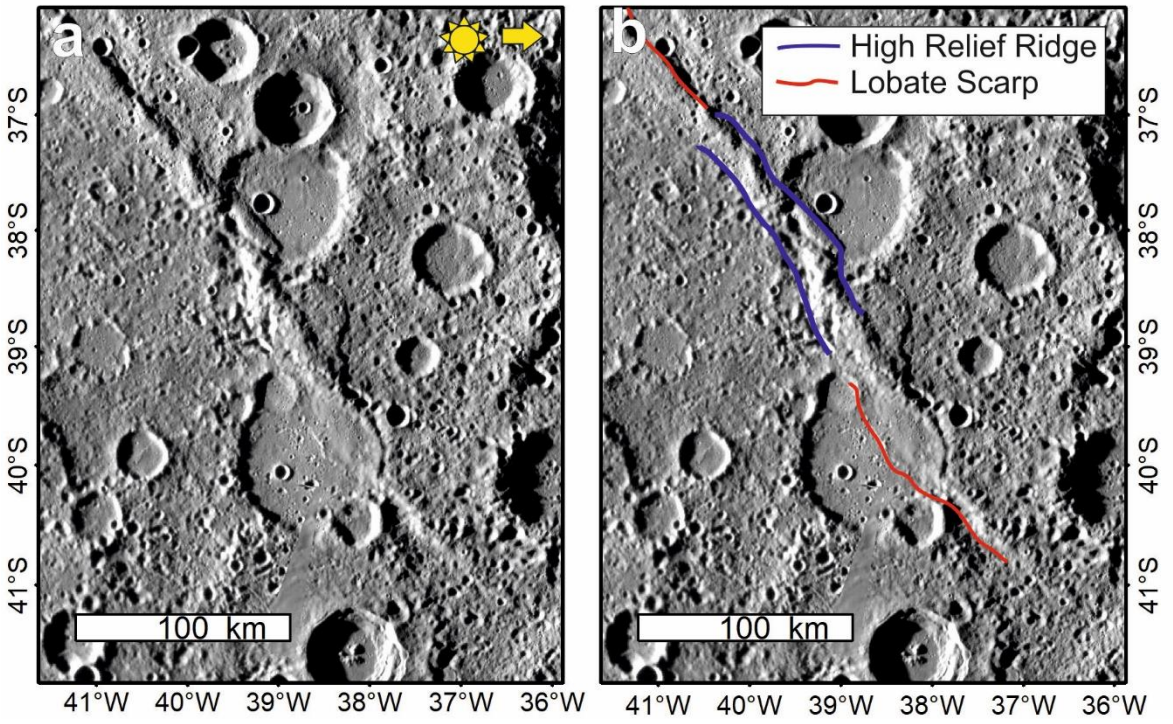

Figure 2.22 Example of lobate scarp transitioning to high relief ridge and back to lobate scarp on Mercury on bulk data record (Denevi *et al* 2018a). *a. example without annotation. b location of high relief ridge.*

2.7.5 Extensional Features

Extensional features are observed only within basins (Byrne *et al* 2014, Strom *et al* 1975, Watters *et al* 2009c, Watters and Nimmo 2010, Watters *et al* 2009a). They form graben structures that can be both basin-concentric and radial (Figure 2.23), usually only a few 100 m deep and with shallow slope angles <5° (Blair *et al* 2013, Strom *et al* 1975). The cross-cutting relationships between grabens and contractional features within basins can be used to study their history. Basins have a complex history of volcanism and topographic changes linked to isostatic changes following from the impact and subsequent volcanism (Ferrari *et al* 2015, Watters *et al* 2009c, 2009b). The best examples are within the Caloris impact basin, where Pantheon Fossae forms a complex radial structure within the basin (Watters *et al* 2009c, 2009b).

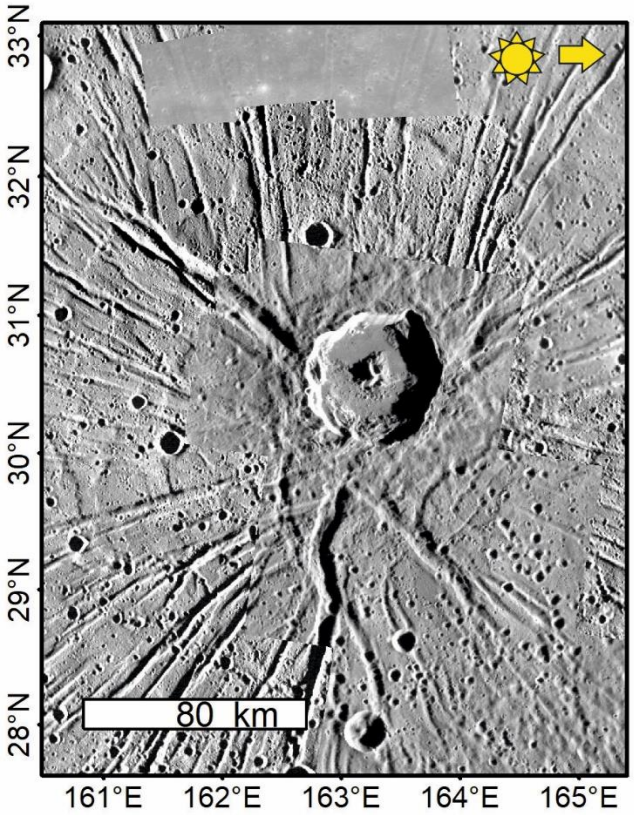

Figure 2.23 Pantheon Fossae showing radial grabens inside the Caloris basin using bulk data record map (Denevi *et al* 2018a).

2.7.6 Global Tectonics

There is a range of suggestions for the controls on global tectonics: including global contraction, tidal despining, and true polar wander (Solomon 1977, Watters *et al* 2015, Byrne *et al* 2018a, Klimczak *et al* 2015, López *et al* 2015, Watters and Nimmo 2010).

The cooling of the planet and the crystallisation of its inner core has led to global contraction, which generates compressive stress on the lithosphere (Solomon 1977, Crane and Klimczak 2017, Klimczak *et al* 2015). All types of plains likely accommodate shrinkage. Peterson *et al.* (2018) have shown the Smooth Plains, dominated by wrinkle ridges, accommodates as much strain as the lobate scarp dominated Intercrater Plains.

Estimates of the amount of global contraction are between 2 and 10 km (Grott *et al* 2011). Byrne *et al.* (2014) measured the amount of contraction accommodated by structures (Figure 2.24) and showed between 1.2 km and 7 km of global radial contraction. A note of caution should be applied here as this used modelled angles of between 25-35°, and the actual average dip over the planet is not known.

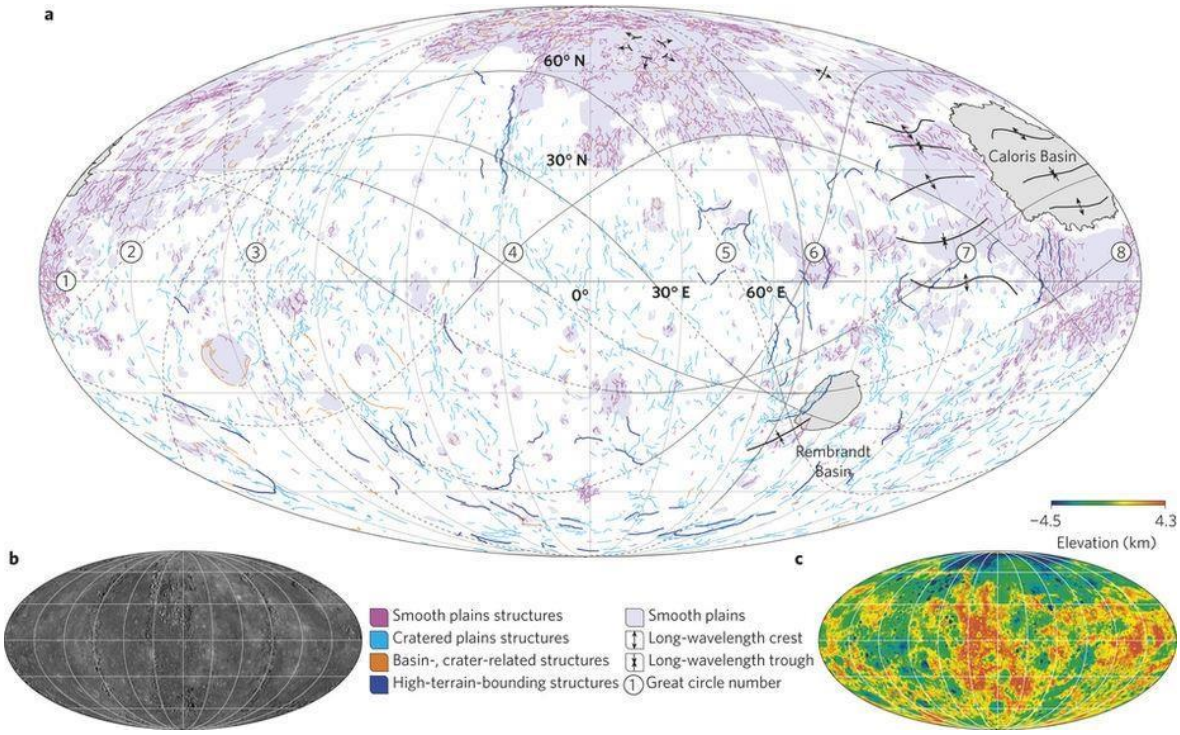

Figure 2.24 a. Global map of thrust related landforms and Smooth Plains. Black lines mark the crests and troughs of mapped long-wavelength topographic features. b. The global MDIS combined high-incidence-angle image used to make the image and c. topographic map. Taken from (Byrne *et al* 2014).

Mantle convection and true polar wander caused by the Caloris impact event are also suggested mechanisms for generating stress in the crust (e.g. Matsuyama and Nimmo, 2009; Grott, Breuer and Laneuville, 2011); however, these processes are poorly understood on Mercury.

Away from regional features, there is a debate over the control mechanism on the orientations of lobate scarps. Cooling induced global contraction explains why contractional features dominate the tectonics but not their orientation. If the contraction is the primary control, then a broadly random orientation should be apparent (Watters *et al* 2015). However, there appears to be a north-south alignment to many (but not all) of the structures (Byrne *et al* 2014, Watters *et al* 1998, 2009c).

At Victoria quadrangle, a set of lobate scarps show strain is localised around the High Magnesium Region (section 2.5.4), interpreted to a rheologically stiff block within the crust (Galluzzi *et al* 2019), the first identification of such a block at Mercury. The spatial resolution of the geochemical data for the southern hemisphere is too low to identify additional regions.

Mercury's proximity to the Sun and its eccentric orbit has meant that it has lost much of its rotational energy between its formation and slowing to its current spin-orbit resonance. This tidal despinning will have led to the collapse of its equatorial bulge, which would be expected to cause purely north-south alignment concentrated at the equator (Burns 1976, Melosh and Dzurisin 1978). Tidal despinning likely stopped generating stress on the surface of Mercury early in its history (Noyelles *et al* 2014), so it is not clear if Mercury will have kept any evidence of the resulting strain in its crust.

Illumination bias likely contributes to the apparent predominance of north-south features. Without an atmosphere to diffuse sunlight, north-south orientated scarps are more likely to generate shadows than east-west scarps, as seen in studies of basin edge scarps (Fegan *et al* 2017). Studies which use high incidence angle imagery, as well as multiple lighting directions, should be able to help reduce this effect.

While global contraction is the dominant driver of Mercury's tectonics, it is clear the complex interaction between shrinking, large basins and geochemical provinces can affect the type of tectonic features found within a region.

2.8 Weathering and Regolith

In addition to large scale cratering, Mercury's surface is subject to exogenic modification by micrometeoroid impact; impact gardening, in which small impacts churn over the surface (Chapman *et al* 1970); sputtering, solar wind particles breaking of particles from the surface (Hapke 2001); solar desorption, photon-induced transfer of an electron to a cation causing it to become neutral and the atom becomes unbound from the surface(McGrath *et al* 1986), thermal desorption; release of atoms by heating, and chemical sputtering; the chemical reaction between ions from solar wind and regolith which produces some of the hydrogen, hydroxide and water in the exosphere (Crider and Vondrak 2003).

The regolith (layer of unconsolidated rock fragments on the surface of the planet) is thicker on Mercury than the Moon, with regolith thickness calculated to be approximately 20 – 40 m on the Smooth Plains as compared to 2- 5 meters at Lunar Maria (Kreslavsky and Head 2015). This thicker regolith is due to a higher micrometeorite flux (Domingue *et al* 2014). This higher flux leads to faster degradation of topographic features on Mercury, with diffusion rates of $17m^2$/Myr, approximately twice the rate on the Moon (Fassett *et al* 2017). This diffusion and mixing lead to features degrading over time, with superficial features such as crater rays and faculae mixing in with their surroundings faster than large features such as lobate scarps or impact basins.

2.9 Hollows

Mariner 10 images show bright patches inside Balzac, Hopper, Tyagaraja, Theophanes, Zeami craters (Hapke 1977, Dzurisin 1977, Schultz 1977). These 'Bright Crater Floor materials' are relatively blue (high UV/orange reflectance ratio) and at the time interpreted as shocked crystals from impact events (Schultz 1977) or post-impact physical or chemical alteration of crater floors (Dzurisin 1977).

The superior image data returned by MESSENGER's orbital campaign confirmed that these features are characterised by high albedo regions, reflecting more light towards the blue end of the spectrum. However, details were revealed within them, notably clusters of shallow depressions with an uneven shape measuring 10s of meters to kilometres across (Figure 2.25) and 10s meters deep with flat bottoms but steep sides that lack a rim or ejecta. These features are now called hollows (Blewett *et al* 2011, Chabot *et al* 2011). Some hollows do not have high albedo associated with them.

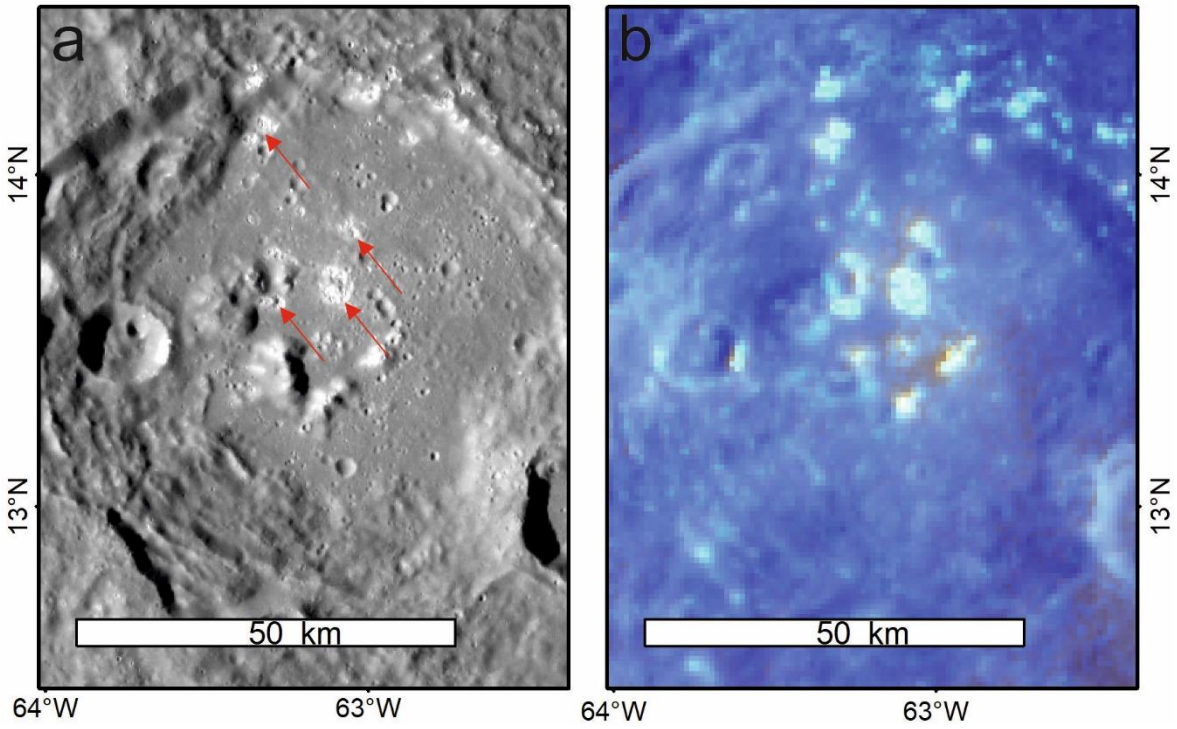

Figure 2.25 Hollows in an unnamed crater a. global bulk data record mosaic (Denevi *et al* 2018a) *with red arrows pointing at the hollows, b enhanced colour image highlighting albedo features* (Denevi *et al* 2018a)*. The high albedo white spots seen in both images represent the fringes of hollows, shallow rimless pits linked to the loss of volatiles from within the regolith.*

Hollows are found globally but regularly cluster together. Impact craters often host hollows in either the walls, floor, or central peaks/ring (Blewett *et al.*, 2011, 2016; Thomas *et al.,* 2014). They are less common in areas of Smooth Plains and are associated with regions of LRM (Blewett *et al.*, 2013; Thomas *et al.*, 2014; Thomas *et al.*, 2016). Hollows have a weak tendency to be found towards the hot pole longitudes (Thomas *et al.,* 2014) and are found preferentially on Sun-facing slopes (Blewett *et al.*, 2013; Thomas *et al*., 2014).

The latitudinal and facing controls on the location of hollows suggest that insolation and solar weathering play a role in their formation (Thomas *et al.,* 2014). The exogenic controls and links with LRM suggest hollows form by volatile loss from the areas of regolith high in volatiles such as carbon and sulfur (Blewett *et al* 2013). Hollows grow through the loss of volatile phases along their edges, creating bright interiors of the eroding faces, the build-up of lag limiting the depth.

The crisp morphology of hollows, little signs of modification by impacts, a high blue albedo, and some being found within rayed craters suggest they are amongst the youngest features on the planet (Blewett *et al* 2013) and may represent an ongoing surface process. It is likely that after activity ceases at these sites, they end up losing their brightness and become subdued due to space weathering and degrade into the hermean regolith (Blewett *et al* 2013, Wang *et al* 2020, Chabot *et al* 2011). A better understanding of rates of surface degradation in the hermian environment will help constrain this better. These features are a further example of the volatile-rich nature of Mercury.

2.10 Polar Ice

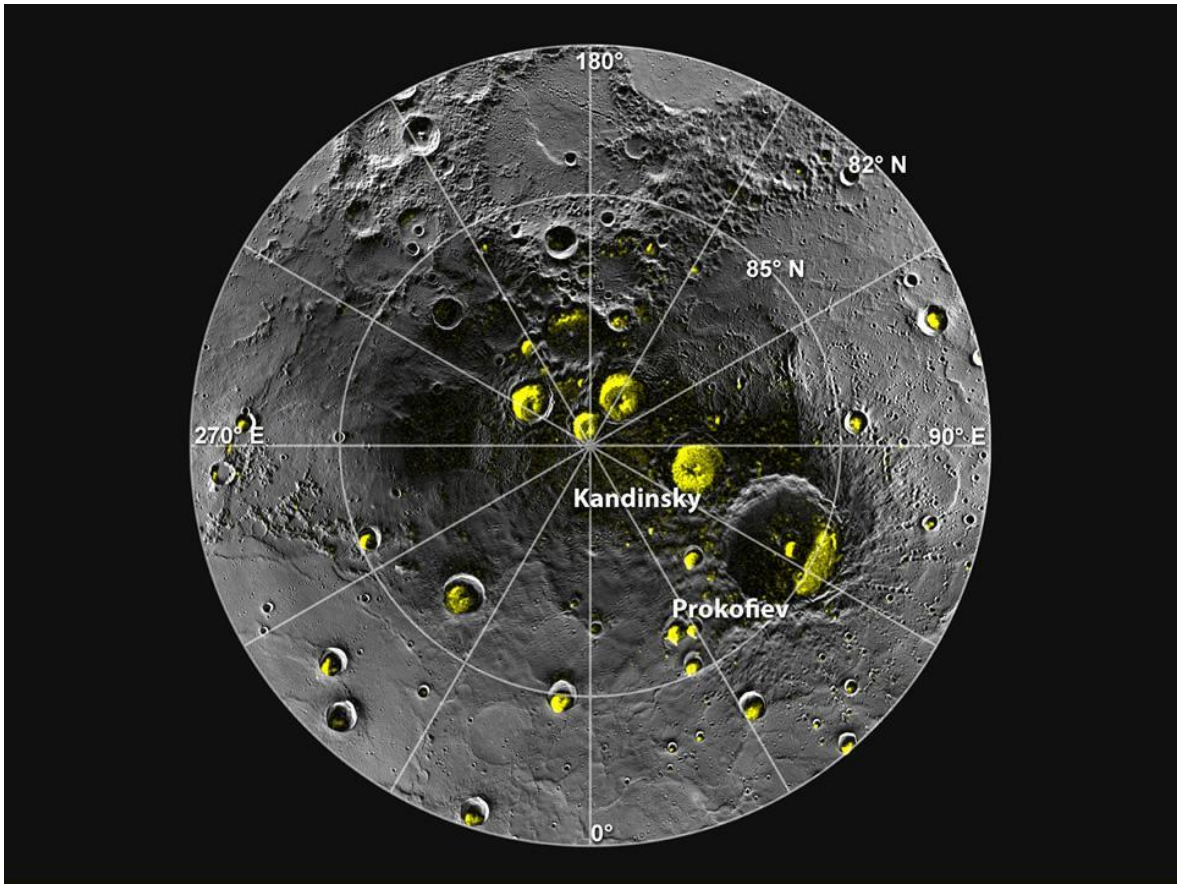

Figure 2.26 Radar image of Mercury's north polar region (yellow) is shown superposed on an image mosaic of the same area. All of the more extensive polar deposits are located on the floors or walls of impact craters. Further from the pole, the deposits are concentrated on the north-facing sides of craters (Chabot *et al* 2013). *Image: NASA/Johns Hopkins University Applied Physics Laboratory/Carnegie Institution of Washington/National Astronomy and Ionosphere Center, Arecibo Observatory.*

At the poles of the planet, Earth-based radar has shown that there is radar-bright material inside craters permanently shadowed from the solar illumination (Slade *et al* 1992). The MESSENGER imaging campaign found these to have well-defined boundaries. Variations in brightness across the deposit show that there is both water ice and organic compounds in these cold traps (Chabot *et al* 2018, 2016, 2013). This is not studied further as I did not choose a polar quadrangle.

2.11 Planet Formation

Hollows (section 2.9), carbon, sulfur and the high K/Th ratio in Mercury's crust (section 2.5.4), and explosive volcanism (Section 2.6.2) all show the planet has a high volatile content. However, the planet has a large iron-rich core and a relatively thin layer of silicates (Section 2.4). To form a planet with a large iron core and

also a volatile-rich silicate layer, either the planet underwent catastrophic modification, or it formed with this unusual composition.

There are multiple styles of collision possible: two large bodies with the cores merging, a large body being hit by a small body which carried away the silicates, or Mercury being the smaller object in a glancing blow with a large body (a 'hit and run' impactor). If Mercury formed from chondritic material and became differentiated before the silicates were stripped away, it would have had to have lost the equivalent of 1480 km of the mantle to reach its current density (Ebel and Stewart 2018). This could be done with the collision of two large bodies stripping the planet's core by a giant impact, ejecting the silicate layers of the planet allowing cores to merge. However, the collision model does not explain the volatile enrichment as collision should preferentially remove these elements, (e.g. Ebel and Stewart, 2018). Though it is possible a hit-and-run impact with a much larger body may not preferentially lose the volatiles from the smaller body (Asphaug and Reufer 2014).

If Mercury's unusual composition is due to where it formed within the nebula, it would likely come from the inner solar system in a region significantly reduced and rich in metals and carbon (Ebel and Alexander 2011), potentially where enstatite chondrites, which are metal and carbon-rich (Keil 1968, Udry *et al* 2019), formed. Currently, both the formation and modification theories are unsatisfactory, and the formation of Mercury is an unanswered question.

2.12 Conclusions and Research Questions

Mercury remains poorly understood compared to many of the other rocky bodies in the solar system (except for Venus). Mapping of the planet is underway at a scale of 1:3 million but is not yet complete.

This thesis aims to build on this knowledge and improve it. As part of this thesis, I have constructed a geological map of H-14, the Debussy quadrangle. In the process of mapping, I became interested in the explosive volcanic vents which cover the planet and I so I investigated the following features:

- What is the Geological history of the Debussy quadrangle, and how does it relate to the known geological history of the planet? (Discussed in chapters 3 and 4).
- What further can I learn about explosive volcanic vents on a contracting world, and did most of them erupt once or multiple times? (Discussed in chapters 5 and 6).

3 Mapping the Debussy Quadrangle

A major component of my research is producing the map of the Debussy quadrangle. I set out with the following aims for the map: It should (i) enable further understanding of the chosen quadrangle, (ii) help construct the geological history, (iii) link to the rest of the planet, (iv) be replicable, and (v) provide context for future researchers who wish to use it. To achieve this, I have produced a geomorphic map. This style of mapping divides the surface of the planet by shape and textures into distinct units and features related to how the surface formed and evolved through time (Smith *et al* 2011). In this chapter, I set out the map parameters, mapping process, and geomorphic units and criteria used to map them. I defer detailed interpretation and discussion of geological history to chapter 4.

3.1 Selection of the Quadrangle

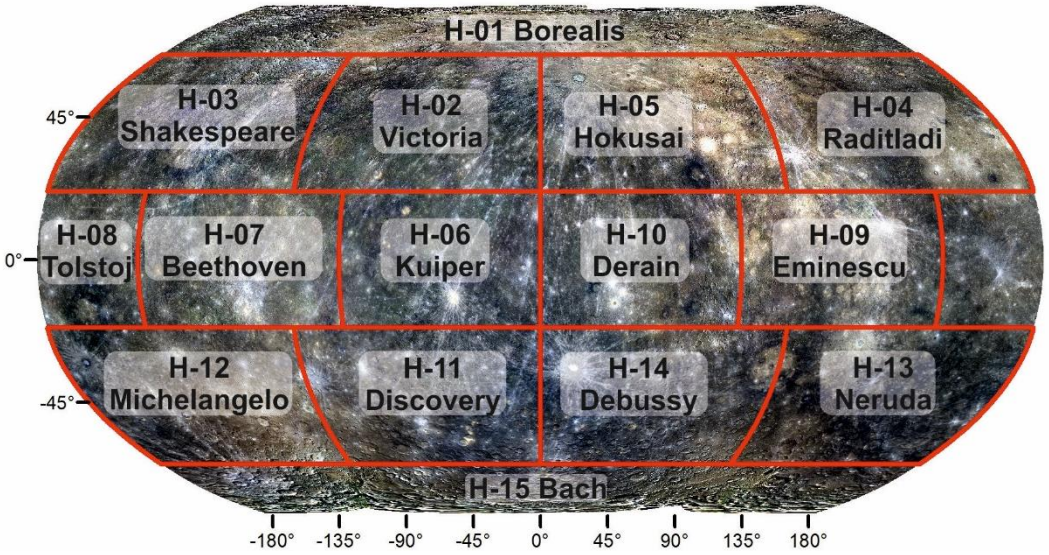

Figure 3.1 Colour map of Mercury (Denevi *et al* 2018a) *in Robinson projection showing the location of each of Mercury's quadrangles.*

Mercury is divided into 15 Quadrangles (Figure 3.1), H-1 to H-15, the H standing for Hermes (Davies *et al* 1978). I based the selection which quadrangle I would map on the available quadrangles not yet completed or underway at a scale of 1:3 million, a review of the 1:5 million scale maps produced after Mariner 10, and the identified features in the available quadrangles.

3.1.1 Mariner 10 Maps

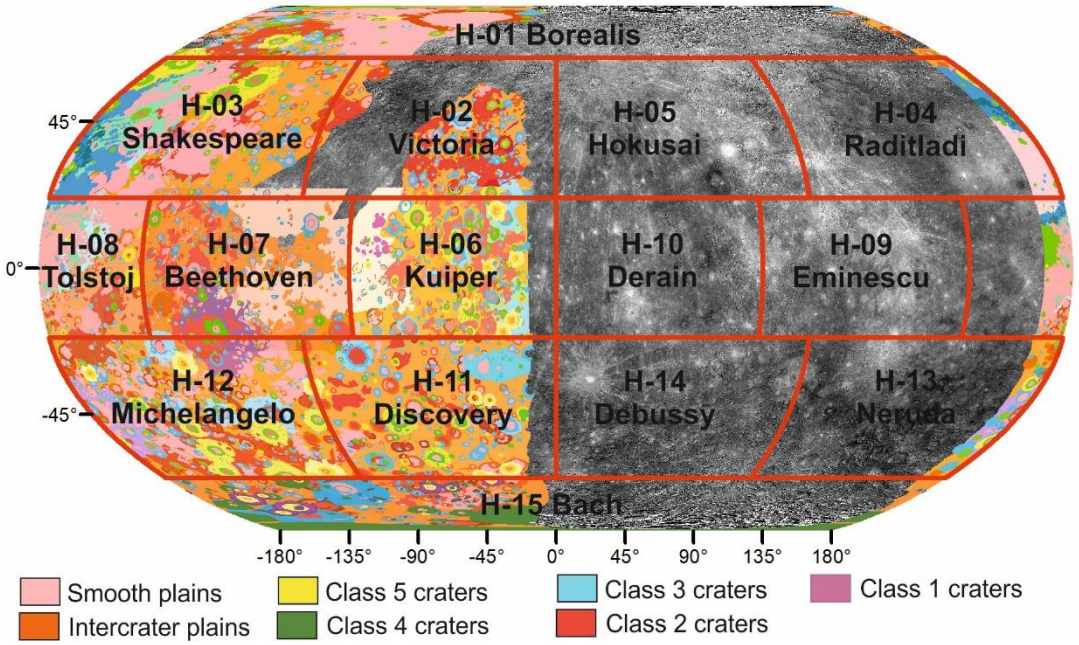

Figure 3.2 Quadrangles of the planet Mercury superposed on the 1:5M scale geological maps (Strom *et al* 1990, King and Scott 1990, Grolier and Boyce 1984, Trask and Dzurisin 1984, De Hon and Scott 1981, Spudis and Prosser 1984, Guest and Greeley 1983, Schaber and McCauley 1980, McGill and King 1983) *completed after the Mariner 10 mission. The basemap is the Low incidence angle (LOI) MESSENGER WAC/NAC image mosaic* (Denevi *et al* 2018a).

After the Mariner 10 mission, 40% of the planet had sufficient image data to be mapped at a scale of 1:5 million (Figure 3.2). Within the eight quadrangles (some only partially mapped), the surface has been divided into cratered units and plains. The maps used five degradation classes for craters (see section 1.7.1), and three types of plains were recognised between impact basins (see 2.5.2 and Section 1.7.2) with additional units specific to the Caloris impact basin.

3.1.2 Post-MESSENGER Maps

The MESSENGER team is producing a complete 1:15 million scale map of Mercury (Prockter *et al* 2016, Kinczyk *et al* 2018). At the time of writing, this still has not been published. It uses a 5-class crater system in keeping with the Mariner 10 maps. The MESSENGER team's map includes only two classes of plains units (Intercrater and Smooth, see Chapter 2.5.2, chapter 4.3.1) with additional units at both the Rembrandt and Caloris impact basins.

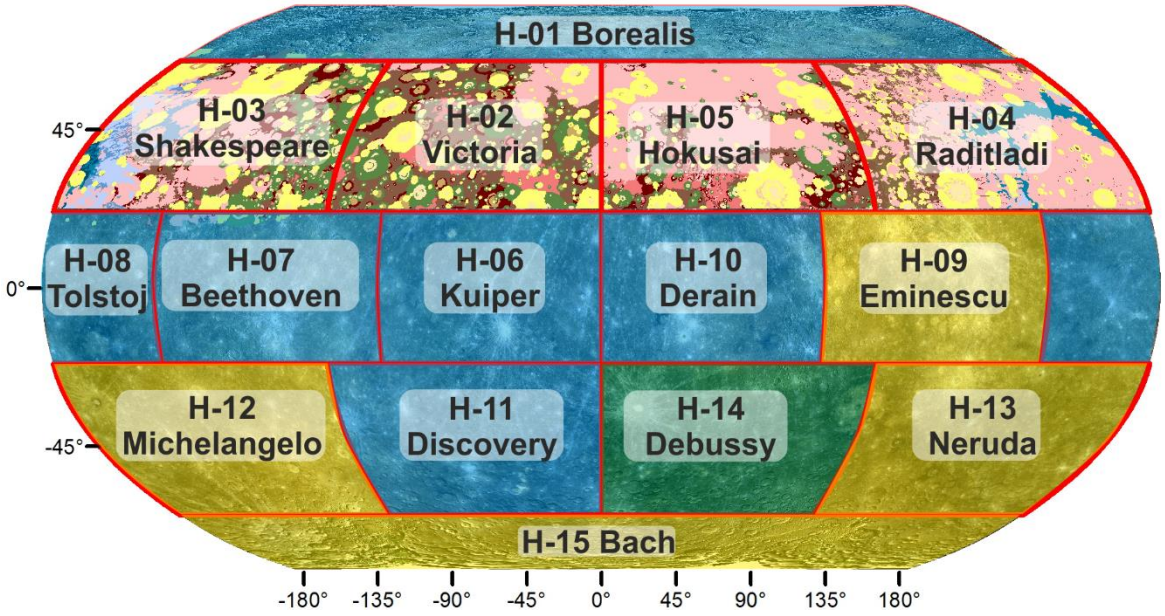

Figure 3.3 Map of quadrangle mapping at 1:3 million, of which H-02 (Galluzzi *et al* 2016)*, H-03* (Guzzetta *et al* 2017)*, H-04* (Mancinelli *et al* 2016)*, H-05* (Wright *et al* 2019) *are complete and published. Mapping of the quadrangles in blue started before this thesis but are not yet published; those in yellow started after I made my selection. The quadrangle in green is the one that I chose to map.*

Hynek *et al.* (2017) has started at a scale of 1:2 million of the Rembrandt impact basin. Semenzato *et al.* (2020) also produced a map of Rembrandt as part of a project to understand the volcanic fill and tectonic history of the basin.

In addition to these maps, my map feeds into a project to map the planet at a scale of 1:3M, which is ongoing (Figure 3.3), intending to map the entire globe in readiness for the arrival of BepiColombo in orbit. So far quadrangles H-02, Victoria (Galluzzi *et al* 2016), H-03 Shakespeare (Guzzetta *et al* 2017), H-04 Raditaladi (Mancinelli *et al* 2016), H-05 Hokusai (Wright *et al* 2019) are complete. Mapping is underway on H-10 Derain (Malliband *et al* 2020), H-06 Kuiper, H-07 Beethoven, H-08 Tolstoj, and H-11 Discovery. Since I selected my quadrangle, mapping has also started on H-13 Neruda quadrangle (Man *et al* 2020), H-09 Eminescu, H-12 Michelangelo and H-15 Bach. Some of these maps distinguish only three crater degradation classes, while others also include the 5-class system (see section 3.7.1). A map of H-15 Bach will be begun as part of an OU PhD scheduled to start in February 2021.

At the start of my project, I reviewed the available quadrangles. I selected The Debussy quadrangle (H-14) because it contains features of geological interest such as the Rembrandt impact basin, Enterprise and Belgica Rupēs, as well as several other scarps (Figure 3.4), and had not been mapped in the Mariner 10 era.

The Debussy quadrangle (H-14) is named after an impact crater which is itself named after Achille-Claude Debussy, a French composer (International Astronomical Union Working Group for Planetary System Nomenclature 2010). The quadrangle is in Mercury's southern hemisphere and covers from 0° to 90° E and from -27° to -66° North. Figure 3.4 shows the extent of the quadrangle overlain on a mosaic derived from MESSENGER images and indicates all the named features. Names were sparse when I began my mapping, so

I submitted to the International Astronomical Union and had accepted new names for three rupēs, two craters, and two faculae that had not previously been described.

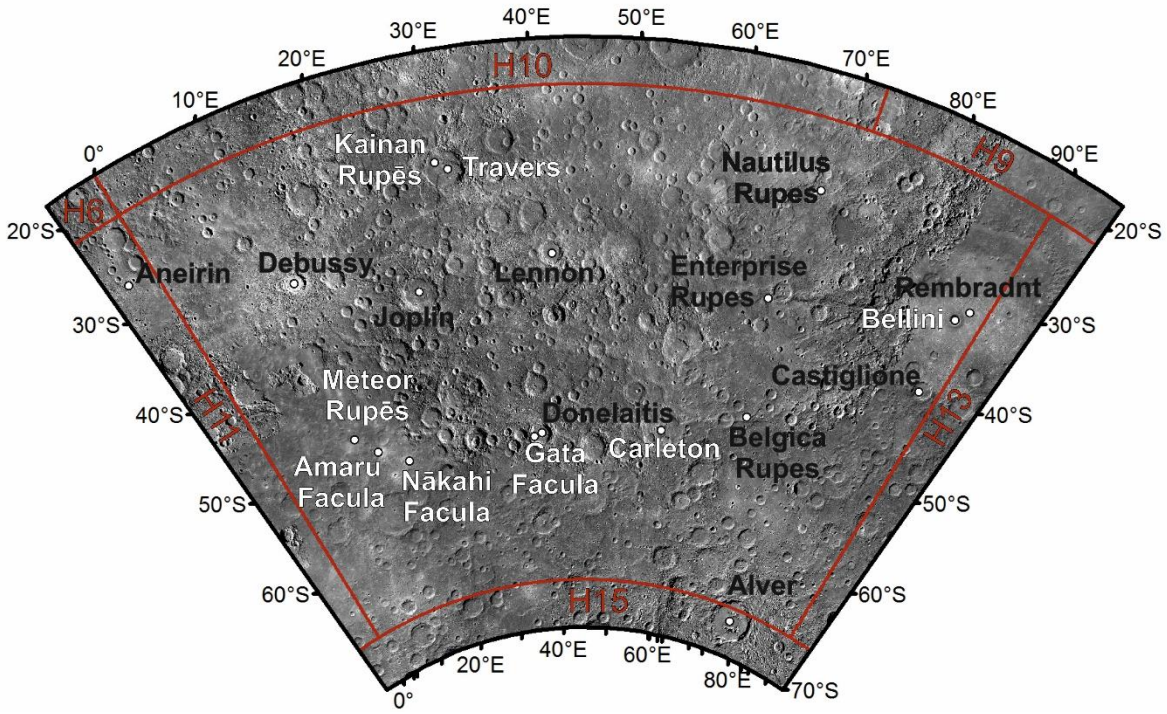

Figure 3.4 Named features within the mapping area (which includes a 5° buffer for cross-checking purposes –see section 3.5). If the feature type is unspecified, the name refers to a crater. Black shows features named before the start of the mapping process, white shows those named after the start of mapping to 20/10/2020, all of which I requested to the IAU apart from Bellini.

3.2 Data

I used several different basemaps during the mapping of H-14. These all come from MESSENGER global mosaics produced during and after the mission. Image data from MDIS (Mercury Dual Imaging System) were the only data I used for the mapping of this quadrangle. Though Mercury Laser Altimeter data were used for delivering the global digital elevation model (DEM), due to MESSENGER's elliptical orbit, it does not reach this far south, so the DEM for this area was produced from stereo images (Becker *et al* 2016). This part of the planet was not imaged by Mariner 10.

The primary data source for the map is the global image mosaics produced from the MDIS data after the end of the orbital mission. Numerous images have been stitched together to form the MESSENGER global mosaics (Denevi *et al*., 2018). Although I could have used additional non-mosaic image data from MDIS, the quadrangle's location in the southern hemisphere, and MESSENGER's elliptical orbit, meant that most of the additional images available are of low resolution so I did not use any other data for the mapping. However, I did make use of these during the detailed studies of volcanic vents (chapter 5) and faulted vents (chapter 6).

3.2.1 Basemaps

The basemaps used for mapping include the bulk data record (BDR), a 250m/pixel basemap, Low angle incidence (LOI), High Incidence West/East basemaps (HIW and HIE), as well as colour and enhanced colour.

Multiple mosaic datasets with different incidence angles were necessary due to shadows obscuring areas of the planet's surface. As such, knowing the illumination geometry for the images is essential. The incidence angle represents the angle between the sun and a line normal to the surface of the planet at the centre of the image (Figure 3.5). In this instance, when the sun is at the horizon (sunrise/sunset), it would have a ± 90° incidence angle. The emission angle represents the angle between the perpendicular line and the spacecraft. For a nadir image (looking directly down), the emission angle is 0°. The phase angle is the sum of the emission angle and incidence angle. For a nadir-facing image at local noon, the phase, emission, and incidence angle would all be 0°; there would be no visible shadows or topography, the only variation in tone caused by albedo differences. The differences in the shadows between the different image mosaic products are shown in Figure 3.6. I will now describe each of the basemaps used in detail:

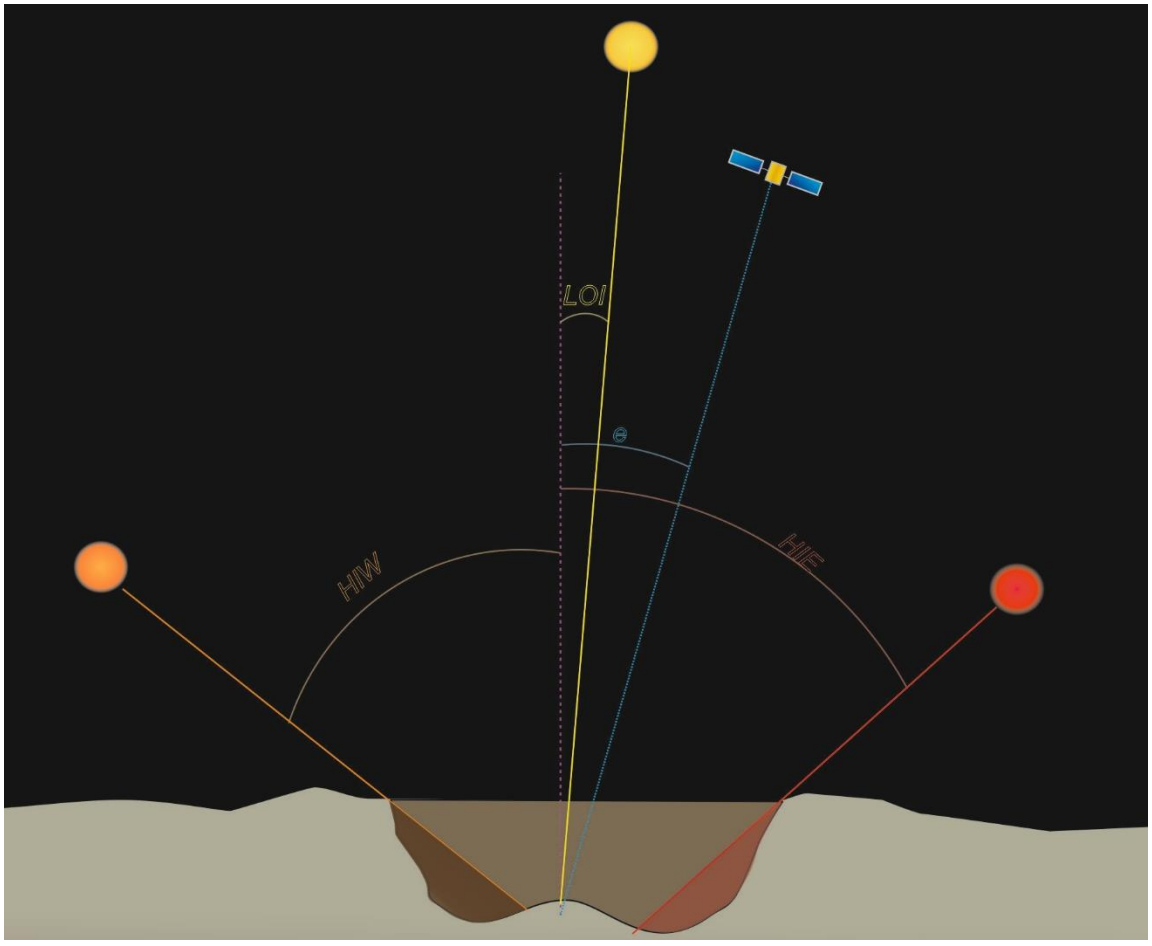

Figure 3.5 Diagram showing phase, emission and incidence angles for a satellite with High incidence West (HIW), High Incidence East (HIE), Low angle of incidence (LOI). The BDR basemap uses images recorded at an incidence angle intermediate between high incidence and low incidence, and used images illuminated from both the east and west. Authors own schematic.

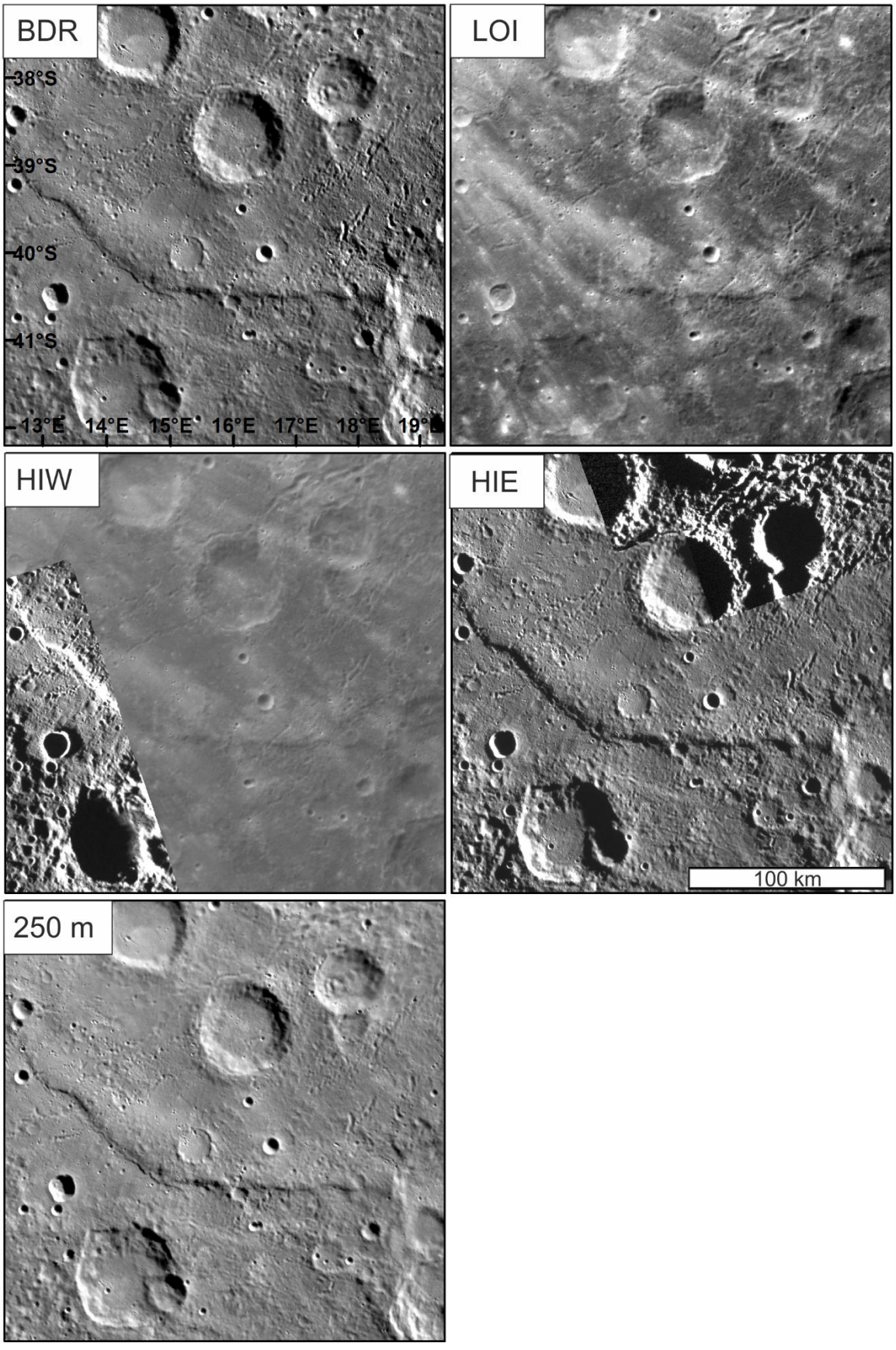
BDR
38°S
39°S
40°S
41°S
13°E
14°E
15°E
16°E
17°E
18°E
19°E
LOI
HIW
HIE
100 km
250 m

Figure 3.6 Image showing the same area with different basemaps with different illumination directions. Notice the incomplete image coverage for the HIW and HIE mosaics where limited numbers of high angle images are available so that gaps in the mosaic is infilled with lower incidence angle images.

3.2.1.1 Bulk Data Record Global Basemap

The main basemap that I used was the 166 m/pixel (256 pixels per degree) Bulk Data Record (BDR) mosaic. It is a global monochrome map using MESSENGER's NAC and WAC-750 nm image data (Figure 3.7). This mosaic uses image data with a low emission angle and an incidence angle as close to 74° as possible. This angle provides the best illumination conditions to identify morphological features through shadows without these shadows obscuring a large proportion of the terrain (Murchie *et al* 2016). The BDR basemap is used in the map sheet and as background images unless otherwise specified.

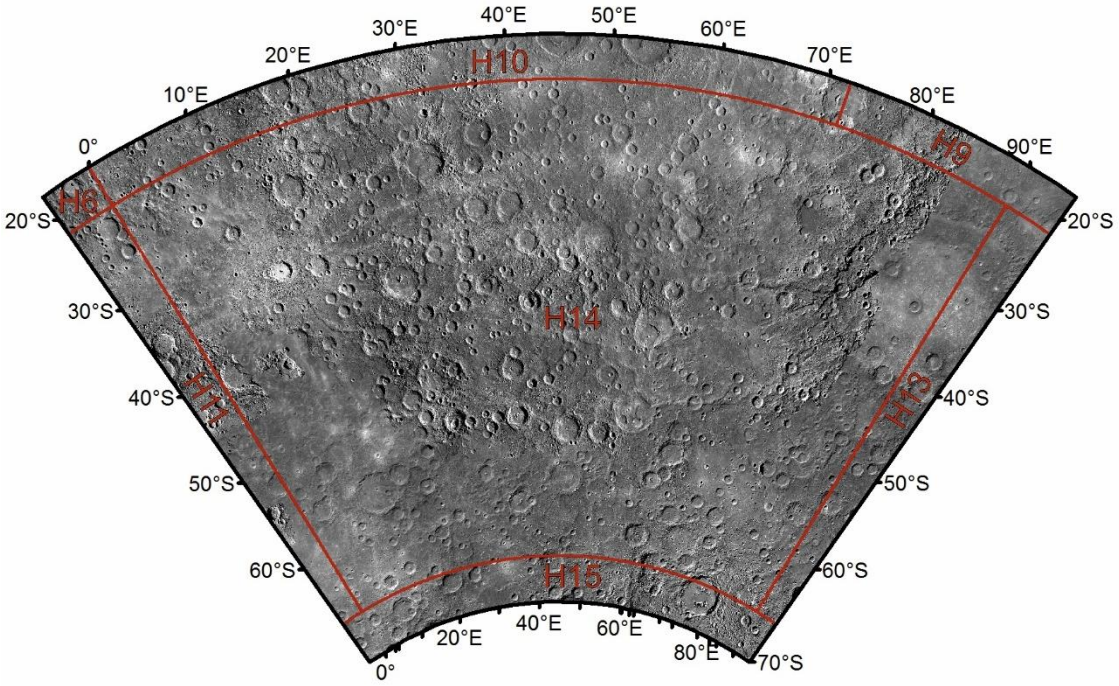

Figure 3.7 Bulk Data Record (BDR) mosaic 166 m/pixel global basemap (Denevi *et al* 2018a) *of the H14 quadrangle with a 5° overlap with adjacent quadrangles.*

I also used a 250 m/pixel version (Figure 3.8) of this basemap produced earlier during the MESSENGER mission (referred to as the 250m/pixel basemap). Some areas of this mosaic have lighting geometries closer to the 74° incidence angle or fewer joins between images than the 166 m/pixel BDR image mosaic. So despite the lower resolution, it can sometimes be superior to the 166 m/pixel BDR image mosaic for mapping terrain type or tectonic features.

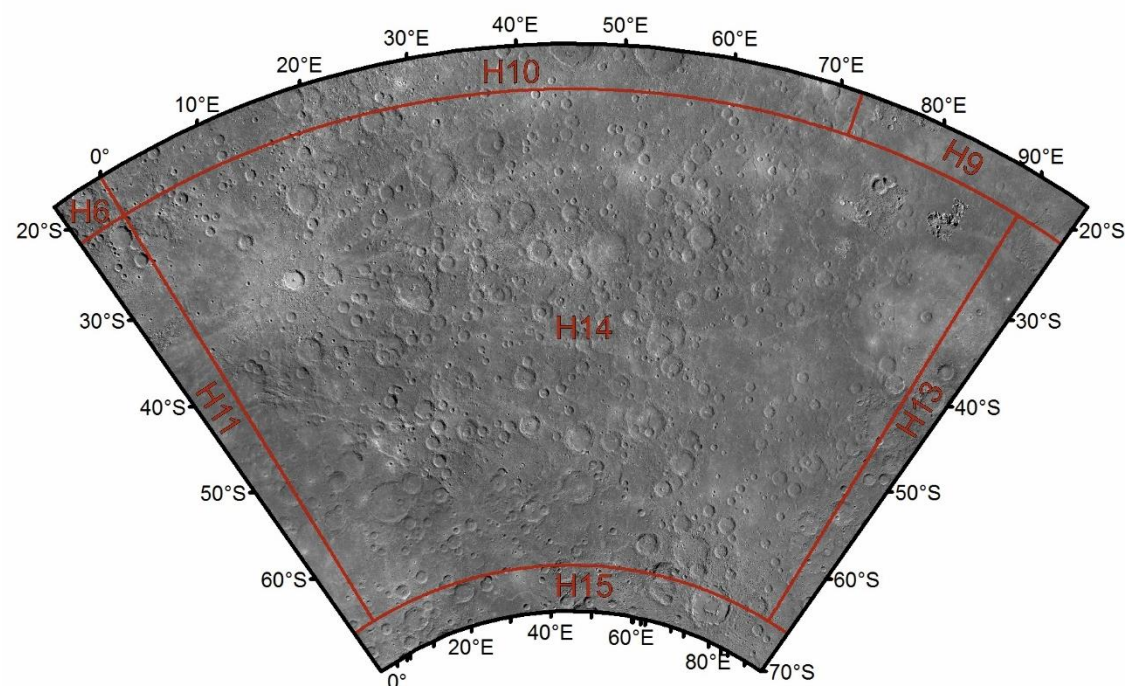

Figure 3.8 t 250 m/pixel basemap (Denevi *et al* 2018a) *of H14 the quadrangle with a 5° overlap with adjacent quadrangles.*

3.2.1.2 Low Incidence Angle

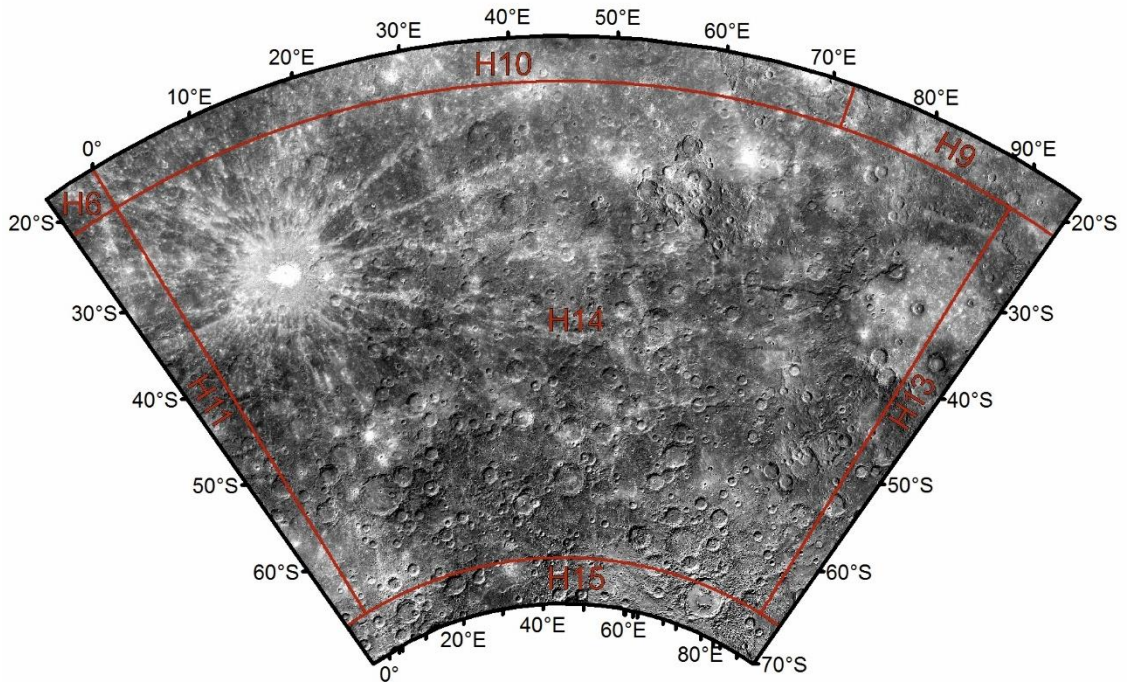

Figure 3.9 LOw Incidence (LOI) basemap at 166 m/pixel (Denevi *et al* 2018a) *of the H14 quadrangle with 5° overlap with adjacent quadrangles.*

The LOI reduced data record (Figure 3.9) comprises images with incidence close to 45° (Murchie *et al* 2016). The LOI basemap was useful for mapping features identified more clearly by albedo than by morphology (which appears subdued due to lack of shadows) including ejecta contacts and patches of Smooth Plains. It is also useful for mapping crater rays and faculae.

3.2.1.3 East and West Illumination

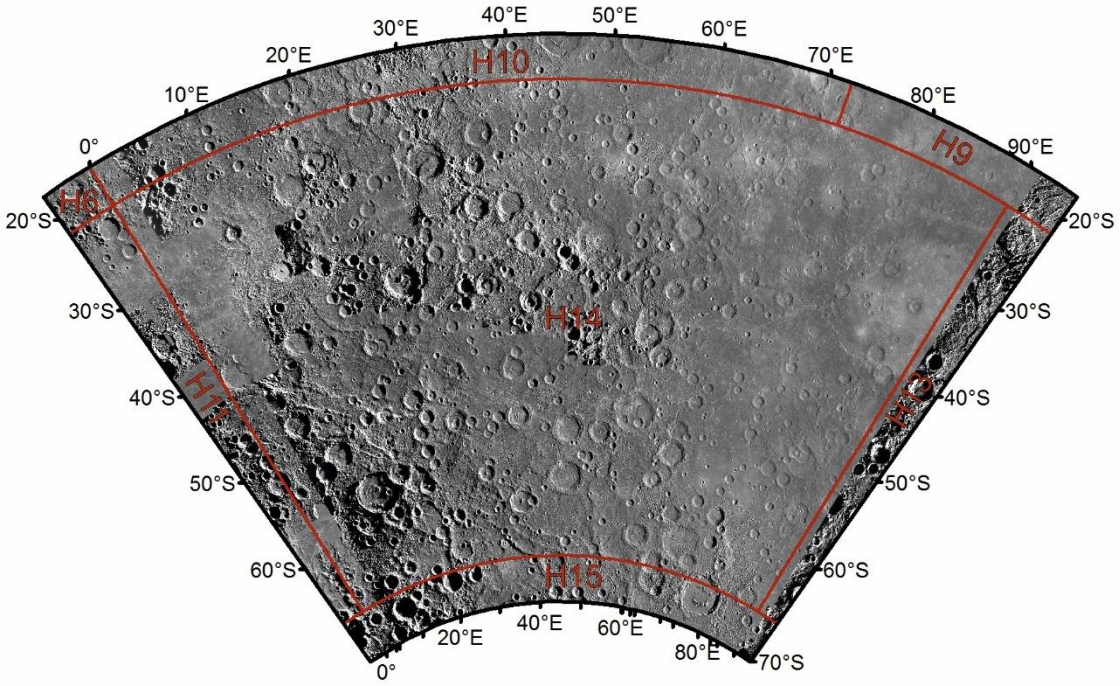

Figure 3.10 High Incidence East (HIE) 166 m/pixel basemap (Denevi *et al* 2018a) *of the H14 quadrangle with a 5° overlap with adjacent quadrangles.*

High solar incidence angle images accentuate low relief morphology and highlight asymmetric topography more steeply sloped towards the direction of illumination. These basemaps are useful for picking out subtle features. I used both East (HIW; Figure 3.10) and West (HIW; Figure 3.11) high incidence angle images during mapping. They represent the best images close to an incidence angle of 78° with that specific direction of illumination (Murchie *et al* 2016). These basemaps have a spatial sampling of 256 pixels per degree (166 m/pixel). There were limited high incidence data collected (in east or west illumination) between 60 and 80°, and so there is little difference between the BDR, 250m/pixel basemap, HIW and HIW basemaps in this area of the quadrangle, for this reason: they are all using the same or similar images.

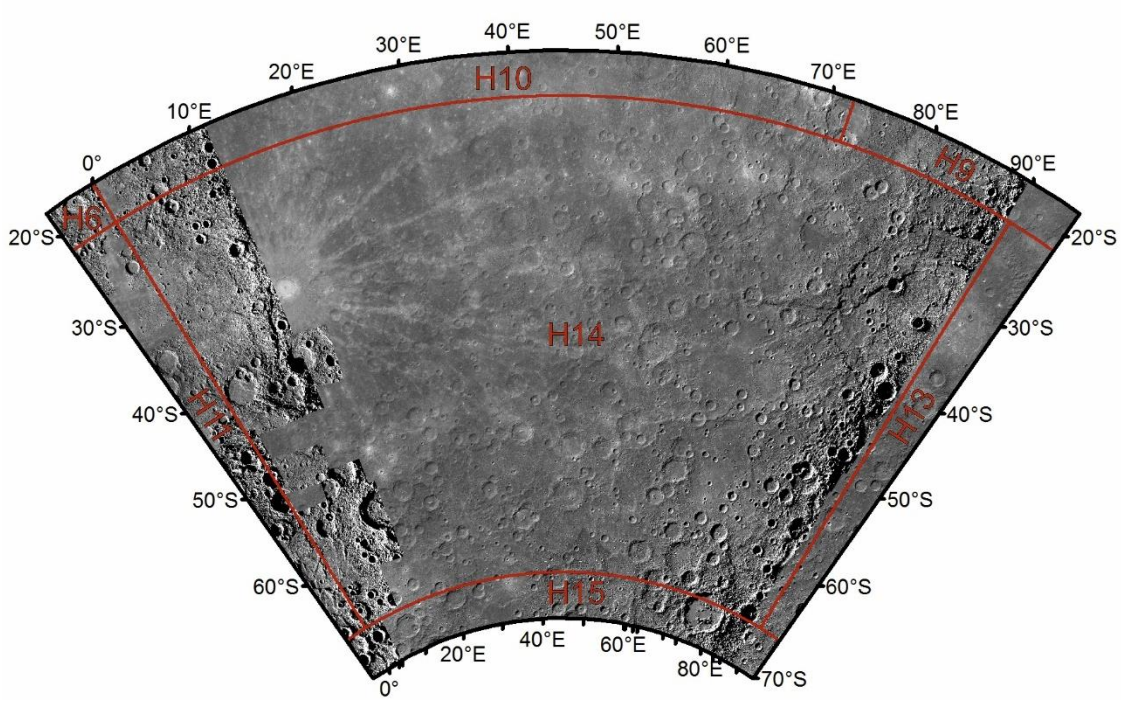

Figure 3.11 High Incidence West (HIW) Basemap 166 m/pixel (Denevi *et al* 2018a) *of H14 quadrangle and 5° overlap with adjacent quadrangles.*

3.2.1.4 Colour and Enhanced Colour Basemaps

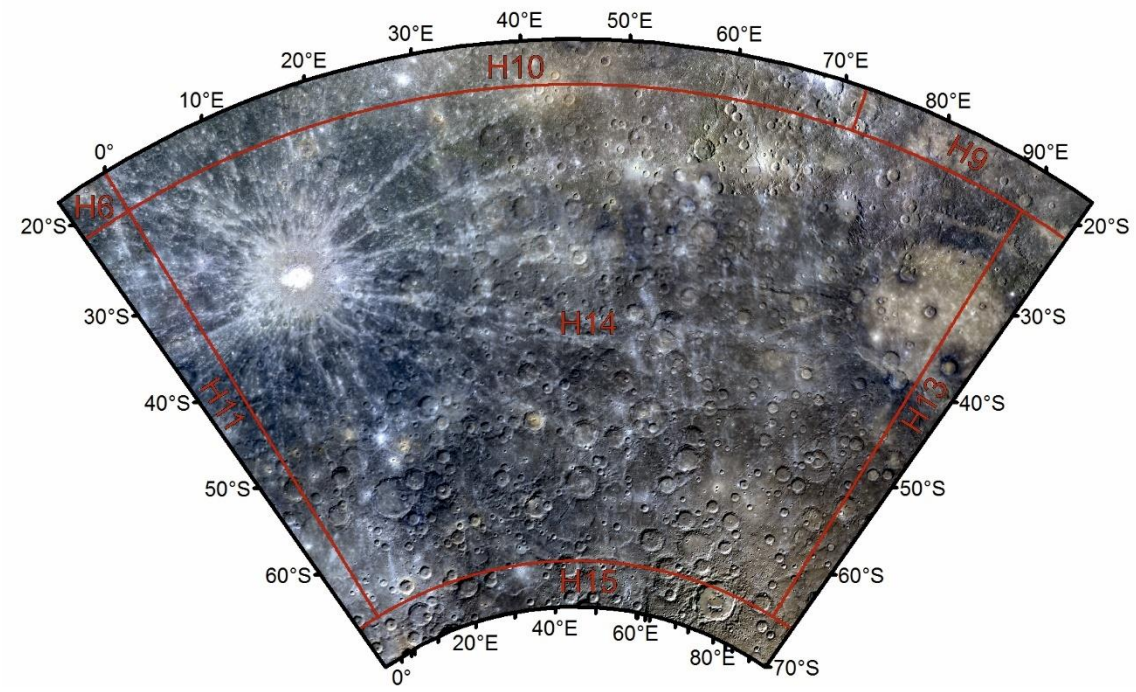

Figure 3.12 Colour 665 m/pixel global mosaic (Denevi *et al* 2018a) *of H14 quadrangle with 5° overlap.*

The "Mercury MESSENGER MDIS Basemap MD3 Color Global Mosaic 665m" Figure 3.12 uses MDIS filters at 1000 nm, 750 nm, and 430 nm in the red, green, and blue channels in the resulting mosaic (Denevi *et al* 2018a). The resolution is lower (665 m/pixel) than the monochrome basemaps used. However, this product is still useful to identify the approximate location of crater rays that I could then more precisely locate using the monochrome basemaps.

The "Mercury MESSENGER MDIS Basemap Enhanced Color Global Mosaic 665m" (Figure 3.13) is a global mosaic employing data from the 430, 750, and 1000 nm bands. It uses the second principal component, the first principal component, and the 430/1000 ratio respectively for the red, green, and blue channels in the mosaic. It also has a resolution of 665 m/pixel and was useful for mapping crater rays and identifying faculae (albedo spots) as well as mapping the interior of Rembrandt and some patches of Smooth Plains.

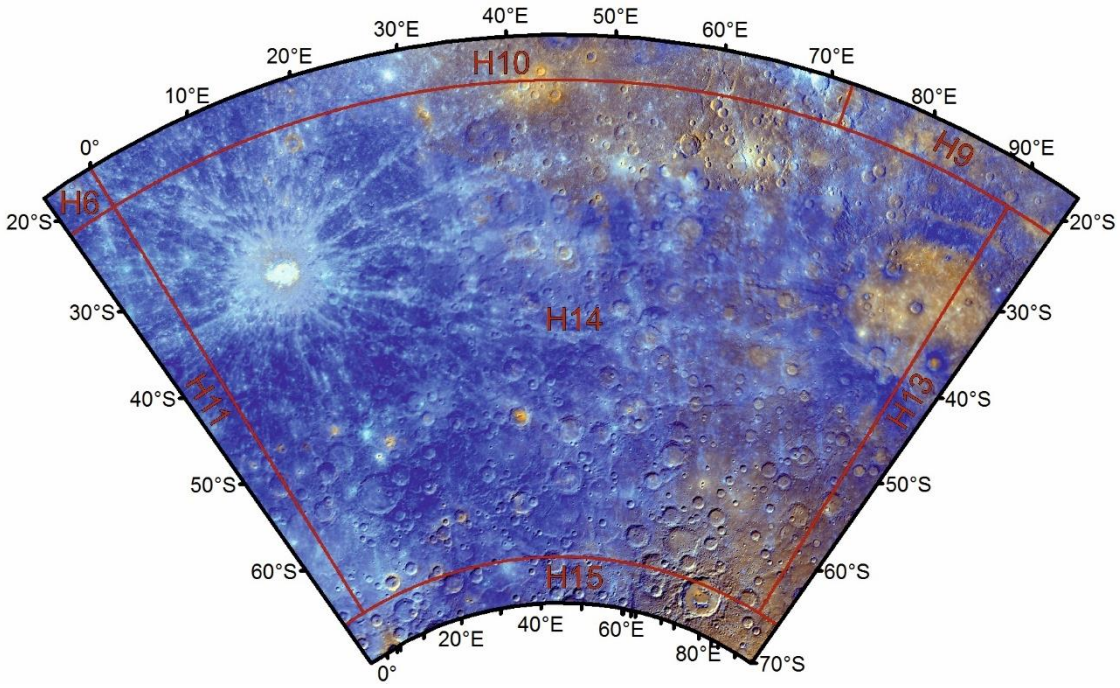

Figure 3.13 The 665 m/pixel Global Enhanced colour basemap (Denevi *et al* 2018a) *of H14 quadrangle with 5° overlap.*

3.2.1.5 Digital Elevation Model (DEM)

Becker *et al*. (2016) produced the 665 m/pixel DEM basemap (Figure 3.14) using image data from MDIS. It was created using ISIS3 and OpenCV to match together overlapping images of the planet's surface and combining the image geometry, spacecraft location and the match points to generate a 3D model of the planet's surface (Becker *et al* 2016). During mapping, I used the DEM to verify the locations of tectonic features (by observing sudden steps in the topography) and the edges of large impact basins by circular areas of relatively low topography. The DEM also aided the identification of Smooth Plains, which tend to be in lower-lying portions of the map.

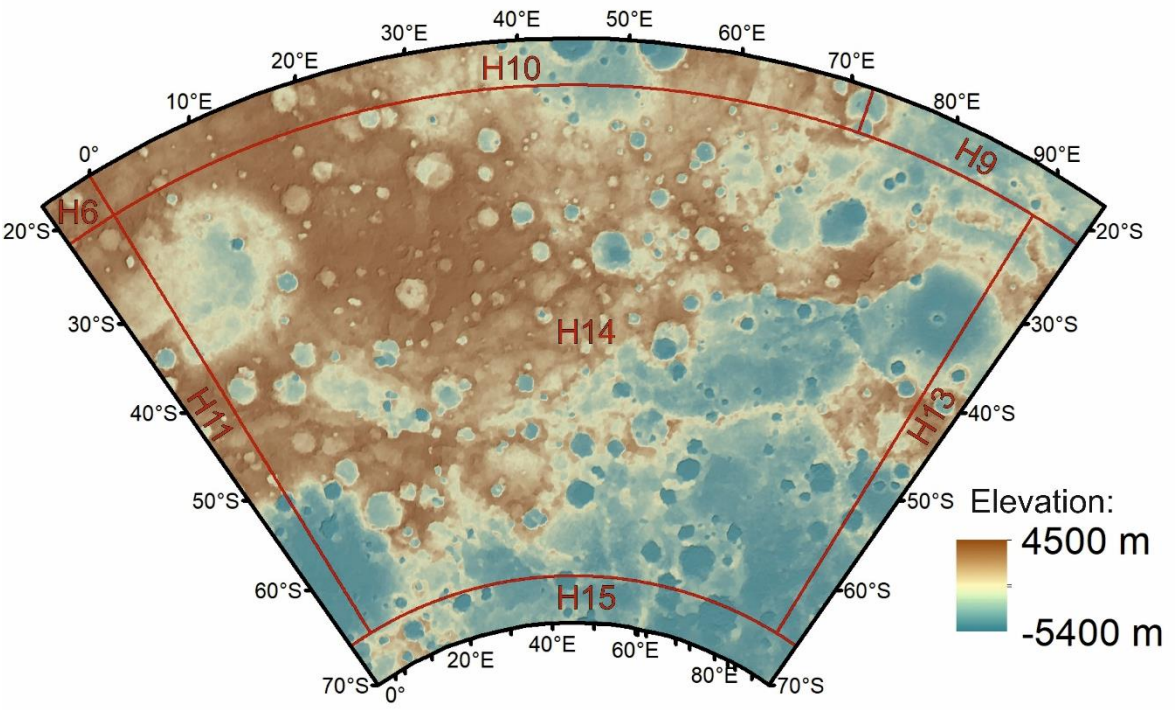

Figure 3.14 The 665 m/pixel DEM basemap for Mercury (Becker *et al* 2016) *H-14 including 5° of adjacent quadrangles. To enhance visibility, a hillshaded relief map has been applied.*

3.3 Software and Basemap Processing

The basemaps provide the basis for the geomorphic mapping. I produced the basemap using the global image mosaic produced from MDIS by the MESSENGER team. The mosaic is divided into tiles, each one ¼ of a quadrangle. They are publicly available at the online storage systems of the Mercury Orbital Data Explorer (https://ode.rsl.wustl.edu/mercury/index.aspx) and also the MESSENGER Planetary data system (PDS) (https://pds-imaging.jpl.nasa.gov/volumes/mess.html). I processed the tiles using the Integrated Software for Imagers and Spectrometers software Version 3 (ISIS3) from the United States Geological Survey. The processing pipeline I used (Figure 3.15) takes native '. IMG' files and converts them into projected '. CUB' files which are compatible with a geographic information system (GIS), or reprojects and trims the derived products from the MESSENGER team (such as global basemaps tiles) ready for mapping (Becker and Becker 2015). I maintained these divisions to minimise computer resources required when focusing in on an area. Tiles externally bordering the quadrangle were trimmed to show a 5° overlap into adjacent quadrangles to aid computational efficiency (see section 3.5).

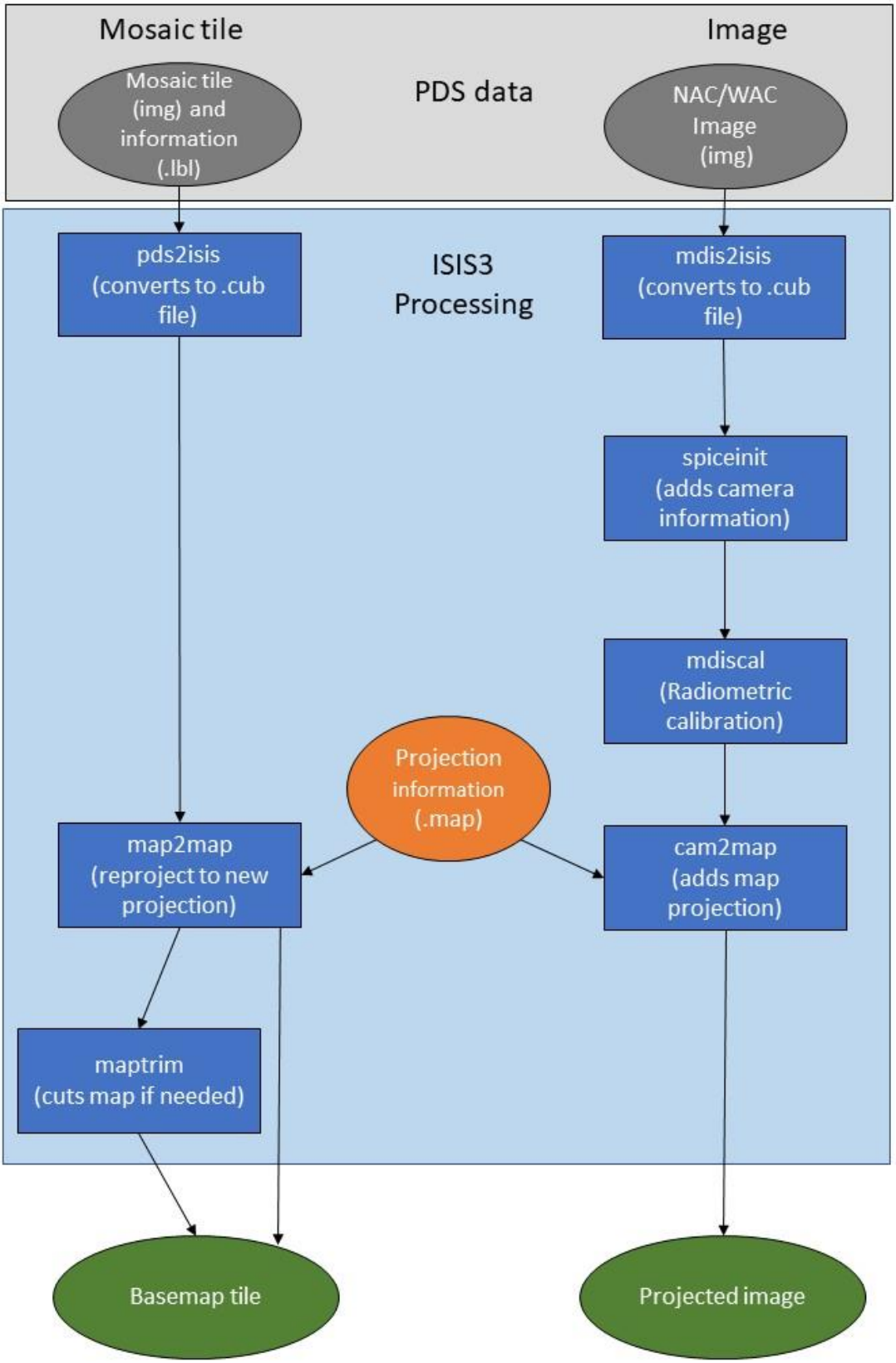

Figure 3.15 ISIS 3 workflow diagram for ISIS3 commands for a mosaic tile or an individual image to produce data compatible with a GIS. Authors own schematic

To perform the digitising for the mapping, I used ESRI's ArcGIS Desktop software version 10.5.1. This is a computer-based GIS system that projects images at a known scale and enables rapid switching or overlaying between different 'layers', such as the various basemaps, aiding interpretation during mapping. I used this software to produce the map by drawing lines, polygons, and points. A geodatabase stores the basemap tiles and map data for handling and transfer.

3.4 Mapping Parameters

To create a map of a quadrangle, a spheroid, reference frame, coordinate system, projection, and scale must be defined.

3.4.1 Spheroid

The most recent estimates from MESSENGER data gives the planet an equatorial radius of 2439.36±0.02 km with a polar radius measuring 1.65 km less (Perry *et al* 2015). The IAU considers the difference between the polar and equatorial radii to be inconsequential for mapping based on MESSENGER data (Archinal *et al* 2018). H-10 and H-02 use the same spheroid of 2440 km. For consistency, I also used this spheroid. The map for H13 is using a radius of 2439.4 km. The difference between these spheroids on the surface is 942 m over 90°. This length would be equivalent to 0.3 mm total (the map is 875 mm across) at a scale of 1:3 million (see section 3.4.4) and so unlikely to be consequential when 'joining up features' between quadrangles. The largest feature in both H13 and H14 is the Rembrandt impact basin with a diameter of 715 km. The difference between the two spheroids projections over that length is 178 m, ~1 pixel of the basemaps used, so again likely to be inconsequential when matching up the maps.

3.4.2 Reference Frame

The fixed reference frame for the surface of a planet allows the repeated identification of a location and requires a coordinate system for which the prime meridian and the pole must be defined. North for any planet in the solar system is the hemisphere that lies on the north side of the invariable plane (Archinal *et al* 2018).

The prime median has been defined as the subsolar point at the first perihelion passage of 1950 (Hall *et al.* 1971). Mariner 10 should have enabled the definition of a surface-based feature to represent this point. However, the location previously identified was always on the planet's nightside during Mariner 10 flybys, so was never imaged. Murray *et al.* (1975) defined the longitude 20°W line by the 1.4 km diameter Hun Kal crater (meaning 20 in Maya, making this the only crater on Mercury not named after a person). (Stark *et al* 2018) found that Hun Kal crater is offset by 0.09° from 20°W. The IAU adopted this new reference frame, which means the prime meridian no longer lies precisely on the subsolar point during perihelion but is offset by approximately 2.2 km. However, this varies over time due to libration-related effects (Archinal *et al* 2018).

3.4.3 Projection

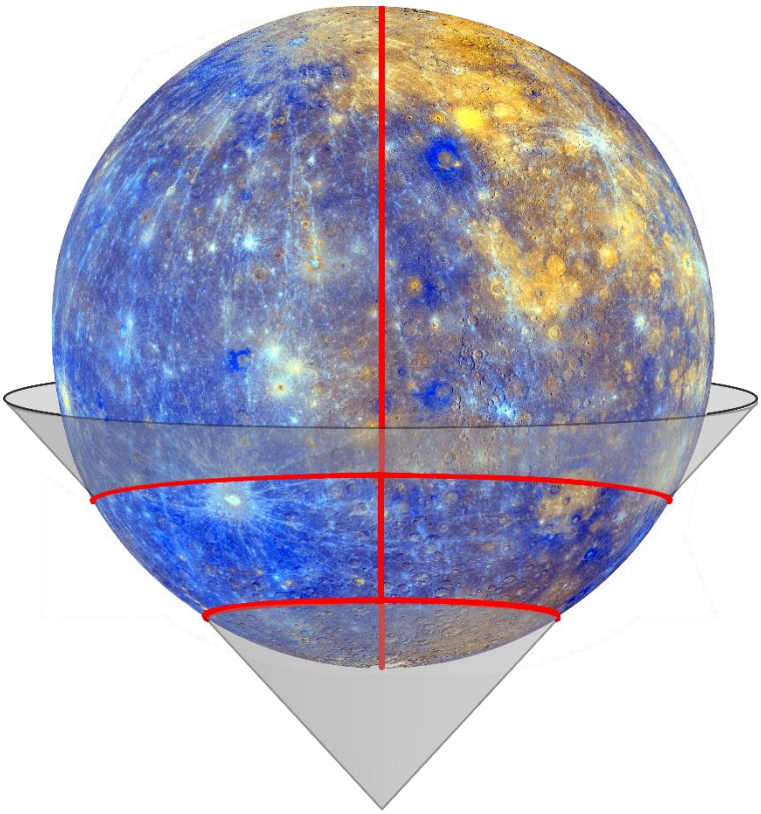

Figure 3.16 Image showing how the two parallels (curved red lines) of the Lambert conformal conic projection represent the intersection of a cone with the globe and the location of the meridian used in the projection (vertical red line). Authors own schematic. I produced the map using a Lambert conformal conic projection (Lambert 1772), which is considered a standard projection for the mid-latitudes. It preserves angles, and so preserves the shape rather than the area of a feature (Snyder 1982); this is useful for craters and tectonic features and so is appropriate for geological mapping. It is the equivalent of a section of a cone placed over a portion of a planet. It has two standard parallels where lengths are at true scale and which represent the intersections between the theoretical cone that is the map surface and the planetary surface. Between the parallels, the lines of latitude get slightly closer together as the cone and the planet's surface diverge. The scale decreases as the projection compresses it into the map surface. Outside the parallels, the lines of latitude get progressively further apart as the planet's surface curves inwards away from the cone and they have to be stretched by increasing amounts intersect the cone, and so the scale increases.

For the basemaps for H-14, I used 30° and 58° S as the standard parallels, following the convention of 1/6 and 5/6 of the latitudinal range (Snyder 1982). The central meridian of the projection is 45° E, which is the middle of the quadrangle.

To quantify the distortion caused by the projection, I produced a Tissot's indicatrix of distortion (Tissot 1880). This shows that a 300 km diameter circle at the final mapping scale measures 10 cm at the standard parallels (-58°, -30°) but is shorter between these (9.7 cm at −44° latitude) and longer beyond them (10.9 cm

at -72° and -16°). This change in scale does not have a significant effect on the appearance of the map (Figure 3.17). However, studies requiring precise size measurements should use a more appropriate projection.

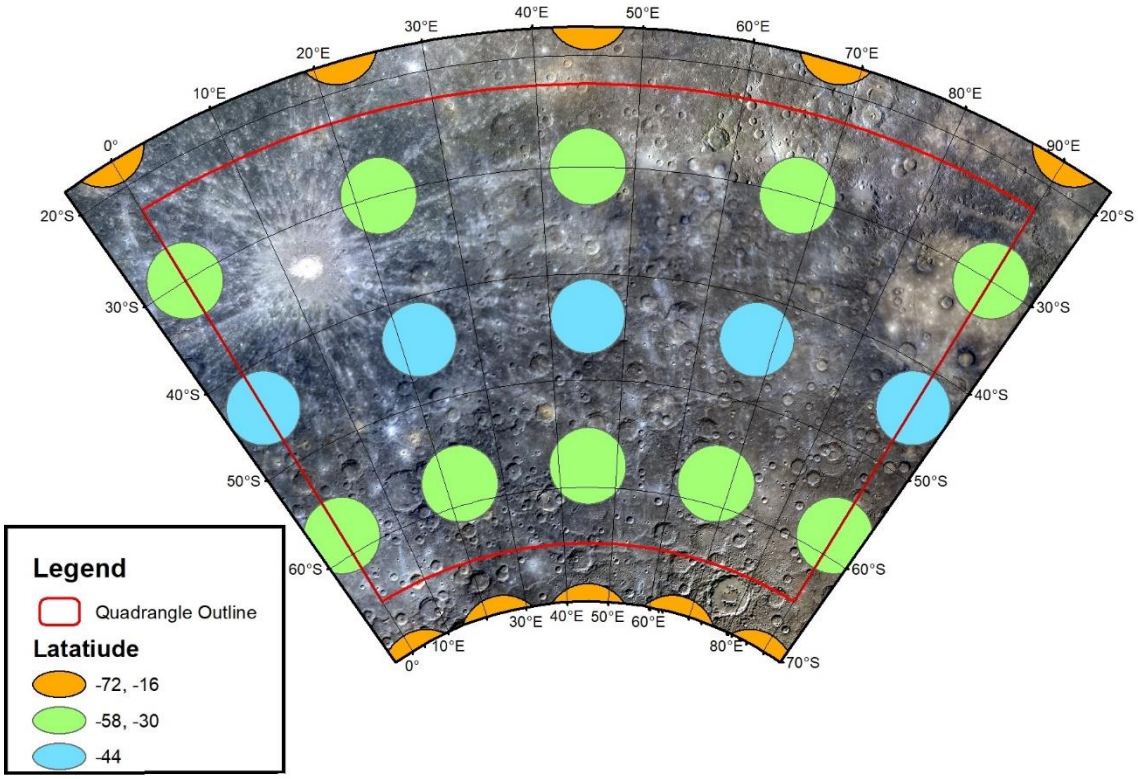

Figure 3.17 Tissot's indicatrix of distortion for the mapped quadrangle with 5° overlap. The background image is the Mercury MESSENGER MDIS Basemap MD3 Color Global Mosaic at 665 m/pixel (Denevi *et al* 2016).

3.4.4 Scale

A scale of 1:3 million was chosen for the map to be consistent with other post MESSENGER quadrangle maps (Galluzzi *et al* 2016, Wright *et al* 2019, Guzzetta *et al* 2017, Mancinelli *et al* 2016). Two methods are commonly used for the mapping scale: either 2 to 5 times larger than the final production map (Tanaka *et al* 2011) in this case giving a range of 1: 1,500,000 – 600,000, or using a scale that is 2,000 times the raster scale (Tobler 1987). In the case of the 166 m/pixel basemap, this would equal 1: ~300,000. To produce the highest fidelity, I chose to work at a scale of 1: 300,000. Features needed to be at least 3 km wide to be mappable; this forms an element at least 1 mm across on the final map at this scale.

I used a streaming length (the frequency that individual points, which control the position of a line, are automatically placed along a line whilst it is constructed) of 900 m as this represents 0.3 mm at mapping scale, as suggested by Tanaka et al. (2011). This length between points on a line produces a balance of fidelity and smoothness at the map scale without creating too many data points and bloating the size of the files; for a 5 km diameter crater this would produce an outline ~17 points (corners) with straight lines between each point.

3.5 Mapping Process and Philosophy

All maps are an interpretation of the data; however, I have tried to avoid including a genetic interpretation (which I explore in Chapter 4) with the morphological one. Compromises with this approach include features such as grabens where the morphological description also has links to a genetic term. I do this to be consistent with other maps, e.g. (Galluzzi *et al* 2016) and as it gives the informed viewer a better understanding of the appearance of these features. Likewise, the Rembrandt specific units are named after the Rembrandt impact basin, and I acknowledge the name implies a genetic link as well as the spatial relationship; however, I feel this compromise aids the viewer in locating and understanding these units better.

In general, I have followed the mapping standards of the United States Geological Survey (USGS) (Tanaka *et al* 2011) and Planmap (Rothery and Balme 2018) as well as those set out by the other 1:3 million scale maps of Mercury (Galluzzi *et al* 2016, Wright *et al* 2019). To make the geomorphic map, I first produced polylines. The first linework identified structures and crater rims (section 3.6), and after that, delineated contacts between morphological units (section 3.7). I then converted these lines into polygons, with attribute information applied relating to morphological interpretation such that each polygon shows a geomorphic unit as a coloured block. This technique reduces the risk of gaps between polygons. Multiple line styles represent both the type of feature and the certainty of the location of the line. I did the same for the superficial units (section 3.8). I used point symbols to mark probable volcanic vent sites and fields of hollows which are <3 km in size and so too small to be portrayed by a shape.

To produce a consistent map interpretation, I interpolated lines over features smaller than the mappable scale even when they might cause offsets in mappable features (e.g. <20 km diameter impact craters displacing contacts). However, if they moved features at a larger than mappable scale (e.g. the displacement of crater wall-floor contacts by a subsequent small impact on this boundary), these were adjusted to represent what seemed most representative of the surface of the planet. This is consistent with other mappers (Wright *et al* 2019, Galluzzi *et al* 2016) and reduces any sudden angular changes in the map's lines.

A 5° overlap with the adjacent quadrangles enabled quality control of the map. A comparison of the overlap with the completed and in-progress adjacent 1:3M scale maps allows consistency checks between them. I also checked for (and removed) dangles (contact lines that do not close), the intersection of lines and self-intersection and self overlapping lines.

3.6 Linework

Mapping started by creating lines to digitise tectonic and crater features, and to identify the boundaries between geomorphic units. I then converted the boundaries into polygons representing these units. Different types of craters, tectonic features and unit boundaries used different styles of lines to enable differentiation between them.

3.6.1 Crater Rims

The mapping of craters larger than 5 km in diameter, but less than 20 km, uses a single unbroken line along the rim (the upper break in slope on a bowl-shaped feature). 5 km craters become 1.7 mm diameter circles on the map at the scale used. This cut-off produces a resolvable set of features while preventing the map from being cluttered by excess detail. Mapping smaller diameter craters would generate even more craters as minor features, cluttering and potentially obfuscating the map but without any significant geomorphic information benefit.

Craters wider than 20 km diameter produce component features of sufficient size for more detailed mapping, and so these craters are split into several morphological units. The rim is shown with a double tick on the downslope side to differentiate it from those craters >5 km but <20 km in diameter. Outlines of features such as central peaks/rings and the surrounding ejecta use contact lines that represents the confidence and style of any particular boundary (see section 3.6.3).

Crater rims that are subdued or buried by other materials (such as ejecta from other, nearby, craters) had a distinctive line style applied to help identify the continuation of craters. Those that are covered entirely by lavas but only shown by faults generated by differential shrinking (ghost craters) were highlighted by a wrinkle ridge pattern (see section 3.6.2.2, Chapter 2.7.3, chapter 4.4.1.9).

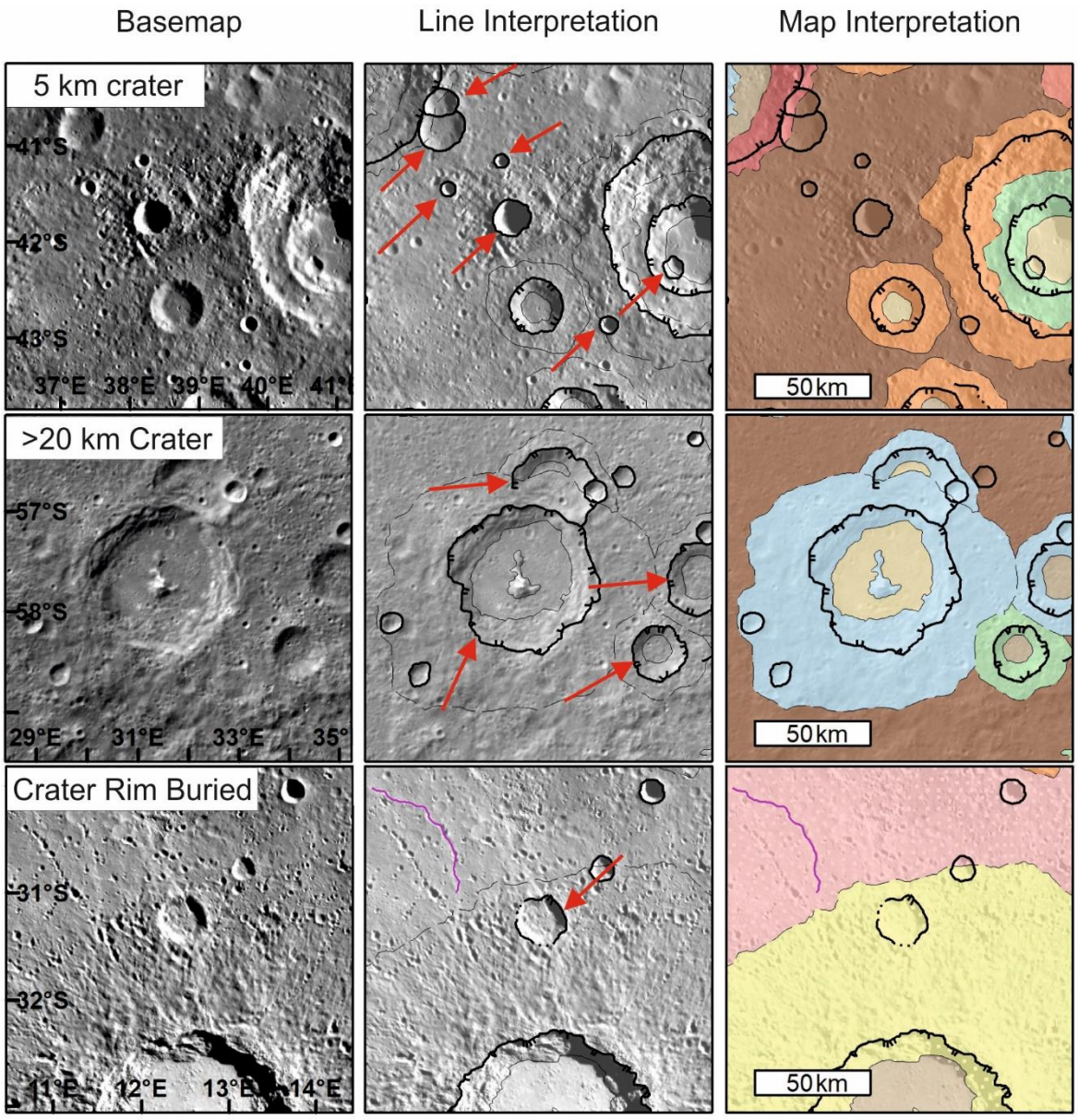

Figure 3.18 Types of crater outline with 5 km, >20 km and buried crater rim examples illustrated on the BDR basemap. Red arrows point to examples of each type. North to the top in all images.

3.6.2 Tectonic Features

The mapping area contains both extensional and contractional features. To highlight the different stress regimes, structures were designated either contractional (lobate scarps and wrinkle ridges) or extensional (grabens, Figure 3.19).

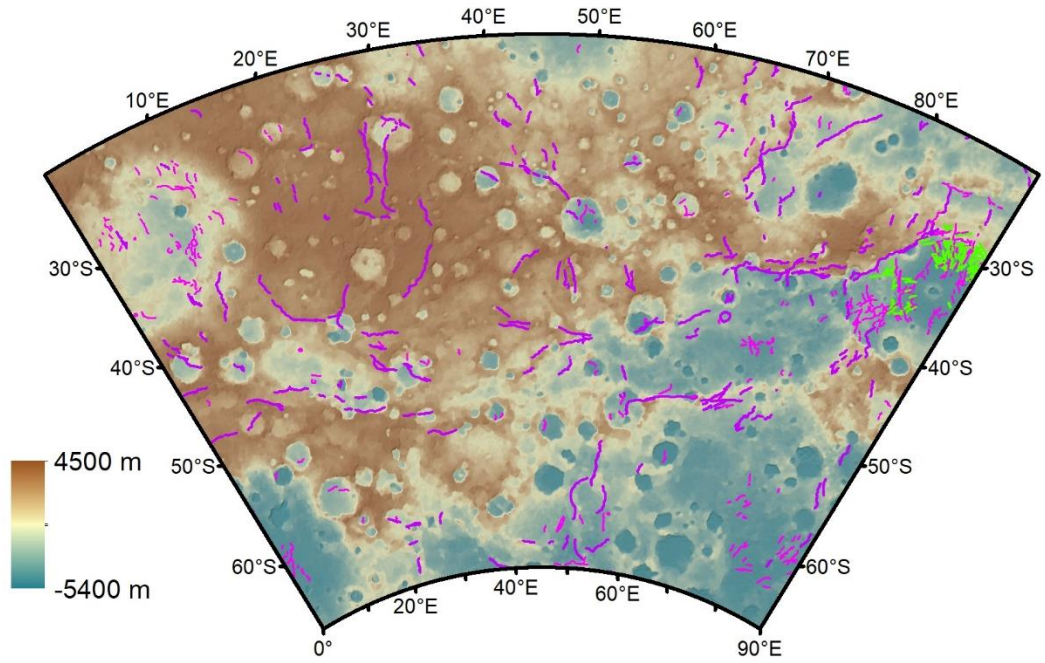

Figure 3.19 Map of contractional (purple) and extensional (green) structures within H-14.

To differentiate between them and to aid the interpretation of the geological history, these structures are divided into different types and represented by different styles of lines.

3.6.2.1 Thrust Certain, Thrust Uncertain

Thrusts are manifest on the surface of Mercury as lobate scarps (chapter 2.7.1); their asymmetrical form identifies them. The linework is drawn at the break of slope at the base of the steeper side of the feature. This location represents close to where the fault intersects with the surface. The triangular teeth point towards the hanging wall and represent the downdip direction on the fault plane. The levels of certainty reflect how clear the break in slope is; solid lines show clearly defined examples. More degraded faults, those poorly illuminated, or those where the fault expression is weak, and the location are uncertain and shown by dashed lines to reflect this (Figure 3.20).

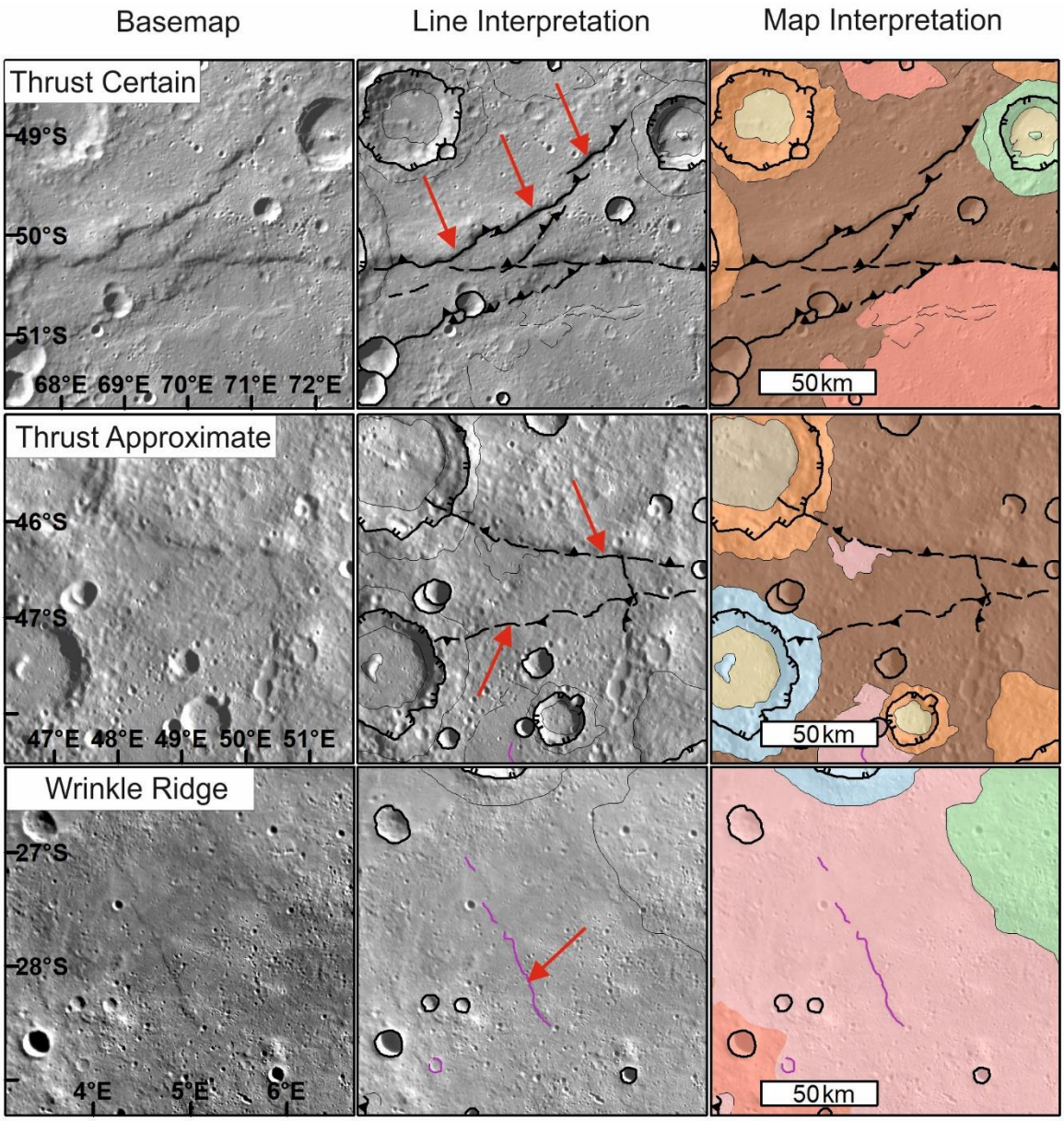

Figure 3.20 Examples of linework for contractional features, including thrust faults both confident and approximate and wrinkle ridges (indicated by red arrows in appropriate panels). The background is the BDR basemap, where line interpretation is shown the transparency of basemap is 20%.

3.6.2.2 Wrinkle ridge

Wrinkle ridges are identified by their more symmetrical profile and lower relief than lobate scarps—the ridges are marked by a single continuous pink line placed over the crest. (Figure 3.20). I have not provided a confidence level for these as they are smaller features than lobate scarps and so always relatively subtle and all therefore considered somewhat 'uncertain'. Ridges that are degraded or poorly illuminated would be unlikely to be identified during mapping.

3.6.2.3 Grabens

Grabens are the only extensional structures that I have identified within the mapping area. They are manifest as a negative relief (as shown by shadows), linear structures with sharp edges, and are generally the width of a single-line at mapping scale or less. Some grabens in the Rembrandt impact basin are wider than the width of a line; at these locations, the centre of the graben is used as the location of the line (Figure 3.21).

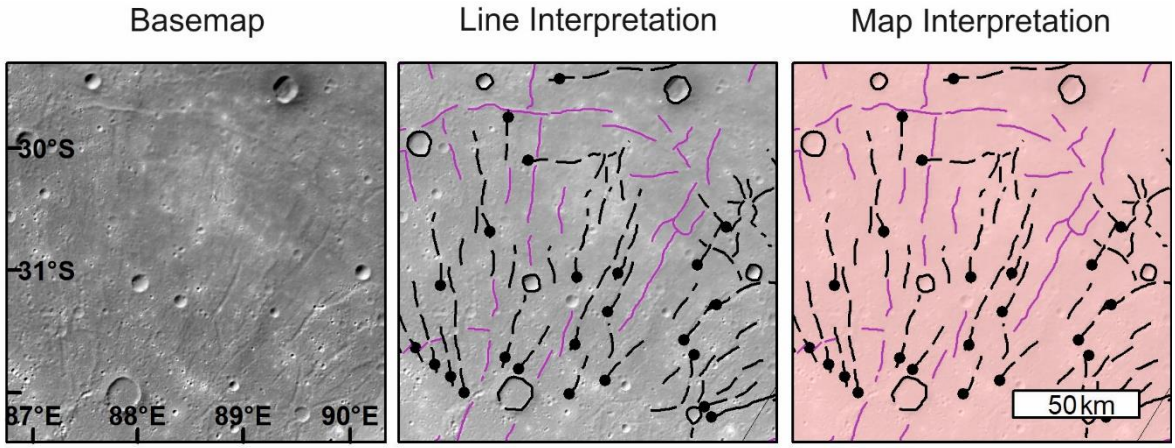

Figure 3.21 Mapping of graben structures, represented by dashed lines with circles on them. The background is the BDR basemap, where line interpretation is shown the transparency of basemap is 20%. Pink lines are contractional wrinkle ridges. North towards the top in all images.

3.6.3 Contacts

The interface between geomorphic units is known as a 'contact'. In some cases, this occurs at a lobate scarp, such as where Smooth Plains abut onto the edge of scarp or edge of a crater floor, but the majority of the boundaries occur without any other structure. These lines were drawn based on where the unit morphology changed; the type of boundary and the confidence in its location dictated the style of the line.

3.6.3.1 Contact Certain

These unbroken lines are based on clear, abrupt contacts between units. They represent confidence in the precise location of the contact at the scale mapped (approximately ±1 km). Most commonly, these are found at the edge of Smooth Plains, or at the boundary between crater floor material and its wall/central peak.

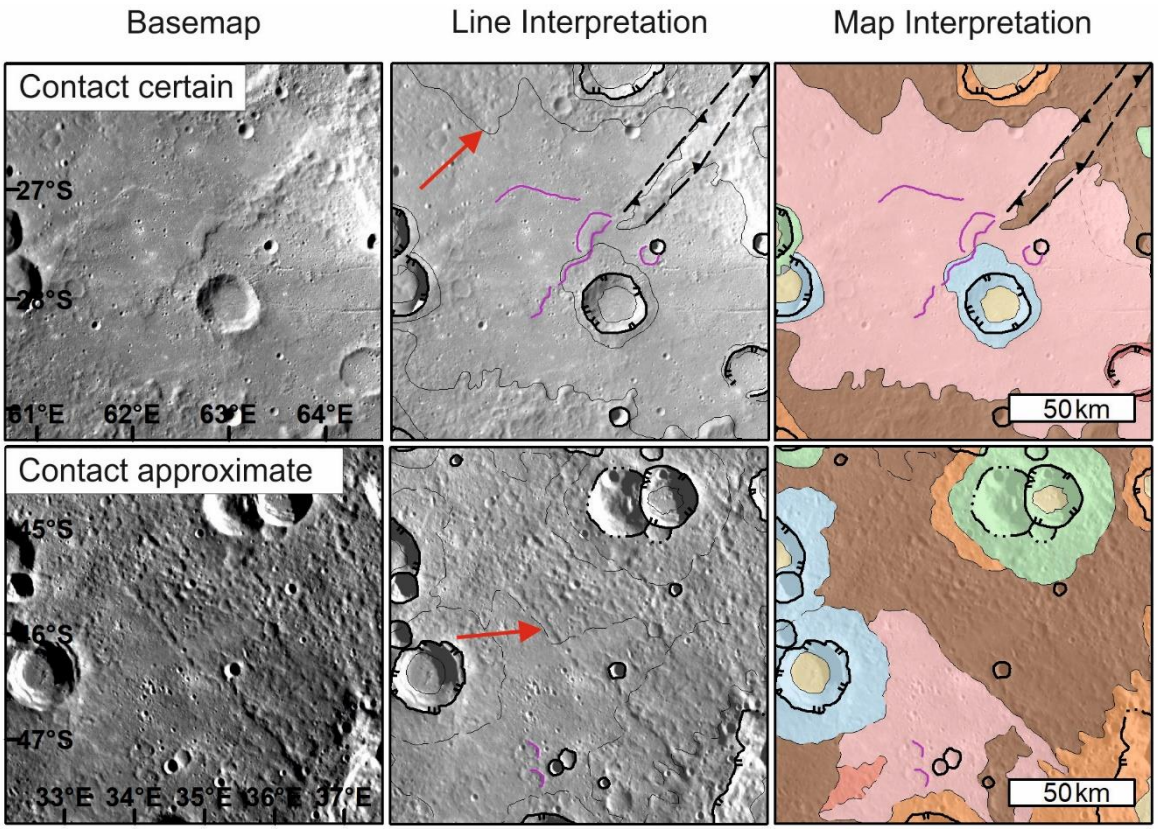

Figure 3.22 Different styles of contact. The background is the BDR basemap, where line interpretation is shown the transparency of basemap is 20%. Red arrows point to the line style. North towards the top in all images.

3.6.3.2 Contact Approximate

Approximate contacts occur where a transition is observed between units, but the exact location cannot be identified due to uncertainty in interpretation with the available data. Such contacts are often present between Intercrater Plains and Intermediate Plains, or craters with intermediate age ejecta, as space weathering and secondary impacts have degraded and mixed these boundaries and make it hard to locate precisely (Figure 3.22).

3.7 Geomorphic Map Units

I divided the map into geomorphic units. These units represent the different textures of the planet's surface and reflect the type of landform and its modification by geological and surface processes (Smith *et al* 2011). There are two distinct types of morphological unit on Mercury identified in all maps so far, including the Mariner 10 maps and MESSENGER large scale and detailed maps (Section 3.1): crater materials and plains materials. On Mercury, morphological units are controlled by; the process that formed them, the age of formation, and the amount of subsequent modification through impact, the effects of space weathering and tectonic modification.

I continue to use the main morphological units identified in the Mariner 10 maps and the other 1:3 million scale maps as they help understand the geological history within the quadrangle. Using the same geomorphic units used in other quadrangle maps also allows compatibility and comparison with other maps. It helps to put the geomorphology of the quadrangle in a global context. I chose to designate a few new units specific to the area in and around the Rembrandt impact basin, by analogy with units defined around the even bigger Caloris basin (Trask and Guest, 1975; Fassett *et al.*, 2009, chapter 2.5.1.1) and the maps already completed for Rembrandt (Hynek *et al.*, 2017; Semenzato *et al.*, 2020, chapter 2.5.1.2). Table 3.1 lists the type localities. I now describe each unit.

Table 3.1 Type localities for each unit.

Feature	Easting	Northing
C3	12.2°	-33.4°
C2	29.4°	-47.5°
C1	56.3°	-40.1°
c5	12.2°	-33.4°
c4	52.9°	-42.5°
c3	5.9°	-25.8°
c2	39.4°	-32.5°
c1	68.7°	-38.0°
Crater floor smooth	41.4	-36.0
Crater floor hummocky	57	-53
Smooth Plains	6.5°	-41.0°
Intermediate Plains	69.5°	-25.0°
Intercrater Plains	51.0°	-45.0°
Rembrandt Hummocky unit	89	-26.5
Rembrandt Massifs	83.2	-29.4
Rembrandt Rim Materials	79.0	-31.0
Rembrandt Linear unit	82.5	-25.2
Rembrantd Ejecta	78.2	-27.5
Hollows	45.3°	-37.4°
Bright crater rays	2.9°	-27.8°
Facula	9.2°	49.1°
Pits	38.1°	53.0°

3.7.1 Crater Materials

I followed the methodology of Galluzzi et al. (2016) by classifying all craters of 20 km diameter and larger by degradation state. In the majority of cases this reflects how long these have been exposed to, and modified by, processes of subsequent smaller impacts and space weathering. There are, however, two different systems used to classify crater degradation (which is usually a proxy for age) on Mercury. The maps produced by Mariner 10 and the global maps produced after MESSENGER use a 5-class system, but several post-MESSENGER 1:3 million maps use a simplified 3-class system (Galluzzi *et al* 2016). I produced 3- and 5-class versions of my map. To avoid confusion, I use the same convention as Wright et al. (2019) and use a capitalised 'C' for the 3-class system (e.g. C1, C2, C3) and a lower case 'c' for the 5-class systems (e.g. c1, c2, c3, c4, c5). Wright et al. (2019) took advantage of the digital GIS system allowing polygons to have multiple attributes and produced an alternate version of their map classified using both systems. I have done the

same as this enables comparison between different map systems. See chapter 4.2.1 for discussion on the merits of the different crater classes.

3.7.1.1 3-Class system

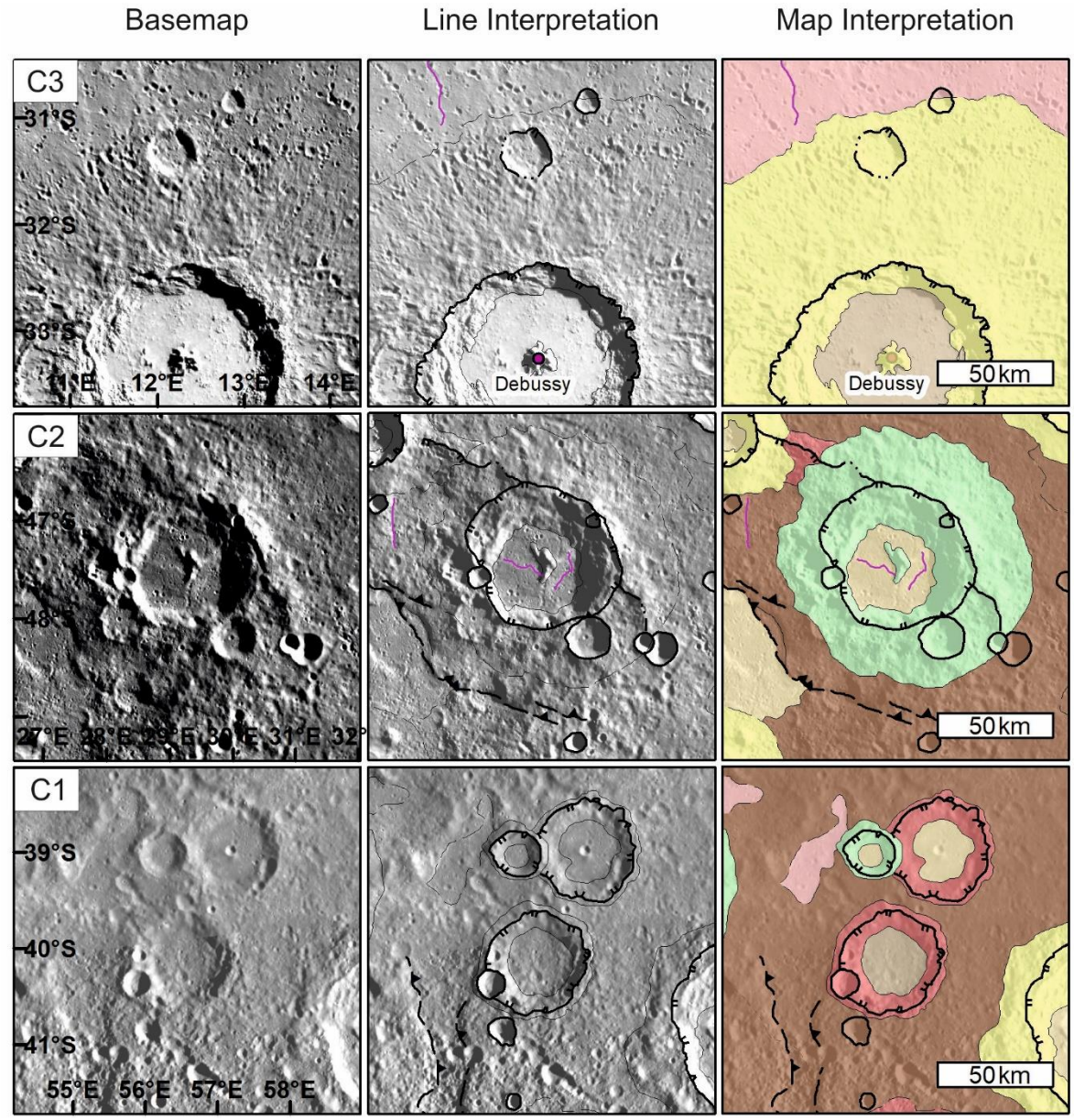

Figure 3.23 Examples of the 3-class system crater types, The background is the BDR basemap, where line interpretation is shown the transparency of basemap is 20%.

Galluzzi et al. (2016) introduced the three-class system for crater degradation, with C1 being the oldest and most degraded and C3 the least degraded (and so youngest) and C2 being an intermediary. This degradation classification is based on the rim sharpness, ejecta blanket size and continuity, the sharpness of the boundary between the crater wall and floor, and the presence of crater chains and rays (Table 3.2).

Table 3.2 3-crater class system features (Galluzzi *et al* 2016).

Crater class	Rim	Crater floor-wall boundary	Ejecta	Secondary craters	Superposed Craters
C3	Continuous and sharp	Sharp break, continuous	Continuous highly textured	Clear secondary chains and sometimes crater rays	Rare (self secondaries?)
C2	Mostly continuous but subdued	Gradational break, continuous	Continuous but degraded		Some craters superposed on rim and crater floor
C1	Subdued and non-continuous	subdued break and discontinuous	Not always continuous, degraded		Crater floor and rim heavily cratered

3.7.1.2 5-Class System

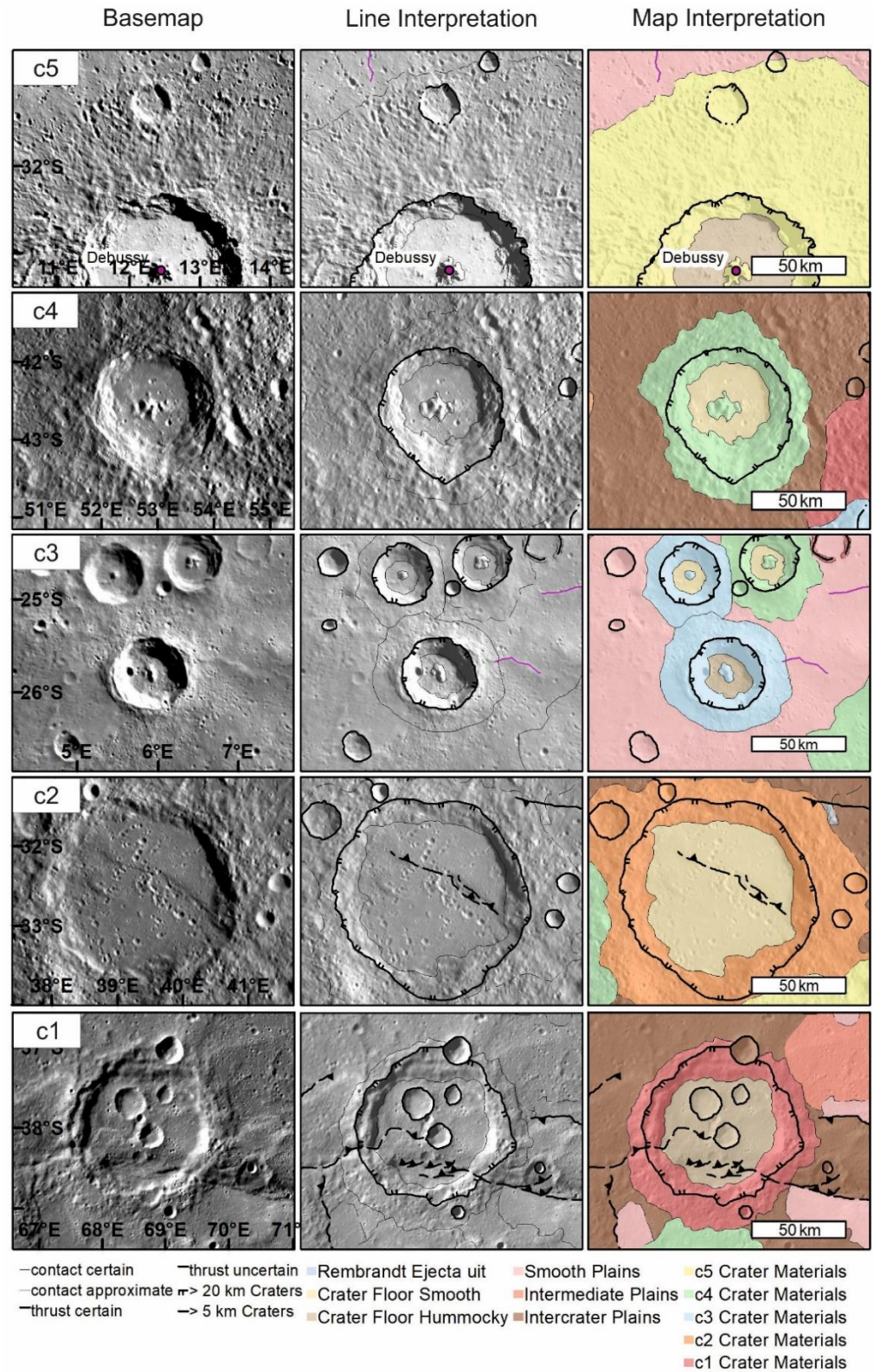

Figure 3.24 Examples of 5-class crater classification showing a progression from least degraded c5 to most degraded c1. The background is the BDR basemap, where line interpretation is shown the transparency of basemap is 20%.

The Mariner 10 maps used a 5-class system for craters > 30 km. Class c1 is the most degraded and c5 the youngest and least degraded (Mccauley *et al* 1981). This approach was based on the Lunar stratigraphic system. At the time, it was noted that there were difficulties with consistently classifying class 5 and class 4 craters. In the map of the Shakespeare quadrangle, Verdi crater was mapped as c4 despite being a typical example of c5 (Spudis and Guest 1988), thus highlighting the importance of standardisation between different mappers.

Equally, it has been noted that there are issues with matching crater degradation class to age; one example is Dostoyevskij crater in Michelangelo quadrangle, which was identified as a c3 even though the crater density suggested it was one of the oldest basins on the planet (Spudis and Prosser 1984). However, some of these misidentifications are probably because of image quality and illumination hindering precise, consistent classification. Recent analysis with MESSENGER data has suggested that Dostoyevskij crater is c4 and Tolstojan (Kinczyk *et al* 2016), matching up with the crater density data and emphasising the importance of multiple viewing angles for assessing landforms.

Following on from MESSENGER, the 5-class system has been reanalysed for craters ≥ 40 km (Kinczyk *et al* 2020a) and applied to the 1:15M scale geological map being produced (Kinczyk *et al* 2018). Initially, the numbering system was reversed; c1 youngest, c5 oldest (Prockter *et al* 2016, Kinczyk *et al* 2016, 2018, Denevi *et al* 2018b) following the example of (Wood *et al* 1977). However, this decision was subsequently reversed to follow the USGS definition from the Mariner 10 era maps (Kinczyk *et al* 2020a, Wright *et al* 2019), with c1 as the most degraded and c5 as the least degraded. I choose to use the system where c1 is the most degraded and c5 is the least to match the style of Mariner 10 maps and Wright et al. (2019). The different orders of c1-c5 have been in the literature for a long time, and the possibility for the confusion was remarked upon in Strom (1978). In this thesis, all references to the 5-class system refer to c1 as the most degraded and c5 as the least degraded (Table 3.3).

Table 3.3 5-crater class system features based on Kinczyk *et al.* (2020).

Class	Rays	Rim	Terraces	Floor-wall boundary	Ejecta	Secondary craters	Central peaks	Superposed craters
c5	Bright rays present	Clear, crisp, continuous rim	Crisp wall terraces	Distinct contact between the two	Radially textured continuous ejecta	Well defined continuous field of crisp secondary craters	Crisp	None
c4	No Rays	Crisp, continuous rim	Crisp to slightly degraded wall terraces	Distinct contact between the two	Radially textured continuous ejecta	Well defined secondary craters	Crisp	Low density
c3	-	Continuous rim, but showing degradation, often slightly rounded	Most wall terraces very degraded	Floor wall boundary indistinct but still identifiable	Mostly continuous ejecta with some interruptions around the radius	Some but not continuous and highly degraded	Subdued	Low to moderate density
c2	-	Continuous to discontinuous degraded rims with a rounded appearance	Remnant wall terraces in larger craters	Floor wall boundary generally indistinct unless embayed by lava in some areas continuos	Ejecta blanket is discontinuous to absent	No secondary craters	Rare central peak rings, heavily degraded	Moderate density
c1	-	Discontinuous degraded rims only slightly above surroundings	No wall terraces or wall structures	No floor wall boundary Continues between wall and floor	No ejecta deposit away from the rim, boundary unclear	No secondary craters	No central peak rings	Moderate to high density

I undertook an exercise in comparing the classification to check the consistency of classification with the other maps in production.

The 5-class system had not yet been implemented within the Derain quadrangle while I undertook my mapping, so I could not use the 5° overlap as a comparison. Instead, the author of Hokusai quadrangle H-05 Wright *et al.* (2019) reviewed ten random craters with different levels of degradation and compared them to mine. The match rate was 80%. The main difference was between class c2 and c3 and arose from issues with the interpretation of terrace degradation, the walls of large craters, and the level of degradation of rims. These are mostly class 2 in the 3-class system. It seems likely that this issue will always be present as an inherent part of the discrete classification of a continuum of crater degradation, especially where illumination bias can obfuscate features.

I undertook a similar blind check for the 3-class system, and 9 out of 10 examples from within H-14 examined by the author of Hokusaiai quadrangle (H05) Wright *et al.* (2019) agreed with the classification of the map. The exception was a crater that I had classified as a class 1 crater. Still, Wright considered it buried; in discussion, he agreed with my classification when considered in the broader context of the nearby ejecta; however, the case was marginal as there was a significant modification by secondaries.

3.7.1.3 Crater Floors

Crater floors are divided into two morphological units based on their texture. Smooth crater floors are generally flat; they are confined to crater floors but are otherwise similar in appearance to Smooth Plains. Hummocky crater floors are more undulating than smooth crater floors (Figure 3.25); while they do not have actual hummocks on them, they appear texturally rough and are disrupted by cratering and faults, similar in appearance to Intercrater or Intermediate Plains. I use this term as it is widely used in the literature (e.g. Galluzzi *et al.*, 2016).

The floor of Rembrandt is the exception to this. Its large area contains multiple internal units, which I distinguished during mapping. The Smooth Plains within it share spectral and morphological properties with the nearby Smooth Plains outside the basin. It also contains ghost craters which are indicative of lavas emplaced after the impact event. As such, it is mapped as a Smooth Plains unit rather than as a smooth crater floor. These Smooth Plains are similar to the mapping for the interior of the Caloris impact basin, although the unit was given a specific "Caloris Smooth Plains" denomination (Trask and Guest 1975, Fassett *et al* 2009). Other craters mapped with "Smooth Crater Floor" may be deposits of Smooth Plains lavas rather than impact melt and cannot be reliably distinguished without flooded/ghost craters to demonstrate a time gap after the formation of the crater floor.

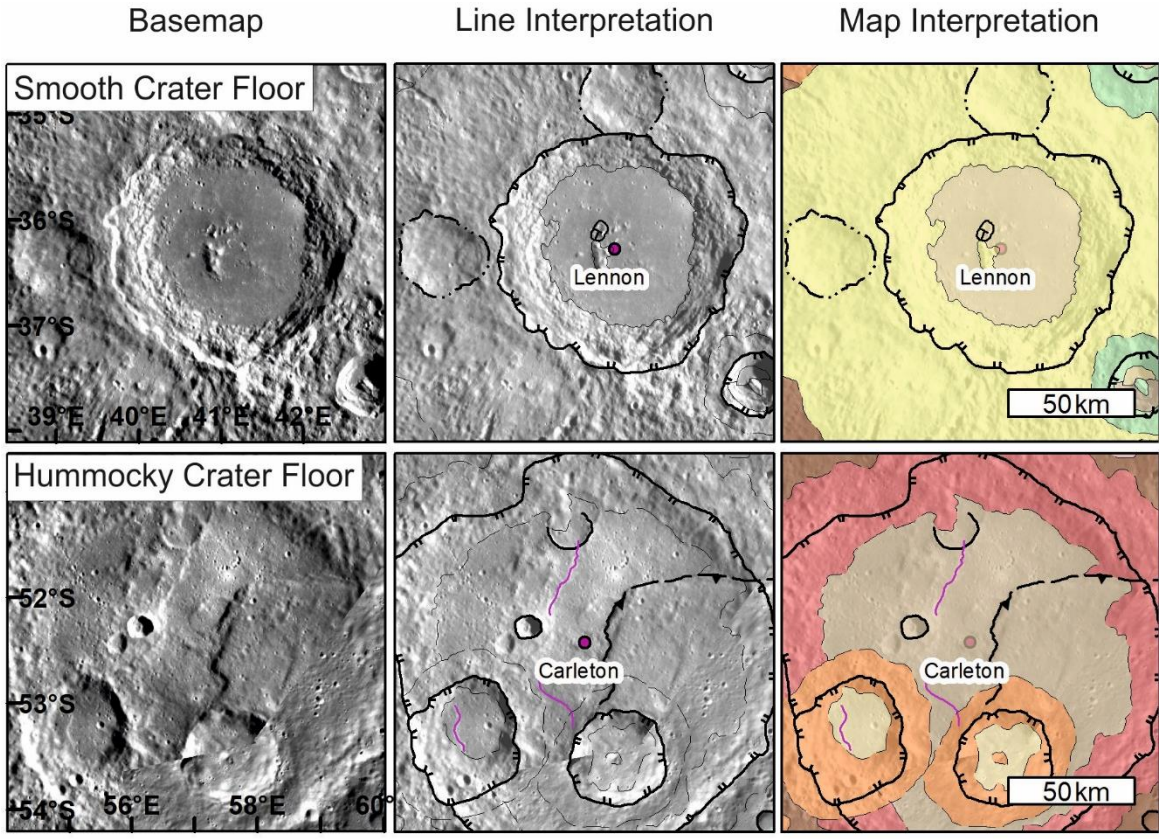

Figure 3.25 Smooth and Hummocky crater floor examples The background is the BDR basemap, where line interpretation is shown the transparency of basemap is 20%.

3.7.2 Plains units

Outside of craters, I have followed previous maps of Mercury, (e.g. Galluzzi *et al.*, 2016; Schaber and McCauley, 1980) by dividing the surface into expansive plains with different textural features. These are Intercrater, Intermediate and Smooth. I will leave the description of Intermediate Plains until I have described the other two as they are an intermediary and their existence is a debated feature on Mercury's surface.

3.7.2.1 Intercrater Plains

These plains are gently rolling and undulating over 10s -100s of kilometres (Trask and Guest 1975). Small (5 – 15 km) craters dominate their surfaces (Figure 3.26). The craters' shallow nature suggests that they are likely secondaries, although they cannot be linked directly to their parent craters (Spudis and Guest 1988, Whitten *et al* 2014a). Within the quadrangle, Intercrater Plains vary in texture, with some areas undulating and others flatter but still highly cratered. They have highly variable spectral properties, though they tend towards the blue/brown in enhanced colour images (Denevi *et al* 2009). They are the most widespread plains on Mercury (Kinczyk *et al* 2018, Murray *et al* 1975, Strom *et al* 2011, Whitten *et al* 2014a) and contain craters with a wide range of sizes and of all degradation stages.

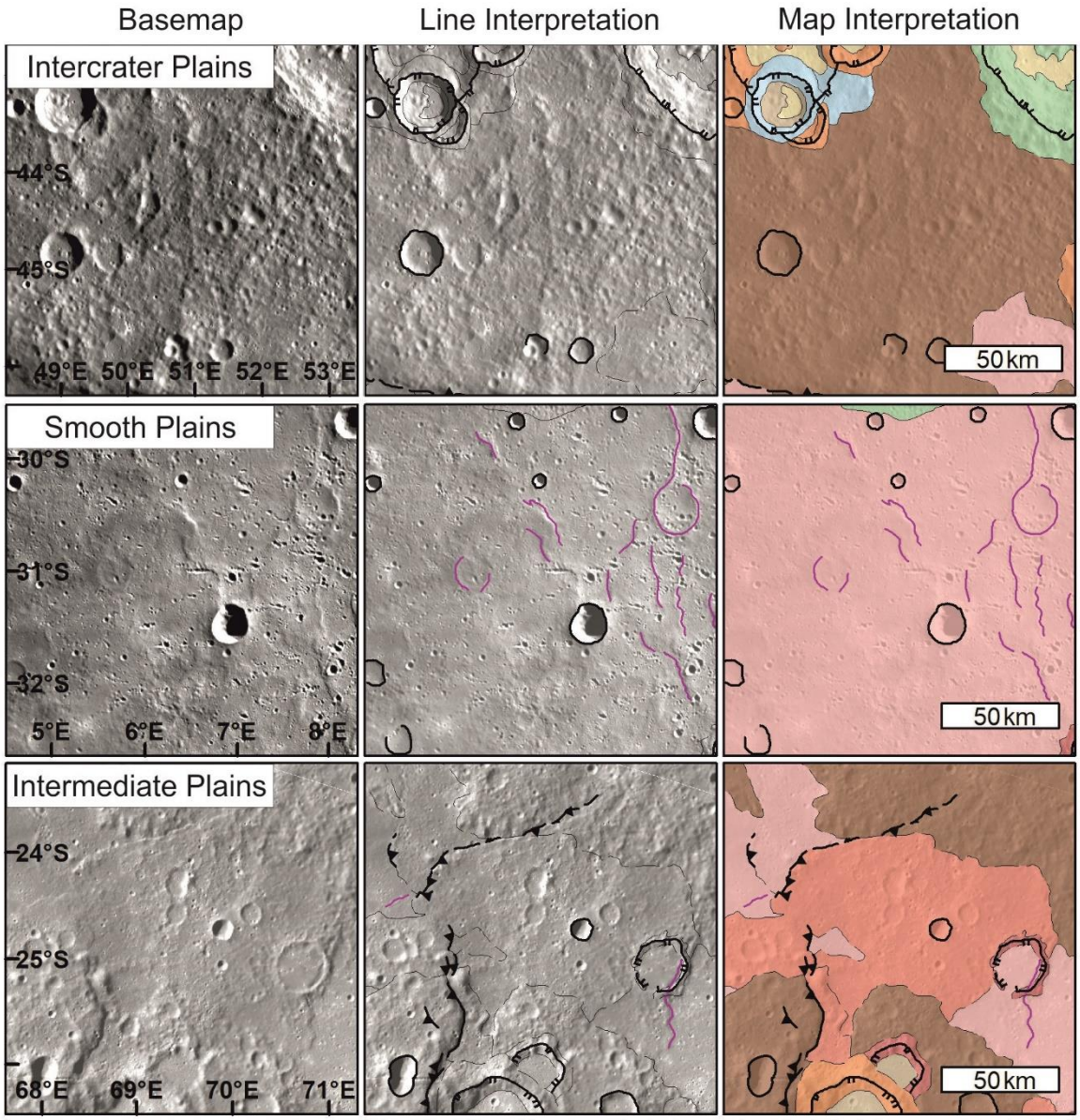

Figure 3.26 Different plains units on BDR basemap. The background is the BDR basemap, where line interpretation is shown the transparency of basemap is 20%.

3.7.2.2 Smooth Plains

Smooth Plains are relatively flat over 10s to 100s of kilometres, with few superimposed impact craters or secondaries (Denevi *et al* 2013). They often have distinct boundaries with surrounding units. Smooth Plains are found as discrete patches, usually occupying low-lying areas, such as old basins or within the Rembrandt impact basin. Smooth Plains tend to have a higher albedo and are spectrally more red in colour than Intercrater Plains. However, this is not always the case, especially in the immediate exterior of Rembrandt. They often have wrinkle ridges on their surface and contain ghost craters (Figure 3.26). Contacts with Intercrater Plains are distinct and sharp. Contacts with the Intermediate Plains are more muted and subtle. Older craters are infilled, often only showing part of the rim and ejecta. Younger craters retain a highly textured ejecta blanket.

3.7.2.3 Intermediate Plains

Intermediate Plains contrast with the Smooth Plains by having a more undulating texture and more superimposed craters. However, many of these craters are subdued or mantled. Unlike the Smooth Plains, Intermediate Plains do not have a distinct boundary with older and underlying units. Intermediate Plains are less cratered than the Intercrater Plains. They do not have any particular spectral features and share some spectral characteristics with both the smooth and Intercrater Plains. They often contain patches of either smooth or hummocky Intercrater Plains that are not mappable at the chosen scale. The existence of a distinct Intermediate Plains unit is a controversial subject in Mercury science. Whitten *et al.* (2014) suggest they are different levels of degradation of Intercrater or Smooth Plains and so they are not included in the global map (Kinczyk *et al* 2018). However, Galluzzi *et al.* (2016); Guzzetta *et al.* (2017); & Wright *et al.* (2019) see them as necessary in showing the whole variety of surface types, rather than just the two used in the global map. I have decided to map Intermediate Plains as a separate unit (Figure 3.26).

3.7.3 Rembrandt-Specific Units

As the second-largest impact basin on the planet, Rembrandt has some noteworthy features within it and several styles of ejecta. This led to my decision to map several basin-specific units. Basin-specific units were adopted in maps of the Caloris basin (Fassett *et al.*, 2009; Guest and Greeley, 1983; Guzzetta *et al.*, 2017; Mancinelli *et al.*, 2016; Solomon *et al.*, 2007; Trask and Guest, 1975). Rembrandt-specific units have been created by other maps of the impact basin (Hynek *et al* 2017, Semenzato *et al* 2020). I did not define a Rembrandt-specific Smooth Plains unit inside the basin, as others have done in the case of Caloris, because the plains here have the same morphology as the Smooth Plains observed elsewhere on the planet.

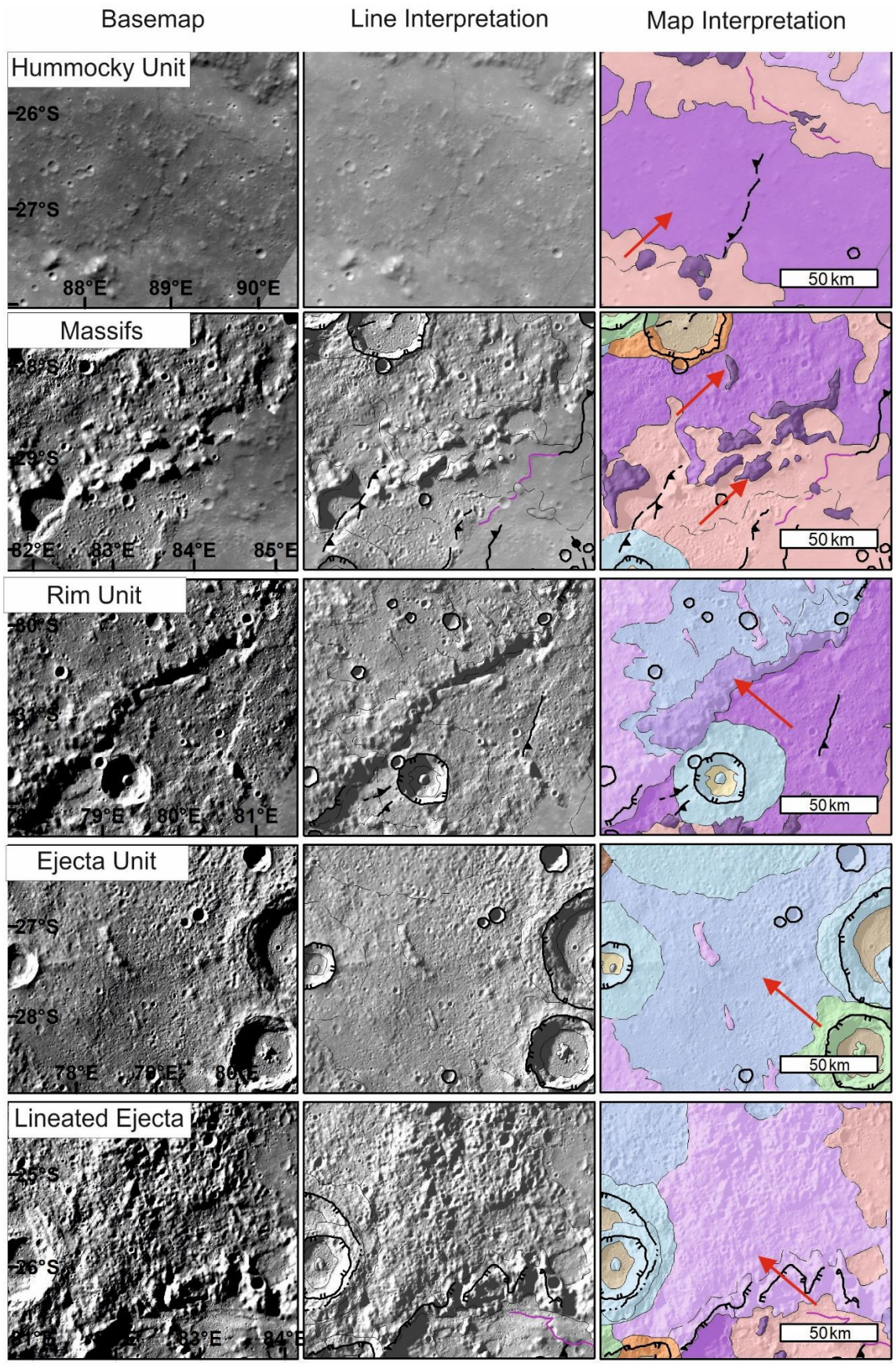

Figure 3.27 Rembrandt-specific units The background is the BDR basemap, where line interpretation is shown the transparency of basemap is 20%.

3.7.3.1 Hummocky Unit

Within the basin floor of Rembrandt is a hummocky unit with an uneven floor (Hynek *et al* 2017, Watters *et al* 2009a, Semenzato *et al* 2020). The edges of this grade into smoother, less hummocky units. The unit is morphologically different from typical crater floor units in that discrete hummocks occur throughout this unit, and there are also tracts with smooth undulating floors between the hummocks (though these are too small to map as a separate unit). The hummocky unit has a lower albedo than most of the Smooth Plains that fill the floor of Rembrandt, except on the western edge of the basin, where they have a similar albedo to the hummocky material and plains surrounding the crater (Figure 3.27).

3.7.3.2 Rembrandt Massifs

These are blocky hills and mountains that protrude above the units within the basin (Figure 3.27). They do not contain strong fabric. They are similar to, but less continuous than, the Rembrandt rim materials with heights of up to 1 km (the hummocks in the Hummocky unit are only 15-50 m high). They are found both within the Smooth Plains and the Hummocky unit.

3.7.3.3 Rembrandt Rim Material

The Rim unit was first identified by Hynek *et al.* (2017), who describes it as bounded by a "rugged high relief basin-facing scarp". It comprises a series of massifs that make up part of the rim of Rembrandt, predominantly on the northwest side of Rembrandt, but fragments are also on other parts of the basin's edge. These massifs have no strong radial features or alignment, distinguishing this unit from the ejecta units radiating from the edge of the basin. However, the contact is gradational and in some areas, and a basin-radial fabric begins to form. It is similar to Caloris Montes, which forms a boundary around the outside of the Caloris basin (Figure 3.27).

3.7.3.4 Rembrandt Linear unit

This unit is representative of a surface texture radiating away from the Rembrandt impact basin in the form of ridges and troughs (Watters *et al.*, 2009; Whitten and Head, 2015; Hynek *et al.*, 2017). It includes blocky areas and areas of smoother patches that would be too small to map as individual units (Figure 3.27).

3.7.3.5 Rembrandt Ejecta

Similar to Intercrater Plains, this unit comprises undulating rolling hills over 10s of kilometres in scale. However, it is smoother than the Intercrater Plains, has a lower density of craters, and often contains flat "pools" that look like filled craters. In the south-west, it extends almost up to the Rembrandt rim material unit. North and west of the basin, it is found exterior to and interfingered with the Rembrandt Linear unit. Its boundaries with both the Intercrater Plains and the Rembrandt linear unit are not clear, so I mark these contacts either as uncertain or gradational (Figure 3.27).

3.8 Superficial units:

I created a GIS layer of superficial units separate from the morphological units. This layer represents various kinds of modification of the underlying geomorphic units but does not prevent the underlying unit from being identified. I mapped these using the same line conventions as the geomorphic units but placed them in a separate layer that can be applied over the top as a semi-transparent 'overlay'.

3.8.1 Crater Rays

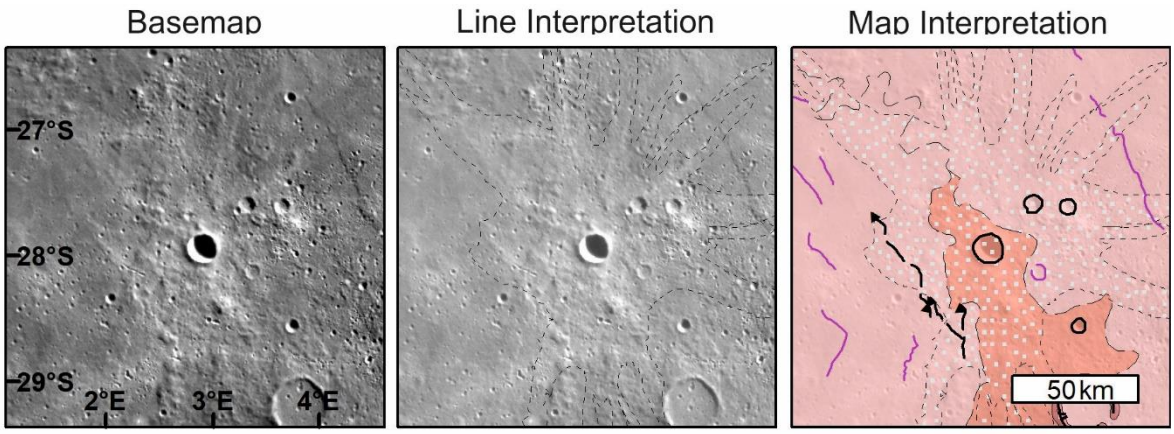

Figure 3.28 Crater ray image: The background is the BDR basemap, where line interpretation is shown the transparency of basemap is 20%. The bright crater rays are a stipple layer on top of the geology.

Crater rays are linear ejecta patterns with high-albedo at low phase angles, deposited radially during the formation of an impact crater. They appear to be more transient than other impact ejecta facies and fade from visibility over time (likely a function of being only a relatively thin layer), which is why they are associated with the youngest crater class only (Robinson *et al* 2008). Rays are only thinly draped, allowing the identification of underlying materials (Figure 3.28).

3.8.2 Catenae

Catenae are continuous chains of secondary craters, usually (but not always) radiating away from nearby impact craters. They tend to be shallower than primary craters and often highly degraded.

3.8.3 Hollow Clusters

While the overall sizes of individual hollows (Chapter 2.9) are too small to be recorded at the chosen mapping scale, these rimless, irregular, flat-floored depressions likely represent a thermo-chemical degradation or modification of the underlying units. Their relative high albedo compared to the surrounding units makes them a superficial unit that can be identified and recorded on the map (Figure 3.29).

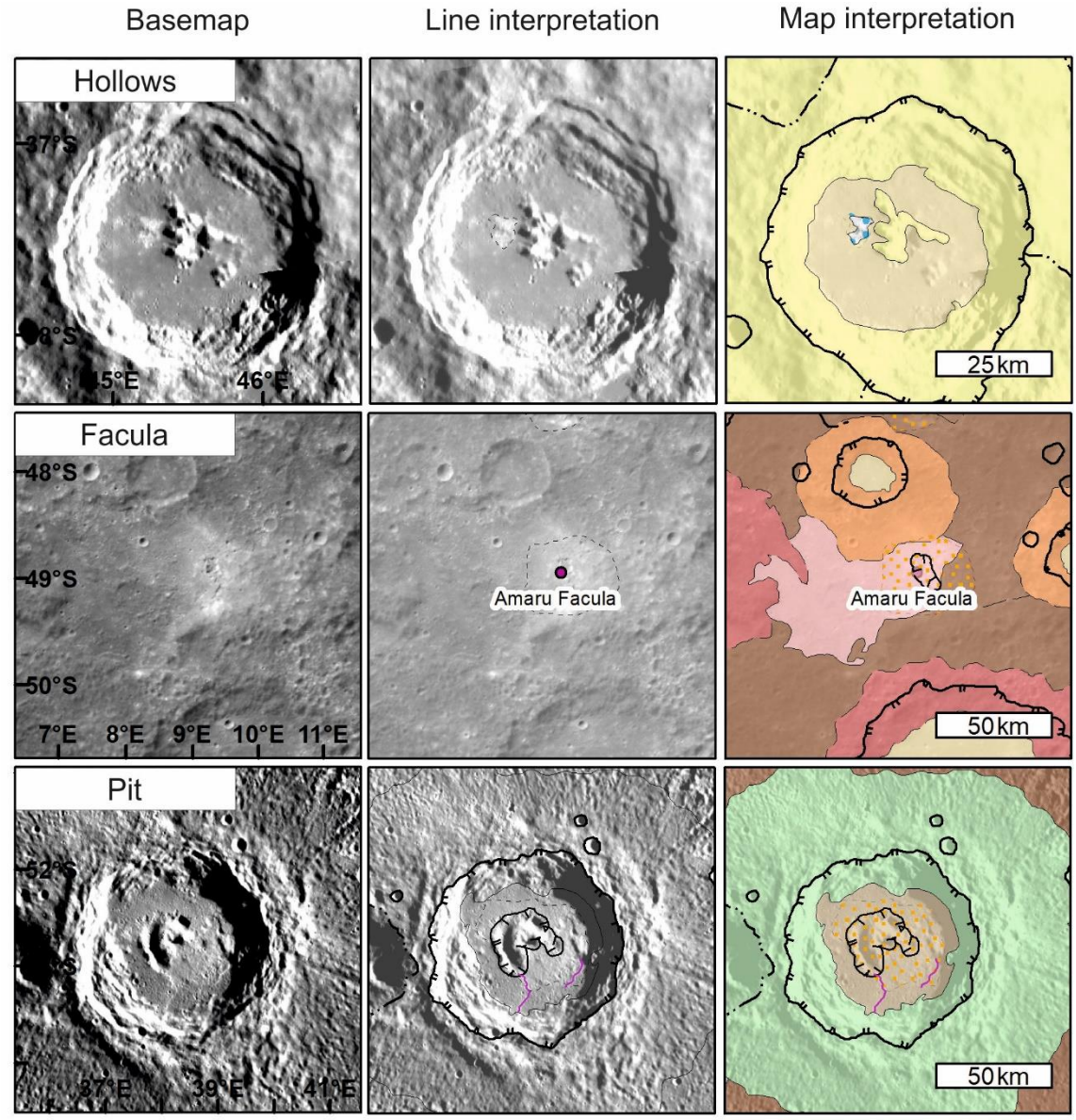

Figure 3.29 Example of hollow clusters, a facula and a pit. The background is the BDR basemap, where line interpretation is shown the transparency of basemap is 20% the bright crater rays are a stipple layer on top of the geology.

3.8.4 Faculae

Faculae are high albedo spectrally red spots with diffuse outer edges. Most have a km-scale rimless pit (a probable volcanic vent) at their centre and are interpreted to be explosive volcanic ejecta (Kerber *et al.*, 2009; Thomas *et al.*, 2014a). Some faculae lack large visible pits and may have a different explanation, such as resulting from the interaction of hot lavas/impact melt with underlying volatile-rich layers (pitted ground), as discussed in chapter 2.6.2, I mapped them as polygons (Figure 3.29).

3.8.5 Pits

Pits are holes in the surface of the planet; they do not have the raised rims of impact craters and can be asymmetric in plan view. They are much deeper and more extensive than hollows. They are thought to be

the craters left behind after explosive volcanic events. They are represented on the map by a solid line with inward-facing single ticks. They are only up to a few 10s of kilometres across, so I follow a similar logic to small craters and outline them but do not map internal structure, as there is insufficient resolution at this mapping scale to do so (Figure 3.29).

3.9 Conclusions

I have used MESSENGER data to make the first geological map of the H-14 Debussy quadrangle following the approach outlined in this chapter which employs the mapping standards established in the Mercury mapping community. I am using similar techniques and basemaps to the other mappers at this scale (Galluzzi *et al* 2016, Guzzetta *et al* 2017, Wright *et al* 2019). I have used units already established by other workers, except for Rembrandt where, having considered multiple other works, I have created a group of morphological units. I have created two versions of the map, classifying craters into 3- and 5-degradation states. In the next chapter, I use this map and the observations I made during its production to describe the geological history of this quadrangle and place it within the broader geological history of the planet.

4 Discussion of the Geological History of H-14: The Debussy Quadrangle

4.1 Introduction

In this chapter, I take my geomorphic map of Debussy (see Chapter 3, Appendix 1) and examine the main features within it. I start with impact craters then examine the plains between the craters, before looking at the tectonic history of the quadrangle, and the most recent superficial changes to the planet's surface. I use this map as a basis for studying and interpreting these features, and then build a geological history for the quadrangle and place it into a global context.

4.2 Impact Crater History

Craters are the dominant feature on Mercury and dominate much of the Debussy quadrangle with 41% of the quadrangle covered in materials from craters over 20 km diameter (excluding Rembrandt related materials). I used two systems for crater classification, a 3-class (referred to with a "C") and a 5-class ("c").

4.2.1 Three vs Five Class

The 5-class system was introduced after Mariner 10 (Spudis and Guest 1988) and subsequently updated following MESSENGER (Kinczyk *et al* 2016). Galluzzi *et al.* (2016) created the 3-class system to circumvent conflicts between relative ages based on morphology versus stratigraphic relationships.

Conflicts occur when there is a disagreement in overlapping craters between the order in which they were produced by impacts (based on superposition relationships) and the age deduced from morphology. These conflicts are possible due to size differences between craters; morphological features (such as terracing and ejecta blankets) will be smaller on smaller diameter craters and so degrade faster than those same features in larger craters. Smaller craters of the same age, would degrade faster than larger craters. Equally, features close to a recent proximal impact are likely to show some premature degradation due to localised increase in secondaries and ejecta covering, impacting the morphological features. This relative change in degradation rate on smaller (<30 km) craters applies to both systems, but it is more likely to occur in the 5-class system as it is more detailed. The morphologic types in the 3-class system are broader and thus reduce possible conflicts between crater classes. The 3-class system is decoupled from the five geological periods on Mercury, whereas the 5-class system has been linked to the geological periods (Kinczyk *et al* 2020a, Spudis and Guest 1988). However, if the 5-class system is reliable, then the lower fidelity of the 3-class reduces the amount of information from the map.

I have found two examples of conflicts; in Figure 4.1.a, a 22 km crater (Classes C3 and c3) overprints the ejecta from a 90 km diameter crater (C3 and c4). In the 3-class system there is no conflict but in the 5-class system, the smaller crater rim is more degraded and the floor-wall boundary less distinct than in the larger crater. The second example (Figure 4.1.b) the 140 km diameter Joplin crater (C3/c4) is overprinted by a 23 km diameter crater (C2/c3). They are both partially overprinted by ejecta from a 77 km diameter crater to the east (C3/c4). Joplin's categorisation as a marginal C3 crater is based on its broad, coherent ejecta and terracing; the superposing C2 crater has less extensive ejecta (for its size) and degraded interior walls; this example is the first known conflict between superposition order and degradation state in the 3-class system. Showing simplifying crater classification down to three classes cannot eradicate all 'contradictions' between degradation state and stratigraphic position, and thus provides an argument in favour of the 5-class system that at least gives more precise subdivisions of degradation state and the *likely* relative age.

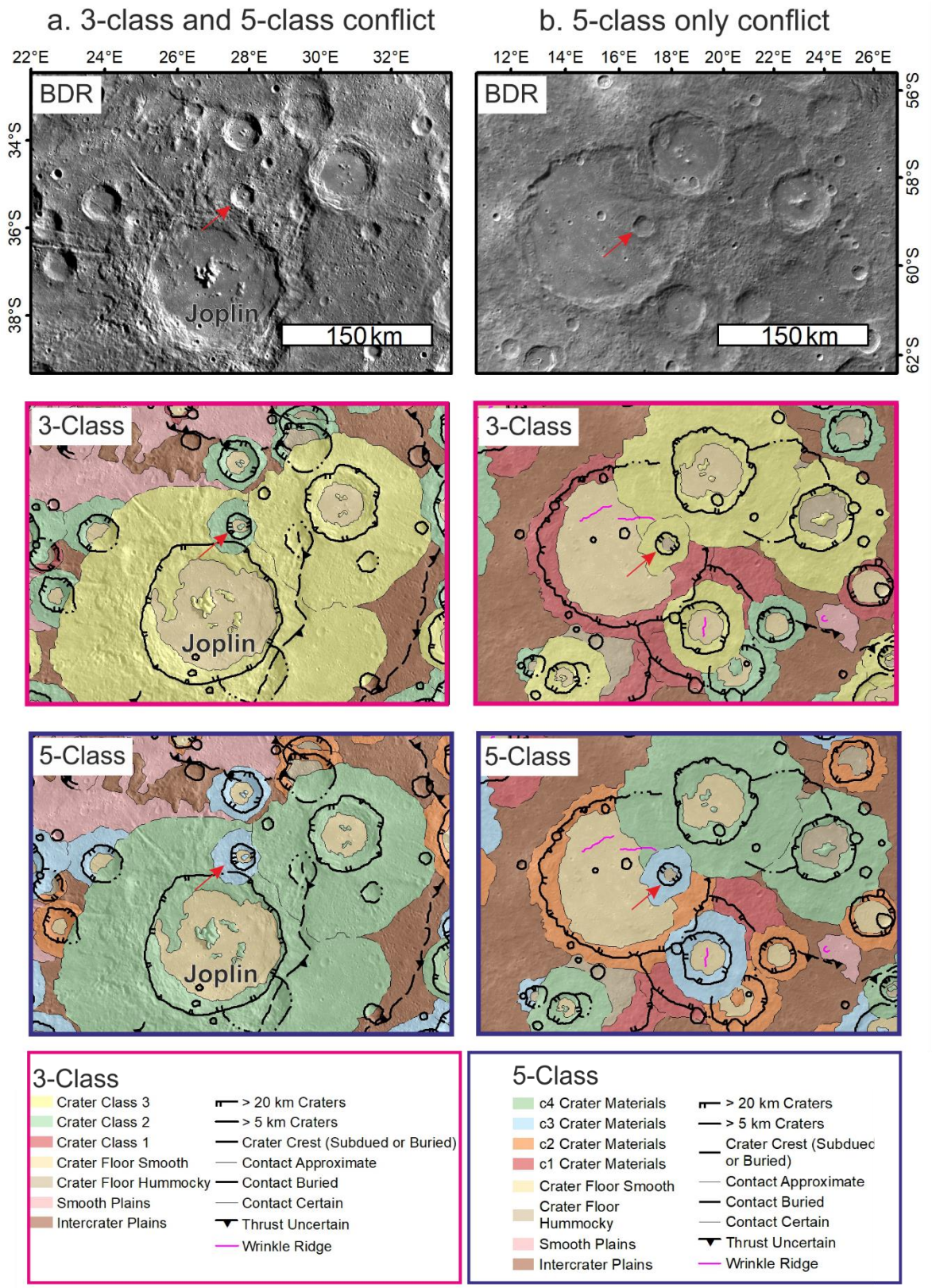

Figure 4.1 Comparison of 3-Class and 5-Class craters system conflicts between degradation stage and superpositional age, top row: bulk data record basemap (BDR) (Denevi *et al* 2018a), *middle row: 3-class crater system map, bottom row: 5-class crater system map. The left column (a) "3-class and 5-class conflict": the red arrow points to a C2 crater on top of Joplin (C3) ejecta; in the 5-class system, the small crater is a c3 on top of the c4 Joplin. The right column (b) "5-Class only*

conflict": red arrow points to a C3 crater on top of the ejecta from another C3 crater but with the 5-class system showing a c3 crater sits on c4 ejecta.

Both the examples I have found show small craters degrading faster than large craters. The higher the number of classes of crater degradation for the same continuum, the more likely that there will be conflicts between craters of different sizes as the divisions become more nuanced and so will highlight differential rates of degradation.

Morphological classification is useful when other methods, such as crater counting, are not possible and to give approximate dates and relationships between craters and features. While I have found two examples of craters with conflicting formation order vs level of degradation, the work of Kinczyk *et al*. (2020) shows that generally, for craters of >40 km, the degradation state of large craters can link features to approximate age ranges, e.g. (Banks *et al* 2015, Kinczyk *et al* 2020a); c1 pre-Tolstojan, c2 Tolstojan, c3 Calorian, c4 Mansurian, c5 Kuiperian. I use the 5-class system as a way of relatively dating features within the quadrangle. Crater counting is model dependant; dependent on substrate and available flat area, the presence of secondary craters on Mercury up to 10 km in diameter (Strom *et al* 2011) makes it challenging to date small areas (due to the low frequency of large craters). In contrast, overall crater degradation is less affected by secondary craters.

The 5-class system provides the ability to place features within the quadrangle within the stratigraphic history of Mercury used widely by the scientific community. The two classification systems are not directly comparable with each other, with each class in the 3-class system potentially containing examples from two classes of the 5-class system. Only two classes of the 5-class system map uniquely into one of the 3-class classes: c1 = C1 and c5 =C3 (Figure 4.2). The 3-class system, while having fewer conflicts in morphology and linking to the other 1:3 million scale maps, (e.g. Galluzzi & BepiColombo Geological Mapping Team, 2017), loses this resolution and links to work completed outside of the 1:3 million European map series (e.g. Whitten, Fassett & Ostrach, 2020). The granularity given by the additional classes, I think in general, adds more useful information, so I have decided to use it for most of the diagrams in this thesis.

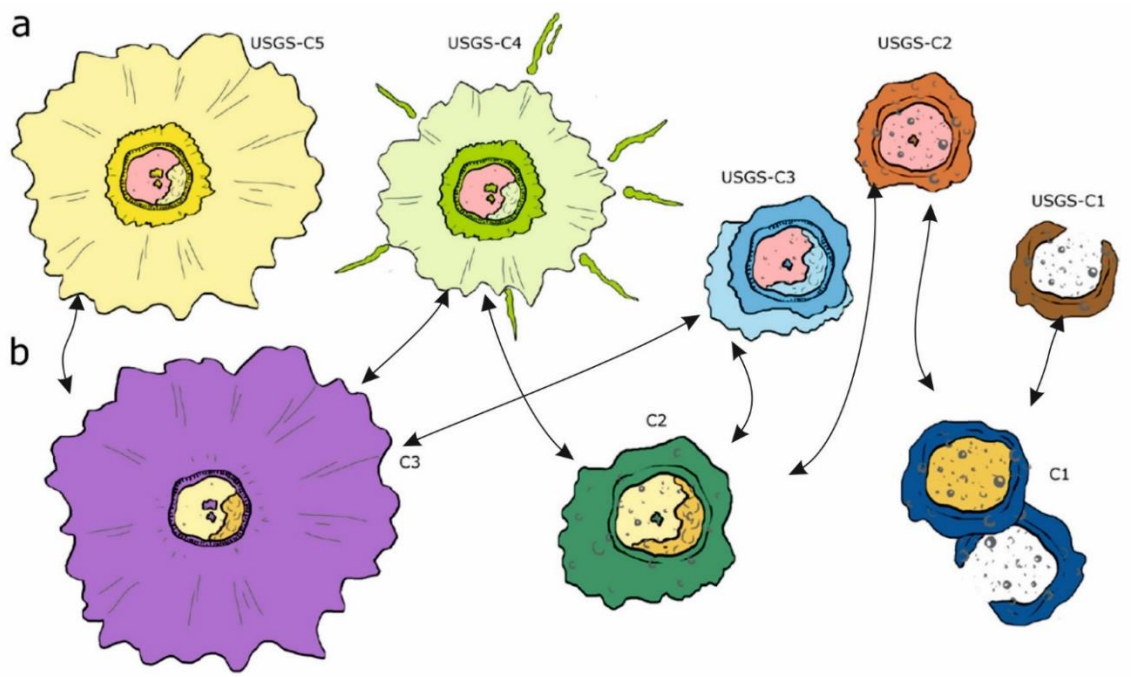

Figure 4.2 Comparison of 3-class and 5-class system from (Galluzzi. 2015) with arrows to show relationships between the 5-class system (a) and the 3-class system (b).

4.2.2 Ejecta Characteristics and LRM

Ejecta on Mercury travels limited distances and rarely does it extend beyond one crater diameter from the impact basin (Gault *et al* 1975). This distance is similar to the situation on the Moon (Wilhelms and McCauley 1971). Ejecta is apparent at greater distances from younger craters: only ½ crater diameter from c2 craters but one crater diameter from c5 craters. Topography plays a role in the extent of ejecta following an impact event. Away from the rim, flat surfaces and downslopes allow ejecta to travel further than if travelling up, say, a nearby rim.

Within the quadrangle, 16 craters show low reflectance material (LRM) in their ejecta or peak element. Four of these craters are the Rembrandt impact basin, and the rest are in Intercrater Plains (Figure 4.3, Figure 4.4). The LRM is probably the excavated remains of Mercury's flotation crust (Chapter 2.5.3, Murchie *et al.*,

2015; Vander Kaaden and McCubbin, 2015) which has been covered over by later volcanic plains, and is the oldest material in the quadrangle.

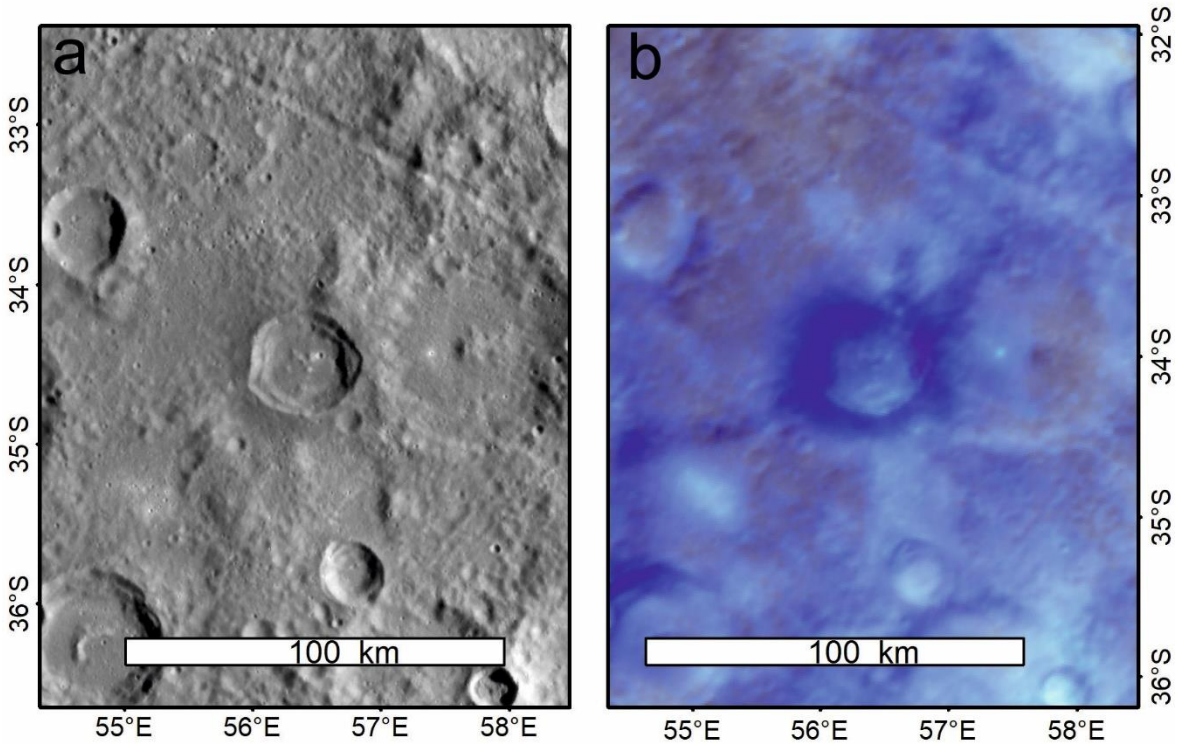

Figure 4.3 A crater with LRM ejecta. a. showing the crater in BDR, b. showing the same crater in enhanced colour, in which the LRM in ejecta is apparent. Image centred: 56.4°E, 33.5°S. Basemaps (Denevi *et al* 2018a).

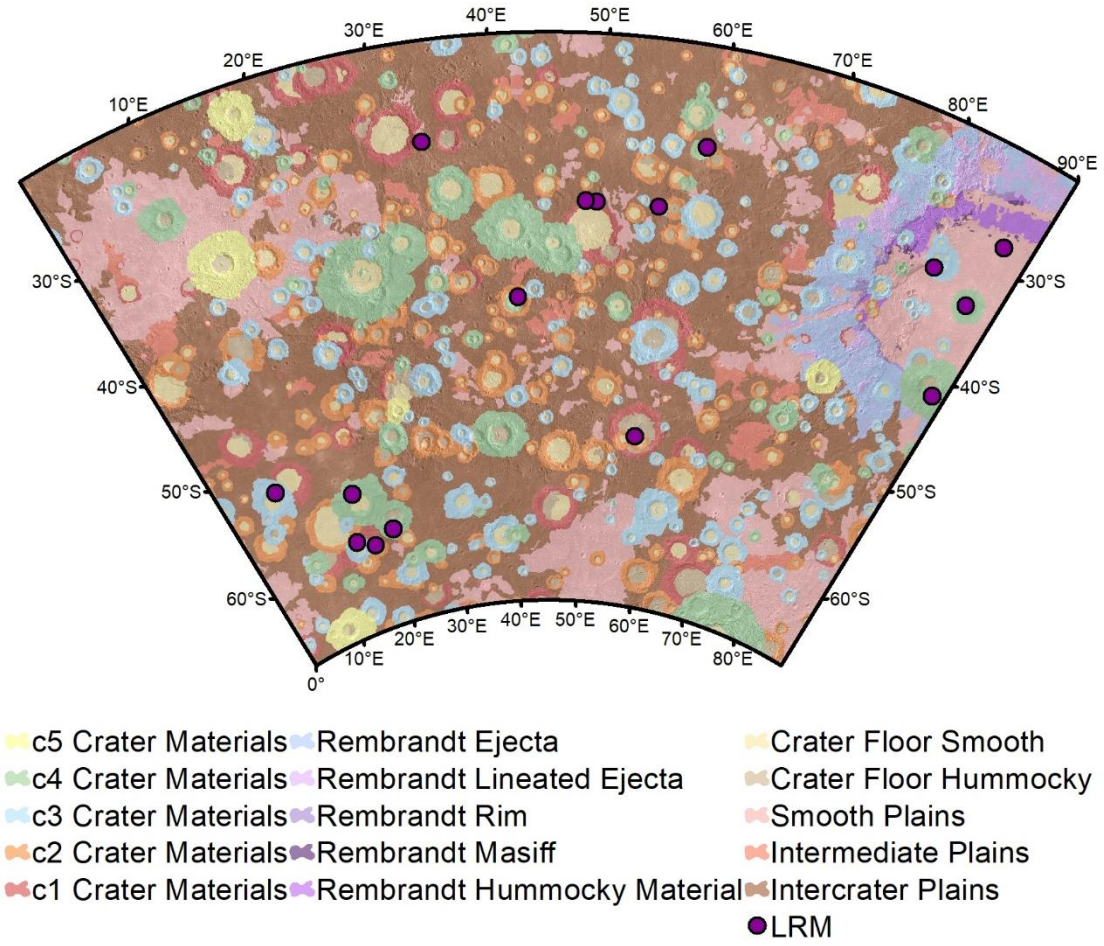

Figure 4.4 Geomorphic map of the Debussy quadrangle showing the location of LRM.

4.2.3 Large Impact Basins

Rembrandt is the largest impact basin identified within the quadrangle, and I further examine it in section 4.3.2. Fassett *et al.* (2012) and Orgel *et al.* (2020) suggested nine other large impact basins >300 km, in addition to Rembrandt within the mapping area (Figure 4.5), using topography and image data as part of a global study of basins. I have tried to identify them using the data within the quadrangle (Table 4.1) and have confidently identified 5 of them. For the others, there is less evidence inside the mapping area. Aneirin is the only basin other than Rembrandt to have been explicitly studied due to its lava-covered floor (Fegan *et al* 2017).

Tectonic activity on Mercury in the last 1 Ga occurred on the western edge (outside the mapping area) of Aneirin and postdates the Smooth Plains that infill that basin (Fegan *et al* 2017). The portion of Aneirin within the quadrangle overlies b34.

Table 4.1 Basins within H-14 from (Orgel *et al* 2020, Fassett *et al* 2012) *and my interpretation from mapping.*

Orgel et al., 2020/ Fassett et al., 2012					**This Work**	
Basin	**Confidence**	**Visible topography**	**Visible image**	**Stratigraphic age**	**Evidence in H-14**	**My Classification**
b100	Tentative	Partial	No	> b91 b3 Rembrandt b54	Limited topography	
b91	Tentative	Yes	No	> b3	Limited topography	
b71	Tentative	Partial	No	undistinguishable relationship with b56, > b34	No clear evidence	
Rembrandt	Certain	Yes	Yes	Youngest basins in the quadrangle	Topography and image data	Confident
b34	Certain	Yes	Possible	> b37	Topography	Confident
b37 (Aneirin)	Certain	Yes	Yes	—	Topography and image data	Confident
b56 (Lennon-Picasso)	Certain	Yes	No	> b36	No clear evidence	
b3	Probable	Yes	Possible	—	Clear Topography possible image	Confident
b57	Certain	Yes	No	> b44 Rembrandt b25 b101 b12	possible Topography	
b54	Certain	Yes	No	—	Clear topography	Confident

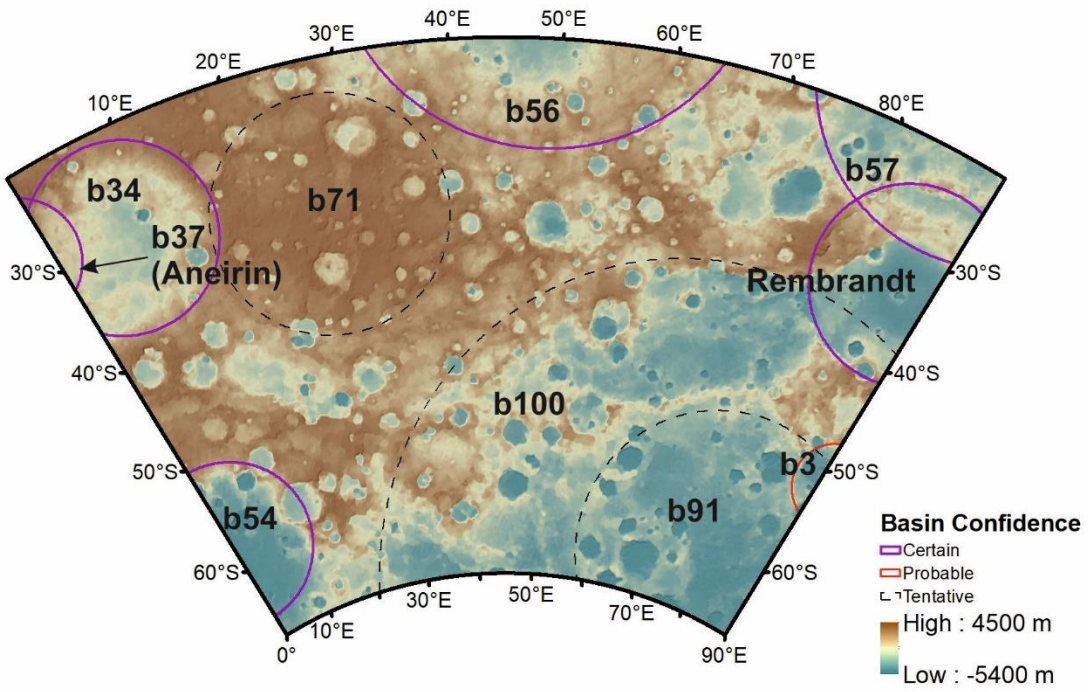

Figure 4.5 Map of H-14 Showing the location of >300km basins (Orgel *et al* 2020, Fassett *et al* 2012) *on top of the topographic map* (Denevi *et al* 2018a).

The geomorphic mapping reveals that the majority of these large impact basins have Smooth Plains associated with them (Figure 4.6), and this is discussed further in section 4.3.2.1. I did not observe any other morphological features associated with the tabulated basins (apart from Rembrandt) within the quadrangle, such as remnants of ejecta or radial scouring, showing that the heavy cratering and modification of the surface has obliterated most other signs of these basins. The lack of morphological signatures suggests that these basins formed early in Mercury's history; the presence of c1 craters within all of them other than b3, b54 and Rembrandt suggests that most of these basins formed during the pre-Tolstojan. The age of b54, which has a clear topographic expression, and of b3 (which is relatively small with a diameter of 159 km) is uncertain; however, the lack of rim and ejecta also points to a Pre-Tostojan age.

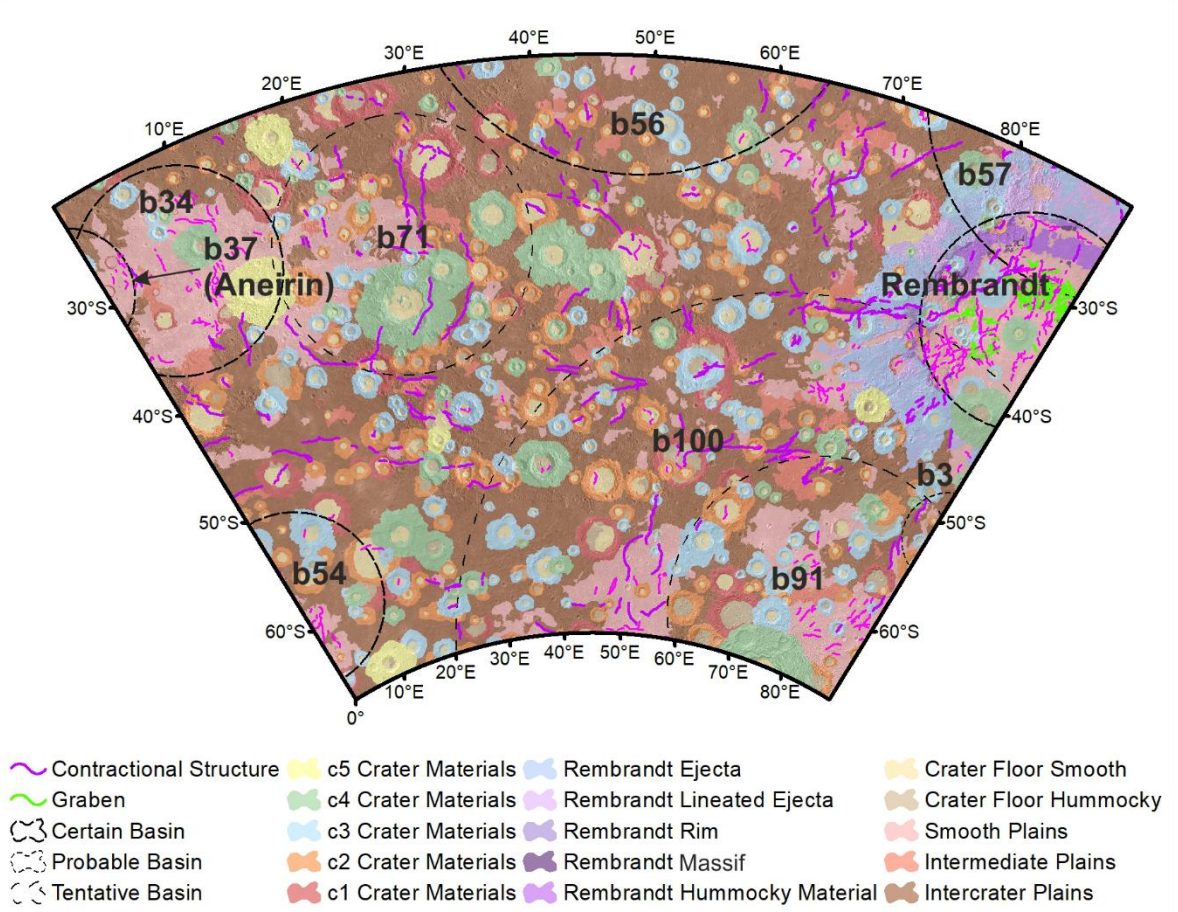

Figure 4.6 Geomorphic map with simplified tectonics of H-14 with basins from Orgel et al., (2020).

Rembrandt is the youngest large impact basin in the quadrangle; it dates to the start of or just before the Calorian Period with an N(20) of 58±16 (Whitten and Head 2015, Watters *et al* 2009a) compared to 58 ±13 or 54±12 for Caloris (Spudis and Guest 1988, Fassett *et al* 2009, Watters *et al* 2009b).

4.3 Geomorphic Units

I now go through each of the main units and discuss the findings of the mapping. I will discuss the implications for their origin and how this relates to the current understanding of those units.

4.3.1 Plains Units

The plains make up 54% of the quadrangle, covering the ground between the impact craters. I have identified three plains units: Smooth Plains, Intermediate Plains and Intercrater Plains.

4.3.1.1 Smooth Plains

Smooth Plains are the second most common map unit and make up 30% of the plains within the quadrangle. These Smooth Plains are found: within the Rembrandt impact basin; as three large patches, one in the west of the map (into which Debussy crater impacted), the other two in the south and south-eastern edge of the

map separated by the Alver impact ejecta; and as many smaller patches of Smooth Plains within the quadrangle (Figure 4.7).

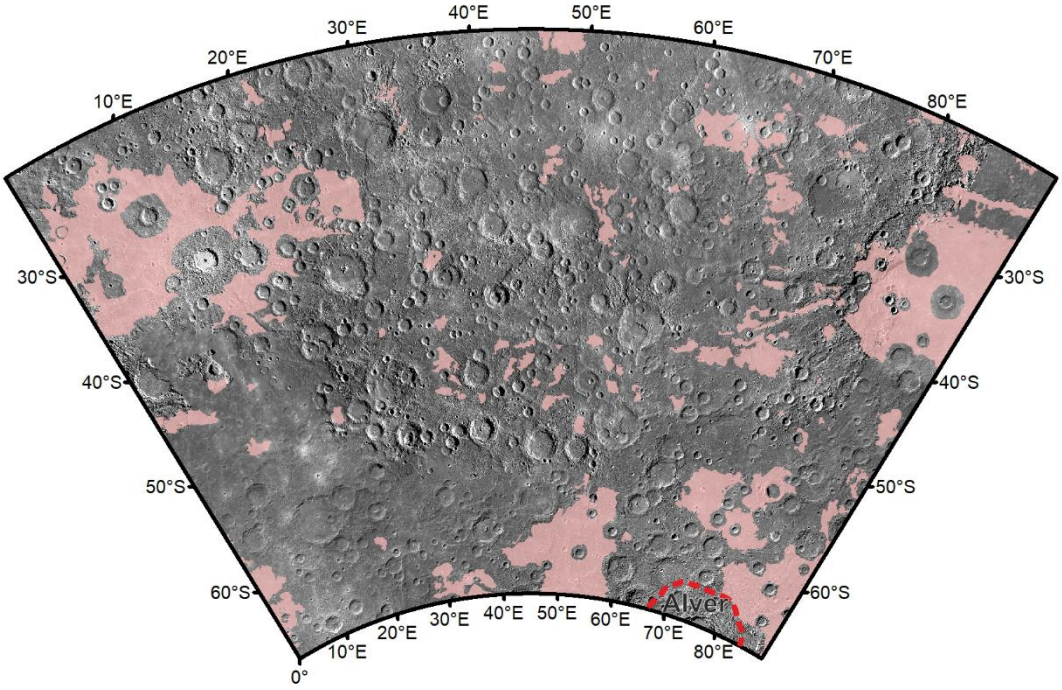

Figure 4.7 Location of the Smooth Plains (pink) within H-14, with the outline of Alver Ejecta shown in red line superimposed on BDR basemap.

My map of Smooth Plains correlates moderately well with Denevi *et al.* (2013; Figure 4.8). I have identified additional small patches and a larger extent for some of the previously mapped Smooth Plains occurrences. The differences are not surprising as the Denevi *et al.* (2013) map was produced at a smaller scale and using a combination of Messenger and Mariner 10 images with fewer illumination directions. There may be some additional patches of Smooth Plains lava in crater floors that I have mapped as smooth crater floors.

The Smooth Plains are predominantly in low lying areas (Figure 4.8). The plains are relatively flat and uncratered compared to Intercrater Plains (section 4.3.1.3), though they are deformed by wrinkle ridges (section 4.4.1.9), some of which indicate the rims of ghost craters. I classified all partially filled craters within the Smooth Plains as c1, this is due to localised ageing: covering parts of ejecta blankets can increase the levels of degradation. If lava breaches part of the rim, then the crater's floor and parts of crater walls are covered. This covering obscures the morphologies used to identify the craters (terracing, floor wall contact, ejecta etc.) and so ageing the morphology of the craters. Thus I do not use these craters for relative dating. Smooth Plains have been impacted by c3-5 craters indicating they have existed since the Calorian. Low resolution and low incidence angle image data made the Smooth Plains in the south of the map the hardest to delineate. The Smooth Plains in the south host several c2 craters, suggesting they are older than the other plains. This region is heavily modified by the c4 impact crater Alver.

To check to see if there is any link between the location of Smooth Plains and the impact basins, I reprojected the Smooth Plains and the basins within the quadrangle into a sinusoidal projection (this records equal areas). I then measured the total area of Smooth Plains and areas of basins within the quadrangle; I cut out the Smooth Plains within the basins from Orgel & Fasset (2020) and measured the area of these. The size of the basins is the largest source of uncertainty, so errors were calculated by fitting circles to the digital elevation model(Becker *et al* 2016) on the largest and smallest size possible diameters for each basin then repeating the measurement of Smooth Plains for each

Table 4.2 Area and Percentage of Smooth Plains within the basins in the quadrangle. Errors calculated using minimums and maximum possible basin diameters as calculated from DTM.

Feature	Area (km^2)	Area of basins as a percentage of Quadrangle	Area of Smooth Plains (km^2)	Percentage of Smooth Plains within basins	Percentage of basin interior area covered by Smooth Plains
H-14 Quadrangle	5,189,408	-	831,306		-
All Basins	3,412,172	66% ±16	715,931	86 ±7%	21% ±17%
Confident in H-14	773,612	15% ±8	344,376	41 ±3 %	45% ±9%
Rembrandt	274,017	5% ± 14	155,263	19 ±6%	57% ±16%
Confident minus Rembrandt	499,594	10% ±17	189,113	23 ±7%	38% ±18%

Both "all basins" and the "confident basins" have more areas of Smooth Plains than the proportion of the quadrangle they take up (Table 4.2). Even removing Rembrandt, which is a relatively young basin compared to the others within the quadrangle, the other confident basins take up 10% of the mapped area but include 23% of the Smooth Plains. The link suggests that large impact basins on Mercury's surface host more Smooth Plains patches than the surrounding plains. Given the relative age of Smooth Plains is thought to be Tolstojain to Calorian (Whitten *et al* 2014a, Strom *et al* 2011, Byrne *et al* 2016), these basins likely provide long-lasting crustal weaknesses/patches of thin-crust which facilitated magma ascent, and long-lasting thermal anomalies may encourage magmatism (Padovan *et al* 2016, 2017). Unfortunately, the position of MESSENGER's orbit relative to H-14 means the gravity data are currently insufficient to examine whether the area is isostatically-compensated or whether the crust is locally thin.

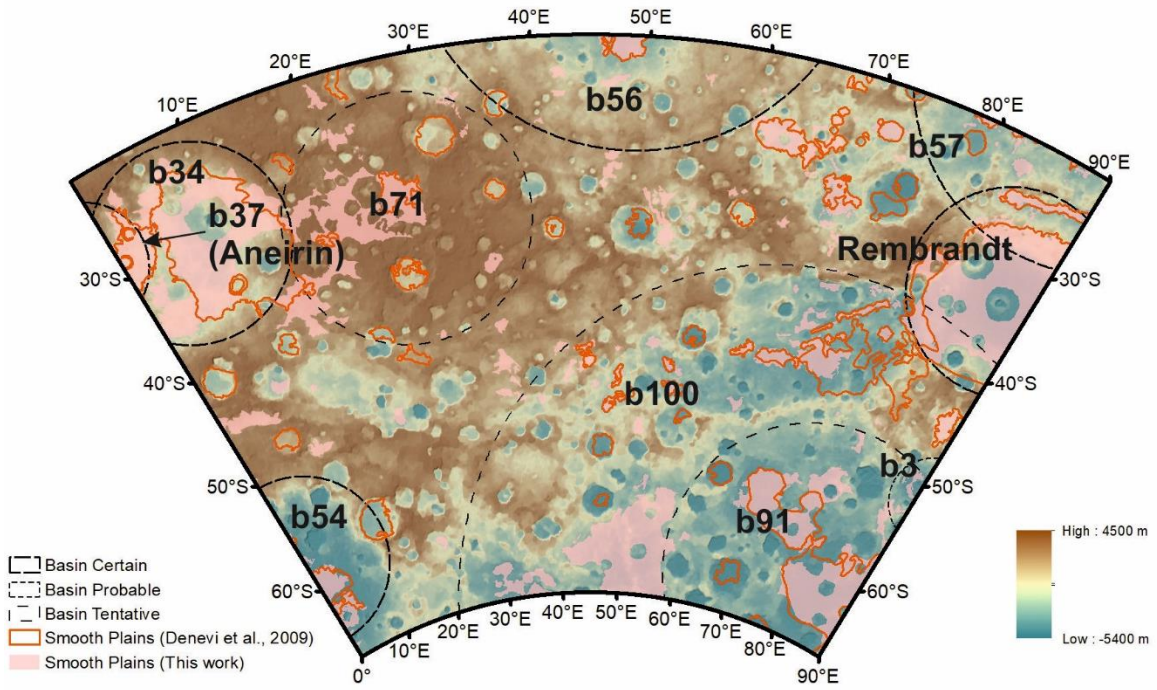

Figure 4.8 Location of Smooth Plains from this work and global mapping on a topographic map. Large impact basins from Orgel *et al.* (2020) *and the outline of Smooth Plains from global work of Denevi et al. (2009).*

Several small patches of plains occur next to lobate scarps (Section 4.4.1); the best example is an 80 x 30 km patch abutting to the south of Enterprise Rupes (see Figure 4.9). The patch at Enterprise is directly next to a c3 crater and may overlap some of its ejecta, giving the smooth patch the tentative of Calorian at the oldest; the majority of Smooth Plains on Mercury are thought to have formed during the Tolstojan and Calorian period (Section 4.4.1.3, 2.6.1), so if these patches are younger they may represent some small volcanic activity after the cessation of most volcanic activity(Malliband *et al* 2018, Malliband 2020). Malliband *et al.* (2018) and Malliband (2020) point out that fault planes beneath lobate scarps would be excellent conduits for magma, and such patches of Smooth Plains maybe some of the last areas of effusive volcanism on Mercury.

None of the examples of Smooth Plains patches abutting faults within the quadrangle have relationships with craters younger than Calorian. Additionally, there are no clear examples where Smooth Plains cover part of a fault scarp (Watters and Nimmo 2010). The embayment of a fault surface would not be apparent if fault activity continued after the emplacement of Smooth Plains patches. It is also possible the Smooth Plains patches existed before the faulting and are unrelated: the lobate scarp just partially covered them. These features can be better studied if more examples are found during mapping of the rest of the planet at a 1:3 million scale.

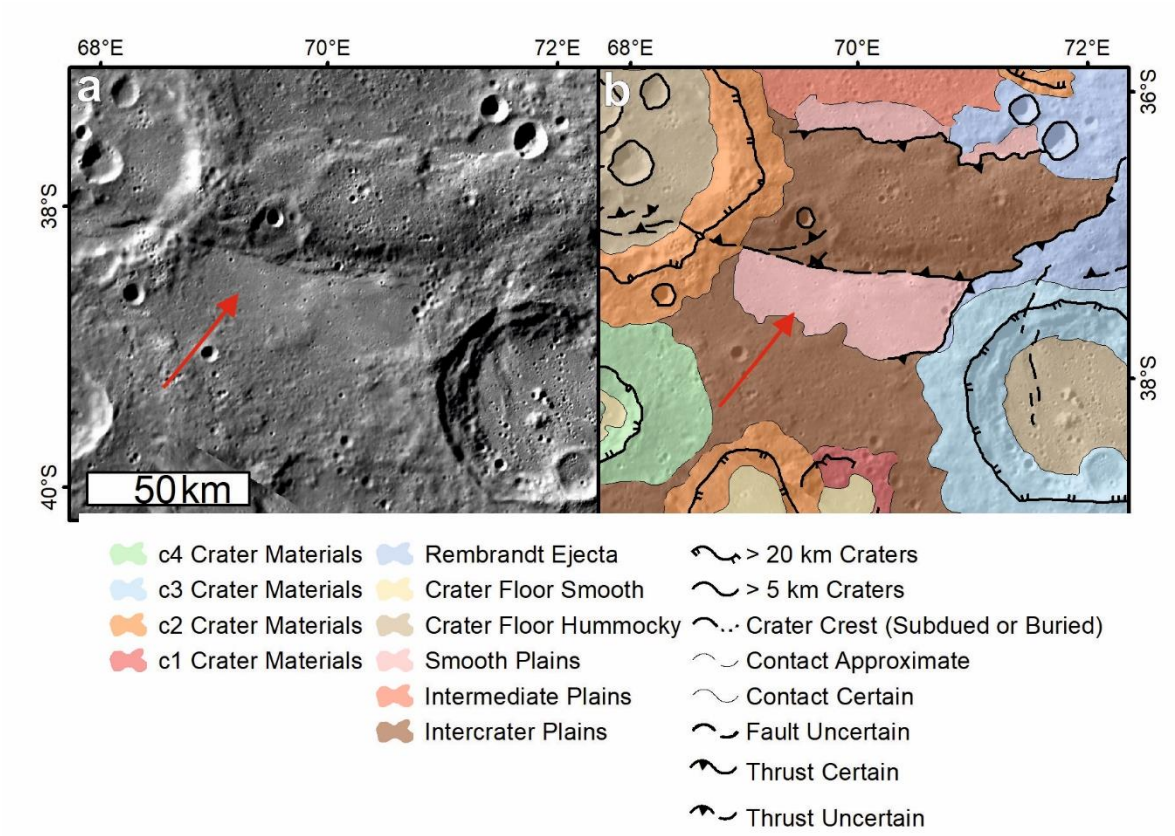

Figure 4.9 A patch of Smooth Plains next to Enterprise Rupes, arrow points to Smooth Plains south of Enterprise Rupes. a. bulk data record (Denevi *et al* 2018a) *b. geomorphological interpretation.*

Unlike at the Caloris basin, where there are clear connections between Smooth Plains inside and outside the basin, the connection between Smooth Plains between interior and exterior to Rembrandt is ambiguous (Figure 4.10) and only possible in one location. This connection would be between what I interpret as undulating plains of exterior impact melt and ejector linked with interior dark Smooth Plains by a narrow ramp on the rim and could be clarified with higher resolution data.

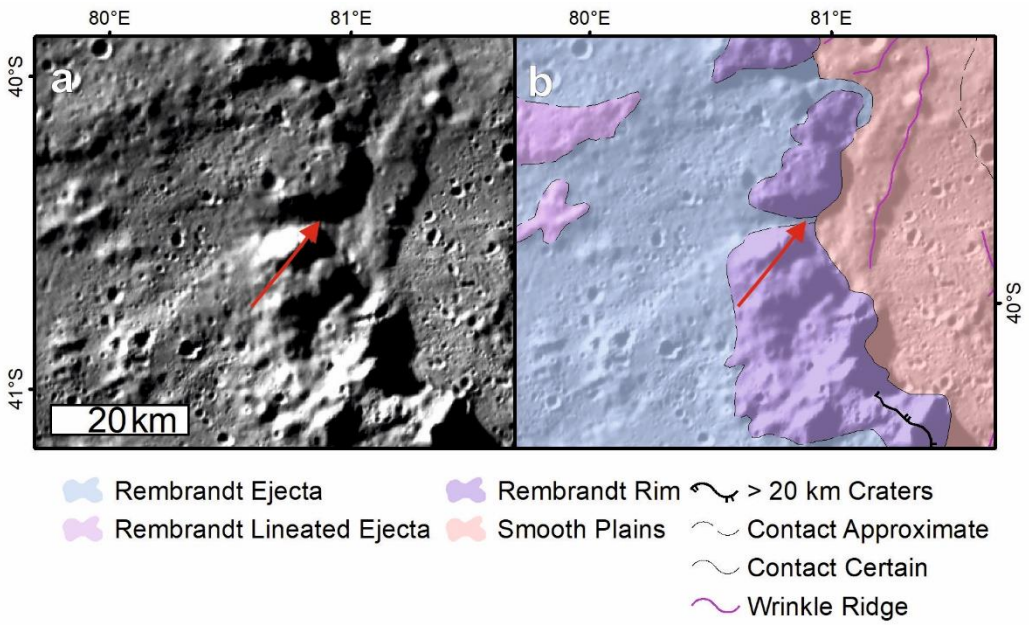

Figure 4.10 Image showing the possible connection between exterior ejecta and interior Smooth Plains in the Rembrandt basin. a. bulk data record (Denevi *et al* 2018a) *b. geomorphological interpretation.*

After Mariner 10, Wilhelms (1976) suggested Smooth Plains were ponds of impact melt. To help understand their origin, I look at the morphological features found within Smooth Plains. These include ghost craters (Figure 4.11) which are the surface expression of craters buried by lavas (Klimczak *et al* 2012) that are then faulted by differential stress caused as the lava cools. The lava is thin above the crater rim but thick within the crater itself and so contracts by different amounts, leading to a ridge that outlines the entirely buried crater (Cruikshank *et al* 1973). Within the quadrangle, I have also mapped several embayed craters. These show the floor and part of the rim covered in this Smooth Plains materials, confirming these plains flowed into and partly filled these craters.

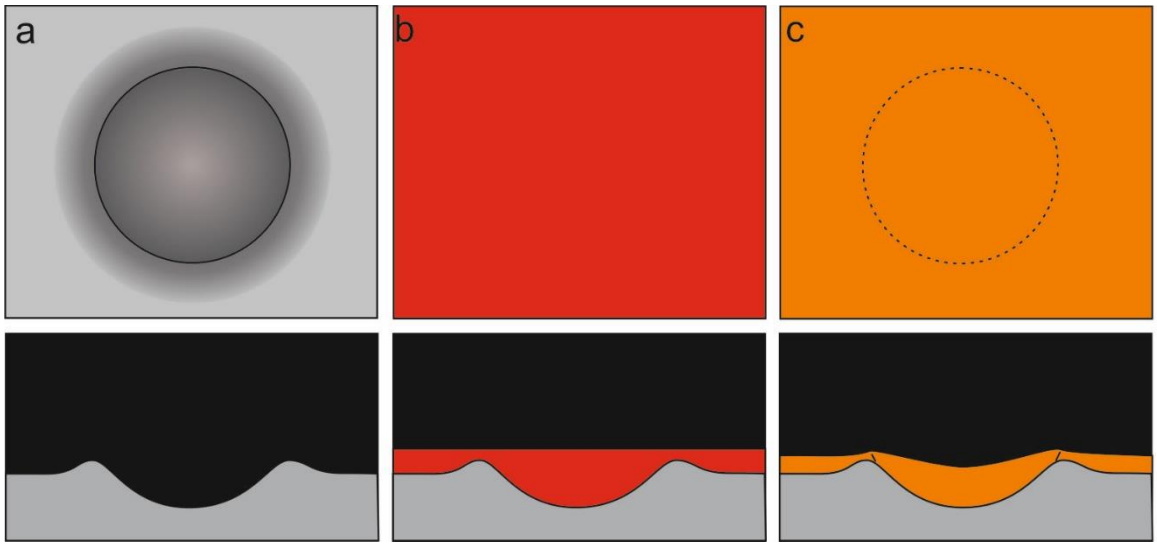

Figure 4.11 Ghost crater formation with a plan and sectional view. a. Crater on the surface of a planet. b. lava completely covers the crater at hydrostatic equilibrium, the lava is thin above the crater rim and deeper in the middle of the crater. c. as the lava cools, it shrinks; greater shrinking occurs in the thicker lavas in the centre of the crater. Less contraction

occurs in the lava over the rim; the difference in strain leads to faults and folds forming wrinkle ridges that outline the rim of the crater. Authors own schematic.

The presence of a ghost and embayed craters within the Smooth Plains is not conclusive evidence for lava flows or impact melt. The presence of most Smooth Plains in low lying areas but without mantling nearby topographic highs (as would be expected if an impact event had generated the plains) suggests materials flowed rather than being emplaced from above. The absence of large basins in the west of the quadrangle, of a similar age to the Smooth Plains, precludes the impact melt source for the large patches of Smooth Plains so adding consilient evidence to the plains' volcanic origin. Thus I agree with the general interpretation that Smooth Plains originated as lava flows (Weider *et al* 2012, Guzzetta *et al* 2017, Denevi *et al* 2009, Byrne *et al* 2013, Strom *et al* 1975, Spudis and Guest 1988), with the tentative exception of some patches of Smooth Plains around Rembrandt (Section 4.3.2.2).

There are no confirmed source vents for these flows, though Byrne *et al*. (2013) identified some tentative vent locations. The lavas were likely low viscosity when they erupted and so covered their vents (Stockstill-Cahill *et al* 2012, Breuer *et al* 2007, Byrne *et al* 2015). The Northern Smooth Plains of Mercury (Borealis Planitia, chapter 2.6.1) show some erosional features from these lava flows (Byrne *et al* 2013), but I did not observe any within this quadrangle. The Smooth Plains have a thickness of 0.2-4 km across the planet (Ostrach *et al* 2015, Fassett *et al* 2009, Whitten and Head 2015).

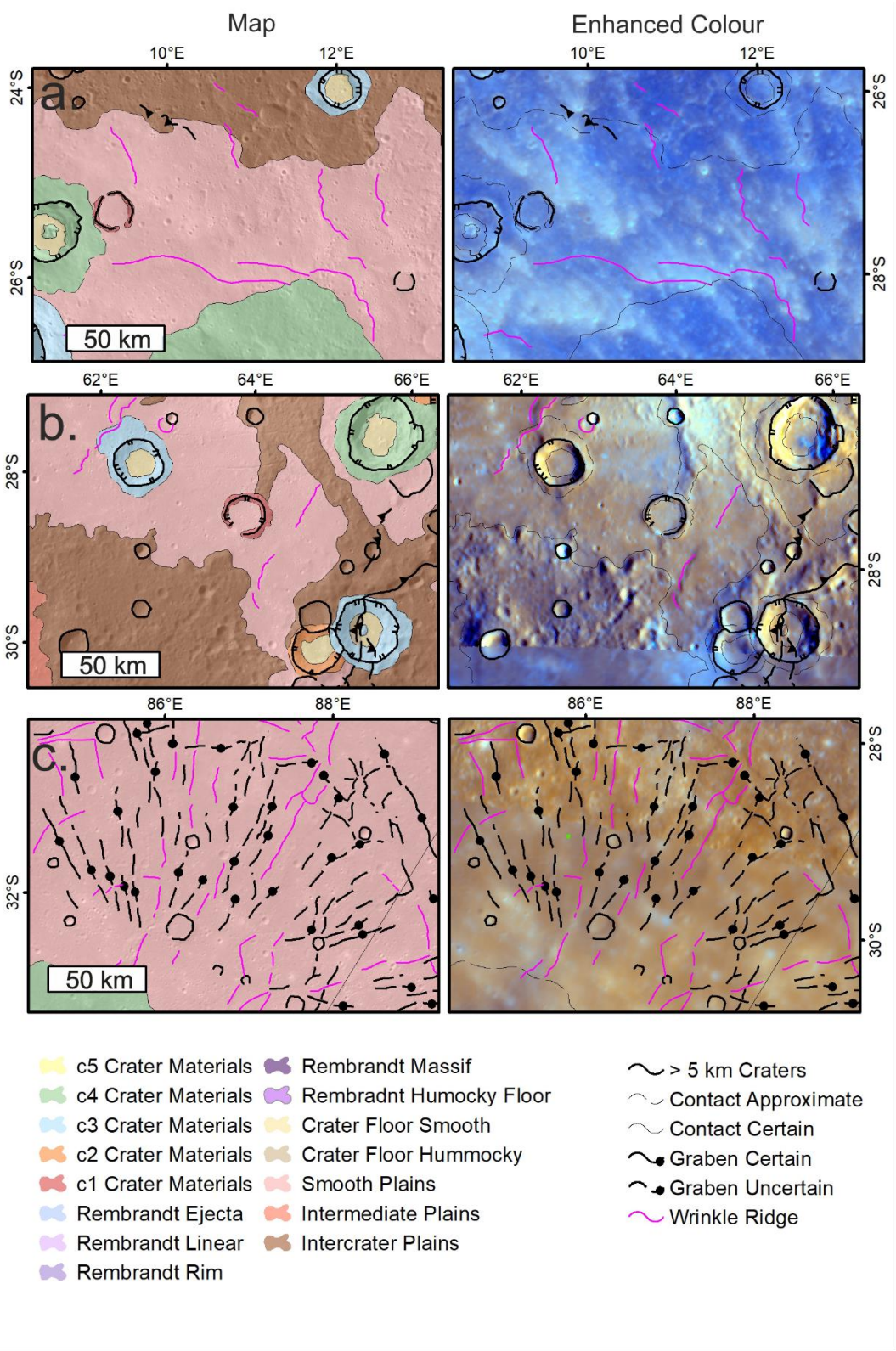

Figure 4.12 a. The range of special associated with the Smooth Plains left column is the map interpretation right the same area in enhanced colour(Denevi *et al* 2018a)*: a. Spectraly bluer plains (with white crater rays on top), b. intermediate colour plains, c. spectrally orange plains.*

While the Smooth Plains are spectrally redder and have a higher reflectivity than the Intercrater Plains, there is a wide range of spectra for Smooth Plains within the quadrangle, as seen in enhanced colour (Figure 4.12.b). The Smooth Plains in the west and south of the quadrangle are dark blue in the enhanced colour basemap (Figure 4.12.a, Figure 4.16), whereas, in the centre of Rembrandt, they are orange colour (Figure 4.12.c). It is likely that the composition of the Smooth Plains varies, with different amounts of carbon and sulfur-producing different levels of reflectivity (Nittler *et al* 2011, Weider *et al* 2012). The blue to red range may represent an evolution in the effusive volcanism on Mercury; this would correlate with the idea that the Smooth Plains in the south of the map, which are more blue/purple in enhanced colour, are older than those in the northeast. In general, a lack of graphite makes the more recent plains appear redder than the older plains (Murchie 2015, Weider 2015). This activity mostly appears to have stopped by about the mid-Calorian 3.5 Ga (Byrne *et al* 2016). The Smooth Plains within H-14 do not provide any new insights but add to the global understanding of Smooth Plains. They show the last phases of widespread effusive volcanism on the surface of the planet.

4.3.1.2 Intermediate Plains

Intermediate Plains were the most challenging unit to delineate on the map. Only 4% of the plains materials within the quadrangle are Intermediate Plains. Intermediate Plains are scattered around the quadrangle in small patches, often but not always on the edge of patches of Smooth Plains. They have a higher density of cratering than Smooth Plains and have a more undulating texture. Wrinkle ridges are rare. One key texture to denote them as Intermediate Plains is flat bottomed craters that are not superposed by other craters, unlike the bowl-shaped craters of Smooth Plains or the close to saturated density of shallow craters in Intercrater Plains.

Intermediate Plains are overlain by ejecta from c2-c4 craters (the lack of c5 and Intermediate Plains in the same area is probably due to the relative sparsity of both), suggesting that the plains existed as early as the Tolstojian.

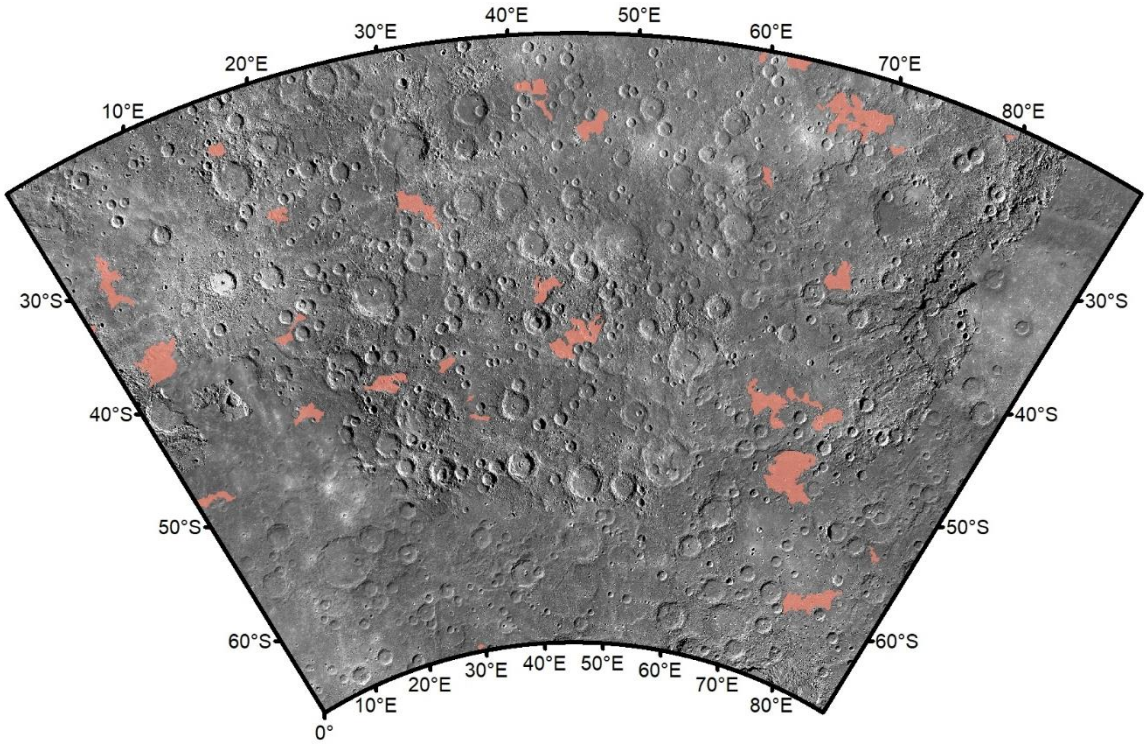

Figure 4.13 Intermediate Plains in pink on the H-14 on BDR basemap (Denevi *et al* 2018a).

Although first identified after Mariner 10 (Spudis and Guest 1988, Michel *et al* 2013), following on from MESSENGER there is some debate about the existence of Intermediate Plains. Whitten *et al.* (2014) suggested that only two plains units exist on the planet: Smooth Plains and Intercrater Plains. They suggested that the Intermediate Plains identified after Mariner 10 are either sparsely cratered Intercrater Plains or Smooth Plains that have undergone local modification by secondaries from recent (c4/c5) craters. These secondaries would modify the plains, prematurely ageing them. However, during one version of her mapping of Derain (H-10) quadrangle to examine plains Whitten *et al.* (2020) included Intermediate Plains, suggesting that they may exist over small areas, though they could not be confident about this due to illumination constraints. The other 1:3 million scale maps so far published (Guzzetta *et al* 2017, Galluzzi *et al* 2016, Mancinelli *et al* 2016, Wright *et al* 2019) and the PhD map of H-15 Derain (Malliband 2020) include Intermediate Plains.

If some patches of Intercrater Plains are sparsely cratered, this would suggest a younger morphological age than the majority of the Intercrater Plains. If they are also not as sparsely cratered as the Smooth Plains, then they would be older than the Smooth Plains. I see this very much as an intermediate stage of modification leading to an intermediate morphology: the Intermediate Plains. Similarly, I can find several areas where the Intermediate Plains are more than two crater radii away from craters of post-Calorian age (Figure 4.14) and so do not have nearby craters to provide a source of premature ageing. If these were related to secondary cratering, I would expect some to form as narrow bands within Smooth Plains, modified by crater chains of ejecta. Instead, they appear more commonly on the edges of Smooth Plains rather than cutting across them (Figure 4.15); as such, I have mapped as Intermediate Plains as a separate morphological unit.

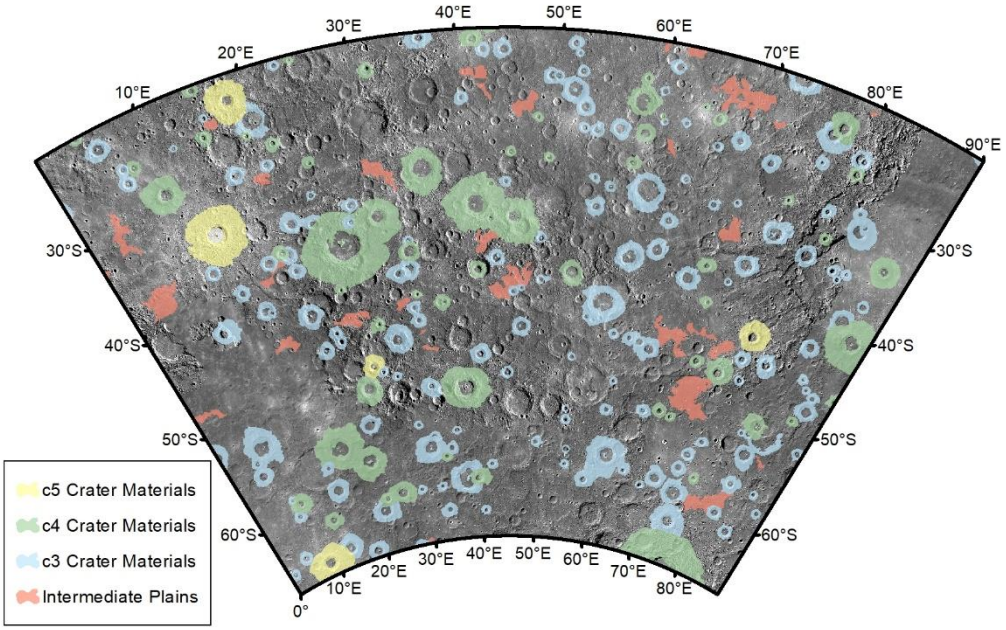

Figure 4.14 Map of H-14 showing the location of Intermediate Plains and the c3, c4, c5 craters. Spatial relationships (such as lack of proximity) give no reason to think that ejecta from these craters transformed Intercrater Plains in Intermediate Plains. Basemap is BDR.

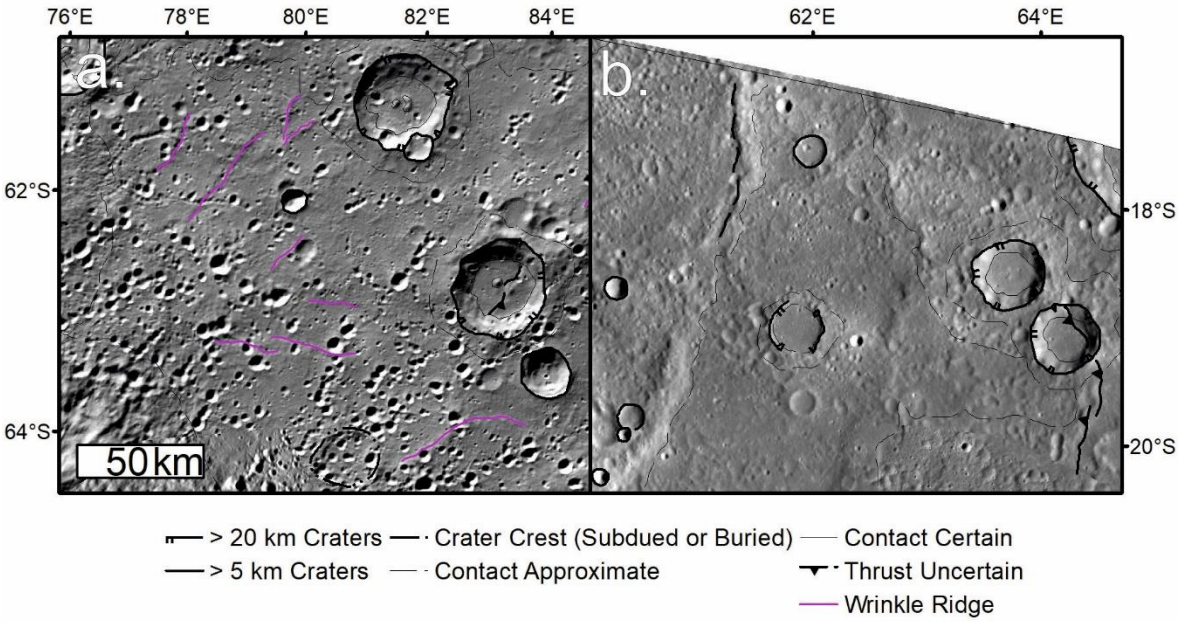

Figure 4.15 a. Smooth Plains modified by nearby impact crater (bottom left of image) b. Intermediate Plains example. Basemap: BDR (Denevi *et al* 2018a).

Intermediate Plains have two possible origins. They could be lava plains of intermediate age that are older and therefore more cratered than the Smooth Plains, but younger and so less cratered than the Intercrater Plains. The other possibility is that Intermediate Plains formed at the same time as Smooth Plains and by

thinly covering/mantling existing terrains with lavas which then deflated, revealing some of the cratered surface underneath.

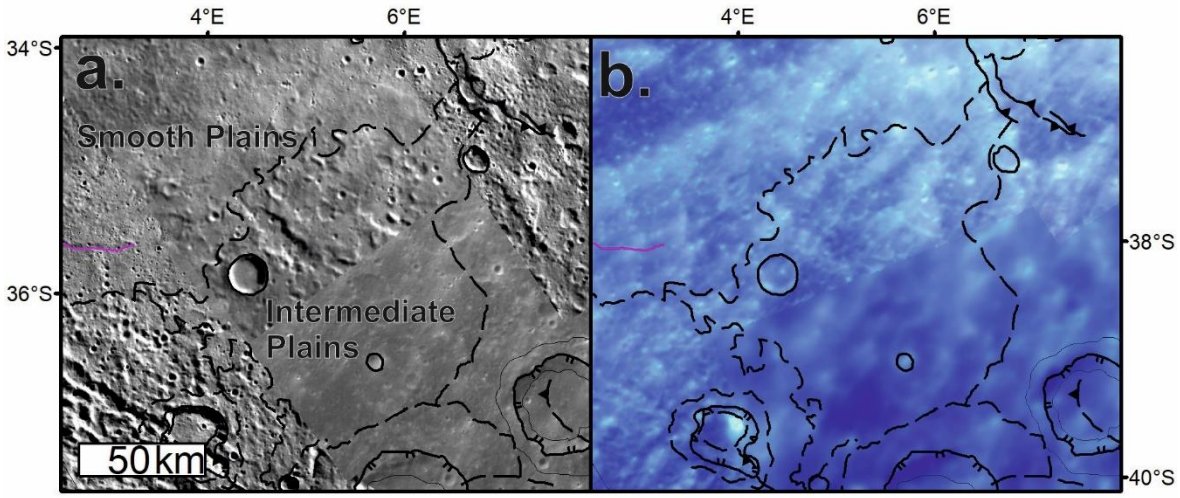

Figure 4.16 a. an area of Smooth Plains and Intermediate Plains from BDR. b, the same area in enhanced colour (Denevi *et al* 2018a).

Around Caloris, lava may have covered areas before deflating and subsiding and draining into the basin (Rothery *et al* 2017). The deflation of lavas would leave some areas covered in a thin layer of lava, giving them a more muted (smoother) appearance than the original Intercrater Plains. This would explain why areas of Intermediate Plains are found around the edges of Smooth Plains, indicating the position to where the lavas extended to but then collapsed. Deflation to this extent could only occur where the lavas have a location to empty into, such as into the Caloris basin. Many of the Intermediate Plains do not have an obvious feature for the lavas to drain into. I, therefore, think deflation is an unlikely explanation for most of these Intermediate Plains.

However, it is possible that during Smooth Plains emplacement, the margins of these plains only cover and fill the smallest craters reducing the apparent density of cratering, rather than completely "resetting" it. This thin layer of lava may explain some Intercrater Plains on the edge of Smooth Plains. However, large patches of Intermediate Plains formed in this way should have a relative absence of small craters compared to larger craters (which is not the case). This formation pathway does not explain some of the topographic undulations seen in these plains, which are not seen in Smooth Plains but should be if formed contemporaneously. It is more probable that Intermediate Plains are an intermediate age of plains volcanism between Smooth Plains and Intercrater Plains.

The significantly lower area covered by Intermediate Plains compared to Intercrater and Smooth plain noted by both Whitten *et al.* (2020) and I suggest, if they are a separate morphological class, either: they represent a short period of the planet's volcanic history, the rate of volcanism was slower during this period, or later Smooth Plains covered (and thus hid) most of the Intermediate Plains.

While there is a wide range of dates for Smooth Plains volcanism, they are within error of each other and may represent a sudden pulse of volcanism (Byrne 2020, Hauck *et al* 2018). If this is the case, Intermediate Plains could represent a period when effusive volcanic activity was muted and resurfaced only small areas. Linking crater statistics with Intermediate Plains will help solve this and help identify out when they occurred relative to the Intercrater Plains and Smooth Plains emplacement. This can only be done by compiling data from Intermediate Plains in several quadrangles to have a statistically significant areal sampling.

Another possibility for the scarcity of Intermediate Plains is that the subsequent Smooth Plains utilised many of the same ascent pathways as the Intermediate Plains, as compressional tectonics and thickening crust reduced the number of pathways available and a reduction in cratering rate reduced new pathway generation. Continued volcanism in the same areas would cover over Intermediate Plains with Smooth Plains. If the volumes of Smooth Plains in those areas were less than the underlying Intermediate Plains, or tectonic activity isolated them, then only the extremities of the Intermediate Plains would be left. In areas where the Smooth Plains were more voluminous, they would completely bury the Intermediate Plains.

I agree with Whitten *et al.* (2014) that illumination makes identifying the morphology of an intermediate stage of plains difficult. The range of illumination angles available from MESSENGER data makes some areas of muted texture much more challenging to interpret. This true of all terrains, but Intermediate Plains is the most challenging. However, there is a mappable plains unit that is neither Intercrater Plains nor Smooth Plains, and I interpret this to be a volcanic unit of intermediate age, most likely midway through the Tolstojan. Further data from multiple times of solar day may help identify this morphology more clearly and then completing crater statistics will help identify if they are low volume production or just formed over a short period.

4.3.1.3 Intercrater Plains

Intercrater Plains are the most common map unit, covering 36 % of the surface of the quadrangle and making up 67% of the plains mapped. Its densely cratered and undulating texture makes it a distinct feature on the planet. It hosts all age ranges of craters. Intercrater Plains in this quadrangle, in general, match the blue-purple spectral pattern seen elsewhere on the planet (Denevi *et al* 2009, Murchie *et al* 2015). Lots of small (<10 km) shallow craters, often overlapping, superpose the plains.

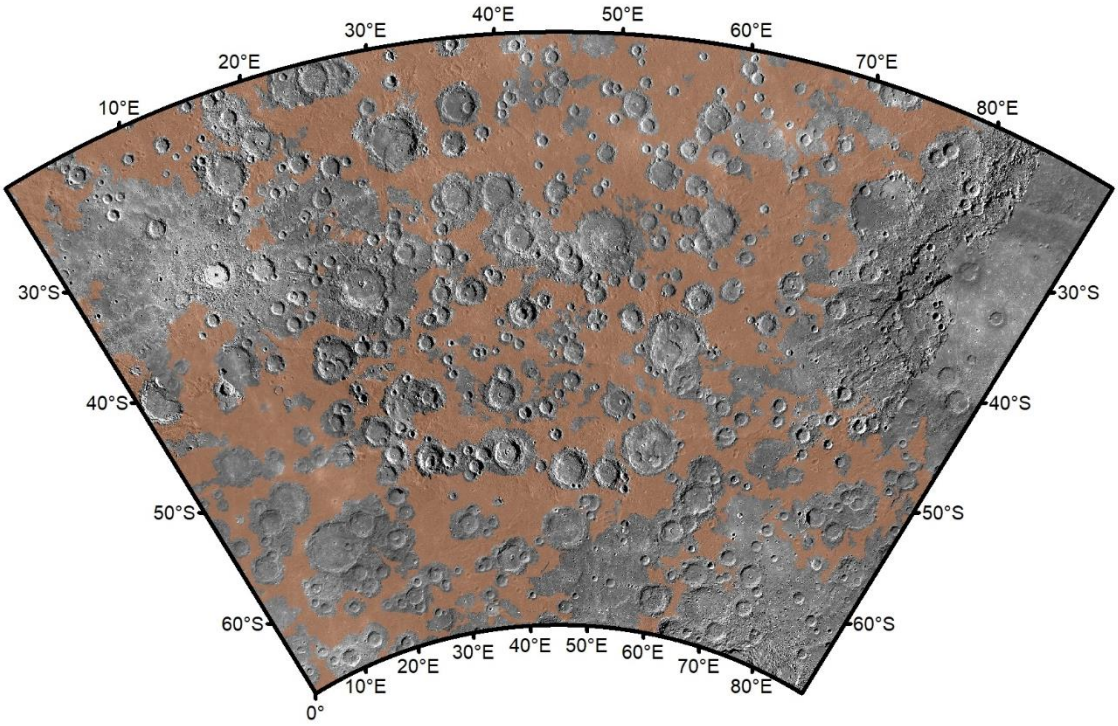

Figure 4.17 The location of Intercrater Plains (brown) within H-14. Basemap is the Bulk Data Record (BDR) (Denevi *et al* 2018a).

Within the Intercrater Plains, there are some very prominent topographic features surrounded by lower features (Figure 4.18). The Intercrater Plains undulate on a kilometre to 10s of kilometre scales, but these blocks stand out as features within the plains. These features do not have a distinct spectral character, and both blocks and the surrounding Intercrater Plains are heavily cratered. These blocks are too infrequent and indistinct to map as a separate unit (as compared to the Rembrandt Massif unit, which mostly occurs within Smooth Plains (see section 4.3.2.1). The blocks may be parts of old basins/ejecta or parts of tectonic features no longer apparent, or potential basement covered over by subsequent ejecta and so weathered they no longer have a distinct spectral signature.

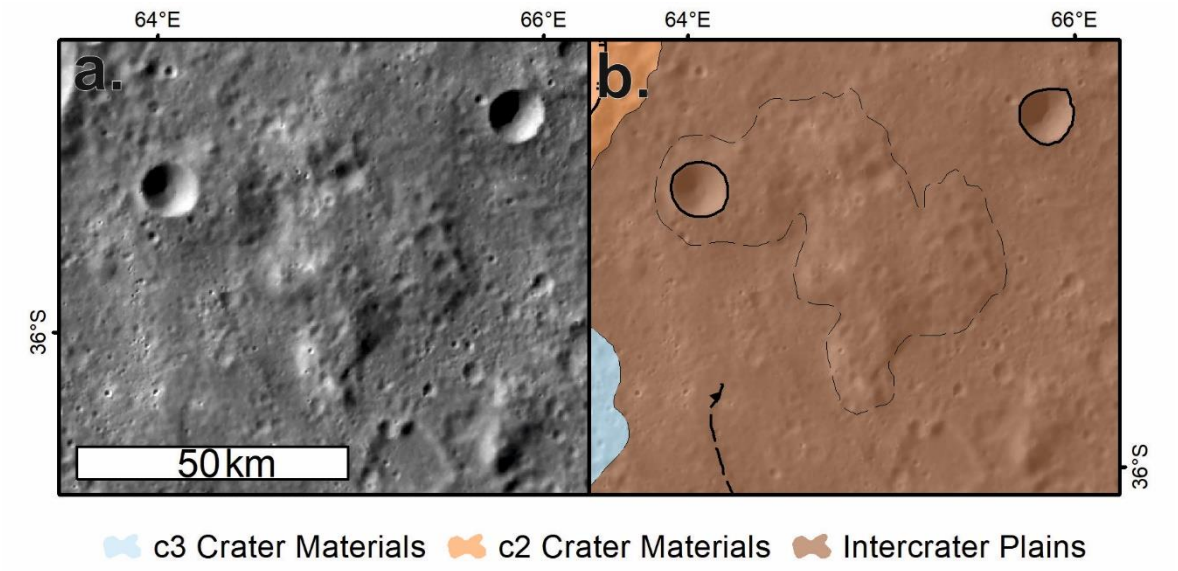

Figure 4.18 Location of a block within Intercrater Plains a. BDR image (Denevi *et al* 2018a) *b. geomorphic map interpretation with 30% transparency and BDR map underneath.*

After Mariner 10, Intercrater Plains were defined by their high abundance of craters that were modified by subsequent impact craters across all size ranges (Trask and Guest 1975, Whitten *et al* 2014a), yet the density of superposed craters is lower than the oldest surface on the Moon, the Lunar Highlands (Murray *et al* 1975, Fassett *et al* 2011, Strom *et al* 2011). Mercury's high gravity and position within the Solar System mean the cratering rate is three times that of the Moon (Marchi *et al* 2013). A lower density of craters on a body with a higher cratering rate means that the Intercrater Plains must be younger than the Lunar Highlands (e.g. Murray *et al.*, 1975; Fassett *et al.*, 2011).

The Lunar Highlands are the remains of a flotation crust, forming from buoyant phases (mostly anorthite) that rose to the surface of the magma ocean (Walker and Hays 1977). As the Intercrater Plains on Mercury are younger, it is unlikely to represent such a primary flotation crust, fragments of which are represented by the carbon-rich LRM (e.g. Section 4.2.2 Chapter 2.5.3, Peplowski *et al*., 2016).

I have found no evidence for the origins of the Intercrater Plains from the mapping process. However, as they are not flotation crust, the Intercrater Plains are likely formed by lava flows, subsequently heavily modified by impact events and distorted by tectonic activity (Malin 1976, Trask and Guest 1975, Whitten *et al* 2014a). Whitten *et al.* (2014) show using crater statistics that different patches of Intercrater Plains have a wide range of dates from pre-Tolstojian to just before the Caloris impact event. However, this work does include some plains that would I would class as Intermediate Plains within Intercrater Plains.

I interpret the Intercrater Plains as lava flows from the planets' early history (relatively older than the subsequent Intermediate and Smooth Plains) which have been subsequently heavily modified by impact events to leave a heavily cratered landscape of ejecta materials. The high topographic features within the Intercrater Plains suggests there may be multiple generations of features, offering the potential to divide them further. However, currently, insufficient data resolution prevents this. Better image data and

compositional data may provide ways of splitting Intercater Plains into more functional units given the wide range of time these plains seemed to form over.

4.3.1.4 Plains Summary

I have identified three plains units: Smooth, Intermediate, and Intercrater. They are all different generations of volcanic lava flows that cover and modify the planet. It is not clear if volcanism occurred in pulses, was fairly continuous until it stopped at 3.5 Ga (Byrne *et al*., 2016) or gradually waned. After Smooth Plains emplacement, widespread changes to the surface of the quadrangle ceased. Subsequently, impacts gradually degraded the plains.

4.3.2 Rembrandt Impact Basin

As the second-largest clearly defined impact basin on the planet, Rembrandt offers us significant insight into Mercury and its impact crater history. 65% of the basin is within the quadrangle. I did not map the entire basin as this has been done in other works (Hynek *et al* 2017, Semenzato *et al* 2020).

Because of the significant size of Rembrandt, I decided to map it as multiple units (rather than just 'crater materials'), bearing in mind precedents set by Caloris-related units, as well as for other Rembrandt maps (chapter 2.5.1.2, Hynek *et al*., 2017; Semenzato *et al*., 2020). However, I defined units based on my own observations. These units cover 5% of the quadrangle excluding the interior Smooth Plains or 10% including them. I now discuss the features I have mapped inside and outside the basin.

4.3.2.1 The Interior of the Rembrandt Impact Basin

Smooth Plains dominate the interior of the basin. The Bellini impact crater covers part of the basin and the associated faults within the interior break up the plains smooth surface (see section 4.4.2). Semenzato *et al*. (2020) and Watters *et al*. (2009a) divide the Smooth Plains within the basin into multiple units based on smoothness. I have left them as one unit because the ejecta from Bellini (a crater in the middle of the basin) may smooth out some of the structural features of the plains, making them look younger (Figure 4.19). The thickness of the Smooth Plains within Rembrandt is estimated to be between 0.2-0.4 km (Whitten and Head 2015) and 1 -1.5 km (Semenzato *et al* 2020). Rembrandt may be one of the most recent areas of effusive volcanism on the planet, with Semenzato *et al*. (2020) identifying a patch of Smooth Plains within it that, if unaffected by the Bellini impactor, is only 2.3 Ga old (Mansurian).

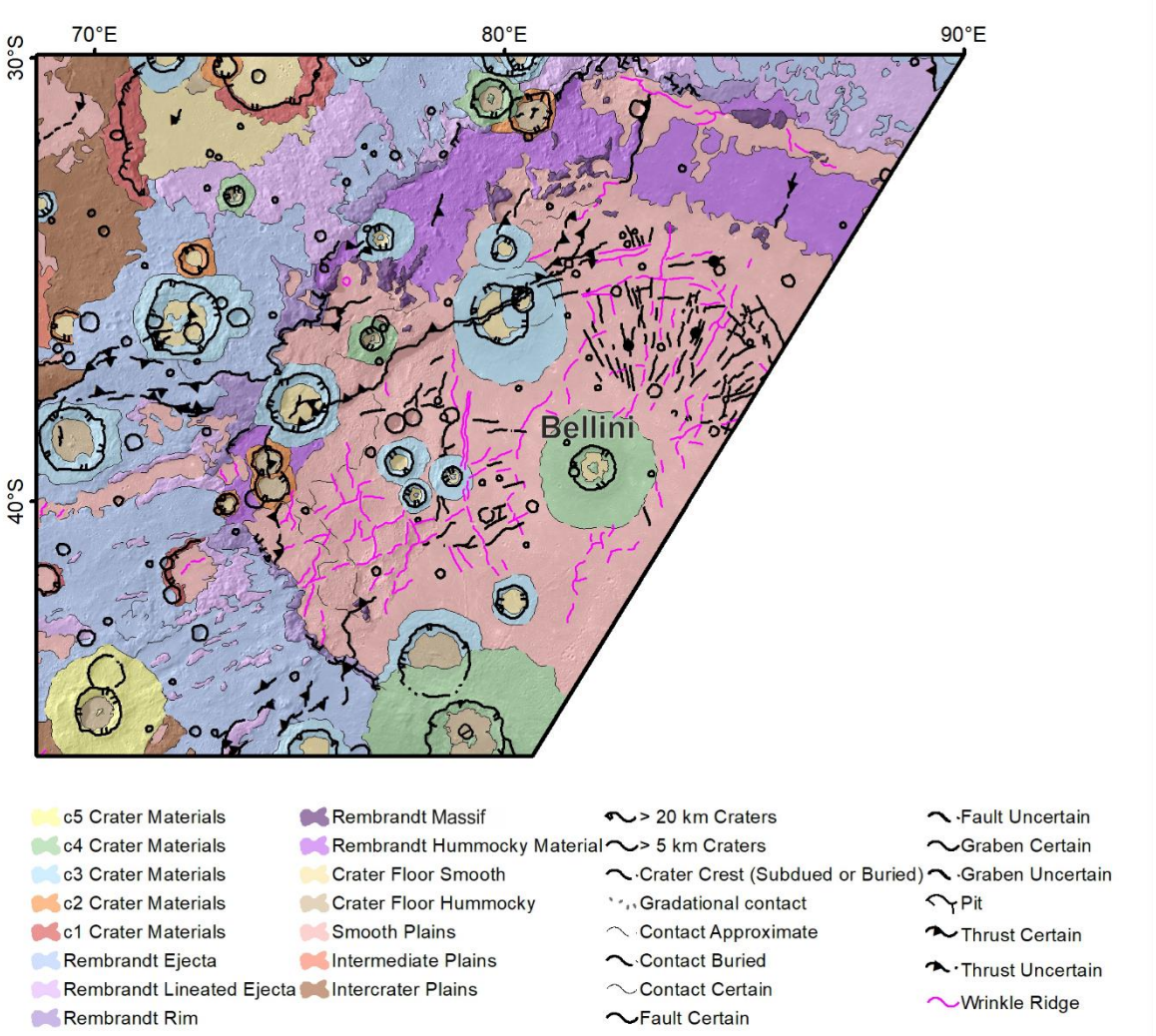

Figure 4.19 Interior of Rembrandt with the geomorphic map on BDR basemap.

The north of the basin floor has an area of hummocky material, which I map as Rembrandt Hummocky Material. This unit is probably a mix of the crater floor materials and impact melt (Ernst *et al* 2015, Hynek *et al* 2016b, Watters *et al* 2009a, Whitten and Head 2015, Semenzato *et al* 2020), similar to the basin related materials termed "knobby terrain" on the Moon, although knobby terrain occurs both inside and outside the lunar basins (Head *et al*., 2010). I agree with this interpretation, especially given its similar spectral characteristics in enhanced colour to the surrounding intercrater plains and ejecta units and its highly cratered appearance.

To the north of the Hummocky Material, craters are embayed by Smooth Plains, showing that these plains postdate the unit. The Hummocky Material is a feature unique to Rembrandt as other large basins on Mercury have their floors entirely covered with lavas. The reason for this low volume of filling is unclear, given that Rembrandt appears to be slightly older than Caloris (Section 4.2.3). The semi-circular shape of the exposed Hummocky Unit suggests that it may originally have been part of an elevated ring feature; however, the Smooth Plains immediately south of it are at a higher elevation than it, suggesting subsequent local topographic changes. These topographic changes could be caused by the effects of loading by the Smooth Plains to the north of the Hummocky unit. This small band of Smooth Plains looks less degraded and cratered

than those in the middle of the basin and may have added loading to the outer edge of the basin. Still, this difference in age may be a factor of Borobudur Fossae, making the central Smooth Plains appear more deformed and so morphologically older.

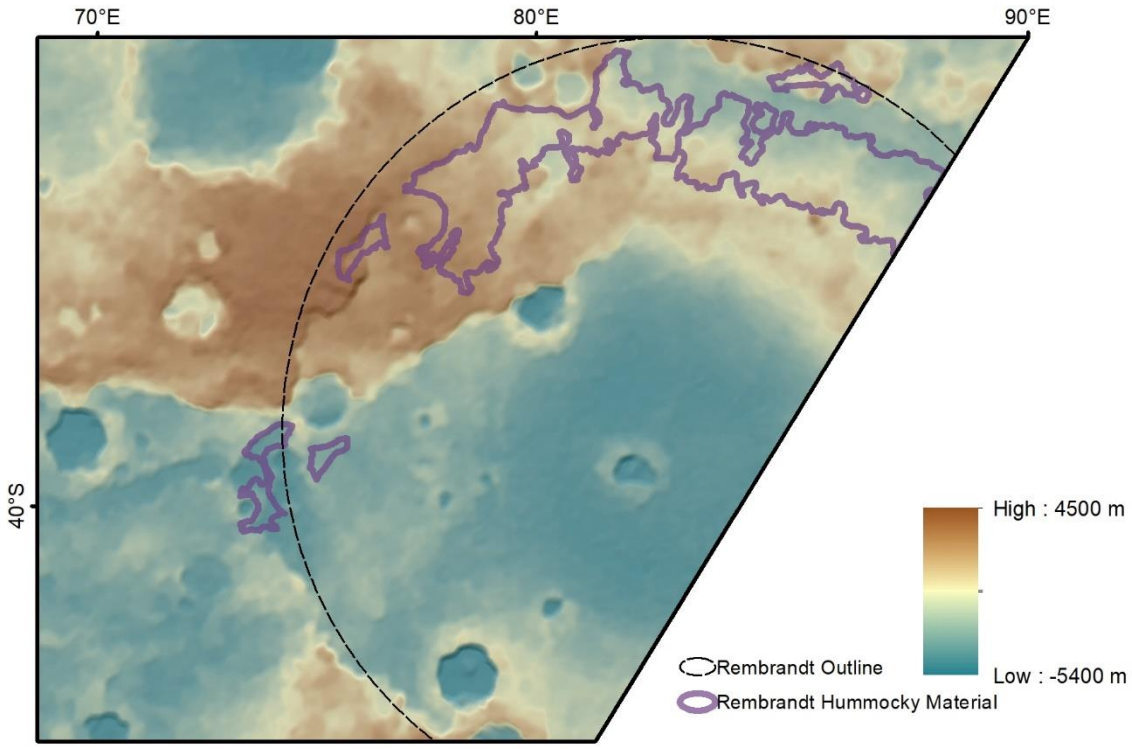

Figure 4.20 Rembrandt Hummocky Material over colour-coded topography (Becker *et al* 2016)*, with hillshade.*

The Rembrandt Massif unit occurs as several isolated blocky mountains up to 2 km in height (Figure 4.21), with a slight preferential radial orientation. They are more abundant in the north of the basin. They rise to 1 km above the surrounding Smooth Plains, but lack of conformity to a clear ring structure suggests that they are large blocks of impact ejecta that fell back into the basin rather than being traces of an incomplete peak-ring structure.

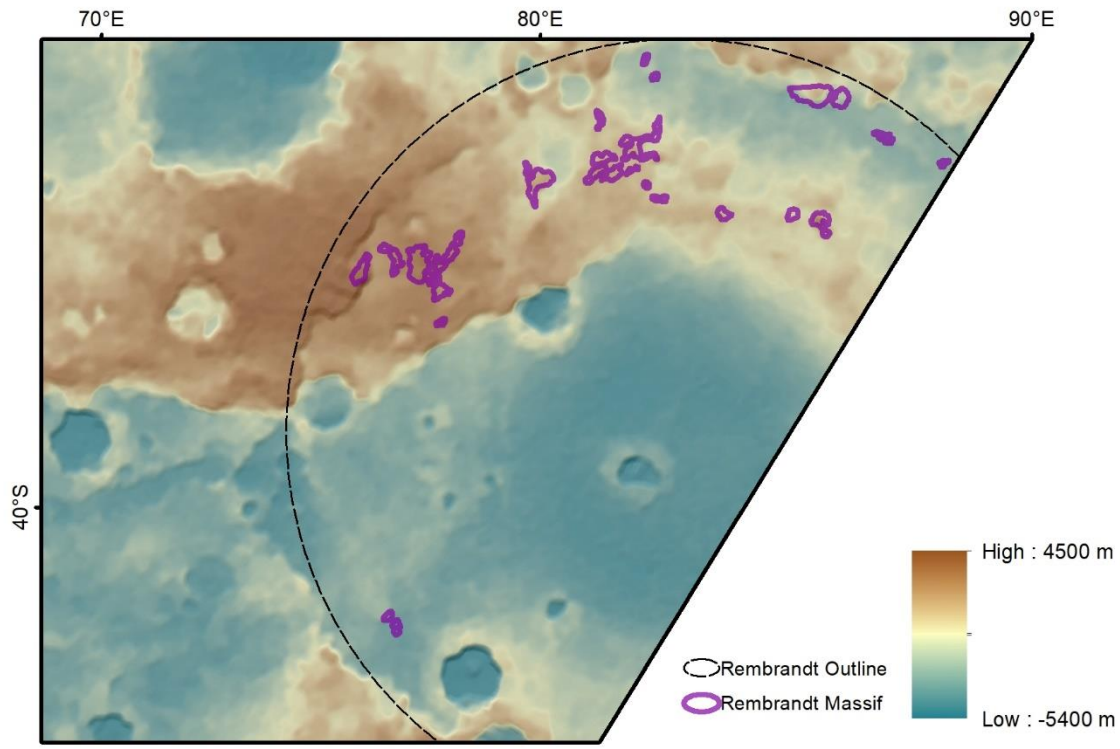

Figure 4.21 Rembrandt Massif unit over colour-coded topography (Becker *et al* 2016)*, with hillshade.*

4.3.2.2 Rembrandt Exterior

The Rembrandt Rim unit consists of large blocks with a basin-facing scarp around part of the edge of the basin floor. This unit is similar to the Caloris Montes and thought to represent the edge of the transient crater of the basin (Watters *et al* 2009a, Fassett *et al* 2009). It is a non-continuous unit and grades into the Rembrandt Lineated Ejecta, which has a distinct fabric radiating away from the basin. This unit was identified by Hynek *et al.* (2017); however, they have a continuous rim unit, whereas mine is not continuous due to other distinct ejecta morphologies (such as the Rembrandt lineated unit starting from the scarp at the edge of the basin).

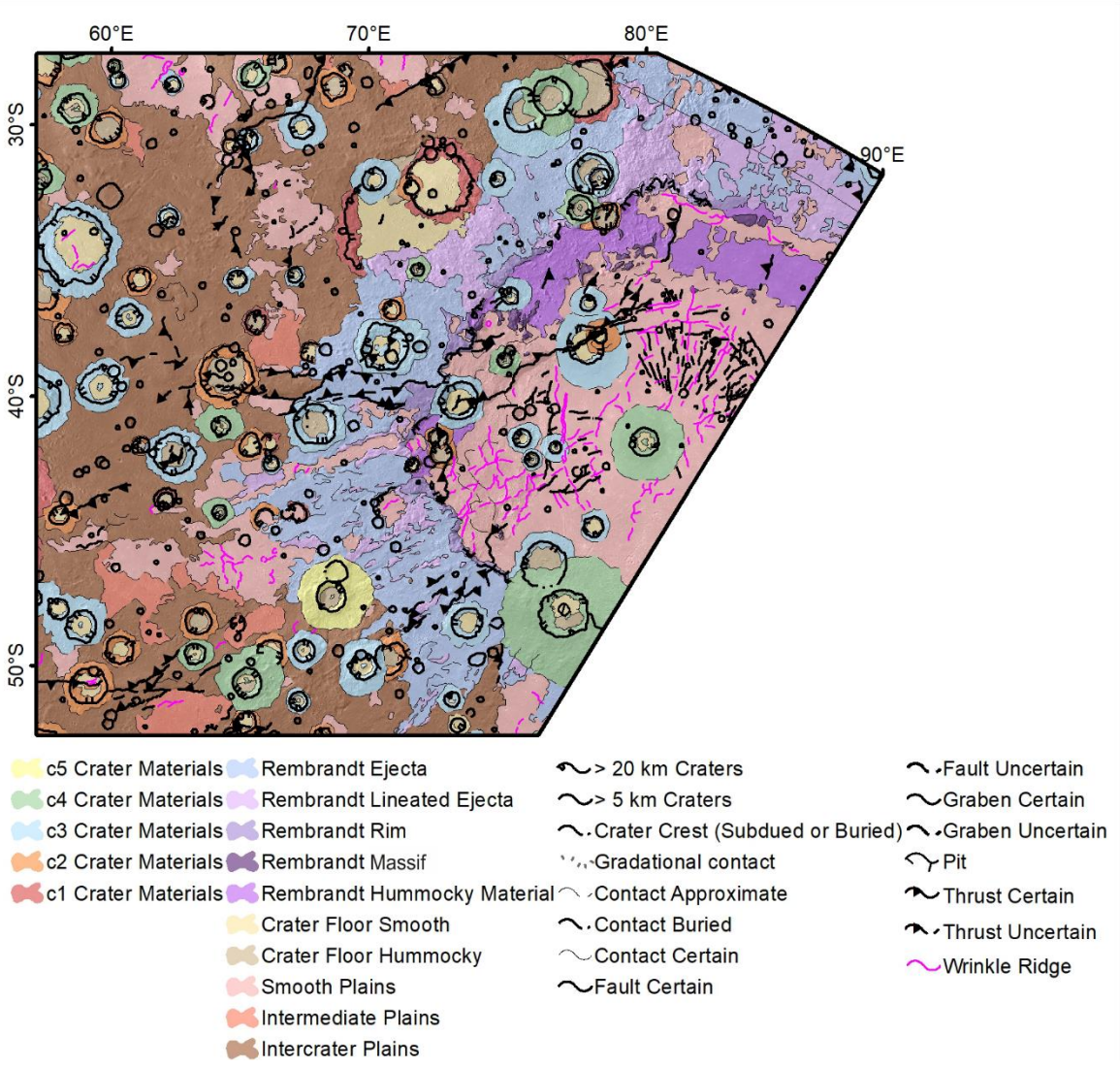

Figure 4.22 Morphological map of the exterior of Rembrandt with 30% transparency on BDR basemap (Denevi *et al* 2018a).

The Rembrandt Ejecta dominates the southwest of the basin as the undulating layer mantling the underlying terrain, likey a mix of ejecta and impact melt. The Rembrandt Lineated Ejecta is more common in the north, radiating directly away from the basin. In the south, the lineated unit occurs further away from the basin. It is a deposition unit, as seen by the unnamed 215 km c1 crater in the northwest (Figure 4.23), where Rembrandt Lineated Ejecta forms high ground obscuring the SW of the crater.

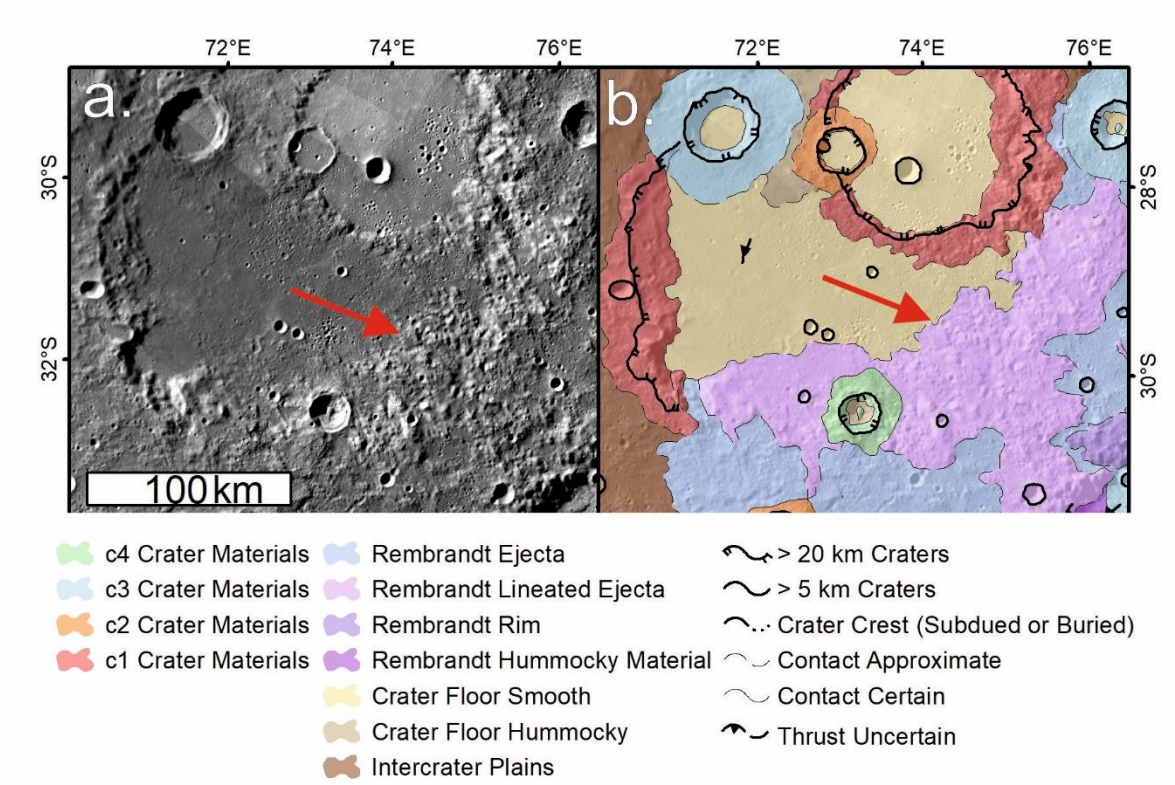

Figure 4.23 Lineated ejecta covered portion of c1 crater In, a. Bulk data record (Denevi *et al* 2018a)*, b. geomorphology map with 35% transparency over BDR. The red arrow points to ejecta deposited on the crater floor.*

In other places, the lineations are carved into the existing surface, suggesting they are a record of the effects of the impact event when the surface was scoured by ejecta (e.g. Oberbeck, 1975). Within this unit, patches of Smooth Plains and Rembrandt Ejecta (described below) occur in round depressions (Figure 4.24). These round depression are probably impact craters whose rim and ejecta have been scoured away by the impact event. Impact melt/fluidised ejecta or lava has filled the interior of these depressions. These smooth ponds suggest that ejecta mantles the area.

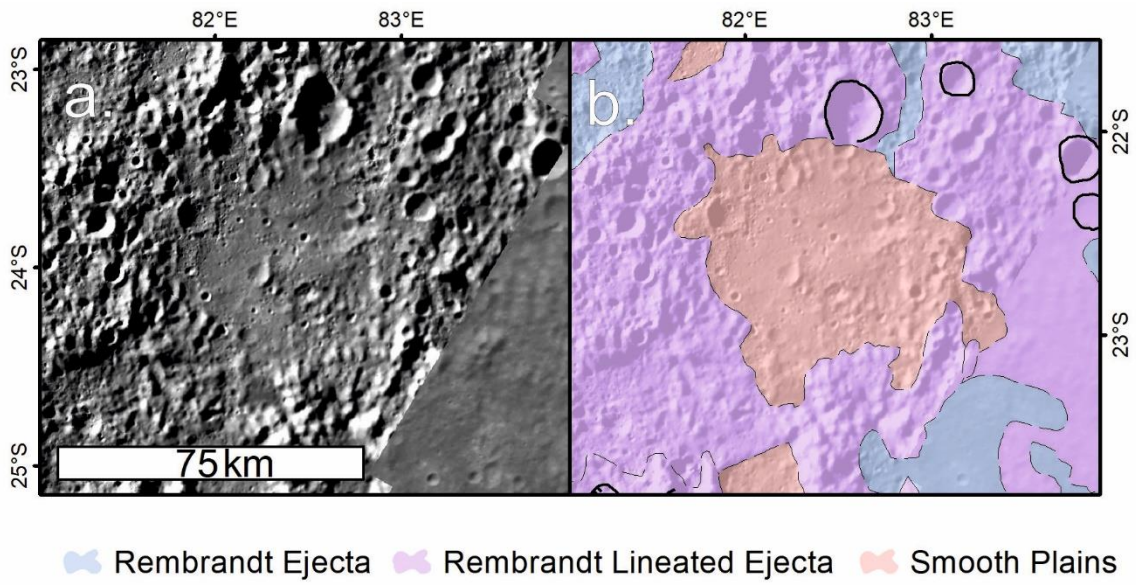

Figure 4.24 Patch of Smooth Plains in the Lineated Ejecta unit. The near-circular outline and location within a depression suggest it was a crater before the impact event. a. Bulk data record (Denevi *et al* 2018a)*, b. geomorphology map with 35% transparency over BDR. The red arrow points to ejecta deposited on the crater floor.*

The Rembrandt Ejecta covers both highly hummocky ground with lots of craters and smooth patches of undulating ground that appears draped over topography. I take this to be various forms of ejecta from the impact event. This unit is likely comprised of small ejecta blocks and impact melt/fluidised ejecta (it is not possible to distinguish these from orbital observations and current data).

There is a continuum between smooth patches of ejecta patches and the Smooth Plains, which is probably dependent on the thickness of impact melt/fluidised ejecta; where the thickness is sufficient, it would become morphologically identical to Smooth Plains, and while more recent lavas are separated by spectral differences in the enhanced colour images (Whitten and Head 2015) some smooth lavas dating from close to the time of Rembrandt would be challenging to distinguish from impact melt.

4.3.2.3 Smooth Plains

The range of reflectivity of Smooth Plains is most evident at Rembrandt, where interior plains are mostly spectrally red and highly reflective. In contrast, the parts of the west of the basin and some of the exterior Smooth Plains are darker blue. The difference at Rembrandt may be because of different origins. Crater statistics, on the exterior relatively blue patches show an N(20) of 53± 11 (Watters *et al.*, 2009), N(20): the number of craters with a diameter >20 km normalized to an area of 10^6 km^2. This overlaps with the Rembrandt impact event N(20) 58±16 (Watters *et al.*, 2009), suggesting they could be impact melt as a similar N(20) shows a similar amount of subsequent modification by impact events, and so a similar age of formation(Watters *et al.*, 2009). The lighter plains inside and outside the basin have a lower N(20) of 45±12; suggesting these features postdate the impact event, and so are likely volcanic in origin (Whitten and Head 2015). An impact melt origin is unlikely for smooth patches in the south and west, which are more than one basin radius from Rembrandt and so are less likely to be ejected impact melt (section 4.2.2). However, impact

modelling is needed to check this for an impact on the scale of Rembrandt. Murchie *et al.* (2015) identified Smooth Plains with a wide range of reflectancies (0.06 – 0.08 at 0.75 μm) during mapping of spectral units, suggesting a low correlation between plains units and spectral characteristics. Hynek *et al.* (2017) split the plains into "Intercrater high albedo plains" and "Intercrater low albedo plains". These are probably Smooth Plains with different albedos. My morphometry map did not split these Smooth Plains by albedo as there are a wide range of albedos for the Smooth Plains within the quadrangle away from Rembrandt.

4.3.2.4 Comparison to Caloris

As noted already, no equivalent to the hummocky material inside Rembrandt occurs in Caloris. Smooth Plains cover the whole floor of Caloris and most of the floor of Rembrandt. These plains postdate the impact events (Trask and Guest 1975, Head *et al* 2009, Fassett *et al* 2009, Watters *et al* 2009a, Whitten *et al* 2014b). Both basins have several large blocks inside them, rising out of the Smooth Plains as inliers (Mancinelli *et al* 2016).

Caloris Montes is similar to the Rembrandt Rim unit: both are large blocks that make up the rim, and both units likely have a similar origin: as the remains of the rim and edge of the transient cavity. Maps after Mariner 10 and MESSENGER both show Caloris Montes unit, but Mancinelli *et al.* (2016) group it in with the "Caloris Rough Ejecta Unit", which groups most of the previously mapped units exterior to Caloris together except for the Odin formation (see below).

The Van Eyck formation is the name for a lineated terrain around the edge of Caloris (Trask and Guest 1975, Fassett *et al* 2009), which is similar to Rembrandt Lineated Ejecta and interpreted result from scouring and secondaries from the impact event. The Van Eyck formation is less continuous than the equivalent at Rembrandt and is seen on the periphery of Caloris more than its equivalent at Rembrandt, where it forms a continuum with the rim unit; this difference may be due to lower impact energies at Rembrandt (due to the smaller scale of the impact) moving the ejecta shorter distances.

The Nervo formation is a section of rolling hills, patches of plains and impact ejecta at Caloris, whose equivalent is the Rembrandt Ejecta unit (Trask and Guest 1975, Fassett *et al* 2009). It is not very continuous at Caloris and is found within 20% of a radius from Caloris' rim. In comparison, the Rembrandt Ejecta unit extends up to 60% of a basin radius from the rim; the reason for this difference is unclear.

The most significant difference between Caloris and Rembrandt is the contrasting morphology of their knobs. Caloris's Odin formation contains lots of low, closely spaced hills called "knobs". These are thought to be ejecta blocks that are then degraded by volatile loss linked to space weathering (Wright *et al* 2020). While there are some ejecta bocks seen in the Rembrandt ejecta unit and the lineated unit, they do not form the same cone shape seen in Caloris's Odin formation. The lack of conical knobs at Rembrandt may be due to more impact melt protecting features from volatile loss. Ejecta blocks may not form knobs if they lack volatiles, and the Rembrandt impact event may have excavated material from a shallower depth than Caloris, probably 12 km depth and still within the crust, compared to Caloris, which may well have ejected mantle (Ernst *et al* 2015). Hence, the lack of knobs in the Rembrandt ejecta unit and the lineated unit could be related to the relative lack of volatiles compared to the Caloris ejecta units.

4.4 Tectonic History

The tectonic history of the Debussy quadrangle is dominated by compressional tectonics (Figure 4.25, Figure 4.26). The most striking (due to scale and complexity) tectonic feature within the quadrangle is Borobudur Fossae, in the Rembrandt impact basin (Figure 4.26). The Enterprise-Belgica Valley (EBV) is a broad wavelength topographic valley between Enterprise and Belgica Rupēs (Figure 4.26). The EBV is not a clear morphological feature but a key part of the tectonic evolution of the quadrangle. I start by looking at the general structures I mapped in the quadrangle away from Rembrandt before looking at Rembrandt itself. Finally, I discuss the EBV.

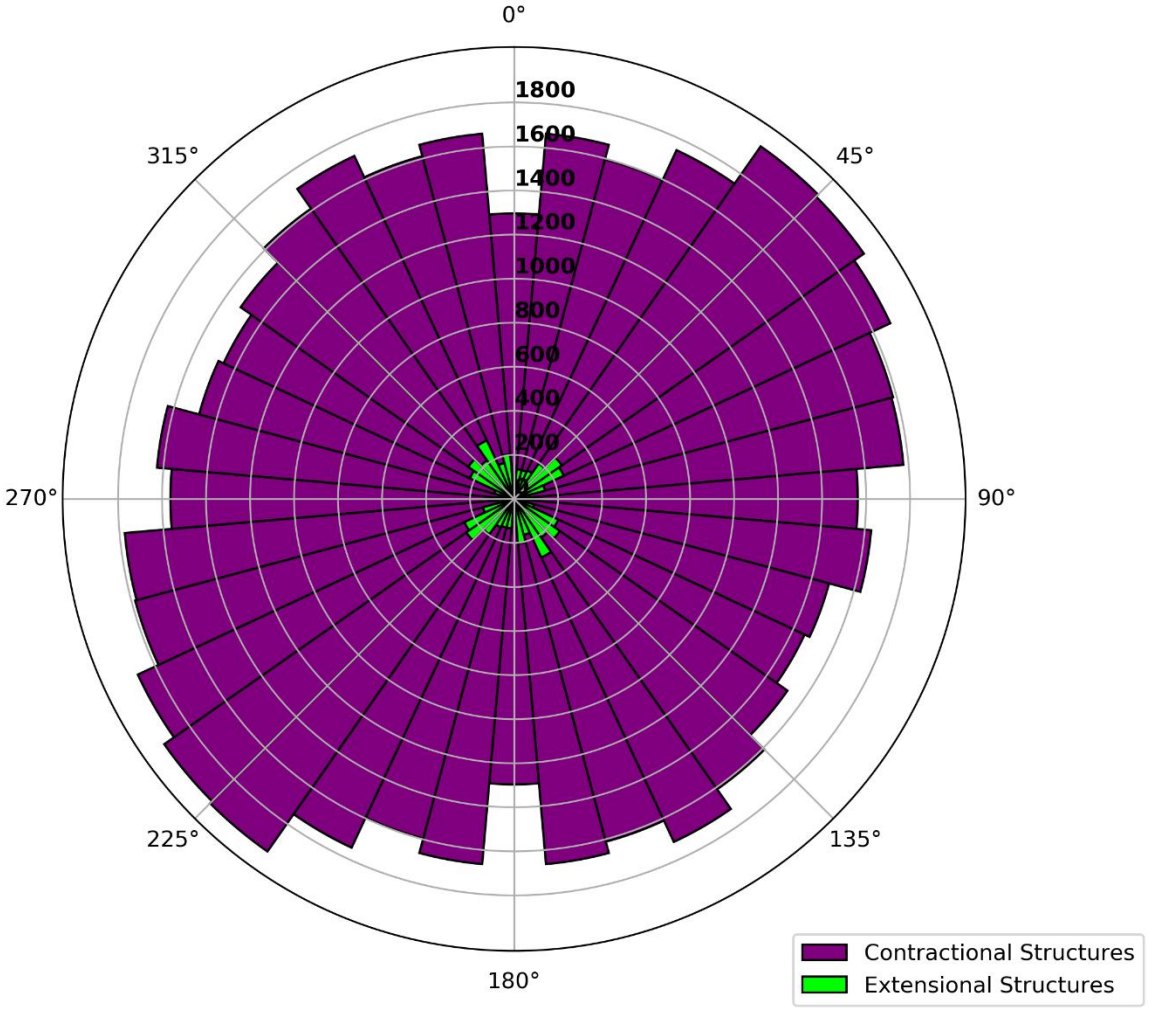

Figure 4.25 Rose diagram of structures mapped in H-14 split into contractional and extensional structures. Strike of features is in 10° bins; the radius of each bin is total kilometres in that orientation.

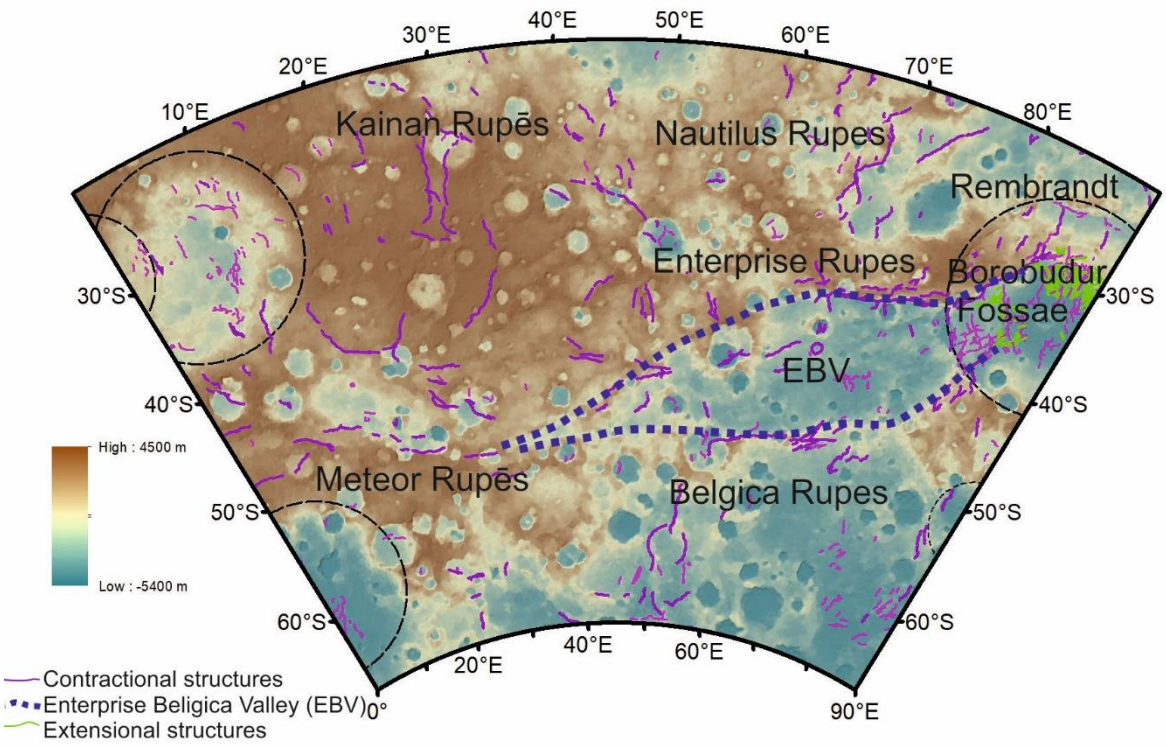

Figure 4.26 Tectonic structures in H-14, contractional structures in pink, extensional structures green. Confident impact basins black, and the Enterprise - Belgica Rupēs valley (EBV) in the dotted purple line. Basemap is a global DEM (Becker *et al* 2016)*; for confident basins, see section 4.2.3.*

4.4.1 Compressional Tectonics

There are two main types of compressional structure mapped: lobate scarps, which have a total length of 14,163 km within the quadrangle, and wrinkle ridges with a length of 8,126 km.

The lobate scarps are the most prominent tectonic features on the map. Because of their asymmetrical ridge form, they are interpreted to be the surface expression of thrust faults (Chapter 2.7.1, Strom *et al*., 1975; Watters *et al*., 2009c). During the mapping process, I successfully applied to the IAU to name Meteor Rupēs (named after a German research vessel) and Kainan Rupes (named after the Kainan Maru, the boat that carried the first Japanese expedition to Antarctica), to add to those already named in the quadrangle: Enterprise, Belgica and Nautilus. Most of these Rupēs are thrust faults, except for Belgica Rupes, which contains a small strike-slip component (Section 4.4.1.3). There are other lobate scarps on the map, but they are shorter features that do not yet merit naming.

Precise dating would require buffered crater counting, e.g. (Giacomini *et al* 2020). I can give approximate timing for when fault activity occurred based on their relationships with craters. If a crater is deformed, then the scarp must have been active after it formed. If the impact crater is on top of the scarp and shows no deformation, then the scarp was no longer active when the impact occurred.

4.4.1.1 Nautilus Rupes

The 390 km long Nautilus Rupes in the northeast of the quadrangle cuts through a c3 crater. While the cross-cutting relationship cannot be used to identify the start of activity at the fault (as the impact event would have destroyed any existing structure at the impact site), I can say that it was active either during or after the Calorian (Figure 4.27). Unfortunately, this crater is cut by two separate lobate scarps, so there may be a slight rotation of the footwall block that makes it challenging to apply to methods of Galluzzi *et al.* (2015) to calculate the amount of fault displacement. Nautilus Rupes cuts Intercrater Plains and Intermediate Plains. Still, several patches of Smooth Plains abut it in the north, suggesting these segments of scarps may have mostly formed by the mid-Calorian.

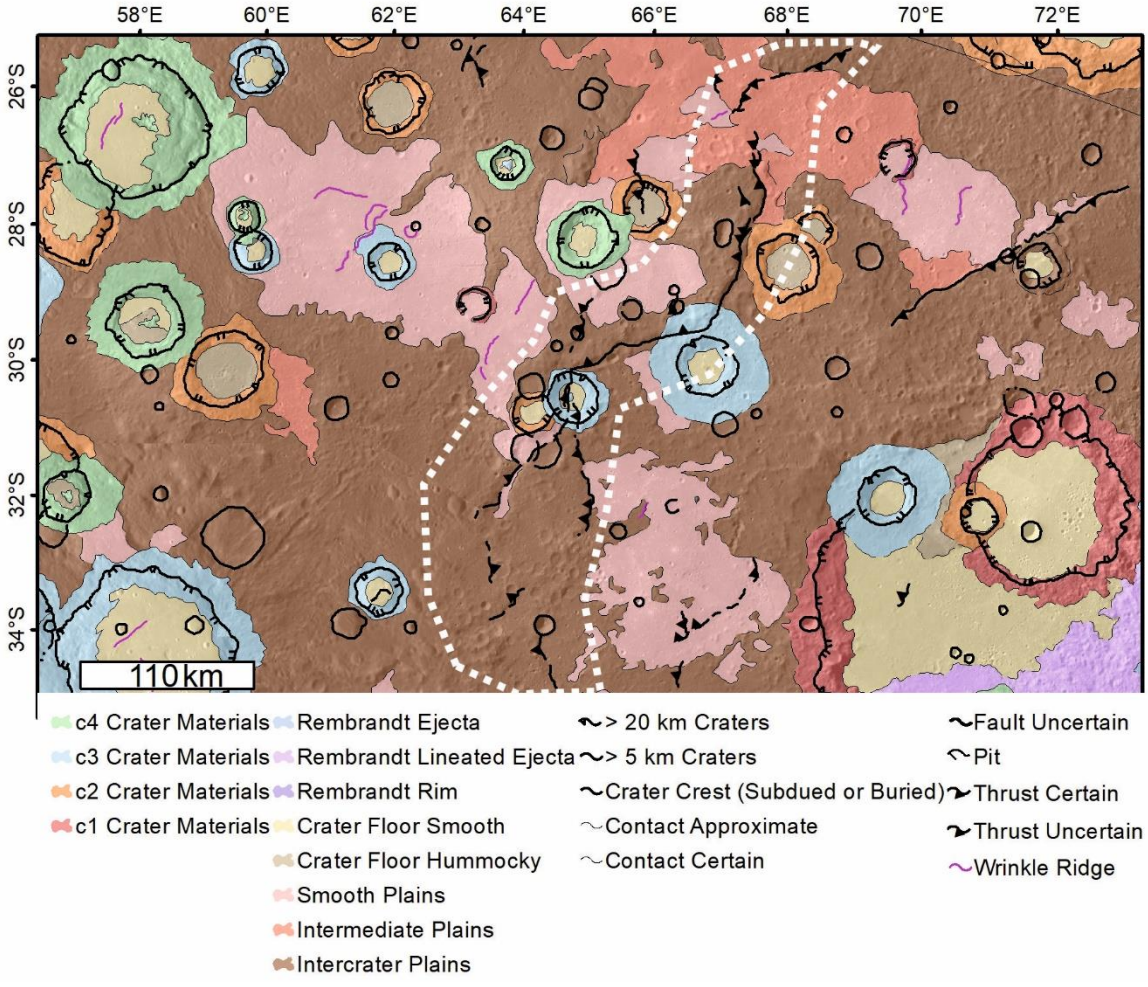

Figure 4.27 Geomorphic map centred on Nautilus Rupes with BDR basemap underneath white dotted line outlines the structure.

4.4.1.2 Meteor Rupēs

Meteor Rupēs is a collection of scarps verging towards the north on the western edge of the quadrangle, Their combined strike is 990 km, and they trend east-west, turning towards the northwest at the western edge of the quadrangle. They cut across c1 and c2 craters, though a c2 crater overprints a northern segment.

Several c3 and c4 craters overprint the eastern strike extension showing variable timing of activity along the fault. This collection of scarps is notable because of the number of pyroclastic deposits associated with it (see section 4.6).

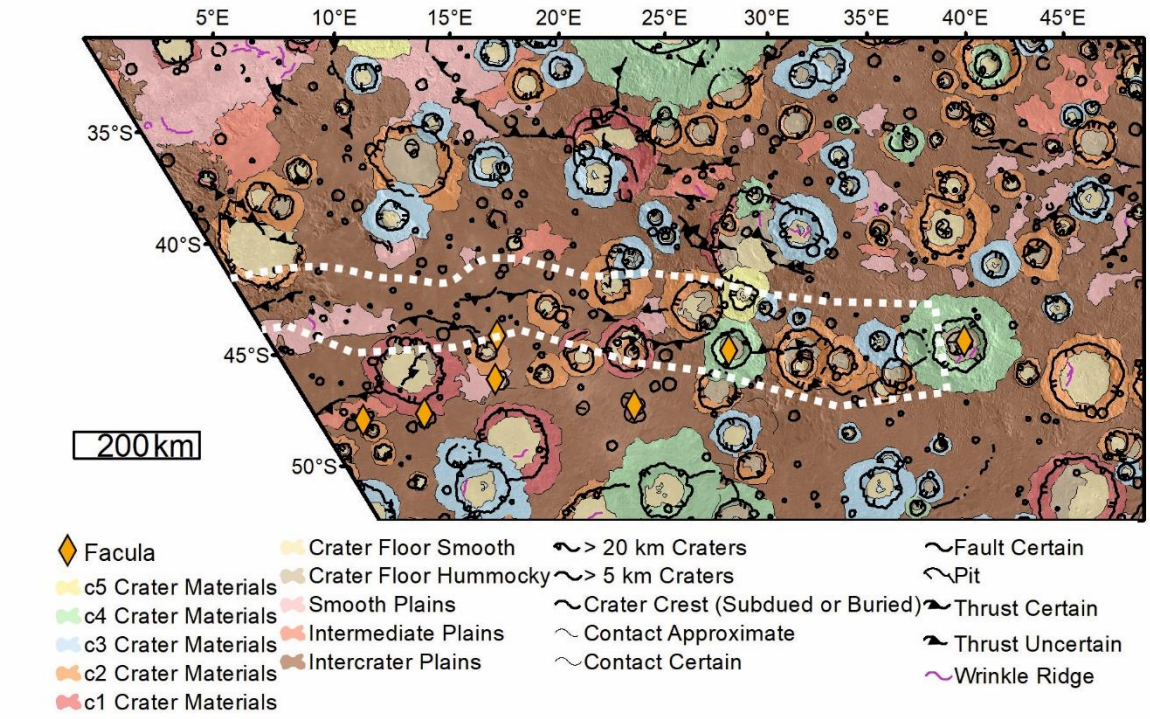

Figure 4.28 Geomorphic map showing the location of Meteor Rupēs on the western edge of the quadrangle. The white dotted line outlines the structure.

4.4.1.3 Enterprise Rupes

Enterprise Rupes is the longest lobate scarp on Mercury (Ruiz *et al* 2012). I measure it to be 950 km long. It has a significant kink in its structure: outside of the Rembrandt basin, it runs east-west, inside the basin it turns towards the north-east. The scarp cuts across some c3 class craters (Figure 4.29) suggesting that it was active during/after the Calorian. This age range is supported by it cutting across Rembrandt Smooth Plains, which are also Calorian (Section 4.3.1.1). This matches with buffered crater counting completed on Enterprise Rupes that shows it dates from between 3.8 Ga to as recently as 950 Ma ± 200 Ma (Giacomini *et al* 2020).

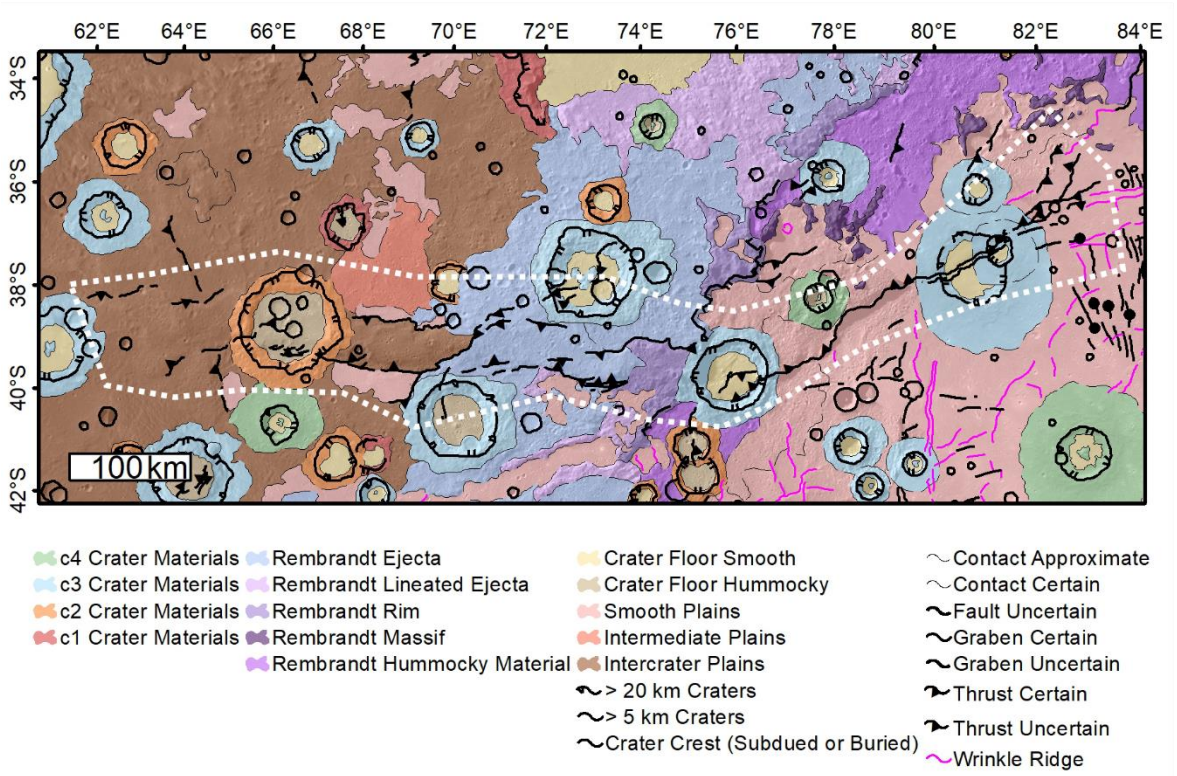

Figure 4.29 Geomorphic map indicating Enterprise Rupes. The white dotted line outlines the structure.

Enterprise Rupes is an unusual lobate scarp; for much of its length outside of Rembrandt, it forms a plateau with scarps on both sides. The south scarp is more prominent and is the direction the fault is verging towards, and the north side scarp dies out as it heads into Rembrandt. Unfortunately, Karsh crater superposes and obliterates this feature making it impossible to study its termination. If Enterprise Rupes had been seen by Mariner 10, it would have been classified as a high relief ridge due to the 80 km wide broad rise at its top (Spudis and Guest 1988, Strom *et al* 1975, Dzurisin 1978). High relief ridges are now considered part of the geometry of lobate scarps and contractional tectonics on Mercury (Klimczak *et al* 2015). The two scarps suggest opposing faults with one a back thrust to the main thrust (Figure 4.30). The weaker north scarp is less continuous and so likely the antithetic scarp to the prominent southern scarp. Reversals of vergence occur in thrust landforms on both Mars and on Earth, where it is caused by complexities generated by antithetic faults, often linked to a décollement (Crane and Klimczak 2019). Galluzzi *et al.* (2015) used three craters to measure the dip of Enterprise Rupes, finding that it ranges from 15° in the east within Rembrandt to 57°in the west. Horizontal displacement is estimated to be 3-4 km.

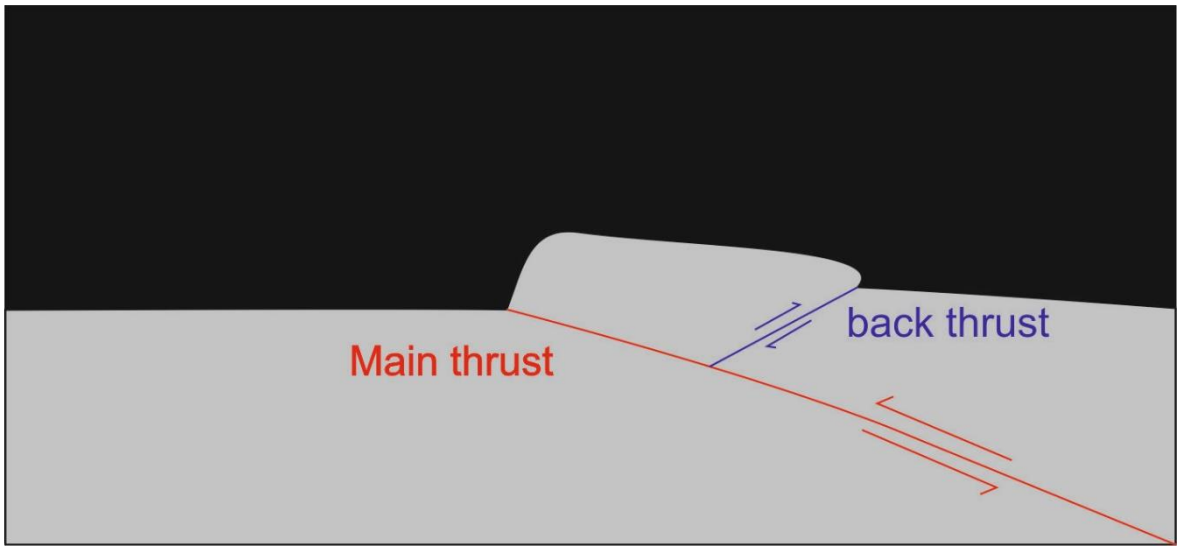

Figure 4.30 Cross-sectional diagram of a back thrust. Authors own schematic. Where Enterprise Rupes enters the Rembrandt basin, influence from the basin architecture becomes expressed, and the fault deflects towards the north. Although Ferrari et al. *(2015) suggest that Enterprise Rupes could have been active before the Rembrandt impact event, the large scale deflection of its strike shows it likely formed after* (Watters *et al* 2016b).

Enterprise Rupes' eastern termination is within the Rembrandt impact basin. Wrinkle ridges replace the lobate scarp as it diminishes in scale. The transition between lobate scarps and wrinkle ridges lends further credence to the idea that wrinkle ridges and lobate scarps are end members on a spectrum of compressional features. Wrinkle ridges are probably a manifestation of contractional structures in areas of thin-skinned tectonics; the faults get steeper and thinner due to the layered nature of the Smooth Plains (Watters *et al* 2015, Byrne *et al* 2014, Peterson *et al* 2019, Byrne *et al* 2018a, Crane and Klimczak 2019). The western termination of Enterprise Rupes is much more gradual; the plateau widens, and the scarp becomes less pronounced until it merges into the plains.

4.4.1.4 Belgica Rupes

Belgica Rupes is 770 km long, according to my mapping, and runs sub-parallel to Enterprise Rupes. It verges mostly towards the north but switches vergence direction east of 66°E, where it forms a complex splay. The scarp cuts across a c2 crater showing it has been active after the Tolstojan (Figure 4.31).

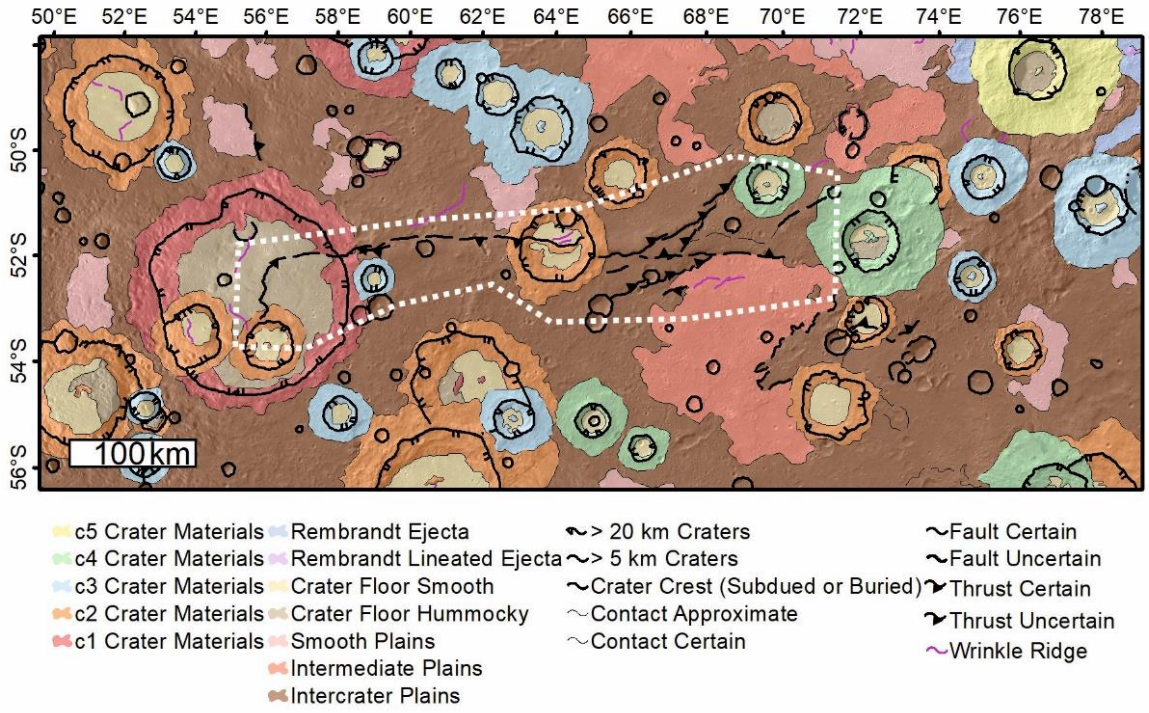

Figure 4.31 Geomorphic map of Belgica Rupes on BDR basemap. The white dotted line outlines the structure.

The termination of Belgica in the west occurs inside a c1 crater named Carleton. The fault turns sharply from east-west to north-south. The north-south section expresses a series of angular steps in plan-view, suggesting that this section of the fault is dominated by a strike-slip component, as the eastern portion moves northward over the main thrust surface. This sense of movement suggests that most of these steps must be releasing bends (Figure 4.32).

The eastern termination of the fault splays off into a sequence of faults. Ferrari *et al.* (2015) interpreted this fault as continuing into the Rembrandt impact basin. I cannot see a continuity of the structure at the surface over the 400 km to the basin, but within the Rembrandt basin, there are wrinkle ridges that follow the same strike as Belgica, so the structure may continue at depth into Rembrandt, likely linked to the EBV, which also continues through the area (Section 4.4.3).

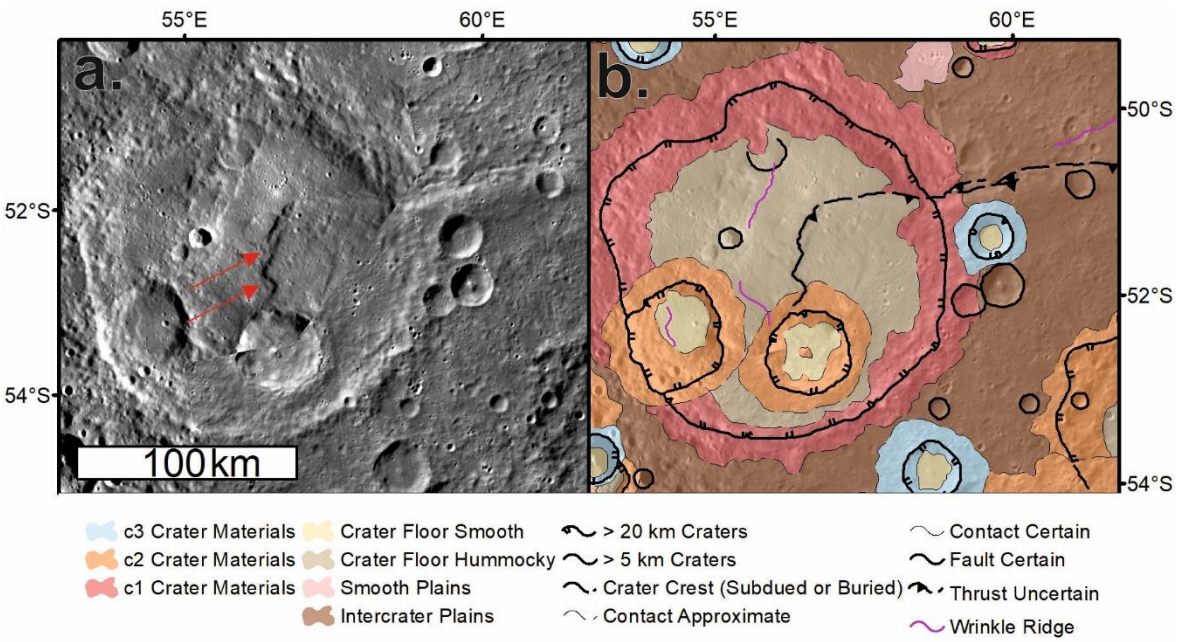

Figure 4.32 Close up of western termination of Belgica Rupes. a. The BDR basemap (Denevi *et al* 2018a) *with red arrows pointing to releasing bends. B. Geomorphic map showing the interpreted location of the scarp.*

4.4.1.5 Kainan Rupēs

Kainan Rupēs comprises of two parallel thrust faults running north-south, verging towards each other. At the north and south ends of these thrusts, there is an east-west trending fault bounding a rectangular block of faulted terrain. These faults cut through the highly degraded c1 Travers cater (a name I suggested to the IAU, referencing the Australian author Pamela Lyndon Travers). The western scarp cuts through c2 crater ejecta (though because the ejecta is draped over the landscape, the ejecta cannot be used for relative timing) and through Smooth Plains. The southern scarp cuts through a c3 crater and the western fault cuts through Smooth Plains showing it was active after their emplacement (probably in the Calorian).

Between the four faults is a block of crust that has been thrust to the south forming an unusual valley. Kainan Rupēs appears to be a much smaller version of the Enterprise-Belgica Rupes system. However, there is no lateral movement apparent between Enterprise and Belgica Rupes, as is apparent from the two south verging faults at Kainan Rupēs.

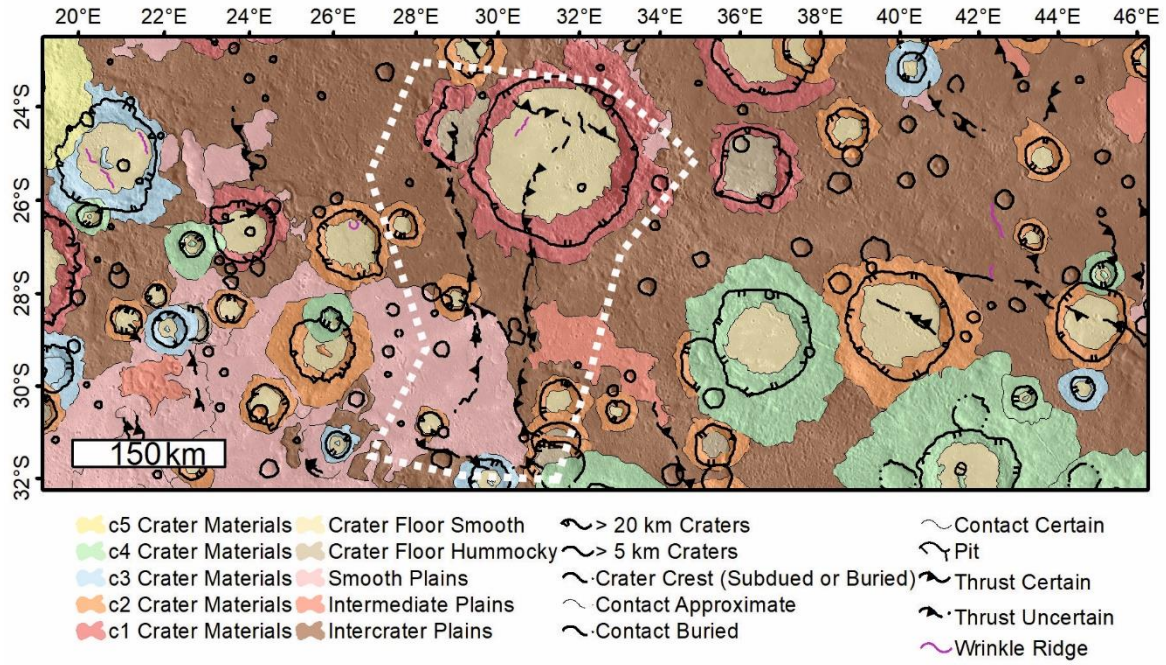

Figure 4.33 Geomorphic map showing Kainan Rupes. The white dotted line outlines the structure.

4.4.1.6 Unnamed example

The only other scarp of note within the quadrangle is in the south, where a lobate scarp traces the rim of a crater filled with Smooth Plains (Figure 4.34). The lobate scarp has probably utilised the weak regolith layer between the original crater floor and the overlying lava flow, causing the scarp to outline the rim (Fegan *et al* 2017). This feature could only form if the lobate scarp was active after the lava flow buried the crater.

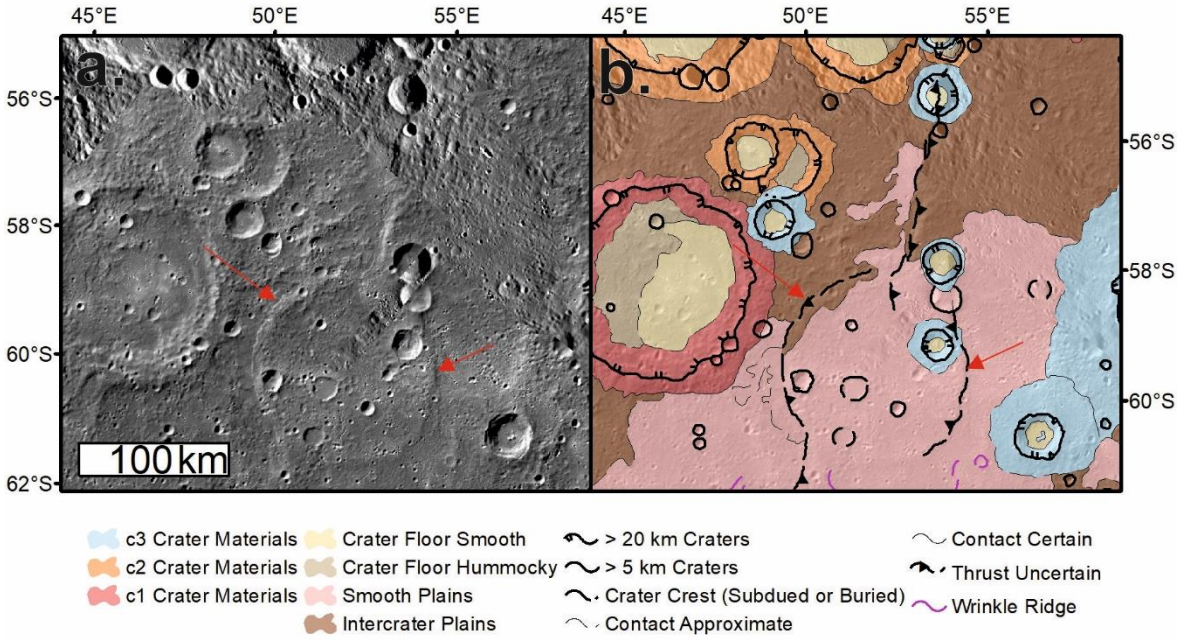

Figure 4.34 Lobate scarp highlighting crater in the south of quadrangle (red arrows). a. BDR basemap, b. geomorphic map.

4.4.1.7 Lobate scarp origins and timings

The lobate scarps are the surface manifestation of thrust faults accommodating global contraction (Strom *et al* 1975). They are similar to smaller structures seen on the Moon and Mars (Watters and Nimmo 2010). They are compared to parts of Rocky Mountain foreland thrust in geometry (Watters *et al* 1998, Watters and Nimmo 2010). However, as shown by Enterprise, Meteor and Kainen Rupēs, lobate scarp systems are complex with back thrusts and reversals in vergence (Watters *et al* 2009a, Ferrari *et al* 2015), making the single thrust plane model an oversimplification of subsurface fault geometry

The cross-cutting relationships with impact craters and volcanic plains show Nautilus, Enterprise, Meteor, and Kainan Rupēs were active during and/or after the Calorian (c3). Belgica cuts across only a c2 crater, so I cannot demonstrate that it was active after the Tolstojan. The Banks *et al.* (2015) global study of lobate scarps showed that they cross-cut craters from the Pre-Tolstojan up to the Kuiperian, with 85% of scarps deforming Calorian craters where they intersect, as did most of my examples. Only 25% of scarps deform Mansurian craters if they intersect, but none of the scarps I have mapped interact with Mansurian craters except with the ejecta, where the relationship is not clear.

Small scarps 10s of meters in scale (Watters *et al* 2016a), and scarps cross-cutting <3 km craters, which should be relatively young (Banks *et al.*, 2015), suggests the surface of Mercury is likely still currently active, although I found no evidence of this in my mapping.

4.4.1.8 Structure Orientations

There is a wide range of structural orientations within the quadrangle (Figure 4.35 a). Removing the interior of Rembrandt (which will be affected by Borobudur Fossae's circular and radial nature), there is an east-west trend to the structures (Figure 4.35 b).

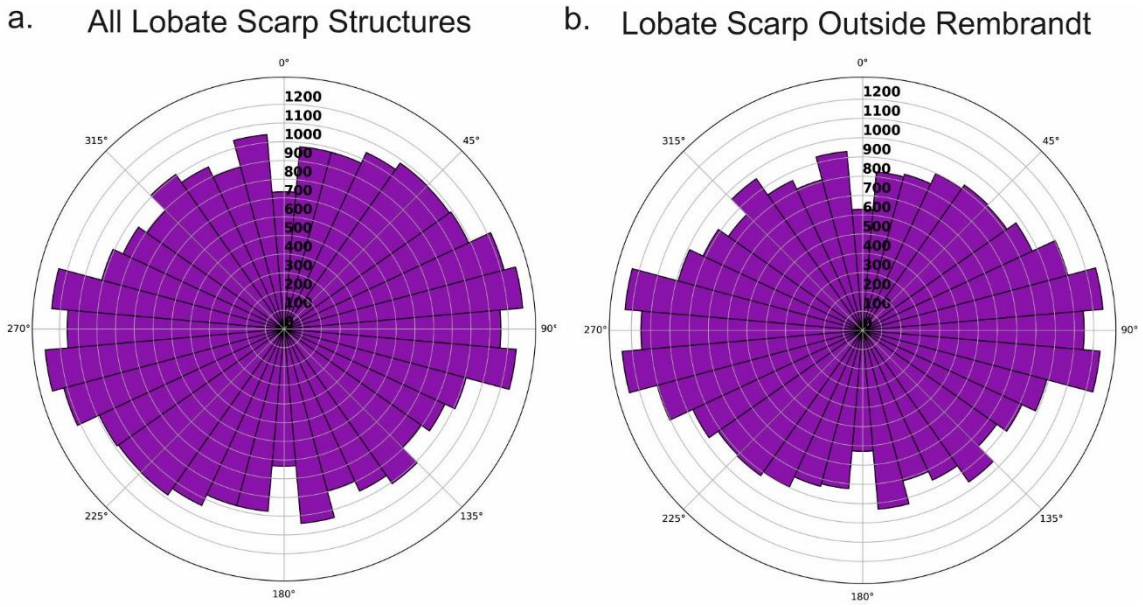

Figure 4.35 Rose diagrams of lobate scarps in quadrangle showing total strike lengths in kilometres for each orientation in 10° bins: a. all lobate scarps, b. lobate scarps excluding those within Rembrandt.

It is not surprising that there is such an east-west trend, given the trends of Enterprise (outside of Rembrandt) Belgica and, to a lesser extent, Meteor Rupēs. These east-west structures likely relate to the EBV (section 4.4.3). This is in contrast to the average global situation, where structures have a preferential north-south alignment (Byrne *et al* 2014, Watters *et al* 1998, 2009c), especially at mid and low latitudes.

In the Victoria quadrangle, the lobate scarps follow the edge of the High Magnesium Region (Galluzzi *et al* 2019), attributed to the regional strain accumulated around the edge of this relatively rigid lithospheric block and leading to localised lobate scarps around it. MESSENGER did not provide elemental abundance data covering H-14 of sufficiently high spatial resolution to indicate whether any of the faults bound a geochemical terrain, but this is something that BepiColombo should be able to test (Rothery *et al* 2020b).

4.4.1.9 Wrinkle Ridges

Wrinkle ridges are predominantly found within large patches of Smooth Plains, some Intercrater Plains or within crater floors. The highest density of these is within the Rembrandt impact basin. However, the other areas of Smooth Plains also host these structures, including smooth impact crater floors.

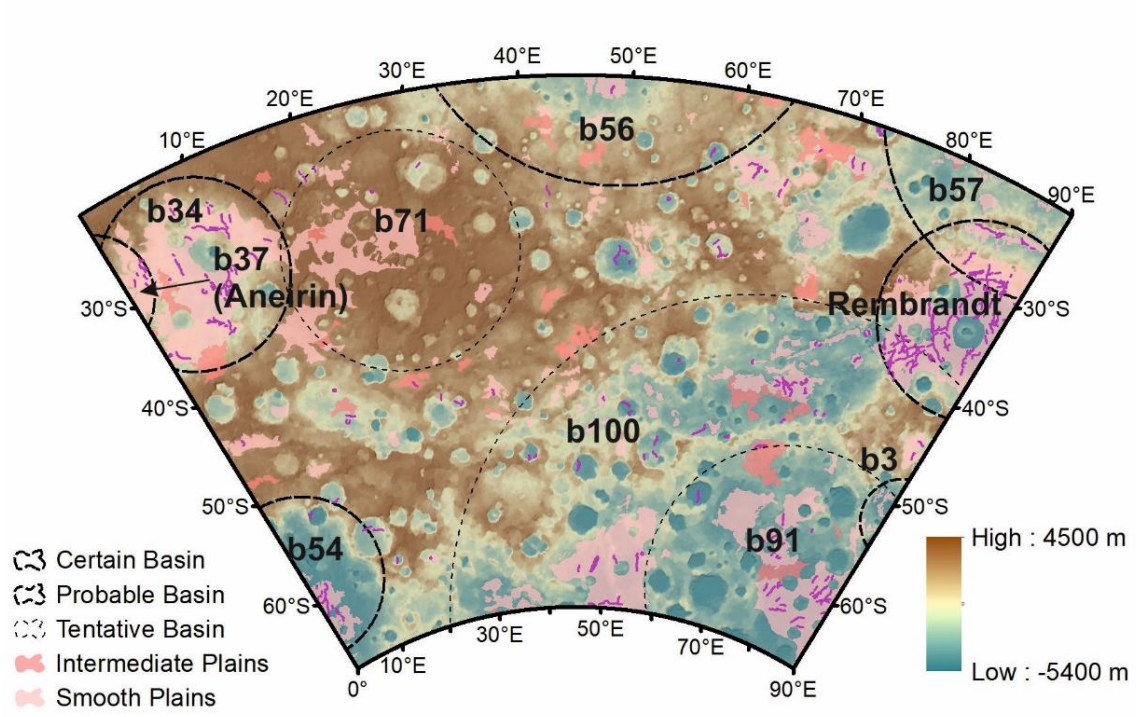

Figure 4.36 Location of Wrinkle ridges (pink line) in H-14 overlain on colour-coded topography and showing the location of Smooth and Intermediate Plains.

The wrinkle ridges all must postdate the Smooth Plains they form in (and so are more recent than the Tolstojan – Calorian). However, I observed no cross-cutting relationships with craters, so I cannot constrain the timing further. Some are linked to lobate scarps, such as those on the end of Enterprise Rupes (Section 4.4.1.3), but many of them have no apparent relationship to lobate scarps.

To study wrinkle ridge orientation, I compiled rose diagrams, one including Rembrandt, expected to be dominated by Borobudur Fossae (and discussed in Section 4.4.2) and one showing the wrinkle ridges outside Rembrandt (Figure 4.37). In both cases, there is a distinct NE-SW trend.

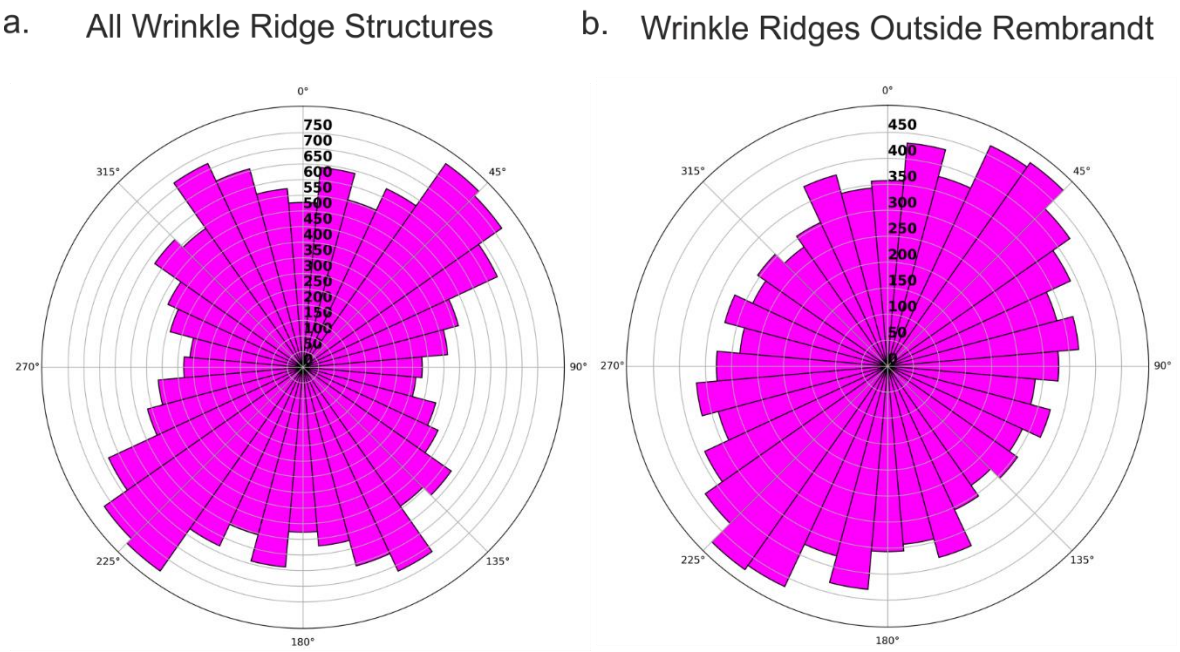

Figure 4.37 Rose diagram showing the strike orientations in 10° bins, where radius represents the total strike in kilometres within that orientation bin. (a) whole quadrangle, (b) whole quadrangle excluding Rembrandt.

The preferred orientation of wrinkle ridges is different from that of the east-west orientation seen in lobate scarps and could be used to argue for a different regional stress regime (and hence possibly a different timing) during the formation of the wrinkle ridges. The stress regime was likely different during the formation of ghost craters, some of which form during cooling of the Smooth Plains (Cruikshank *et al* 1973). Some ghost craters developed during regional stresses utilising the weaker areas of lavas above crater rims (Klimczak *et al* 2012, Watters *et al* 2012); however, they are approximately circular, so ghost craters should not add a directional bias to the rose diagram.

Wrinkle ridges are a lot more subtle than lobate scarps, often only casting very slight shadows, and the average length of segments mapped is 56% of the average length of lobate scarp segments. The lack of diffuse light on Mercury means that east-west trending features produce much less of a shadow than north-south trending features (Figure 4.38). This illumination bias is liable to lead to east-west structures being incompletely recognised (Fegan *et al* 2017), the underrepresentation of east-west wrinkle ridges likely explains the overall trends seen within the quadrangle.

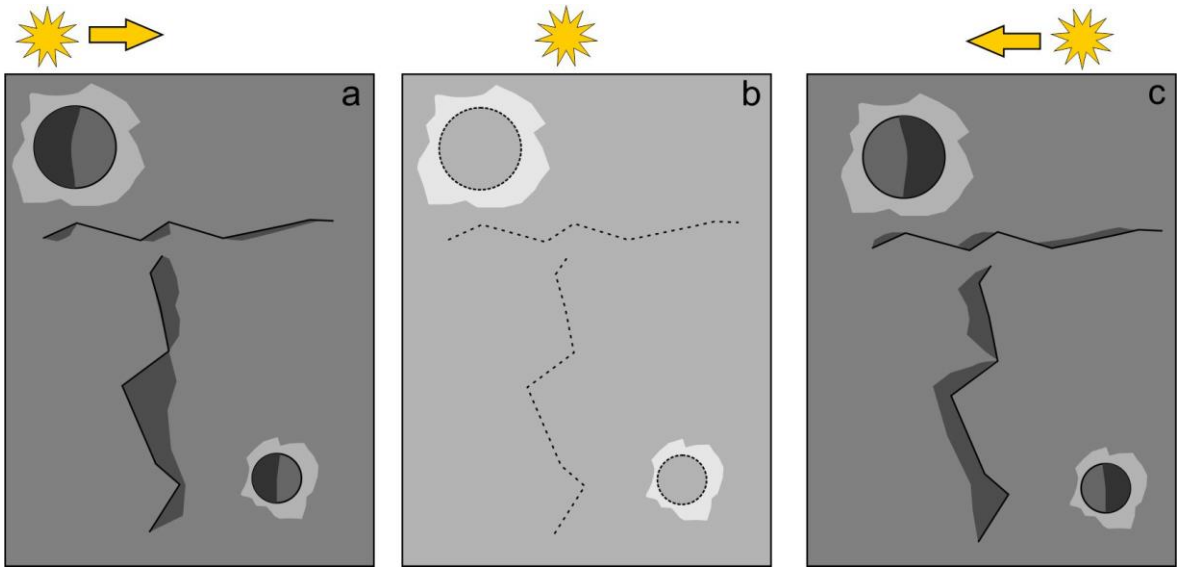

Figure 4.38 Schematic of difference in the shadow between structure orientations based on illumination, a from the west. b. overhead (solar noon) c. from the east. Authors own schematic.

In the Smooth Plains area in the eastern part of Aneirin (b37), the wrinkle ridges run parallel to the edge of the basin. On the basin's western edge (which lies outside the H-14 quadrangle) lobate scarps highlight the edge of Aneirin (Fegan *et al* 2017), the wrinkle ridges are likely the accommodation of strain from the layer on the opposite side of the lobate scarp but manifest within Smooth Plains and so forming steeper but shallower structures (Figure 4.39).

The distribution of wrinkle ridges in b34, b54, and b91 is neither radial nor circular (unlike within Rembrandt). This lack of preferred orientation suggests that the basin structure did not control the strain when the wrinkle ridges formed, but other features, such as other tectonic structures or smaller craters now covered by the lavas. The lack of basin control on wrinkle ridges (excluding Rembrandt) is unsurprising given that the other basins seemed to have occurred well before the emplacement of the Smooth Plains in which the wrinkle ridges form.

Currently, there is no apparent explanation for why the wrinkle ridges outside Rembrandt have a preferred NE-SW orientation and if this is mostly due to illumination bias or not, and it will be interesting to compare to the other quadrangles to see if additional data allow this trend to be explained.

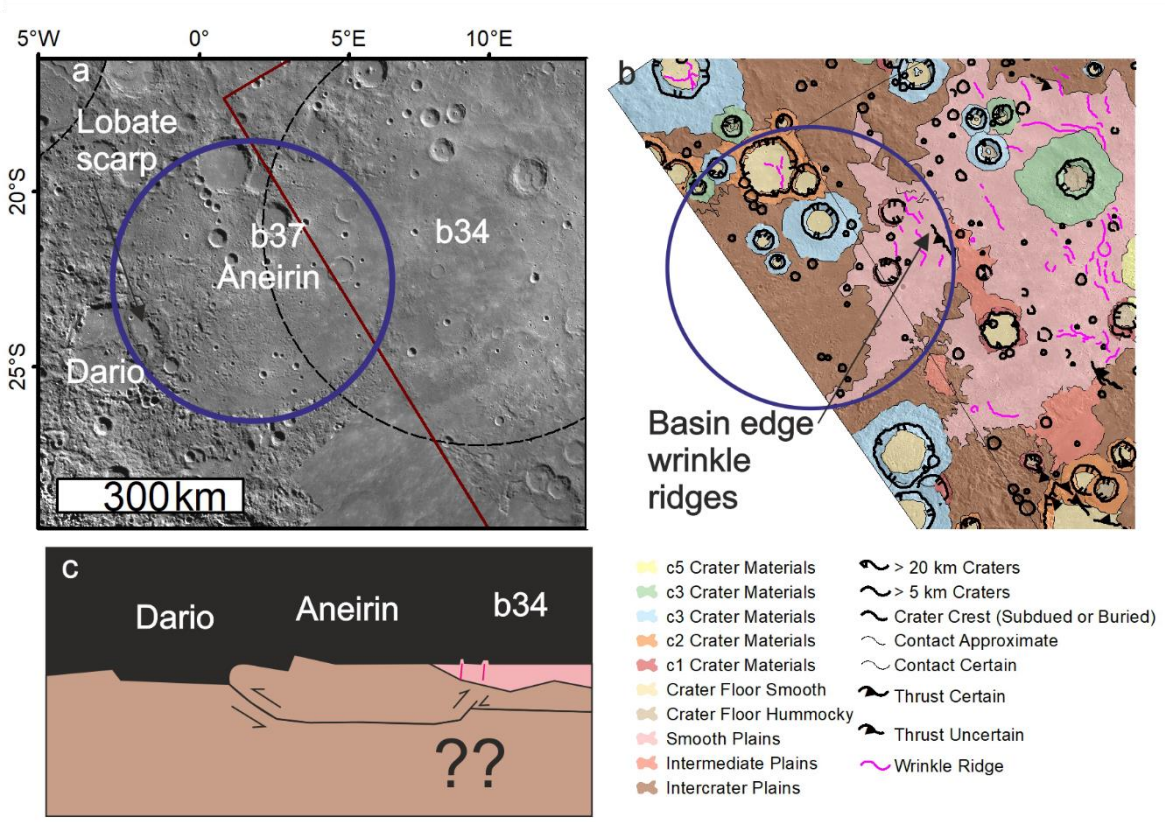

Figure 4.39 a. BDR map (Denevi *et al* 2018a) *of Aneirin (b37) with lobate scarp in Dario, b. morphology map (with 5° overlap beyond the edge of the quadrangle), c. schematic cross-section running west to east showing the location wrinkle ridges in red (vertically exaggerated) and their relation to the other tectonic structures and basins. The intercrater plains are in brown and the Smooth Plains are in pink. Question marks show uncertainty if/how this connects up with other, deeper contractional faults.*

4.4.2 The Rembrandt Impact Basin and Extensional Tectonics

The Rembrandt impact basin is the only location within the quadrangle to contain extensional features. These grabens constitute Borobudur Fossae and have a complex interaction with the contractional wrinkle ridges also found within the basin. Rembrandt also hosts the termination of Enterprise Rupes and contains features along strike from Belgica Rupes and the EBV (Figure 4.40). Here, I examine these structures and consider their interaction.

There are two dominant styles of wrinkle ridge within the basin: radial and concentric. The concentric ridges form a partial circle at approximately 150 km from the centre of the basin. A second, even less continuous circle of ridges occurs 15 km further out from the main ring. The radial ridges radiate away from the approximate geometric centre of the basin; they are best observed in the north and south-west portions of the basin. They are mostly found inside the ring of ridges, although some continue outside. The concentric wrinkle ridges cross-cut the radial wrinkle ridges (Figure 4.41), showing they occurred later.

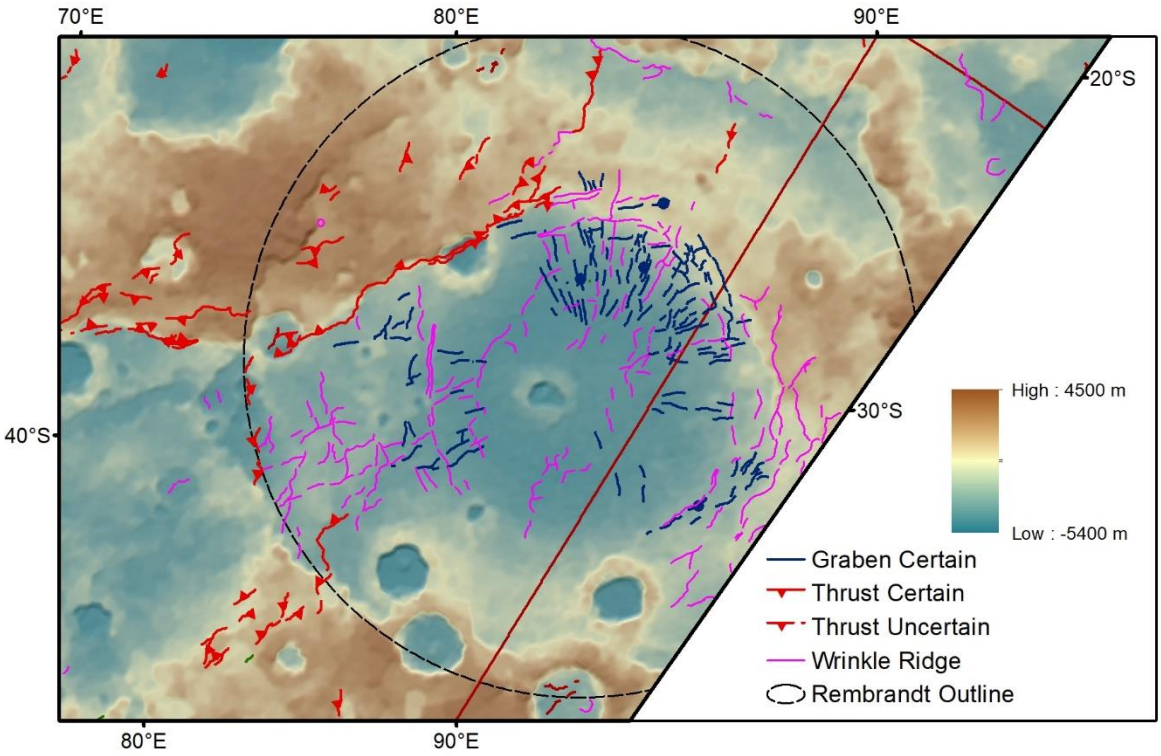

Figure 4.40 Tectonic structures within Rembrandt basin on the colour-coded global DEM (Becker *et al* 2016) *with hillshade.*

In addition to these two main types of wrinkle ridges, a polygonal pattern of ridges is found further out in the basin, predominantly in the south-west (in the region of the EBV (section 4.4.3)and along strike of Belgica Rupes).

The grabens are manifest as narrow valleys in the Smooth Plains portion of the basin floor. Similar to the wrinkle ridges, the grabens are found as both radial and concentric features forming a structure named Borobudur Fossae. They are more concentrated inside the concentric feature than outside. There is a highly complex tectonic history with grabens cross-cutting wrinkle ridges and wrinkle ridges cross-cutting grabens showing multiples phases of deformation (Figure 4.41, Ferrari *et al.*, 2015; Watters *et al.*, 2009a), based on the first images of the basin, suggested that more of the radial and concentric graben cross-cut wrinkle ridges and so contraction pre-dated extension. I disagree with their interpretation and conclude instead that the resolution of images for much of the basin is insufficient to understand the temporal relationship between these structures.

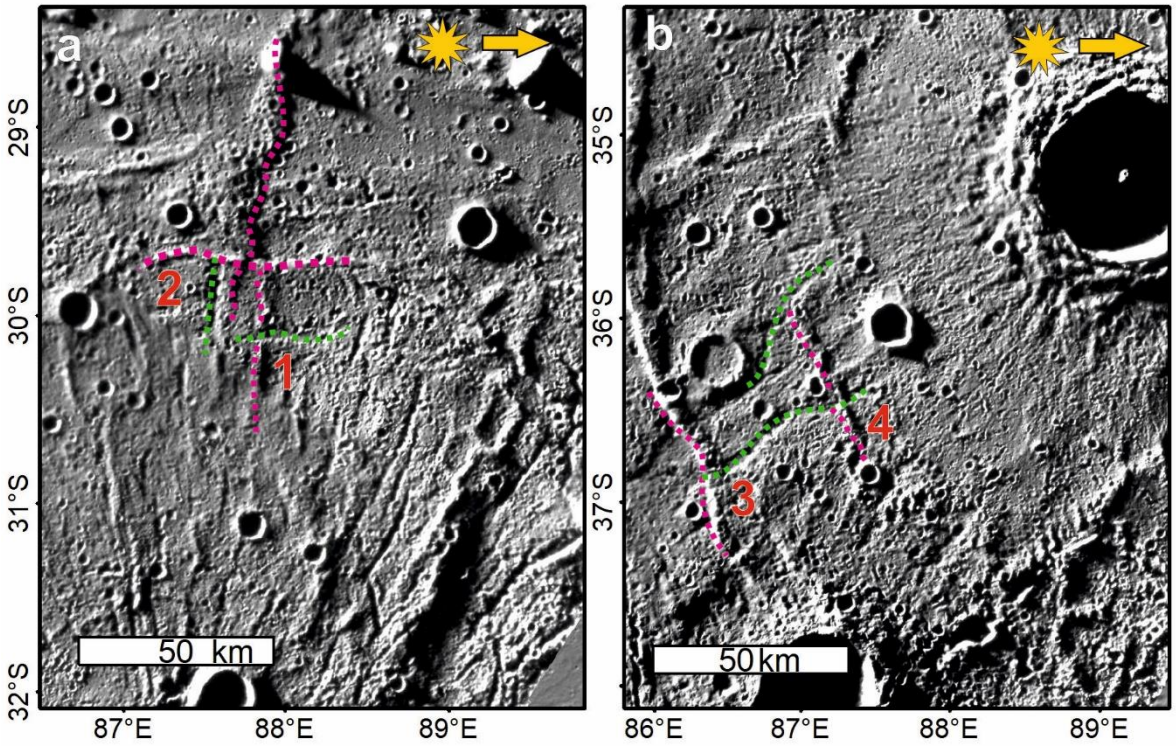

Figure 4.41 Structural relationships between contractional and extensional features within Borobudur Fossae in Rembrandt. Both images use the High incidence west basemaps (Denevi *et al* 2018a). *Green dotted lines are extensional grabens, pink lines contractional wrinkle ridges: a. North West Rembrandt: 1 east-west trending segment of a graben cuts a wrinkle ridge. 2. Concentric wrinkle ridge cross-cuts both a radial graben and a radial wrinkle ridge B. SW within Borobudur Fossae: 3. Concentric wrinkle ridge cross-cuts a graben, 4. The same graben cross-cuts a different concentric wrinkle ridge.*

The concentric grabens are located at the same radial distance as the wrinkle ridges suggesting that they are part of the same structure. These concentric structures occur close to where the topography begins to rise east of the basin (the west is affected by Enterprise Rupes and EBV). The path of Enterprise Rupes gets bent towards the north at the same radius from the basin centre, suggesting a basin structure control rather than just thin-skinned tectonics (which dominate the wrinkle ridges). The wrinkle ridges and grabens that form a circular outline at the same radius as the deflection of Enterprise Rupes suggest they are the surface expression of a crater ring covered by lavas. This ring focuses the stresses that the basin is subject to. A similar feature is thought to control the structures inside Caloris (Oberst *et al* 2010). The presence of radial features inside the ring is similar to what is observed at Pantheon Fossae in the Caloris basin (Klimczak *et al* 2013, Watters *et al* 2009b), though not so highly developed. This is different from Orientale on the Moon, where the structures are focused outside the ring (Watters *et al* 2009a)

Both Pantheon Fossae and Borobudur Fossae have an impact crater close to the centre of the radial pattern of graben. At Pantheon Fossae, Apollodorus crater lies at the centre of the radiating graben and has been suggested as a cause of this pattern (Freed *et al* 2009); however, Klimczak *et al.* (2010) show that the pattern in Caloris is likely due to basin deformation rather than the superposing impact crater. This is corroborated

at Rembrandt by Bellini which is more off centre within Borobudur Fossae than Apollodorus is within Pantheon Fossae and so is even less likely to have caused the structure to form (Figure 4.42).

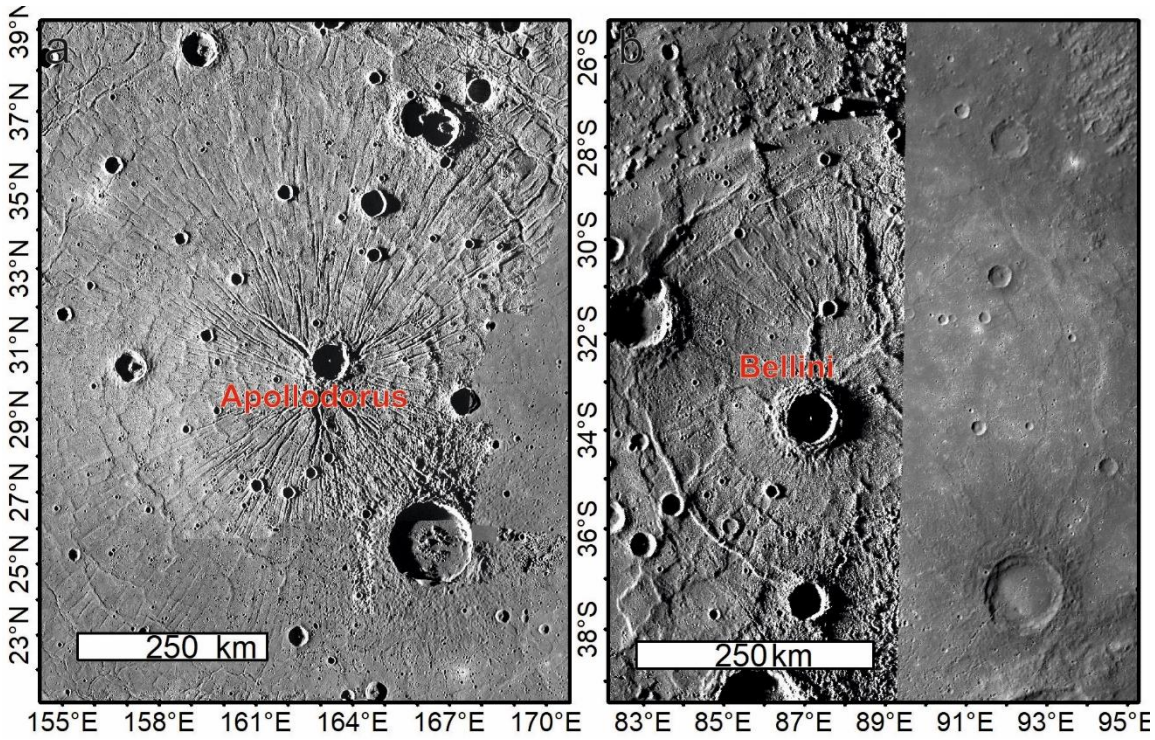

Figure 4.42 The two Fossae on Mercury: a. Pantheon Fossae; a radial set of grabens within the Caloris impact basin, with the location of Apollodorus crater labelled in the centre. Image: 250m basemap (Denevi *et al* 2018a) *b. The Rembrandt Impact basin with Borobudur Fossae as a radiating set of grabens within a ring structure. Bellini crater is labelled. Basemap is the High Illumination West basemap* (Denevi *et al* 2018a).

At least some of the deformation within the Rembrandt impact basin is probably related to the infilling by Smooth Plains and loading associated with that, plus cooling and contraction (generating extension), horizontal pressure from isostasy and crustal thickness differences after the impact (Watters 2008), with the global contraction as an additional factor (Watters 2008).

The emergence of the Rembrandt Hummocky Material towards the NW edge of the basin suggests the nearby Smooth Plains are thin. The lack of grabens continuing in other Smooth Plains outside of the ring is consistent with thinner lavas towards the basin edges, thus reducing the amount of cooling-related contraction and preventing the formation of grabens away from the centre of the basin (Klimczak *et al* 2013). However, the topographic uplift in the basin north of the ring makes it difficult to confirm this.

The interior of Rembrandt may have had multiple phases of Smooth Plains emplacement (Watters *et al* 2009a, Semenzato *et al* 2020), which may have caused multiple phases of contraction and compression associated with loading. For each lava emplacement event, initial compression (caused by the crustal loading with the addition of Smooth Plains) was likely to be followed by extension from cooling (and possible basin uplift due to compensation for crustal loading). Some contractional features are likely linked to both global compression and more localised compression focused around the Enterprise-Belgica-fold fault system. It is noticeable that the Smooth Plains to the north and east of the ring-like structure are topographically higher

than the nearby hummocky ground suggesting that basin uplift continued after the emplacement of the lavas.

The Rose diagram of structural orientations within Rembrandt (Figure 4.43) shows strong NW-SE and SE-NW trends for both extensional and compressional structures. There is a strong correlation between the orientations of extensional and compressional features. The lack of east-west structures, even on a radial structure, suggests that illumination bias may be an issue. However, the NW-SE trend is approximately orthogonal to the large wavelength fold at this point, and the NE-SW trend parallel, suggesting that this structure helped control the wrinkle ridge and graben orientations.

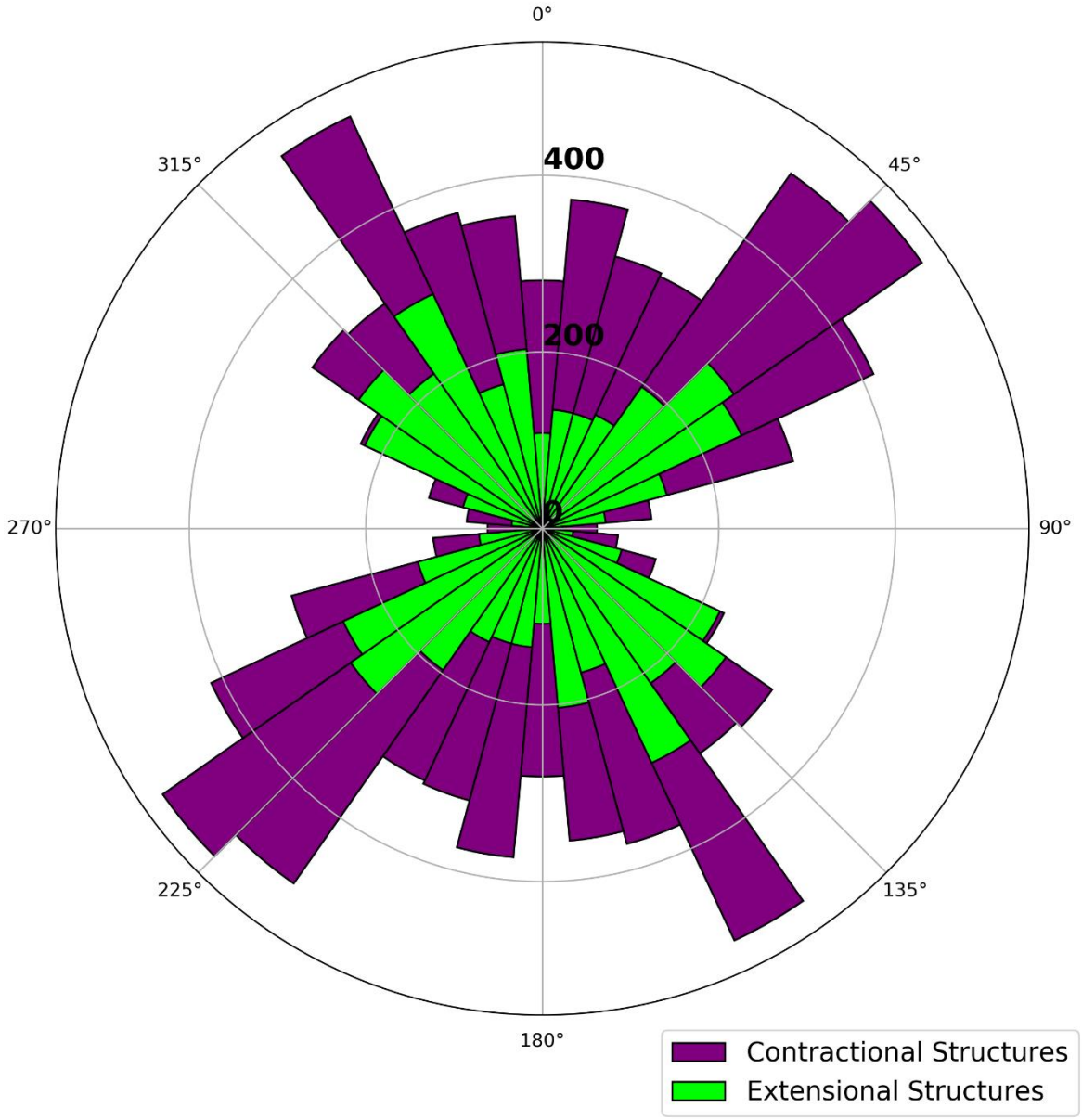

Figure 4.43 Rose diagram of mapped extensional and compressional structures within the Rembrandt impact basin. Radius is strike length (km) grouped in 10° bins.

Rembrandt is a structurally complex basin with multiple stages of extensional and contractional deformation. Rembrandt is the only location in the quadrangle where grabens are present. It would be surprising if none of the other large impact basins developed extensional features. However, the age of these basins means there is little morphological evidence for these basins other than long-wavelength topography, multiple generations of plains, tectonic overprinting as well as cratering and space weathering processes have likely removed evidence of possible past grabens.

4.4.3 The Enterprise-Belgica Valley (EBV)

The EBV valley identified by Watters *et al.* (2016) between Enterprise and Belgica Rupes is not visible in the geomorphic map except for the two lobate scarps, which bound part of the north and south of the valley (Figure 4.26). However, its lateral extent continues further west than the scarps and forms an ellipse shape with a maximum width of 460 km. The valley floor is flat and over 3 km below the surrounding terrains outside of the valley. Originally mapped at 1000 km long (Watters *et al.*, 2016), I suggest it is an up to 1500 km long valley (Figure 4.26). Its western termination pinches in at Meteor Rupēs, and the eastern end is within the Rembrandt basin.

Towards the centre of Rembrandt, the valley structure fades into the basin topography. However, it is apparent in the southwestern portion of the basin which is at a lower elevation and where the basin rim is less distinct. In the SW portion of the basin where the EBV enters, there are fewer grabens and more wrinkle ridges which suggests that less extension occurred in this section of the basin during the formation of Borobudur Fossae. The additional wrinkle ridges suggest the compression that formed the valley was active during the formation of grabens. However, there are issues with illumination angles for this feature which makes interpretation ambiguous. Caloris has a large wavelength fold crossing it, but fault scarps do not bound it (Klimczak *et al* 2013, James *et al* 2015).

The EBV hosts a small section of Smooth Plains units; it is not clear if they are here because of the depression. Both Belgica and Enterprise appear to have similar age (Section 4.4.1.7, Watters *et al.*, 2016). It is likely the valley formed at the same time as the faulting (the Calorian and potentially more recently), as faults bound the structure and so the faults and the valley are likely related; however, it is not possible to date this feature using the crater size-frequency distribution method.

The mechanism for the formation of this fold is unclear. Watters *et al.* (2016b) suggest that the Enterprise and Belgica thrusts are related to the fold, and that they are either crest-localised faults or hinge localised faults. However, this does not explain the relatively flat nature of the valley floor. The origin of the fold bears on Mercury's ongoing global contraction (Watters *et al.*, 2016c). Kay and Dombard (2019) contend that the lithosphere cannot support such a large distortion of the crust, and cooling and contraction alone cannot cause such large wavelength folds, so some form of buoyant support from the interior must be supporting this structure.

4.4.4 Tectonics Summary

Contractional deformation dominates the tectonics of the quadrangle, and the EBV dominates the orientation of contractional structures. While the controls on wrinkle ridge formation outside of Rembrandt (and Aneirin) are not clear, the observed trends in structural orientations suggest that further work is needed to check for Illumination bias and LIDAR profiles could be used in the future to check orientation trends without relying on illumination (Though LIDAR does have its own biases based on the spacecraft's orbit). Rembrandt's interior has a complicated interaction of radial and concentric compressive and contractional features, which reflect both its structure and history of infilling, with multiple stages of compression and extension controlled not only by the basin geometry and plains emplacement but also the EBV.

4.5 Superficial Units

The superficial units are thin and, therefore, likely to be relatively transient features on the surface of Mercury. They represent some of the more recent activity within the quadrangle.

4.5.1 Bright Crater Rays

The most dominant bright crater rays in the quadrangle radiate from Debussy crater, from which the quadrangle gets its name (Figure 4.44). They extend to 1000 km away from their source crater and continue into the adjacent quadrangles to the west and north. Several other smaller patches of bright crater rays exist around small impact craters, some of the craters are below the 20 km limit for classifying, even though the bright crater ray formed by a smaller crater is substantial enough in spatial extent to map. The other c5 craters in the quadrangle have few rays and are all on the cusp between c5 and c4 fitting into c5 due to other definitions such as freshness of internal terracing.

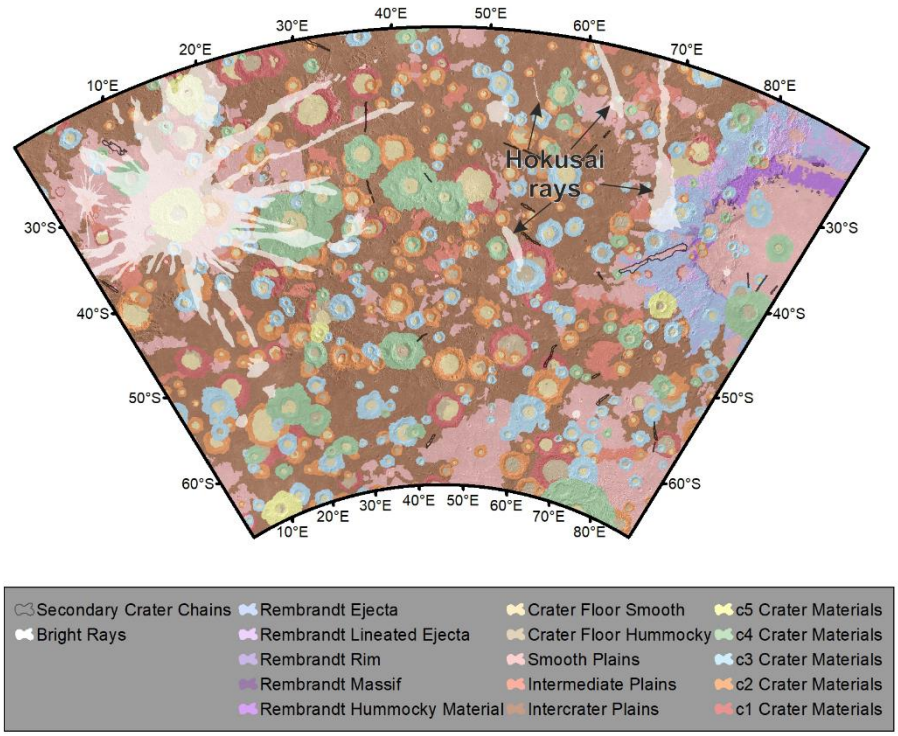

Figure 4.44 Bright crater rays in H-10 shown in white with 35% transparency over the morphology map.

There are three sections of bright crater rays that do not have an originating crater within the quadrangle. They all originate from the NNW, as determined by the direction in which they taper, assuming that the further they travel, the more dispersed they get. The rays originate from the 70 km Hokusai impact crater, located in the Hokusai quadrangle at 75.8°N, 15°E, which likely the youngest large impact crater on Mercury (Xiao *et al* 2016, Ernst *et al* 2018).

Crater rays degrade as they mature until they merge into the underlying older regolith, as a result of space weathering processes, such as radiation and local impact gardening. Mercury's proximity to the Sun (with higher thermal and radiation environment) and higher gravity and impact flux than the Moon means a faster gardening rate (Cintala 1992, Borin *et al* 2009) so that Hermean rays mature very quickly, up to four times quicker than the Moon (Braden and Robinson 2013) which makes them a key indicator for c5 craters (Kinczyk *et al* 2020a)

Secondary crater chains on the map radiate away from nearby craters, usually within 2.5 crater diameters, although some cannot be connected to original craters. One secondary chain that may originate from Rembrandt is 1,000 km away from the basin rim and the furthest feature related to the basin within the quadrangle.

4.5.2 Hollows

There are six hollow clusters on the map (although three occur in the same crater). Five of the clusters are on the walls and floors of c4 craters and one in a c5 crater. Hollows cover a total area of 241 km^2 (Figure 4.45).

While not a significant component of the map, hollow clusters are likely to be the most recent mappable features in the mapping area. There is an overlap in one area with a bright crater ray; however, as both these features are positive albedo features that also cause textural roughness, it is not possible to distinguish relative timing. That hollow clusters are all in c4/c5 craters compares well with our knowledge of hollows as young features on the surface of Mercury thought to be between 50 ky and 1 myr old and linked to recently exposed volatile-rich crust (e.g. Wang *et al.*, 2020). Once hollows stop growing they likely lose their albedo signature, becoming challenging to observe, and weathering process from impacts will rapidly degrade the sharpness and steepness of their edges (Domingue *et al* 2014, Blewett *et al* 2016).

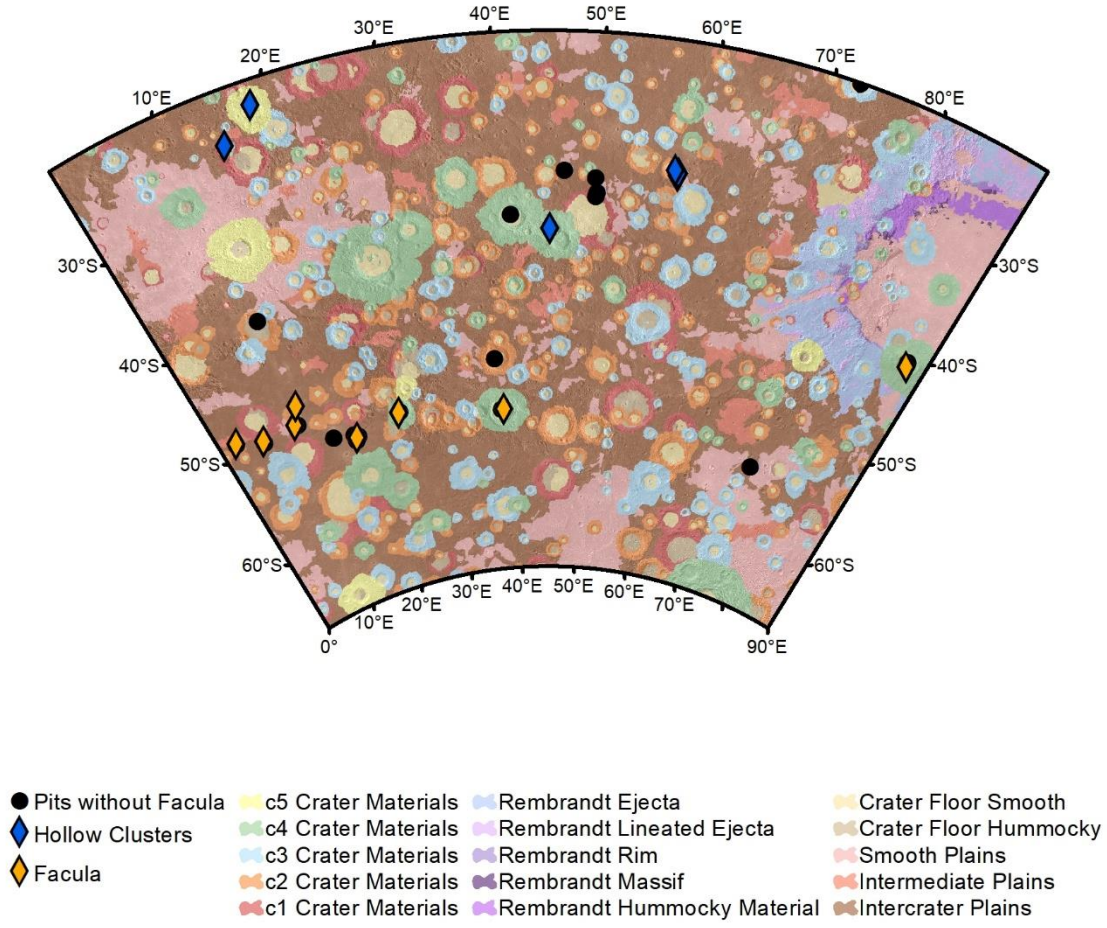

Figure 4.45 Location of hollows, faculae, and pits without faculae on the geomorphic map, with BRD basemap.

4.6 Faculae and Volcanic Vents

H-14 hosts eight faculae (Figure 4.45), which thought to be mostly explosive volcanic ejecta (chapter 2.6.2). The faculae are found predominantly near Meteor Rupes and in Rembrandt. Four out of 11 (36%) are within impact craters, which is significantly lower than the global average of 91% of hosted within craters (Klimczak *et al* 2018). Previous work has suggested that it is impossible on a planetary scale to distinguish from random any association between faculae and tectonic faults (Klimczak *et al* 2018). However, six of the eight vents are within 70 km of the Meteor Rupes scarp, increasing to seven within 160 km suggesting that, within the

quadrangle, there is a link between vents and this structure. This is not so surprising as proximity between vents and tectonic structures on Mercury is almost inevitable because of the high density of tectonic structures (Klimczak *et al* 2018). The lack of vents in impact craters is surprising, and while the complex nature of Meteor Rupēs may provide more pathways for the ascent of lava, it is not clear why vents are so rare in craters elsewhere in the quadrangle.

Globally vents are most common in Calorian craters (Jozwiak *et al* 2018) though they are also frequent in both Tolstojan and Mansurian craters (Goudge *et al* 2014). For the vents within a crater, it is possible to give an approximate oldest age. There are vents in the c4 craters Castiglione, Donelatis (Gata Facula) and Lennon, showing that explosive activity has been ongoing until geologically relatively recently.

During the mapping process, I mapped the pits that are found within vent sites, differentiating them from impact craters by a lack of circularity and lack of ejecta. I identified nine vent sites that lack a prominent facula. The lack of a facula at a vent is most easily explained by the facula having faded over time, caused by surface weathering processes. Four of the vents without facula are in intercrater plains, or c1-3 craters, consistent with this hypothesis. However, a vent without a facula is found in Lennon which is a c4 crater (and so relatively young to have lost its facula due to space weathering); a better understanding of facula thickness and regolith overturning rates may show if weathering and mixing can account for this, searching the rest of Mercury for further examples of vents without facula in c4 craters would also be of use. The resolution of the images used for mapping meant that I could not gain a better understanding of the vents within this quadrangle, but I further explore the nature of the vents on Mercury in chapter 5.

4.7 A Geological History

From all the different aspects of the map, I am now able to construct a general geological history for the quadrangle. I will use the geological time periods (Spudis and Guest 1988, Banks *et al* 2017, Kinczyk *et al* 2020a) based on crater degradation to give a historical account in five stages.

4.7.1 Pre-Tolstojan

Mercury's first differentiated crust was probably a carbon-rich primary crust. While none of this survives on the surface of the planet, the LRM may be the remains excavated by cratering and so the oldest material visible in the quadrangle (Chapter 2.5.3, section 4.2.2). The carbon crust was covered by subsequent lava flows now making up the Intercrater Plains. That is thought to date to the Pre-Tolstojan and Tolstojan (Whitten *et al* 2014a). The history of igneous intrusion within Mercury's crust is obscure, although Byrne *et al.* (2018) argue that by volume, intrusions are likely to be at least as important as extruded lavas, based on other bodies having significantly larger proportions of intrusions to extruded lava.

The oldest features identifiable within mapped areas are ancient basins; they are manifested only in the DEM (the Rembrandt basin is Calorian age and so not "ancient"). These became heavily modified by subsequent cratering, leaving no morphological trace, suggesting they are older than the c1 craters; however, crustal weaknesses remained to allow for multiple generations of lava effusion.

It is unknown if hollows and explosive volcanic vents were active at the time. Given the volatile nature of young crust rich in C and S (see chapter 2.5.4), which likely drive hollow formation, it is reasonable to suppose that both hollow formation and explosive volcanism have been ongoing throughout Mercury's history.

Tidal despining could have occurred from the Pre-Tolstojan (Melosh and Dzurisin 1978, Klimczak *et al* 2015), so it is likely that associated tectonics were active during the Pre-Tolstojain, the timing of thermal contraction is still uncertain, it may have started during the Pre-Tolstojan (Crane and Klimczak 2017) or it may not have started until the Calorian (Tosi *et al* 2013).

The main features within the quadrangle dating from the Pre-Tolstojan are the Intercrater Plains, the c1 craters, and some tectonic features that cut these craters and the plains may have formed during this time (*Figure 4.46*).

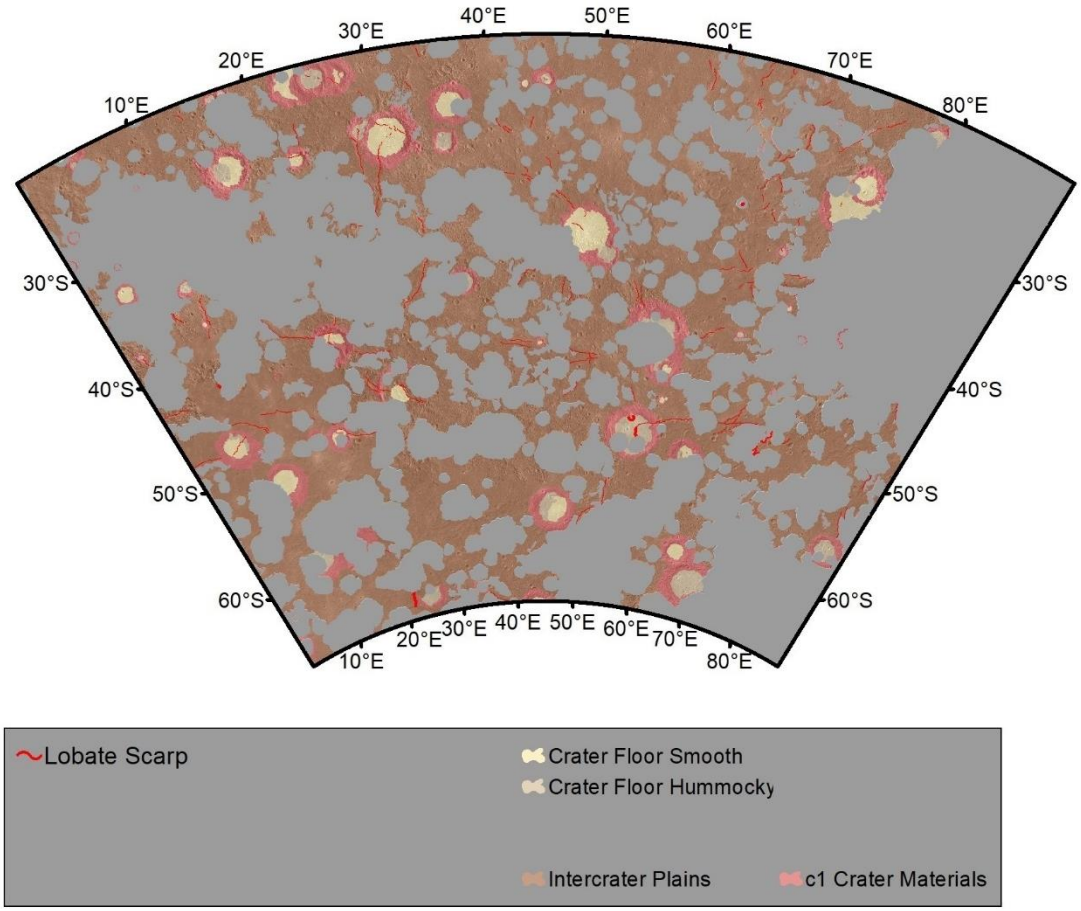

Figure 4.46 Features within the quadrangle from the Pre-Tolstojan, (fault timing uncertain other than post-*dating the formation of craters/ plains during the pre-Tolstojan).*

4.7.2 Tolstojan

Intercrater Plains continued to form during this period, but by the end of the Tolstojan, the last phases of lava flows were the Intermediate Plains, c2 craters formed and superposed c1 craters, c1 crater ejecta is

fading away. Whitten *et al.* (2014) report that the oldest Smooth Plains may have formed during the Tolstojan but their classification of plains does not include Intermediate Plains. (Figure 4.47).

Tectonics are ongoing, with at least Meteor Rupes being active before the end of the Tolstojan (as shown by one segment being overprinted and not deformed), but one segment is inactive. Intercrater Plains are likely emplaced, before Intermediate Plains followed by the oldest Smooth Plains (possibly in the south and west of the quadrangle).

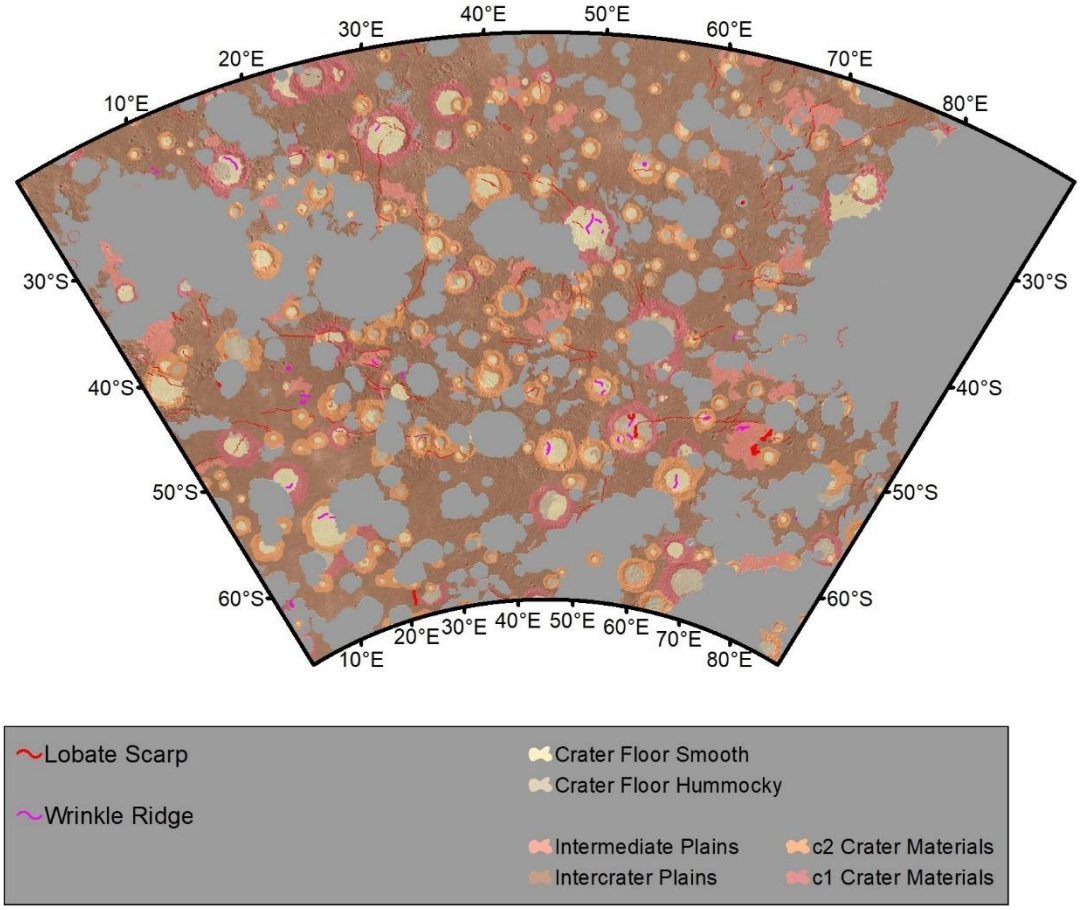

Figure 4.47 Quadrangle map showing features at the end of the Tolstojan period, including emplacement of Intermediate Plains, fault timing uncertain other than the postdating formation of craters/ plains during the Tolstojan.

4.7.3 Calorian

This is arguably the busiest time in quadrangle's history; it may have started with Smooth Plains, or it could have started with the Rembrandt Impact basin (which occurred, within error, at the same time as the Caloris impact), c3 craters formed on the surface during the Calorian (Figure 4.48).

The Rembrandt impact event occurred. During excavation, scouring occurs of the surrounding plains. Blocks and impact melt fall back, creating a hummocky texture with some large blocks forming the Rembrandt Massif and the Rim unit. Lineated ejecta and smooth fluidised ejecta and impact melt cover the surrounding region.

Smooth Plains, including those on the floor of Rembrandt, were emplaced during the Calorian. This leads to the complex tectonic activity within Borobudur Fossae with contraction and extension. The crater density of Smooth Plains over the planet varies by a factor of five. The Northern Smooth Plains, Caloris interior plains, most of Rembrandt's interior plains and many other small patches emplaced are within statistical error of 3.8 – 3.7 Ga (Hauck *et al* 2018, Byrne 2020). This clustering suggests they may have formed over a discrete period. However, this simultaneous mechanism does not explain the variation in the spectral and chemical composition of Smooth Plains, so it is not clear yet if the Smooth Plains occurred in one large pulse of magmatism or a prolonged event over the period.

Crustal folding generating the EBV (Enterprise-Belgica Valley) may have started along with the formation of Belgica and Enterprise Rupes. Repeated lava emplacement within Rembrandt, isostatic effects and regional tectonic forces led to the formation of both wrinkle ridges and grabens due to crustal compensation. At least one segment of Enterprise Rupes stopped forming before the end of the Calorian.

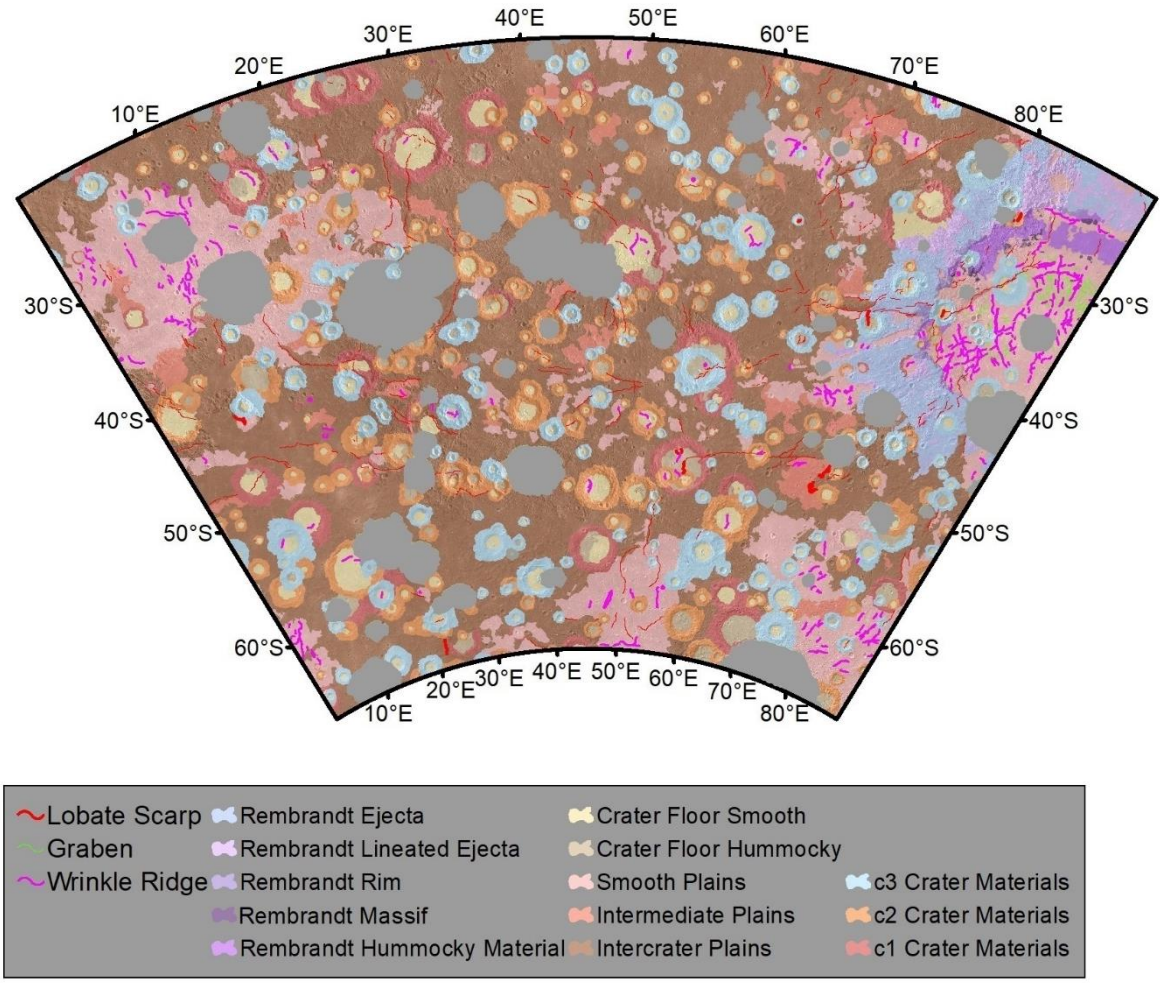

Figure 4.48 H-14 at the End of The Calorian: Rembrandt Impact has covered the surface and Smooth Plains forming, c3 craters cover the surface, Fault timing uncertain other than post-dating the formation of craters/ plains during the Tolstojan.

4.7.4 Mansurian

Crater activity dominates this period, with c4 craters impacting the planet (Figure 4.49). None of the large lobate scarps interact with c4 craters, but tectonism is possibly ongoing although waning. Widespread Smooth Plains volcanism has stopped, but smooth patches may continue to form next to faults, and within Rembrandt, a layer of Smooth Plains may have been emplaced in the middle of the basin, covering part of Borobudur Fossae (Semenzato *et al* 2020). I can tell that the fossae stopped growing because the c4 crater Bellini is not cut by them. Explosive volcanic vents continue to erupt and produce faculae, including within two impact craters that date from this period. Hollows were likely forming before degrading away.

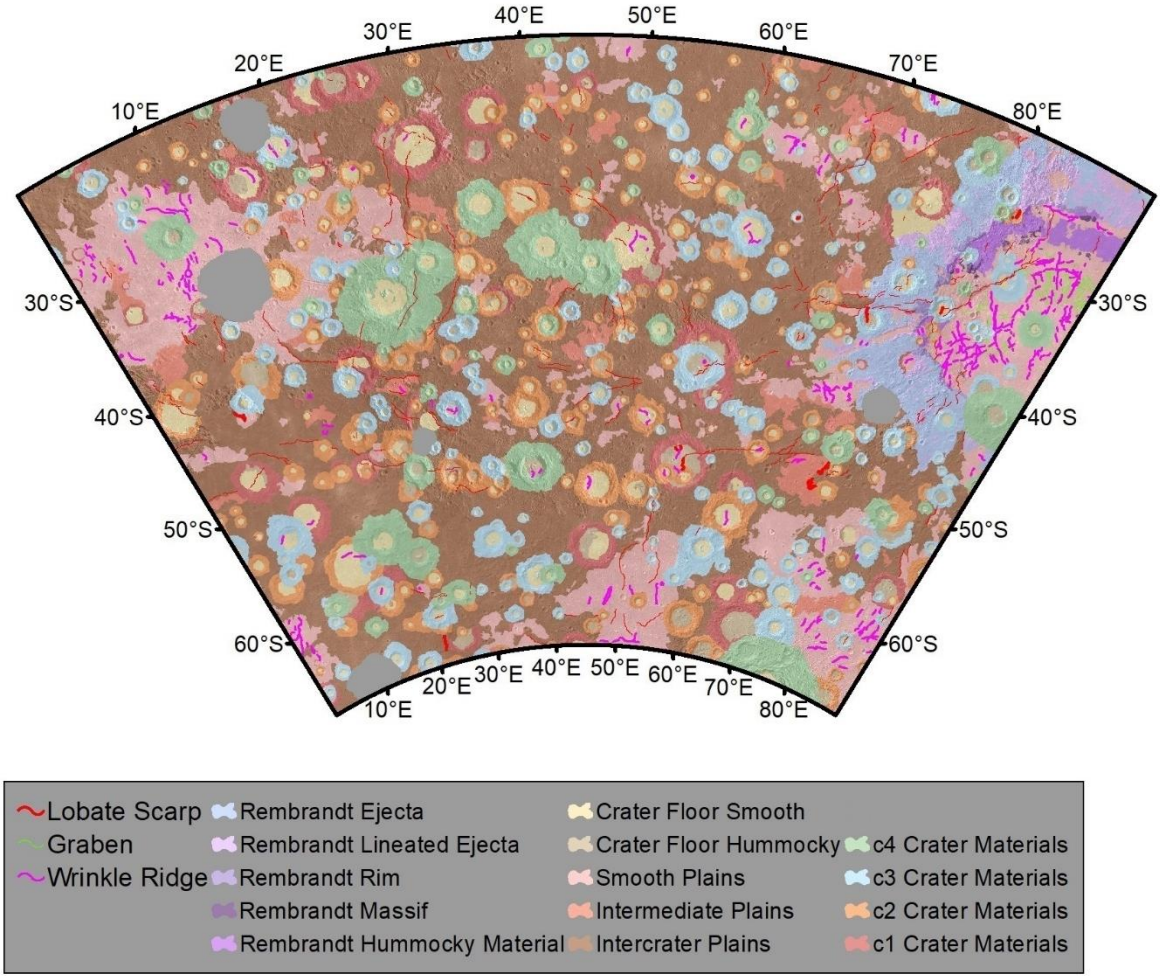

Figure 4.49 H-14 at the end of the Mansurian, showing all plains emplaced, c4 craters added, and lobate scarps developed. Potential new S.P. in Rembrandt and on edges of some faults.

4.7.5 Kuiperian

Most of the geological activity within the quadrangle had ended. External modification dominated any changes to the surface, the most dominant being c5 craters, including Debussy whose rays cover a significant portion of the quadrangle (Figure 4.50). Hokusai rays were emplaced. Hollows continue to form on the surface today, possibly started by small meteorite impacts exposing volatile-rich rocks (e.g. Lucchetti *et al.*,

2018). Explosive volcanism may have continued (Jozwiak *et al* 2018, Thomas *et al* 2014b), though there is no direct evidence for Kuiperian volcanism within the quadrangle. Tectonic activity may also be continuing (elsewhere on the planet small scarps suggest it is still ongoing) but without significant changes to the appearance of any of the features in the quadrangle. All classes of craters continue to degrade and ejecta mix in with the regolith.

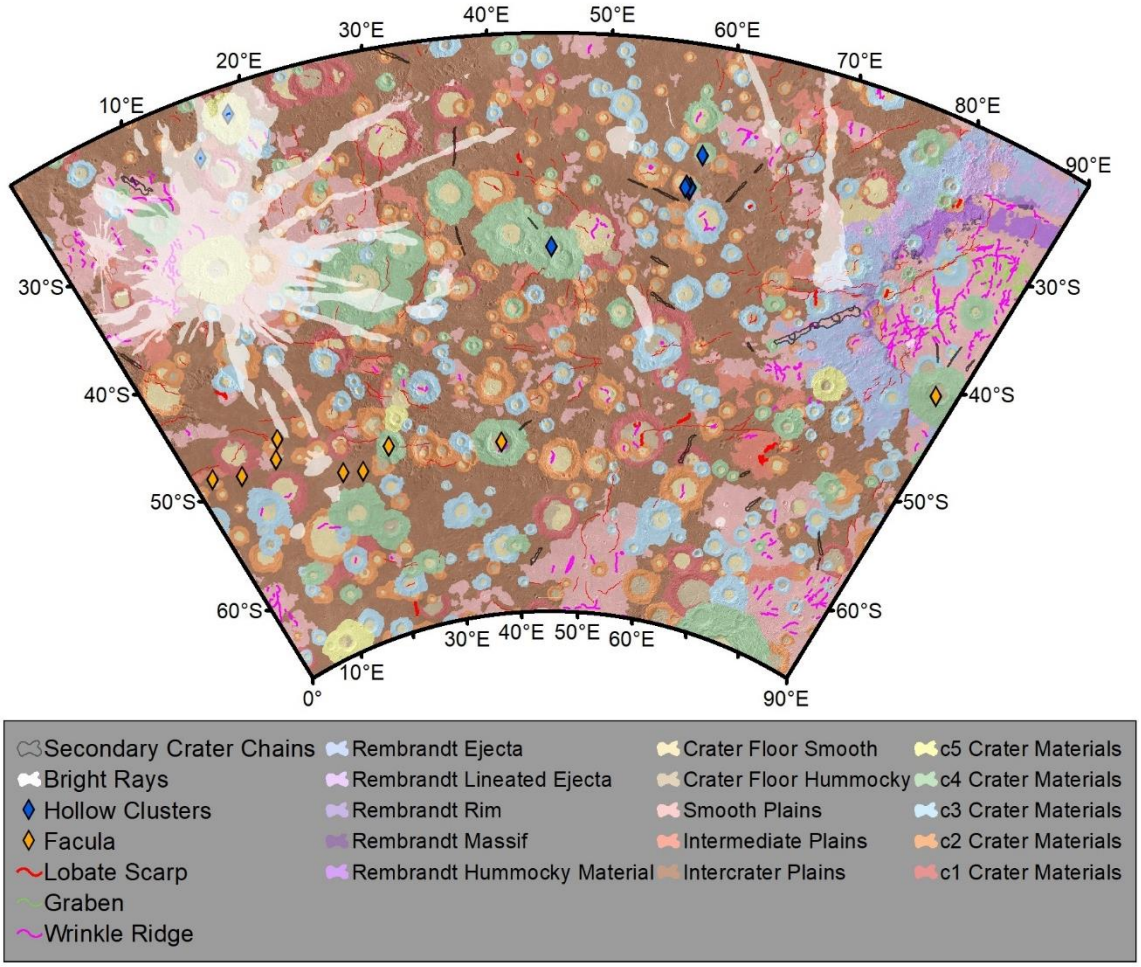

Figure 4.50 H-14 as it appears now with C5 craters and bright rays from Hokusai.

The stratigraphic column (Figure 4.51) summarises the inferred geological history of the quadrangle based on the work in this thesis.

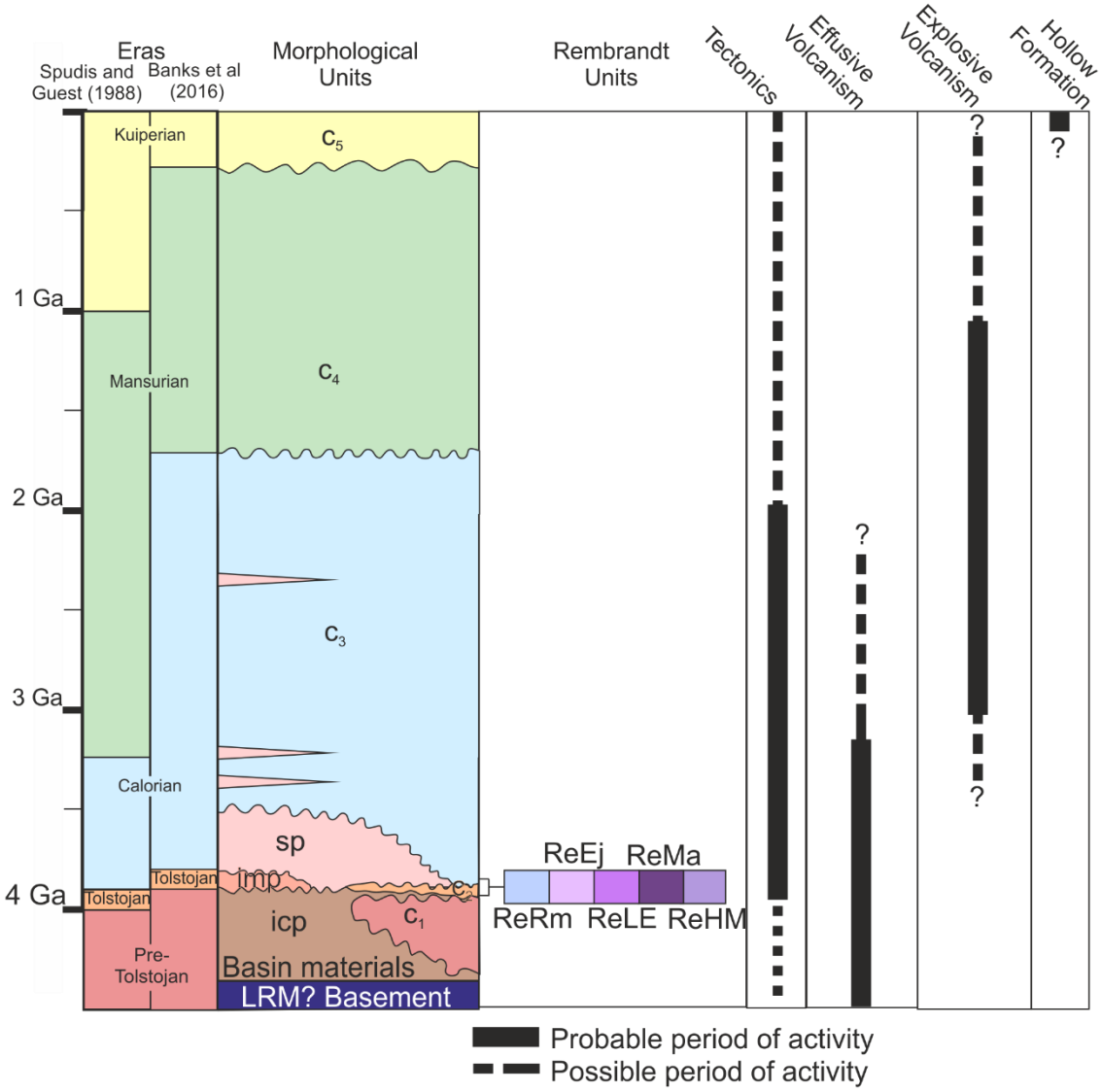

Figure 4.51 Stratigraphic column describing the proposed temporal order of units and processes in the H-14 quadrangle. (sp Smooth Plains, imp: Intermediate Plains, icp: Intercrater Plains, LRM: Low Reflectance Material ReRm: Rembrandt Rim, ReEj: Rembrandt Ejecta, ReMa: Rembrandt Massif, REHM Rembrandt Hummocky material). Authors own schematic.

4.8 A Global Context

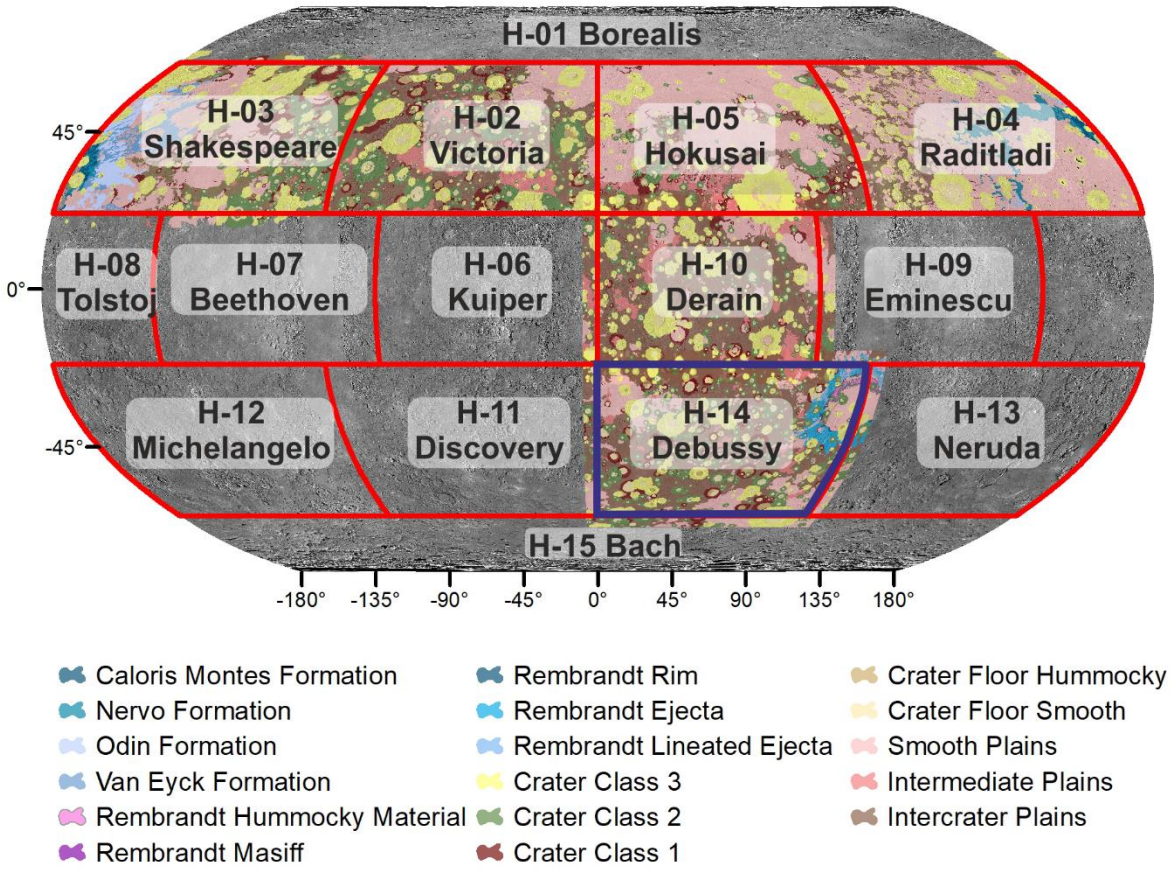

Figure 4.52 Current state of 1:3 million global maps using 3-Class crater system. which H-02 (Galluzzi *et al* 2016)*, H-03* (Guzzetta *et al* 2017)*, H-04* (Mancinelli *et al* 2016)*, H-05* (Wright *et al* 2019)*, H-14* (Malliband *et al* 2020) *and this work (in purple). Basemap is Bulk Data Record basemap* (Denevi *et al* 2018a) *on a Robinson Projection.*

Integration of my quadrangle map into the global map will occur in the time after this thesis is submitted. I am already working with colleagues to reconcile minor discrepancies near the boundaries with H-10 (to the north) and H-13 (to the east).

Like the other 1:3 million maps (Figure 4.52, Galluzzi *et al.*, 2016; Mancinelli *et al.*, 2016; Guzzetta *et al.*, 2017; Wright *et al.*, 2019; Malliband *et al.*, 2020), I have found some Intermediate Plains, and while their existence is currently controversial, I think they are a real but minor unit within the stratigraphy, likely dating to late Tolsojan. Smooth Plains represent the last major surface changing event within the quadrangle and on Mercury in general. The presence of Smooth Plains in basins is exciting, though not surprising. It matches well with other large basins on Mercury, including Caloris, Michelangelo and Picasso. It, however, does not explain the most voluminous extent of Smooth Plains on the planet; the Northern Smooth Plains which are not confined to a basin (Ostrach *et al* 2015), nor is there good evidence of a hidden (flooded) basin from which they could have overflowed.

The tectonics of H-14 on its own a complicated and dominated by two large lobate scarps so I cannot make general conclusions about the tectonic fabric of the planet. However, the data from this map can be combined in the future with the other 1:3 Millon scale maps to study this better, though illumination angle might introduce a bias.

The Rembrandt impact was a significant event affecting a substantial proportion of the quadrangle. While half the size of Caloris, it could provide a useful comparison to Caloris for understanding large-scale cratering processes. It is also an interesting contrast as its floor is only partially covered by Smooth Plains. Its shallower excavation depth provides interesting comparisons for Mercury's volatile history.

4.9 Concluding remarks

I have mapped the H-14 Debussy quadrangle and found its geological history to broadly fit in with that found by other workers for the rest of the planet. I argue that there is a mappable Intermediate Plains unit, though the exact timing and nature of this unit are unclear. The link between Smooth Plains and large impact basins, and between some explosive vents and Meteor Rupēs shows that the volcanic and tectonic history of the planet is interwoven and that building a better understanding of both volcanism and tectonics will build an understanding of how Mercury's surface came to be as seen today. Tectonic analysis within the quadrangle is hindered by illumination angles adding bias to existing datasets, but shows the tectonics dominated by the Rembrandt impact basin and the Enterprise-Belgica-Valley.

5 Compound Volcanic Vents On Mercury

5.1 Introduction

During my mapping, the faculae on Mercury stood out on the map as features for further study (Chapters 3,4). I undertook a global study of the vent sites on the planet to work out how many of them fitted the description of a compound vent site, and I used the findings to examine the implications for the planet's explosive volcanic history. It is this research I outline in the present chapter. This research has been accepted as a paper in Icarus, and is currently in press (Pegg *et al* 2021a).

5.2 Background

Explosive volcanism has occurred on Earth, Mercury, the Moon, Mars, Venus, Io and possibly Titan (Wilson 2009, Wilson and Head 2017, Greeley and Spudis 1981, Wilson and Head 1983, Wood and Radebaugh 2020). On Mercury, explosive volcanism is evidenced through relatively red, high-albedo surficial deposits (compared to the global mean) in enhanced-colour images from Mariner 10 (Rava and Hapke 1987) and MESSENGER's Mercury dual imaging system (MDIS) (Kerber *et al* 2009, Head *et al* 2009), see Chapter 2.6.2. These high-albedo red spots are now known by the descriptor term *facula* (plural *faculae*). These faculae are 10s to 100s km in diameter and are interpreted as ballistically-dispersed pyroclastic products of explosive eruptions mantling (draped over) the surrounding terrain, subduing, but rarely entirely obscuring, underlying textures (Kerber *et al* 2009). They usually contain a central 'pit' (up to several km deep and up to 10s of km wide) that is a probable vent and source for the pyroclastic materials. Not all pits have a discernible facula, and conversely, some faculae lack vents and instead have a highly disturbed surface covered in multiple pits. This "Pitted Ground" may originate from the interaction of lava flows with a volatile-rich substrate (Thomas *et al* 2014c). Within the H-14 (Debussy) quadrangle, I mapped 11 faculae, as well as nine vents without faculae (See Section 4.6).

Some of the vent sites probably represent the latest volcanic activity on Mercury, with faculae forming as recently as the early Kuiperian (Jozwiak *et al* 2018, Thomas *et al* 2014b), and hence no older than 280 Ma (Banks *et al* 2017). Unlike impact craters, the vents are usually non-circular (often scallop-edged) and lack a raised rim. To avoid confusion with the raised rim of an impact crater, the edge of a pit is conveniently referred to by the term 'brink' in preference to 'rim' (Rothery *et al* 2014). The vent sites do not sit within prominent constructional volcanic edifices. Brož *et al*(2018) attribute this to the low gravity and lack of atmosphere leading to the wide dispersal of pyroclastic materials resulting in flank slopes of less than 2.8°.

Compound volcanoes are those that have multiple overlapping vents and edifices (Jackson and Bates 1997, Davidson and De Silva 2000). Overlapping and cross-cutting features show, according to the principle of superposition (Lyell 1853), that they form by a succession of events. A terrestrial example of a compound

volcanic vent is Volcán Aucanquilcha in Chile; this comprises 20 individual vents, some within overlapping craters, ranging in age from 11 Ma to <1 Ma (Klemetti and Grunder 2008). Rothery, Thomas, & Kerber (2014) used the term 'compound volcano' when describing the vent complex inside Agwo Facula, for which Thomas *et al.* (2014b) coined the term 'compound vent' (Figure 5.1). The vent complex consists of nine internal depressions (vents), some separated only by thin walls (septa). They regarded these depressions as individual vents within an overall compound vent site. Cross-cutting relationships between the individual vents and differences in surface roughness between them suggest that eruptions occurred over a prolonged period.

Until now, only limited studies of the eruptive history of vent sites on Mercury have been undertaken, other than to give an approximate maximum age of those occurring within impact craters (Goudge *et al.*, 2014; Thomas *et al.*, 2014b; Jozwiak, Head and Wilson, 2018). Here I study all identified volcanic vent sites on Mercury to determine what proportion are compound. I note relevant small features of interest inside a selection of individual vent sites and discuss the implications for Mercury's volcanic history.

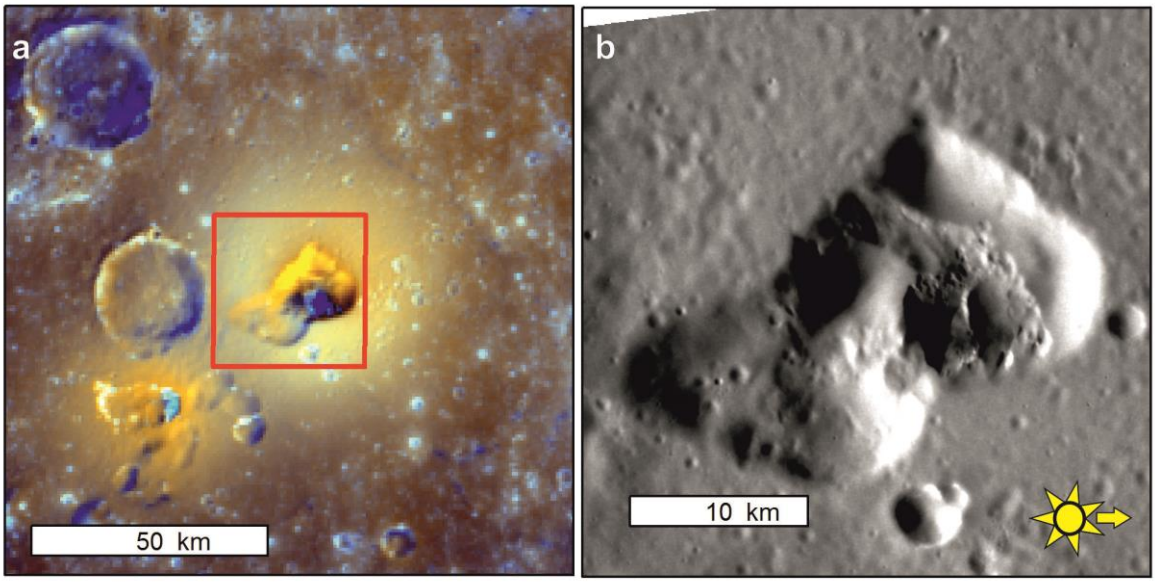

Figure 5.1 a. Enhanced colour image of Agwo Facula and the compound volcanic vent within it from global enhanced colour mosaic (Denevi et al., 2016). Image centred at 146.1° E, 22.4° N. Red box is the outline of 1b. b. The detailed internal structure revealed in a MESSENGER image EN1060657198M (55 m/pixel). Both images are in a sinusoidal projection centred on the mid-point of the vent. North towards the top of all images. Image credit: NASA/ Johns Hopkins University Applied Physics Laboratory/Carnegie Institution of Washington.

5.3 Materials and Methods

To investigate all the known volcanic vent sites on the planet and identify the proportion that is compound, I conducted a review of the existing lists of vents and faculae (Kerber *et al.*, 2011; Goudge *et al.*, 2014; Thomas *et al.*, 2014a; Jozwiak *et al.*, 2018). I identified 27 additional vent sites, and Man *et al.* (2020) identified three additional vent sites. I also re-examined areas previously identified as pitted ground (Thomas *et al.,* 2014) to

assess whether higher resolution image data collected after the Thomas *et al*. study would reveal that these are volcanic vents not correctly identified in previous lower-resolution data.

5.3.1 Image Data

To inspect each known vent site and/or facula, I used the highest resolution (<180 m/pixel) narrow-angle camera and wide-angle camera images captured by MESSENGER's MDIS instrument (Hawkins *et al* 2007) and archived in the NASA Planetary Data System. I projected the image data using USGS ISIS3 software. To study each vent location, I re-projected the images using a sinusoidal projection centred at the midpoint of the vent/facula and displayed images using geographical information system (GIS) software. I used the 665 m/pixel enhanced colour mosaic (Denevi *et al* 2016) to examine faculae, though not all vent sites show faculae, and not all faculae contain vents (Jozwiak *et al* 2018). I used visual determination to verify vent sites as depressions lacking raised rims. Often faculae contain multiple vent sites rather than a lone example. I excluded hollows through their relatively blue reflectance (Blewett *et al* 2011) in the enhanced colour basemap, highly localized albedo (compared to the generally more diffuse anomalies of faculae), generally flat floors and relatively small (~100s of meters) size (Blewett *et al* 2011) compared to vents. I excluded impact craters by their raised rims and ejecta patterns. I defined a vent site as "a depression bounded by a single brink spatially separated from other similar depressions".

I do not consider faculae containing only Pitted Ground to be a vent site (Figure 5.2). Pitted Ground has no well-defined large scale (>1 km) depression and instead consists of a generally disturbed region with a rough floor. It perhaps forms when lava flows over volatile-rich materials causing local volatile release through the lava, thus disrupting the lava surface and creating the albedo feature (Thomas *et al* 2014a). This study focuses on vent sites, and faculae without explicit vent sites are excluded from the rest of the study.

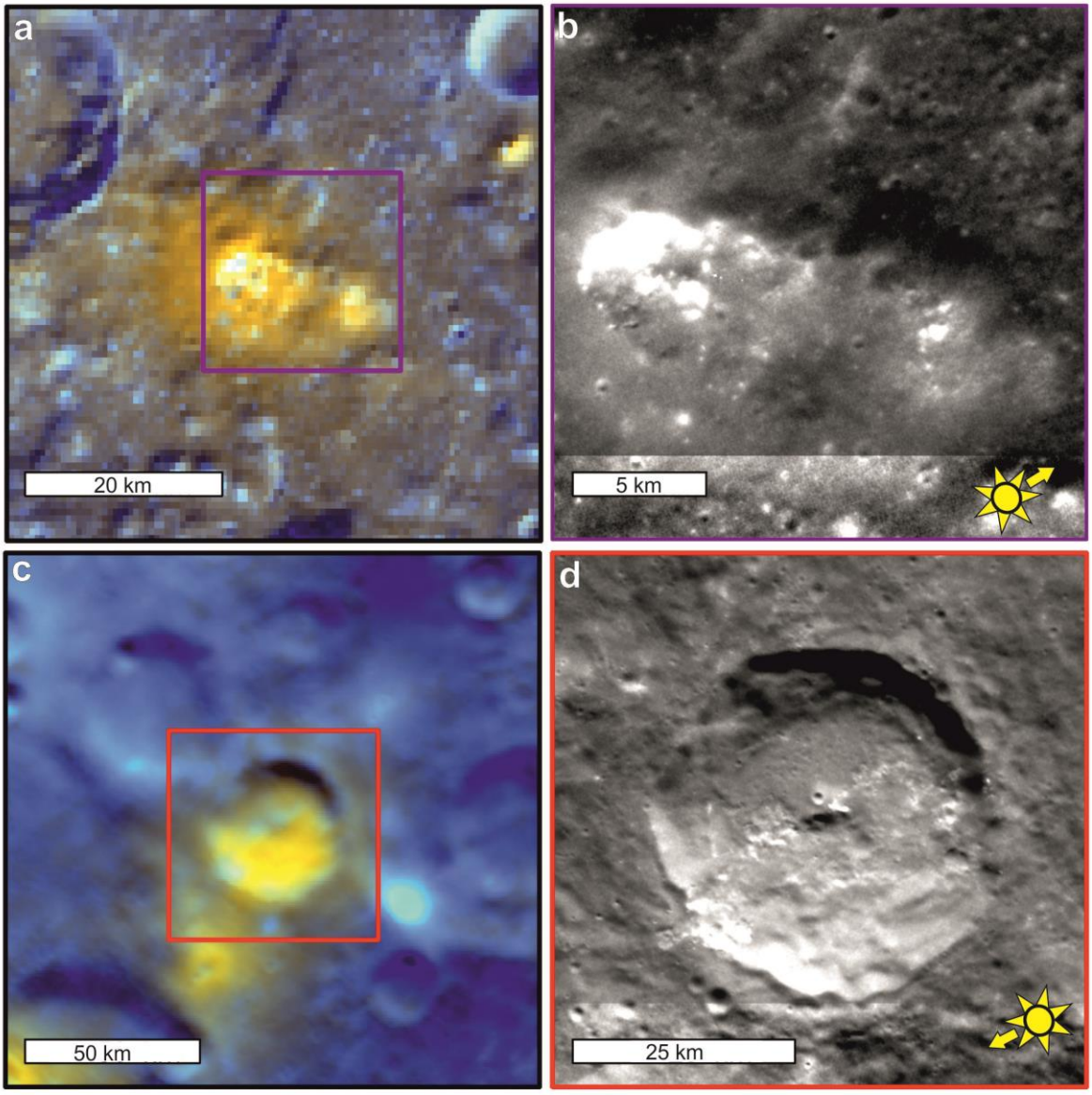

Figure 5.2 a. Enhanced colour basemap (Denevi *et al* 2018a) *showing faculae known only on poorly resolved image data. Box shows the extent of b. Image centred at 141.4°E 38.3°N. b. Image of EN0233460948M poorly illuminated vent and hollows, 33m/pixel. c: Enhanced colour basemap* (Denevi *et al* 2016) *showing a facula with no resolved vent (likely pitted ground). Box shows the extent of d. Image centred at -27.8°E -51.5°N d: Image EN1035383880M showing the high-resolution image of the facula in c without a vent, 118 m/pixel.*

I made digital elevation models (DEMs) of vent site interiors using AMES Stereo Pipeline (Broxton and Edwards 2008). However, I found that the lack of good image pairs at sufficient resolution to identify the detailed internal morphology of vent sites resulted in less information being conveyed in these DEMs than by individual images or by images with much different illumination angles that clearly highlight morphology but are unsuitable for DEM creation. The time needed to produce DEMs for all vent sites and the lack of any benefit in the majority of cases means that the bulk of this study relies on photogeological interpretation (e.g., Allum, 2013).

5.3.2 Identification of Compound Vent Sites

I applied three-level semi-quantitative confidences to the data available to classify the vent sites, based on my assessment of the suitability and quality of the available images. If the image quality was insufficient to distinguish between impact craters and vents or to identify internal structures or features within the vent sites, I recorded the vent sites as "poor image quality". This usually corresponds to vents imaged only once, often with a solar incidence angle >80° or close to 0° (though this is dependent upon the depth of the vent and the natures of any interior or surrounding features, as these factors dictate the extent to which shadows obscure features), or resolution that is insufficient to make out the interior of vents (this is dependent on the size of the vent). Conversely, vent sites with "good image quality" had illumination adequate to show the vent interiors clearly, and perhaps several images with various incidence or emission angles. In between these extremes, "reasonable image quality" vent sites often required inspection of multiple images to identify breaks in slope or to reveal other morphology clearly.

At each vent site, I searched for morphological features that would indicate a compound nature and then decided whether each vent site is compound. Morphological features within vents used to identify compound volcanic vents sites included:

- Presence of internal structures such as septa that subdivide vents (Figure 5.3.a)
- Immediately adjacent vents where parts of the brinks touch (Figure 5.3.b)
- Larger vents that contain smaller vents (Figure 5.3.c)

Septa are internal walls subdividing a vent site. Where multiple vents directly touch (for example with only a thin septum), I consider them to be part of the same compound vent site. When there is intervening flat ground, I log them as separate vent sites even if distributed around the same structure (such as around a crater's central peak). Both these structures are spatial evidence for multiple eruptions because they demonstrate discrete eruption sites. When there is a smaller vent inside a larger vent (e.g. Figure 5.3c), the smaller vent must postdate the larger vent that hosts it because the larger vent floor had to exist before the smaller could form, and so these are also compound vent sites evidencing temporal evidence of multiple eruptions.

On Earth, compound volcanoes are identified either by overlapping edifices or by intersecting vents (Neuendorf *et al* 2005). The lack of significant edifices on Mercury makes our definition, based only on the vent, more conservative than on Earth. However, it follows the same usage of the term 'compound volcanic vent' as previous work on Mercury (Rothery *et al* 2014).

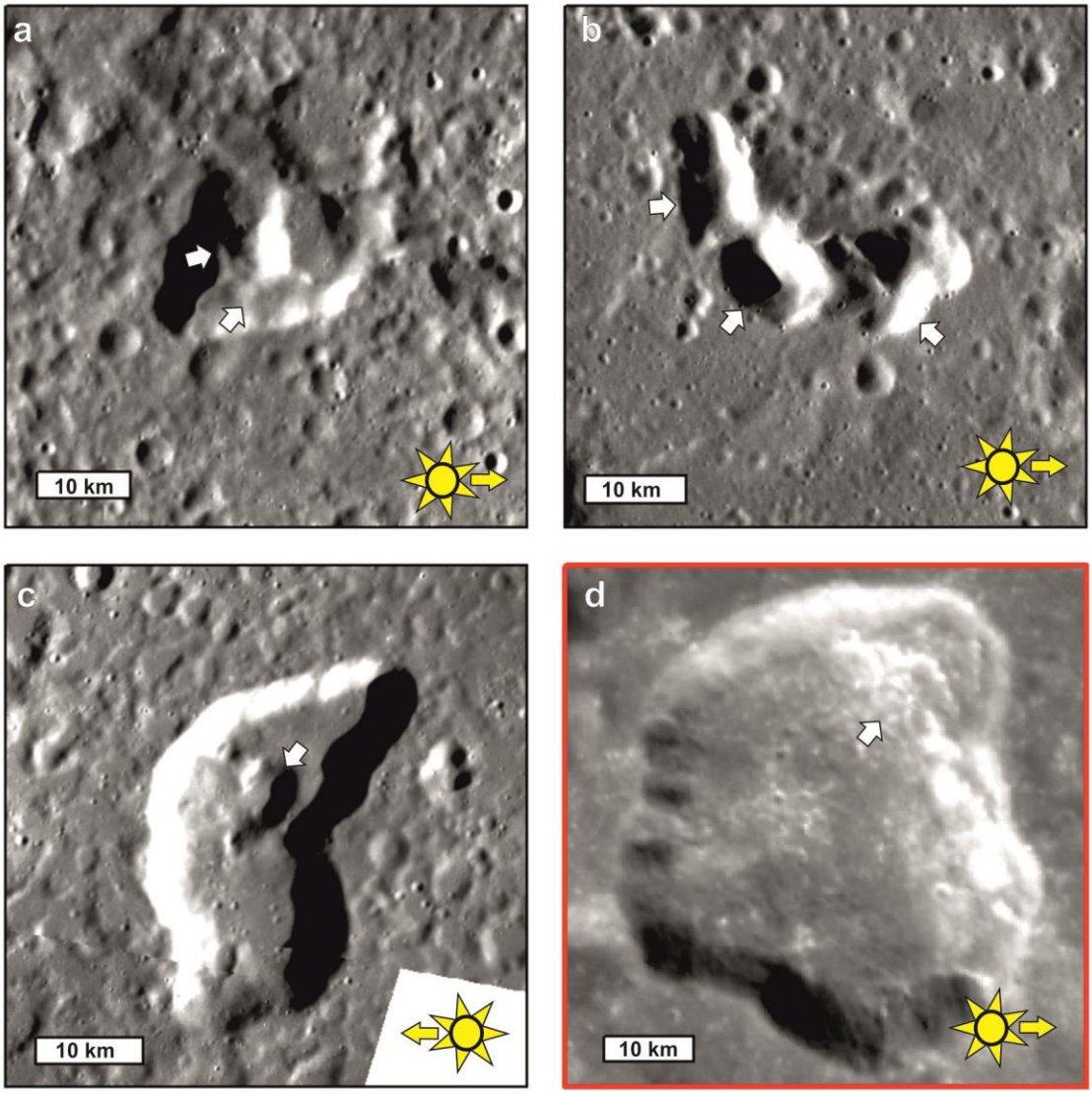

Figure 5.3 Examples of vents with morphological features used to distinguish compound and non-compound (red outline) vent sites ***a:*** *A triangular compound vent subdivided by multiple septa (arrows highlight some of the septa). Image centre: -49.0°E, -27.5°N, image: EN0213201259M* ***b:*** *A compound vent site on a crater floor comprising a set of multiple adjacent volcanic vents around the southern edge of an inferred buried central peak. Arrows point to individual vents. Image centre: 143.6°E, -5.1°N, Image: EN0250970163.* ***c:*** *A smaller vent (arrowed) in the floor of a larger vent, which are classified as compound. Image centre: 22.6°E, 32°N image: EN0220030413M* ***d:*** *Large volcanic vent with concave and convex portions along its brink; this example is not classified as compound. The arrow points to the area of mass wasting in the north. Image Centre: 57.3°E, 36.0°N, image: EW0234906641G. North towards the top of all images. Image credits: NASA/ Johns Hopkins University Applied Physics Laboratory/Carnegie Institution of Washington.*

I applied the following classification to each vent site; compound, tentatively compound, or not compound. Additionally, I noted those examples where image quality was insufficient to enable classification. I recorded as "tentatively compound" those sites that have some form of structure but do not have clearly defined separate vents (for example where septa are missing or incomplete), or where it was plausible to ascribe

internal structures to processes such as mass wasting or fault activity. I took a conservative approach in classifying the vent site inside Nathair Facula (commonly referred to as "the north-east Rachmaninoff vent" before the facula received its formal name in 2018) as "tentatively compound" due to lack of clear structural division, even though differences in mantling and areas with rough floor texture suggest a multi-stage history. I discuss this example further in Section 5.4.2.3. The link to a list of images used to classify vent sites is in Appendix 2.

Processes that could have modified the inside of vents, other than multiple separate eruptive events or migration of the eruption centre during an eruption, include:

1. Gravity-driven mass wasting (movement of rock debris downslope due to gravity)
2. The asymmetric build-up of fallen pyroclastic material
3. Impact catering

Mass wasting is a likely process to occur after the creation of new slopes on Mercury and is known to occur within craters (Brunetti *et al* 2015) and edges of some vents on Mercury (Malliband *et al* 2019). Likely examples are easily identified on the interior slopes of vents (see the north of Figure 5.3.d.) where mass wasting, sufficient to change the outline of the vent, has occurred. Mass wasting could be a cause of some of the unusual shapes of vent brinks and the alternation of convex and concave planform shapes. However, mass-wasting deposits can be identified on the floor of vents by their positive topographic convex-up lobate form (Brunetti *et al* 2015). I do not consider it likely that morphologies created by mass wasting could look similar to the features used to identify compound volcanic vents shaped by volcanic processes.

I consider that the asymmetric build-up of ejected materials (where volcanic materials accumulate on one section of the vent/volcano during an eruption) from the vents is unlikely to produce morphologies similar to compound volcanic vents because the ejecta are so thinly dispersed that departure from radial symmetry would not affect the within-vent topography (Thomas *et al* 2014b, Brož *et al* 2018). Asymmetric distribution of ejecta could, however, produce an asymmetric facula (Section 5.4.2). Impact craters would be noticeable by a raised rim, bowl shape and ejecta.

Where the image data were sufficient to study the relationships of the internal component vents within a compound volcanic vent site, I looked for crosscutting relationships to infer relative timing. I also reason that smoother surfaces in and around vents are likely to represent older portions of a compound volcanic vent than rougher surfaces nearby; due to younger volcanic ejecta from nearby vents subduing their textures, or being old enough to have developed a thicker regolith cover (Rothery *et al* 2014).

5.4 Results

I will here discuss the overall results of the study, followed by looking at some examples of vent evolution and faculae before looking at the vents in H-14, the Debussy quadrangle (chapter 3,4).

5.4.1 Global Results

I have identified a total of 309 vent sites across the planet. Of these, 109 are imaged with good image quality, and 115 have reasonable image quality (Table 5.1). Of the 309 vent sites, 131 are clearly compound volcanic vents, and 57 are clearly not. The remainder are either tentative or too poorly imaged for us to classify (Table 2). Of the 309 vent sites, 87% have an associated facula (Appendix 3 for the list of vents). The presence of a facula has no relation to whether the vent is compound or not.

Table 5.1 shows that 42% of all vent sites are definitely compound, and only 18% are definitely not compound. Excluding all the poorly imaged examples and those with tentative classification, 70% of the confidently classified vent sites are compound, and 30% are not (Figure 5.4). There is a similar percentage of compound volcanic vent sites in the subset of sites with good image quality (71%; Table 5.1, Figure 5.4), showing that "reasonable" image quality is useful for examining vent sites and reliable for identifying the proportion that are compound. Furthermore, the number of "tentative" compound volcanic vents suggests that the actual proportion of compound volcanic vents is likely to be larger than our conservative ~70% estimate.

It is possible that a few impact craters, whose raised rim and ejecta are unclear or degraded, could have been erroneously included in the database as vent sites. If so, they would be in the "non-compound" category, as no common morphological feature of impact craters match those used to classify a vent site as compound. This would artificially reduce the proportion of compound volcanic vent sites, meaning that, if anything, compound vents are likely to be slightly more common than otherwise indicated.

For vents with no interior structures, and thus not classified as compound, I should also consider whether they are likely to have formed by repeated eruptions. Vents' brinks that contain areas of both convex and concave planform shape are suggestive of having been shaped by mass wasting. Still, I observe that their floors often appear to lack mass wasting deposits such as positive relief features with lobate toes (see the north of Figure 5.3.d for a rare example of an area where such a slump is clearly observed, and so explains the shape of the vent wall in that area).

Table 5.1 Numbers of vent sites and the quality of imagery available.

Quality	Count
Good:	109
Reasonable:	115
Poor:	85
Total:	309

Table 5.2 Categorisation of Volcanic Vent Sites.

Category	All	All Image Percent	Confident Classification Percent	Good Images	Good Image Percent
Compound	131	42%	70%	77	71%
Not Compound	57	18%	30%	23	21%
Tentative	61	20%	-	9	8%
Unclassifiable	60	19%	-	-	-
Total	309	100%	100%	109	100%

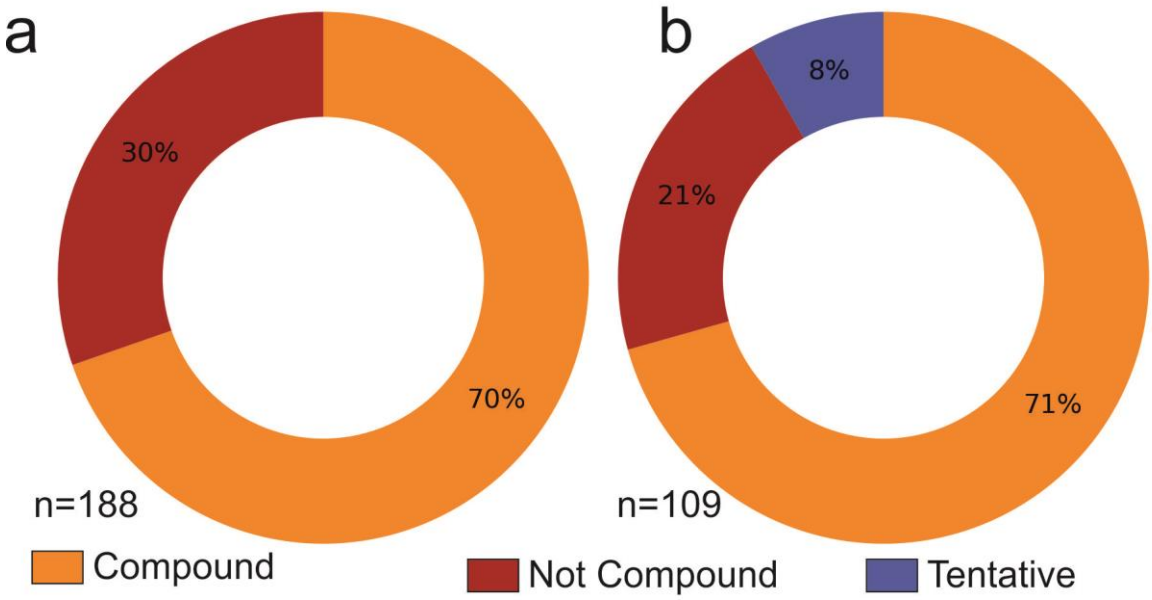

Figure 5.4 The ratio of compound to not-compound volcanic vents on Mercury from all resolvable vent sites in Table 2 (excluding those classified as 'tentative,' or 'insufficient image quality'). ***b.*** *The proportion of vent types in only those vent sites with best quality images (those vents listed as having 'good' image quality in Table 1).*

I plot the geographical location of vents distinguished by type in Figure 5.5. 79% of compound vents and 89% of non-compound vent sites are within impact craters or basins. These percentages are close to the ranges previously reported for all vents (of all types) within craters, such as 91% (Klimczak *et al* 2018) or 81% (Thomas *et al*., 2014c).

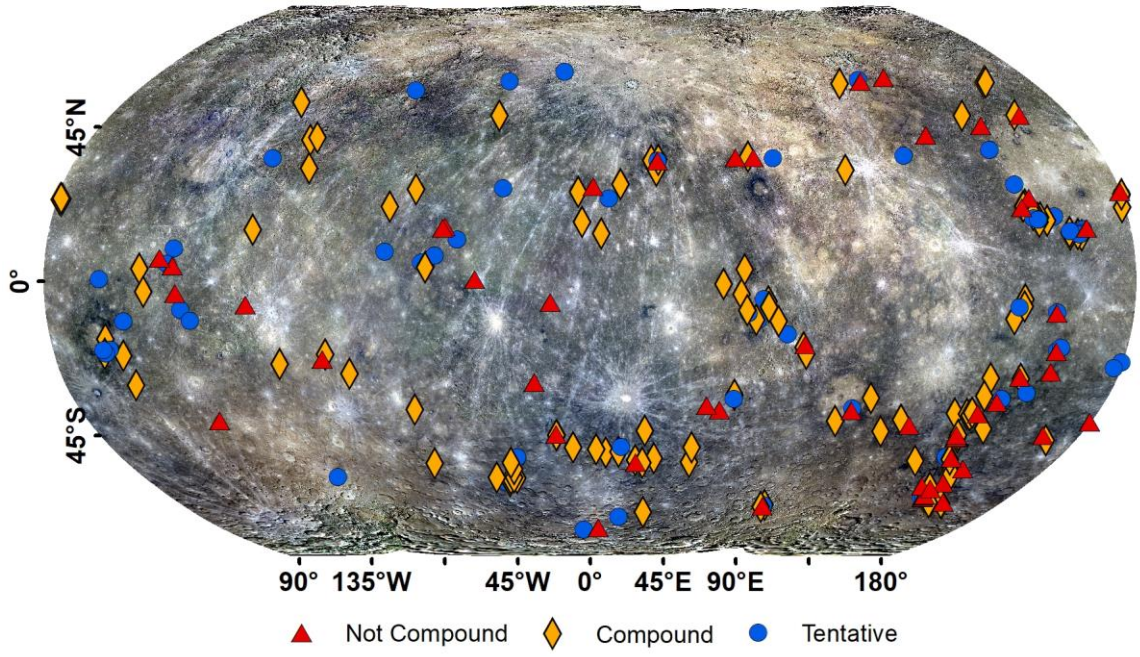

Figure 5.5 Global distribution of vents in this study, superimposed on the global colour map (Denevi *et al* 2016) *using a Robinson projection.*

5.4.2 Examples of Internal Evolution of Vents

To further demonstrate variability in vent types and morphology, and to investigate what this might tell us about explosive volcanism on Mercury, I discuss four examples of compound volcanic vent sites. These encompass the variety of form and illustrate some interesting features observed in the broader survey.

I studied these examples at a scale of 1:2000 times the pixel size (in metres) of the images (listed in the example figure captions). I used the pattern of shadows, in some cases switching between multiple illuminations, to divide the compound volcanic vents into individual vents/depressions. I deduced relative timing from crosscutting relationships, such as where edges of vents further excavated pre-existing floors (Figure 5.3.c), or cut through the brinks of other vents showing that those must have formed earlier (Figure 5.3. b). I visually assessed relative surface roughness and checked this for consistency with the crosscutting relationships. I found no examples of conflicts between crosscutting relationships and relative age implied by surface roughness, as also identified within the vent in Agwo Facula (Rothery *et al* 2014).

The first example is a large vent containing internal structures. The second example is a smaller vent, but still with clear internal structures. The third example focuses on some features that I have identified within the Nathair Facula vent using high-resolution images and that are not observed at other vent sites. The fourth example is particularly unusual and is a dome that I identified within a vent, and which is a possible constructive feature.

5.4.2.1 Example 1. The vent site inside Kipling crater

I used two images with opposite Sun azimuths to identify component vents at this site. The overall compound volcanic vent is 15 km wide and 37 km long (Figure 5.6). Within the vent site, I identified seven internal vents that demonstrate crosscutting relationships and textural variation, suggesting a complex eruptive history. Where possible, I used the crosscutting relationships of the depressions to infer a time sequence. The oldest section is probably the north of the complex (depression *a*). Depression *b* cuts across it and is thus younger than depression *a*. Similarly, depression *c* cuts across depression *b*.

Figure 5.6 A compound vent within Kipling crater. ***a.*** *Illumination from West EN0252180447M (69.7 m/ pixel).* ***b.*** *Image: EN1013780238M (156.8 m/ pixel) illumination from East* ***c.*** *EN0252180447M with interpreted vents (in approximate alphabetical order, oldest to youngest). All images centred at 71.3°E, -19.2°N, North towards the top. Image credit: NASA/ Johns Hopkins University Applied Physics Laboratory/Carnegie Institution of Washington.*

The area in the south of the vent (*f*/*g*) is the most texturally rough and cuts through the floor of *c* and *d*, so it is probably the most recently active. The youngest part, based on texture, is probably depression *g*. It is not possible to determine the age of *e* relative to the rest of the complex because of an intervening segmented ridge (that also divides depression *d* from *c*). The curved nature and position of this ridge within the lava-flooded floor of the host impact crater (Kipling) suggest that it may represent a remnant of Kipling's peak ring structure. It appears that there was a general progression of the locus of the eruption from north to south based on crosscutting relationships and textural roughness.

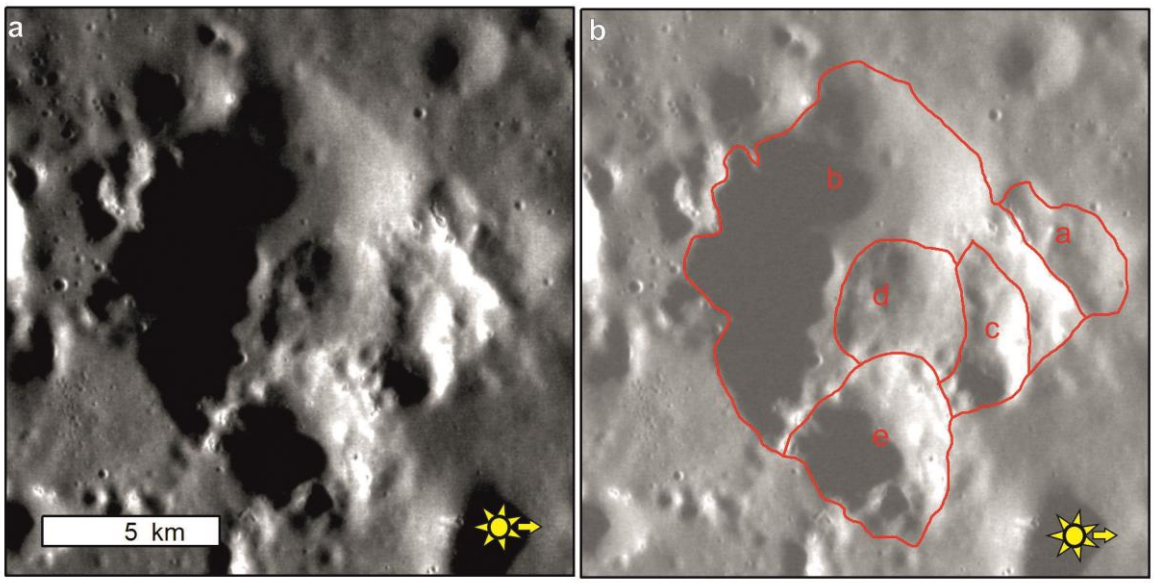

Figure 5.7 A compound vent located in the south of the Caloris basin. ***a.*** *Image centred at 159.3° E, 14.3° N using image EN250796801M (31.8 m/pixel).* ***b.*** *The same image with 40% transparency and interpreted vent history in alphabetical order according to relative age, oldest to youngest. North towards the top image, image credit: NASA/ Johns Hopkins University Applied Physics Laboratory/Carnegie Institution of Washington.*

5.4.2.2 Example 2. *A vent inside Ejo Facula*

This site is a 12 km x 13 km vent located in a plains-flooded re-entrant of the southern rim of the Caloris basin and within Ejo Faculae. This vent site provides another demonstration of internal crosscutting relationships (Figure 5.7). I used image EN250796801M to map out depressions based on the crosscutting relationships of four or possibly five separate depressions. Here, tentative depression *a* (little of which survives) is perhaps the oldest, though its brink is no longer clear. Depression *b* has the largest area. There may be additional vents within the shadowed area of *b*, but images with suitable illumination conditions are of insufficient resolution to confirm this. Depressions *c, d,* and *e* all cut into the floor of *b*. I interpret the divisions to represent a sequence of eruptions that occurred after *b*, with *e* probably being the most recent as it cuts across the other two features and a mantling deposit appears to overlie *b* and *d*.

5.4.2.3 Example 3. The Vent site at Nathair Facula

Nathair Facula is the largest facula on the planet and surrounds the largest (39 km × 30 km) recognized vent structure (Figure 5.8). This vent is an unusual example. It lacks any distinct septa but does contain some distinct pits. The highest resolution available images (37.6 m/pixel) show the floor comprises multiple shallow bowl-like depressions in the floor that I interpret as separate eruption sites. The southern part of the vent floor has a smooth texture, the appearance of which is consistent with being an older area mantled by younger deposits. The floor in the northern half of the vent is rougher and so is presumably not mantled and therefore likely to be younger. Within this northern section, much of the eastern part is rougher still, and thus likely the most recent site to have hosted significant eruptive activity (making up approximately

1/8th of the floor area of the vent). A stereo-derived digital elevation model (DEM) in Thomas *et al.* (2014c) shows that the floor is deepest in the northern part of the vent. These observations suggest there were at least three eruptive sites within this vent (Figure 5.8.d), and I classify it (conservatively) as tentatively compound. However, (Rothery *et al* 2020a) treat it as compound and suggest the northern part was the most recent to erupt as part of an explanation for the asymmetry of the surrounding facula.

Another remarkable feature within the vent at Nathair Facula is the presence of small pits on the floor. These pits are 100 – 600 m diameter, shallow, bowl-shaped depressions (Figure 5.8.c). They do not have the VIS-IR signature or high albedo that characterizes hollows (Chabot *et al* 2011, Blewett *et al* 2013). They do not form the straight or arcuate chains typical of catenae (chains of secondary impact craters) and lack the raised rims associated with impact cratering. The pits are on a scale similar to some of the features seen in 'pitted ground'; however, no example of 'pitted ground' follows such a narrow pattern (Thomas *et al*., 2014). These pits are on the boundary between a rough area of the floor and the smoother area surrounding it. If this area represents the most recent area of eruption, then these pits are on the edge of it possibly formed in the waning phases of an eruption. The small size of these pits means there is no clear way to date them; however, given the intensity of Nathair Facula (Besse *et al.*, 2020; Rothery *et al.*, 2020b), parts of this vent may be atypically young. If that is the case, then in other vent sites, comparable features may have been degraded beyond visibility by space weathering and impact gardening and so could have been compound.

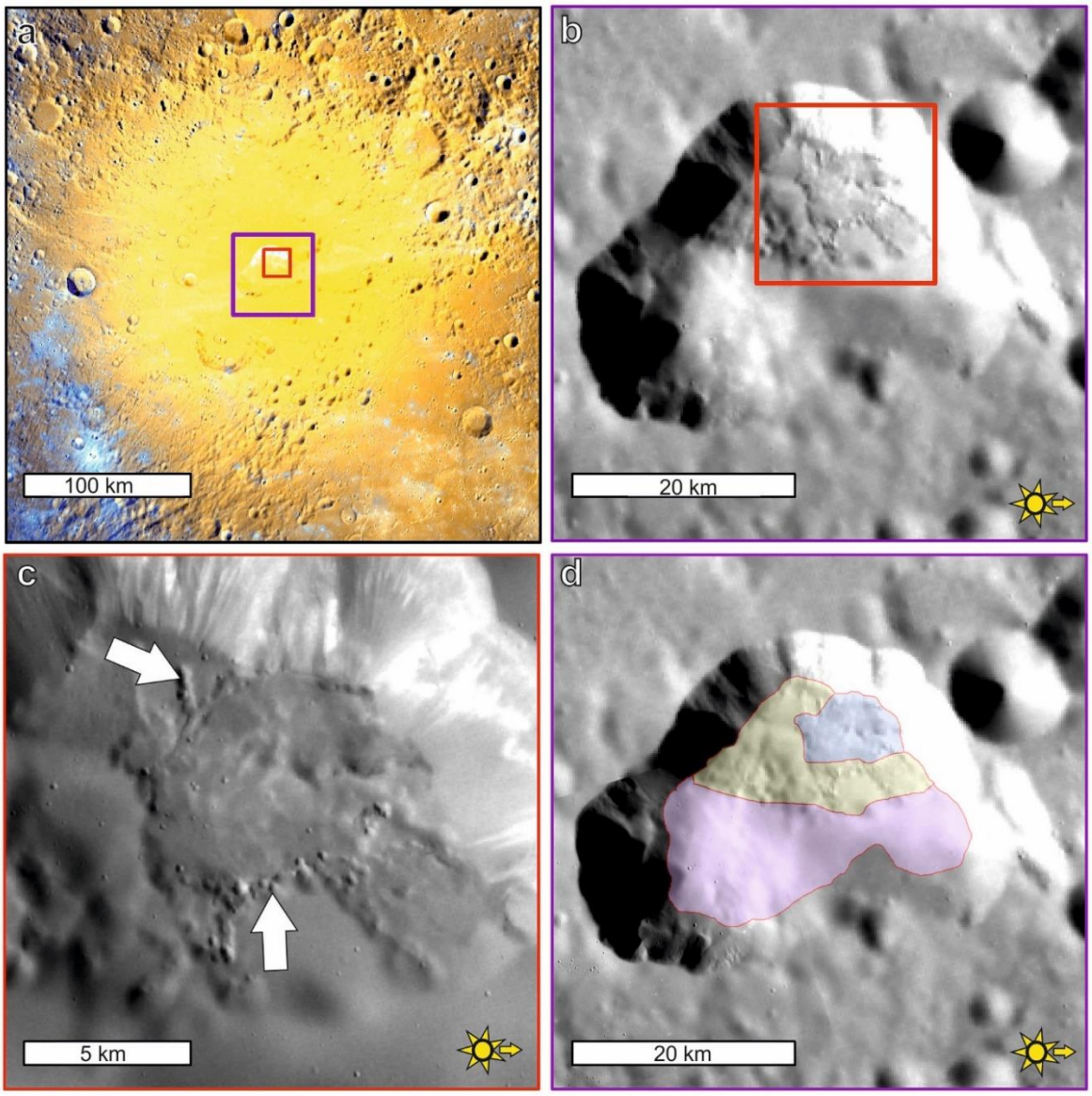

Figure 5.8 Vent inside Nathair Facula; north to the top in all images. ***a****. Enhanced colour basemap* (Denevi *et al* 2016) *showing Nathair Facula. Purple box shows the extent of b and d, and the red box the extent of c.* ***b*** *overview of the pit morphology. A rough texture is visible in the NE part of the floor. Image: EW0254884916G (200 m/pixel).* ***c****: Detailed view of the rough textured floor. Arrows indicate examples of small pit features that outline the rougher area. Image EN0224508427 (37.6 m/ pixel). Both images are illuminated from the west.* ***d****. The floor of the vent divided into areas (potentially representing levels of degradation/mantling) based on texture. EW0254884916G Image credit: NASA/ Johns Hopkins University Applied Physics Laboratory/Carnegie Institution of Washington.*

5.4.2.4 Example 4. A possible dome?

I have located only one feature inside a vent that I regard as a plausible constructional feature. It is a small (500 m across) dome within a 24 km ×15 km compound volcanic vent, centred at 139.6°E, 48.5°N (Figure 5.9). Its position on the floor of a vent demonstrates that it formed after the excavation of the vent.

Unfortunately, the NW edge of the dome is shadowed, which could be hiding important morphological details. Such a positive topographic anomaly on the floor of a vent could have been produced by mass-wasting, but that is unlikely in this case as its top and edge on the side closest to the wall both appear to be convexly rounded (though the shadow impedes analysis). A more compelling alternative is that it is a lava dome formed by very viscous lava, though on a much smaller scale than the two possible constructional edifices identified by Wright *et al.* (2018). Better images and spectral data from the BepiColombo mission (Rothery *et al* 2020b) are likely to improve understanding of this unusual feature, including the fine-scale texture on top of the dome, and I recommend it as a target for that mission.

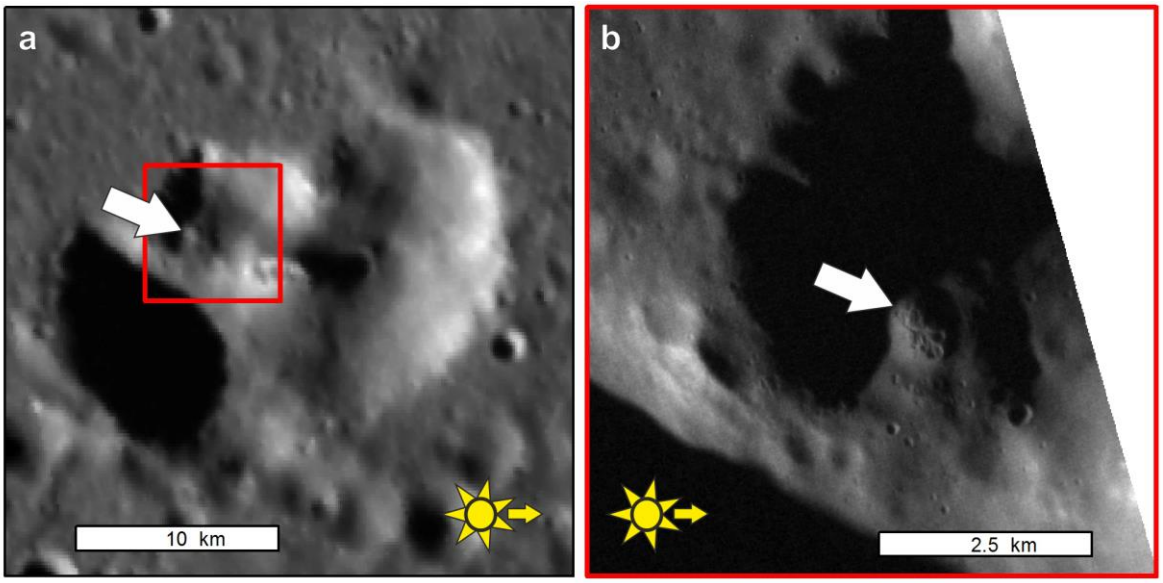

Figure 5.9 a. Overview image from 166/m global basemap (Denevi *et al* 2016) *of compound volcanic vent centred at 139.6°E, 48.5°N. North towards the top. The compound volcanic vent appears to comprise at least three separate smaller vents; the red box shows the location of b.* ***b.*** *Arrow points to the post-excavation structure within a vent that is a candidate for a post-eruptive edifice. Image EN0251055380M (13.5 m/pixel). Sun arrow shows illumination direction for clarity. Image credit: NASA/ Johns Hopkins University Applied Physics Laboratory/Carnegie Institution of Washington.*

5.4.3 Evidence of Vent Migration from Faculae

Supporting evidence for vent migration comes from some of the surrounding faculae. Although the original appearance of a facula must depend on the strength and duration of the eruption, faculae are expected to fade with age as a result of space weathering and impact gardening, e.g. Besse *et al.*, (2020), resulting in the muting of their spectral signature and shrinkage of their visible extent. Here I examine the three clearest examples I have seen of asymmetrical faculae, further may be discovered using more detailed albedo analysis, or chemical analysis such as those undertaken by Besse *et al.* (2020). The unnamed facula inside Picasso crater (Figure 5.10.a,b) shows an uneven distribution along the length of the arcuate vent site. The facula is most intense around the north of the vent, correlating with the position of the roughest textured

area of the vent floor and walls, which I would expect to indicate the most recent eruptions. The facula is weaker south of the vent, and correspondingly the vent floor and walls in the south show smoother textures suggesting that this area is older and is either mantled by later eruptions and then degraded or just degraded by space weathering.

The second example of an asymmetric facula is associated with the compound vent in Figure 5.10.d, which is a cluster of vents around the centre of a complex crater whose floor is covered by a plains unit (likely to be lava). The spectral anomaly is stronger to the east of this compound volcanic vent site, and the east of the vent site is texturally rougher than the west, suggesting it is younger, which is consistent with the more intense area of facula also being younger.

A third example is Nathair Facula, whose mid-point is displaced north-eastwards by between 10 and 30 km north or northeast relative to the centre of its vent complex (Rothery *et al* 2020a). This is consistent with the textural evidence with a rougher, less mantled floor to the north of the vent, suggesting that the youngest activity was in the north (Figure 5.8).

These three asymmetric faculae examples where intensity correlates with the age inferred by superposition relationships add corroborating evidence that some vents have undergone multiple eruptions, with the locus of activity migrating between eruption events. Better constraints on the rates at which faculae fade with age might improve constraints on when the activity occurred, especially in conjunction with spectral data to map out the extents of faculae (e.g., Besse *et al*., 2020).

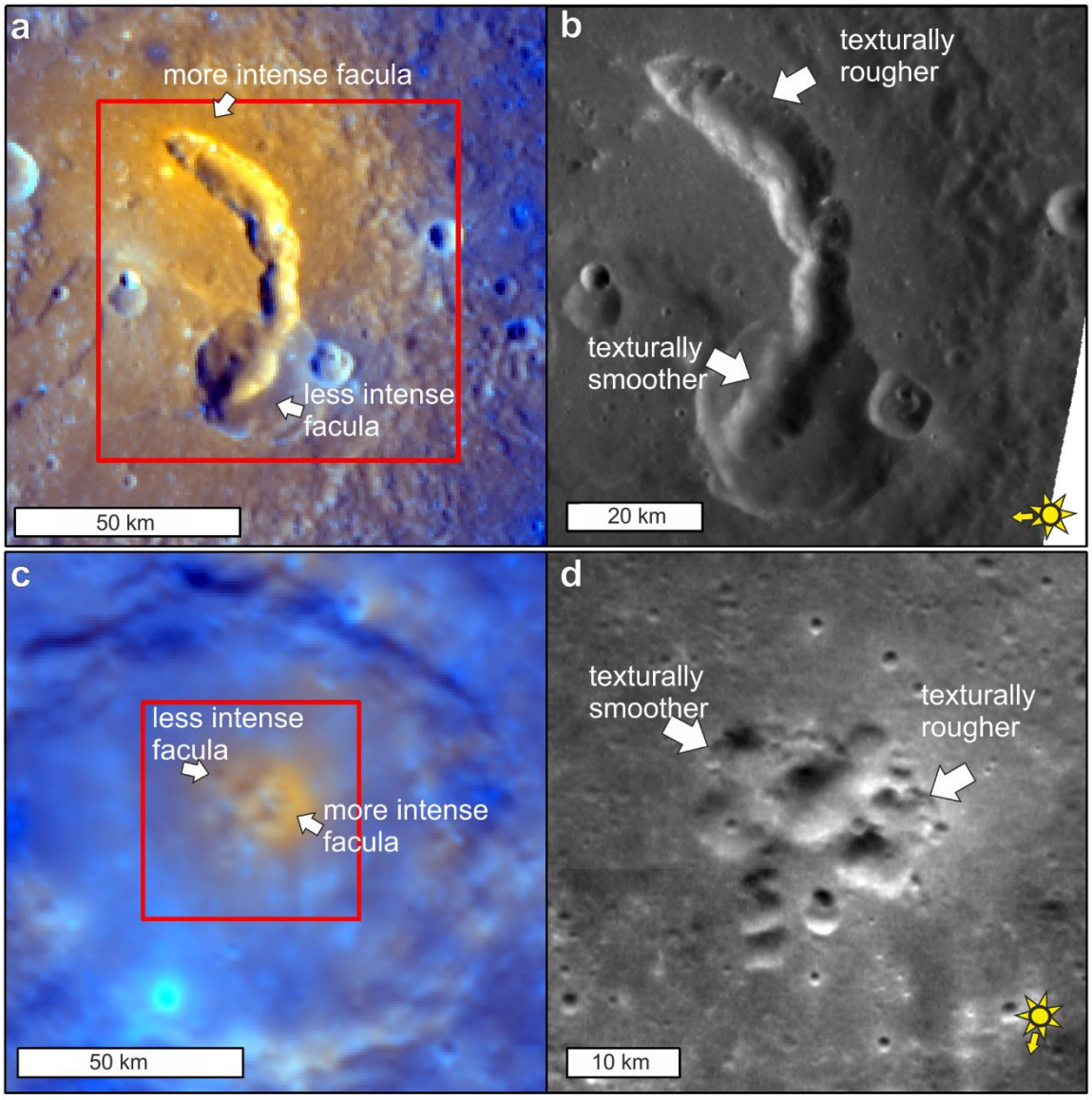

Figure 5.10 Evidence for multiple eruption events from Faculae. ***a.*** *Picasso crater, showing the vent and facula in enhanced colour basemap* (Denevi *et al* 2018a). *The red box shows the location of b.* ***b.*** *Image EN0219816577M showing the compound vent inside Picasso crater (107 m/pixel).* ***c.*** *An unnamed facula within an unnamed impact crater; image centred at -6.5° E -48.4°N on enhanced colour basemap* (Denevi *et al* 2016). *The red box shows compound vent sites in d.* ***d.*** *Detail of the compound vent sites inside the faculae seen in c. Image EN1034978249M (182 m / pixel). North towards the top of images. Image credit: NASA/ Johns Hopkins University Applied Physics Laboratory/Carnegie Institution of Washington.*

5.4.4 Vents within H-14 (Debussy quadrangle)

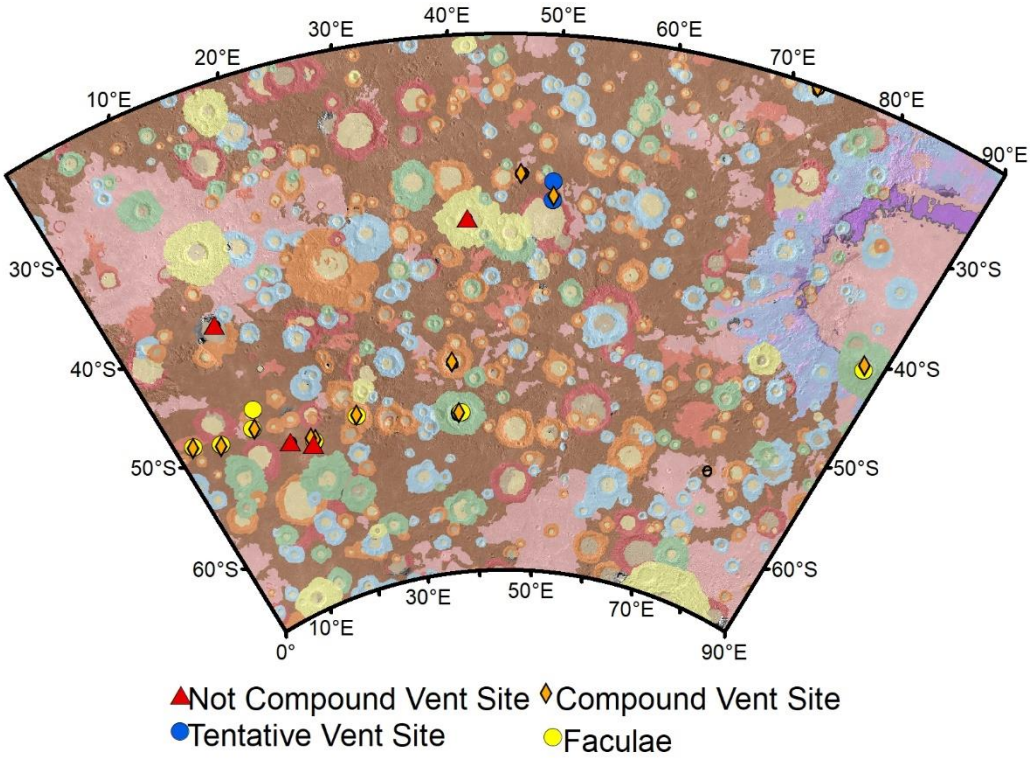

Figure 5.11 Location of faculae, and pits without faculae on the geomorphic map, with BRD basemap.

As part of mapping (Chapters 3 and 4), I found that H-14 hosts eight faculae (Figure 5.11) and 19 vent sites. Four out of 19 vent sites are not associated with a facula; this 21% of vents without faculae is higher than the 13% globally (Table 5.3), though it is a small sample size and so may not be statistically significant. The ratio of vents that are compound (75%) compared to non-compound (25%) is the same as for the global population (given the relative sample size).

Table 5.3 Classification of Vents in H-14

Compound	Total	Confident Classification Percentages
Insufficient Image Quality	1	
Not Compound	4	25%
Compound	12	75%
Tentative Compound	2	
Grand Total	19	16

5.5 Discussion

I now describe the general inferences and interpretations that follow from these results and speculate on their implications (5.5.3)

5.5.1 General Implications

The presence of such a high proportion of compound volcanic vents on Mercury suggests that multiple events occurred at most vent sites, with the migration of the locus of the eruption in increments that can total up to 50 km (for example, Figure 5.10). The question then arises as to whether these formed polygenically (from multiple eruptions) as part of a sequence within the same eruption (monogenetic).

It is not possible to quantify the duration between eruptive episodes at successive vents within a compound vent site. For example, vents have too small an area for reliable model ages to be derived by using size-frequency distribution of superposed impact craters. Also, secondary craters, which are typically clustered, may dominate the crater population up to 10 km crater diameter (Strom *et al* 2008, 2011), further complicating such estimations. Additionally, pyroclastic materials may not preserve impact craters in the same way as the surrounding regolith, with the result that size-frequency distributions might not be comparable with the standard isochrons (Lucchitta and Schmitt 1974). However, visibly contrasting densities of ~100 m diameter impact craters on the floors of individual depressions within compound volcanic vents at Agwo and Nathair Faculae (and perhaps in the vent in Kipling Crater; Figure 5.6) correspond with the order of formation deduced from both crosscutting relationships and differences in surface roughness. I have found no counterexamples where the sequence of events deduced from cross-cutting relationships is contrary to the relative ages suggested by the density of small craters (fewer in younger component-vents) or textural roughness (rougher in younger within a vent site). This supports the suggestion that, in at least some of these vent sites, time gaps occurred between the formation of the oldest and youngest component vents.

Examination of internal structure often reveals smaller vents crosscutting, or entirely within, larger vents (e.g., Figure 5.3.c, Figure 5.6, Figure 5.7). This is consistent with the most recent eruptions being less powerful or briefer than previous ones, as might be expected in a waning volcanic system. In the case of the vent in Nathair Facula, its last major eruption appears to occupy ~1/8th of the vent complex by area. However, I note that significant eruptions would probably destroy evidence of pre-existing smaller vents, whereas smaller vents will crosscut, but not obliterate, larger vents. Thus, I cannot rule out preservation bias in our inference of waning volcanism. There is no significant difference in the ratio of compound vents between vent sites with and without a facula. Assuming space weathering and regolith mixing both dull faculae, then this suggests that the features that describe compound volcanic vents are weathered at a lower rate than faculae.

The putative lava dome in Example 4, and pits at the vent site within Nathair Facula, both suggest later phases of less destructive activity at these vent sites and a switch from explosive to effusive volcanism in the former example.

The composition of faculae around vents is not necessarily the same in every case (Besse *et al* 2020). Furthermore, spatial variations of the intensities of faculae around vent sites (Section 5.4.2) indicate either that eruption strength or duration varied within vent sites or that some faculae are sufficiently older than others to exhibit different degrees of muting by space weathering and mixing into the background by impact gardening. These factors are consistent with vents having undergone multiple eruptions. A detailed study examining the distribution of faculae around vents in terms of composition and thickness may help to refine the eruption history of compound volcanic vents.

While the 21% of vents without faculae found during the H-14 mapping may not be statistically significant compared to the 13% found in the global survey, it should be noted that I only discovered two of these vent sites after I had completed the global survey, and without these additional vent sites, the vent sites without faculae in the quadrangle would be 12% of vent sites. Vent sites are easier to identify if they have a facula, so the global databases of vent sites probably have a bias in the data towards the identification of vent sites that still have a facula, and this possible bias needs further study.

5.5.2 How did the Eruptions Occur?

The possible mechanism for the formation of these vents is either explosive excavation, collapse into a dyke, or a combination of these two (Jozwiak *et al* 2018). I consider explosive excavation as more probable because I did not observe any surface features indicative of ring faults, as usually associated with terrestrial and Martian caldera collapse, in agreement with (Rothery *et al* 2014).

Some terrestrial examples of phreatomagmatic and kimberlite eruptions can undergo migration of the diatreme during a single eruption. Being a continual migration process, such migration is unlikely to leave septa dividing the vent (White and Ross 2011), but this could be analogous to the process on Mercury resulting in vents with an undulating brink but no internal features (which I classified as non-compound vents). Multiple separate eruptions using the same conduit with pauses could, however, lead to multiple component vents at a locality (Fulop and Kurszlaukis 2017) manifested as discrete vents or vents divided by septa.

If compound vents form as collapse pits above a dyke, collapse occurs into the dyke that had fed them (Wilson *et al* 2011, Wilson and Head 2017). A flat, rather than bowl-shaped, floor is expected, as found within lunar rilles (Wilson *et al* 2011), although if the tip of the dyke were deeper, this could result in bowl-shaped pits rather than a flat-floored rille (Jozwiak *et al* 2018). This would suggest that each component vent was formed sequentially as part of the same eruption. This may match with sequential vent sites in the style of the example within Picasso crater (Figure 5.10). Dyke-tip-collapse might explain the formation of the small young pits on the vent floor (Figure 5.8.c).

Given individual vents' bowl-like profiles suggested by photogeology (e.g.Figure 5.7, Figure 5.9), laser altimeter tracks (Thomas *et al.,* 2014b) and digital elevation model data (e.g. the 'simple vents' in Jozwiak *et al*. (2018) and Thomas *et al*. (2014b)), I favour excavation by an explosive eruption as the primary pit-forming process. However, I note that it seems inevitable that after the termination of eruption, various collapse

processes would have choked the evacuated conduit and modified the surrounding pit walls. Both explosive excavation and collapse are probably needed on Mercury to explain the variety of features seen.

Regardless of formation mechanism, the asymmetry of the facula at Picasso and the progression in eruption identified in the vent site at Agwo (Rothery *et al.* 2014) and in example 2 (Figure 5.10.c,d) suggests that at some compound vent sites there were significant pauses between the formation of individual component vents. To enable this, some form of mechanism is needed to recharge the volatiles.

5.5.3 Volatile Recharge

For multiple eruptive events to occur, each eruption must be followed by a recharge of volatiles capable of exsolving as gases in the next eruption. Such recharge could take place by (i) recharge in the source (mantle volatiles), (ii) recharge within the melt (for example, by assimilation or fractionation), or (iii) processes within the feeder dyke (Head and Wilson 2017).

5.5.3.1 Mantle Volatiles

The only pyroclastic deposit large enough to have had its composition measured by MESSENGER is Nathair Facula (Weider *et al* 2016), which is relatively depleted in both sulfur and carbon, suggesting this is the volatile source. This is consistent with iron silicates in the magma having been reduced by the carbon (McCubbin *et al* 2017) and sulfur to generate the gases needed for explosivity, causing sulfur and carbon to be absent from the solid pyroclastic ejecta thought to comprise the facula, the volatile component of the melt is most likely to be dominated by CO and SO_2 (Weider *et al* 2016, Kerber *et al* 2009). The partial melting zones in Mercury's mantle are rich in volatiles (Vander Kaaden and McCubbin 2015). This means the melt likely originates with volatiles inside it, and continued direct connections between the mantle and the surface would allow volatile-rich melts within the mantle to ascend and resupply volcanic vents with new volatiles.

It is often stated that the compressive nature of Mercury's tectonics is not conducive to magma ascent (Tosi *et al* 2013, Michel *et al* 2013, Byrne *et al* 2016). This may explain why there are only about 300 identified explosive vent sites on the entire planet. Repeated eruptions at individual sites imply long-term connectivity to the melt source. The local stress regime must allow repeated magma ascent for eruptions to recur at these sites. It is not surprising, therefore, that the majority of volcanic vents occur within impact craters because the crust below crater floors is expected to be highly fractured (Klimczak *et al* 2018). However, this does not explain all the identified vents: the vent inside Nathair Facula is not inside an impact structure, for example, so other causes of localized differences in lithospheric stresses may be at play, such as variable crustal composition, which can lead to local differences in strain (Galluzzi *et al* 2019).

5.5.3.2 Crustal Volatiles

A second explanation is resupplying the melt with volatiles from the crust. Mercury's crust is rich in volatile elements with up to 4 wt% sulfur (Nittler *et al* 2011). The low reflectance material (LRM), which is probably derived from the lower crust, may be enriched in other volatiles, including up to 5 wt% carbon (Peplowski

et al 2016, Murchie *et al* 2015, Klima *et al* 2018). The LRM may now be present as horizons at several depths in Mercury's crust, occurring as ejecta layers redistributed from a graphite-rich primary crust or buried by ancient lava flows (Vander Kaaden and McCubbin 2015, Peplowski *et al* 2016, Klima *et al* 2018). The subsurface lateral continuity of the LRM source has yet to be constrained, but LRM may constitute a widespread source of volatiles that could be assimilated by melts during ascent. This is supported by the pitted ground which is thought to be formed by lava being disturbed as it flows over volatile-rich substrates (Thomas *et al.*, 2014b) showing the planet's crust is rich in volatiles (at least in some locations).

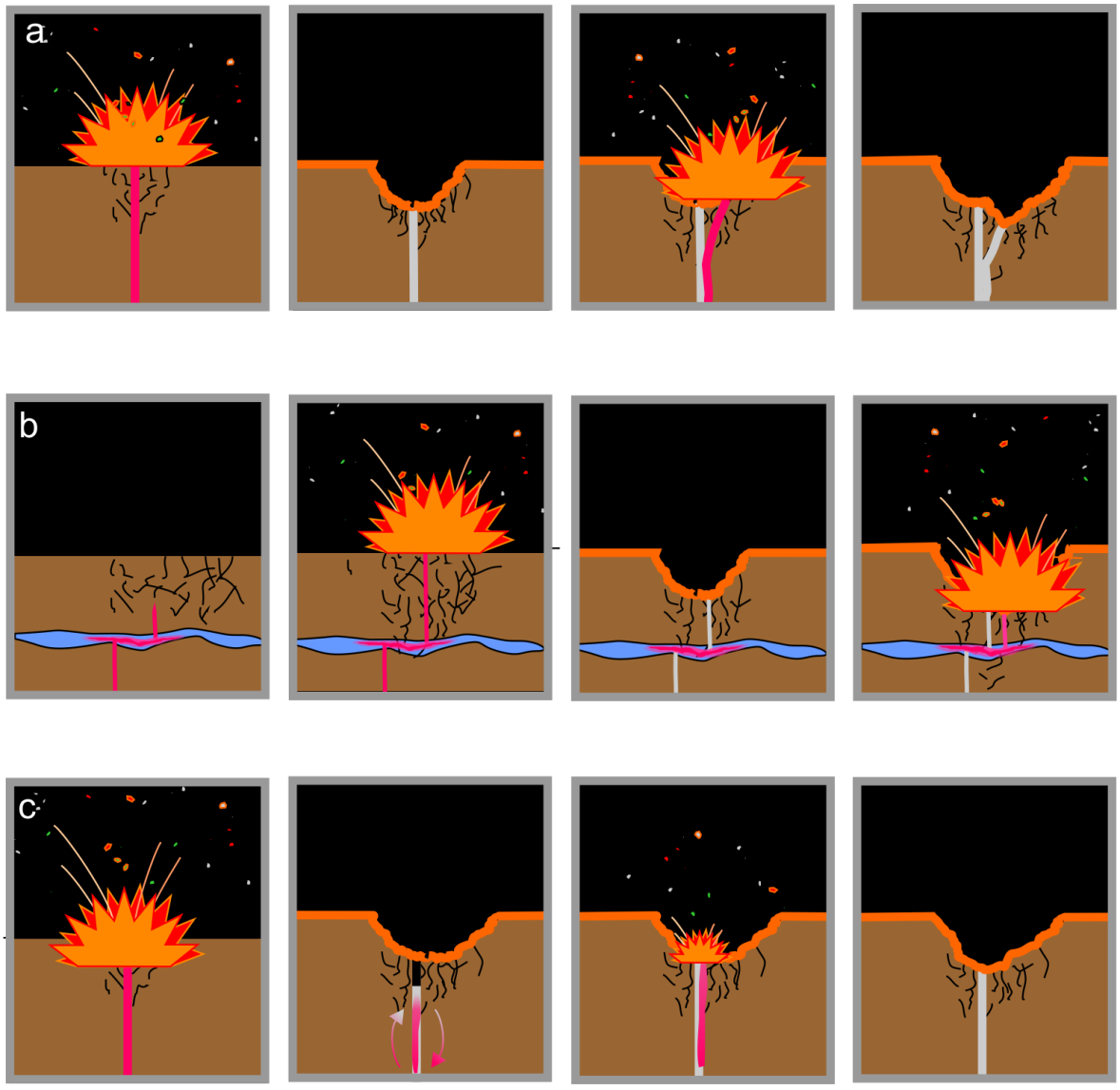

Figure 5.12 Schematics of different volatile recharge methods. a. repeated supply from the mantle, showing dykes rising up and erupting at the same site repeatedly forming a compound vent. b. assimilation from a volatile-rich layer: an intrusion passes through a horizontal layer of volatile-rich material (blue), multiple eruptions are generated through cycles of eruption and assimilation of volatiles in the volatile-rich material, generating new eruptions from the same stock of magma. c. dyke overturn: multiple eruptions are generated by convective overturn of the magma within a dyke bringing volatile-rich melt close to the surface, enabling subsequent eruptions. Authors own schematic.

Assimilation of stratigraphically controlled volatiles (i.e., in layers) into a dyke is likely to be inefficient due to the relatively small surface area of a dyke in contact with any horizon in the crust, so I consider this an unlikely configuration. A sill morphology would be more effective at assimilating volatiles because sills have significantly more surface area that could be in contact with a horizontal or sub-horizontal volatile-rich layer (Figure 5.12.b). In this context, order to assimilate volatiles multiple times would require either stopping (collapse of the wall or ceiling above a sill or larger intrusion) or migration of volatiles through the crust to replenish the volatiles before each eruptive event. Migration of volatiles in the shallow crust (at least 24 m depth) has been suggested as a mechanism for continued hollow formation (Wang *et al* 2020); however, the depth and mechanism (other than partially insolation driven) of this migration is not yet constrained (Wang *et al* 2020).

Current remote sensing data for Mercury provides insufficient evidence to be able to identify whether a sill or dyke configuration is more likely, although the lack of observed floor deformation (specifically fracturing) in craters that have explosive vents on their floors makes shallow sills unlikely, and so favours dykes or deep sills (Jozwiak *et al* 2018, Thomas *et al* 2015).

5.5.3.3 Dyke overturn

A third mechanism for volatile recharge is melt overturn within a dyke, in which volatile-rich magma is brought up from deeper in the dyke to replace an upper zone that had been passively or eruptively degassed (Head and Wilson 2017). Additionally, if there is a main dyke at depth when the critical pressure builds up, it may spawn smaller dykes which would lead to smaller local eruptions within a system (Jozwiak *et al* 2018). As the magma is stored in the dyke, it does not need local stress regime differences to operate; no further connection with melt sources is required (Figure 5.12.c). This mechanism would allow only relatively short intervals between eruptive events before the magma solidified and could not account for the differences in the frequency of small scale craters observed on the floor of the different parts of the Agwo Facula compound vent (Rothery *et al* 2014), but could be associated with other compound vents with a deeper feeder dyke with smaller individual offshoots each producing an individual vent site. While dyke overturn may explain some compound vent sites, it does not match with those that suggest intervals between eruptions

Bearing in mind Mercury's compressive nature and accepting the tentative evidence for prolonged pauses between eruptions at each site, I suggest that the existence of polygenetic vents implies that long-lasting local stress anomalies must have been present to allow continued melt supply from the mantle in at least some examples.

5.6 Conclusions

Where image data have adequate resolution and quality, I find that at least ~70 % of volcanic vent sites on Mercury are compound, reflecting multiple eruption loci and potentially a polygenetic history. Many of the large vents that I do not classify as compound may have lost their internal structures over time and so could also be polygenetic, or could have formed by migration of the locus of an eruption in a fashion insufficiently punctuated to leave intervening septa resolvable with current imagery.

Vent sites without faculae are harder to identify and very likely underrepresented in most studies of vent sites on Mercury. These vents and their faculae should be high priorities for study by BepiColombo.

At compound vents, the volatiles within the erupting magma, necessary for an explosive eruption, were recharged, either at the melt source, in the crust, or by some process within magma stored in the crust. The requirement of volatile recharge has implications for the internal plumbing of these sites, suggesting that, once established, eruption sites can undergo multiple events occurring over a prolonged but currently unconstrained duration. If additional volatile supply was from mantle sources, then the local stress regimes must have allowed the repeated connection between source and vent. Otherwise, volatiles must have been assimilated from the crust, which probably requires recharge by the migration of volatiles within the crust.

My results show that migration of the locus of eruption must be considered when studying the extent of the explosive ejecta deposits that constitute faculae. A single central vent source is often modelled (Kerber *et al* 2009, Brož *et al* 2018), but the dynamic histories shown by our examples suggest that these sites relocate over time. The build-up of faculae from multiple eruption loci could extend the area covered by faculae without needing stronger eruptions, meaning that models using single-source point estimates would over-estimate the eruptive power.

6 A Fault Exposed on Mercury

6.1 Introduction

During my study of Mercury's volcanic vents (Chapter 5), I identified one vent site where I could see a tectonic fault as a fault trace (the visible intersection of a fault with the surface of a planet) running down the side of the vent. This is the first direct observation of a fault surface in three dimensions on Mercury. Although I found other examples of vents crossing lobate scarps, I found only this example where the fault trace is clear, and the geometry is measurable. In this chapter I outline the process I went through to try and measure this fault then place this in context with the current understanding of tectonics on Mercury. A version of this chapter has been accepted into publication by *Planetary and Space Sciences* (Pegg *et al* 2021b).

6.2 Background

Tectonic and volcanic processes have shaped Mercury's surface over its geological history (Strom *et al* 1975, Watters *et al* 2015, Head *et al* 2008, 2009, Solomon 1978). Contractional features are the dominant tectonic landforms on Mercury. Contractional tectonism is manifest in features such as lobate scarps, wrinkle ridges, and high relief ridges (Dzurisin 1978, Watters *et al* 2009c).

A lobate scarp is an asymmetrical ridge up to two kilometres high that is the surface expression of a thrust fault with the hanging wall elevated above the footwall (Strom *et al* 1975, Watters and Nimmo 2010). The hanging wall is flexed over the footwall to form a slight anticline; some lobate scarps even show an occasional small scale extensional graben at the flexure (Banks *et al* 2015), the only setting where grabens have been found on Mercury outside large impact basins.

Wrinkle ridges are usually more symmetrical and lower relief than lobate scarps, and are probably related to asymmetrical antiform folding over a steeper fault than at lobate scarps (Strom *et al* 1975, Watters and Nimmo 2010, Watters *et al* 2009a). Wrinkle ridges are thought to be manifestations of local thin-skinned tectonics (Bryan 1973, Crane and Klimczak 2019).

High relief ridges are broad, symmetrical topographic landforms, interpreted as reverse faults creating the wide broad ridge (Dzurisin 1978, Watters and Nimmo 2010). Another possible interpretation is a lobate scarp type structure with an antithetic fault behind it, creating a broad ridge. Initially, these three contractional tectonic types were thought to be distinct tectonic features (Dzurisin 1978). Still, subsequent observations show high relief ridges can often transition into lobate scarps and thus are part of a continuum of landforms (Watters *et al* 2009c, Byrne *et al* 2014). An example of this transition is Enterprise Rupes; it could be considered a high relief ridge outside the Rembrandt impact basin, inside it is more like a lobate scarp (Chapter 4.4.1.3), the eastern strike extension of Enterprise transitions into wrinkle ridges (Chapter 4.4.1.3, Ferrari *et al*., 2015; Watters *et al*., 2015). It is, therefore, reasonable to consider all shortening structures on

Mercury as part of a continuum, with varying dips of fault and scale, and material they are propagating through accounting for the differences in surface expression (Watters and Nimmo 2010, Byrne *et al* 2014, Klimczak *et al* 2015). It is worth noting that these are all hypothesis for the subsurface structure, and the actual subsurface geometry is unknown.

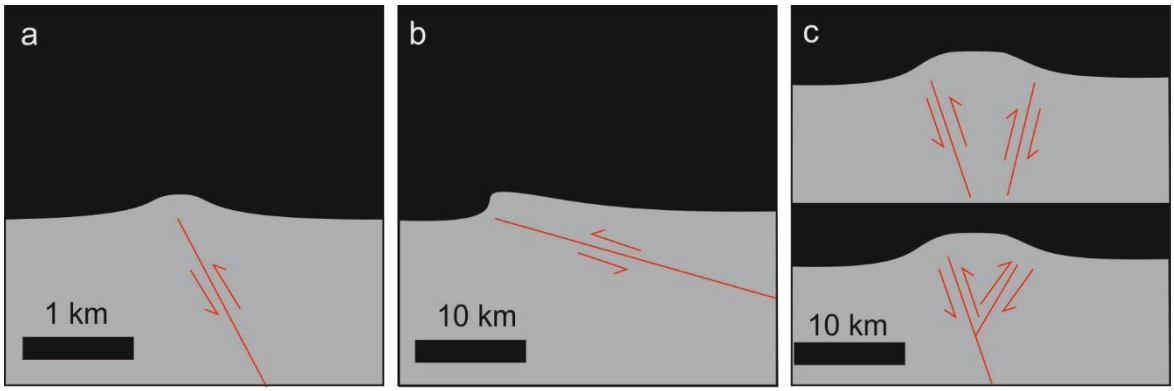

Figure 6.1 Hypothesised underlying structure for different types of contractional structure. a. wrinkle ridge, b. lobate scarp. c. two different styles of high relief ridge: top: two reverse faults creating a ridge, bottom: a main fault with an antithetic fault. Authors own schematic.

Key terminology related to faults in this chapter is defined in Figure 6.2. Terms include the fault surface, which is the surface along which the fault has moved; strike, the azimuth at which the fault surface intersects the horizontal; and the dip, the angle at which the fault surface descends below the horizontal (Neuendorf *et al* 2005).

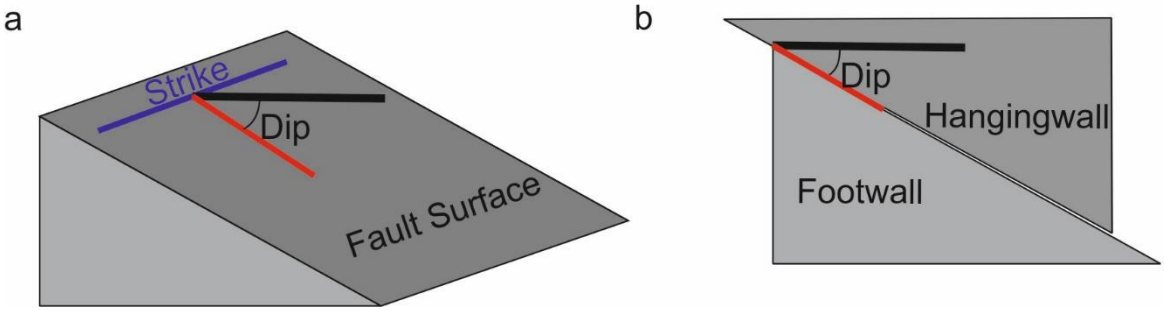

Figure 6.2 Fault nomenclature schematic. a. 3D view of a fault surface showing the strike, dip and fault surface. b. a sectional view of a fault with the hangingwall, footwall and dip. Authors own schematic.

The stresses in Mercury's crust that generated contractional tectonism have multiple possible origins (Chapter 2.7.6), including; global contraction (Watters and Nimmo 2010), tidal despinning (Melosh and Dzurisin 1978, Watters and Nimmo 2010, Burns 1976, Crane and Klimczak 2019), true polar wander (Matsuyama and Nimmo 2009), and mantle convection (King 2008). Some of the faulting is localised at the junction between regional geochemical terrains (Galluzzi *et al* 2019), or at the edges of Smooth Plains confined within impact basins (Fegan *et al* 2017). Although a combination of factors probably influences many of the visible faults, the dominant cause of contractional tectonics on Mercury is widely accepted to be the global contraction of the planet (Klimczak *et al* 2015). Mercury's relatively high ratio of surface area to volume compared to other planets in the solar system means that it has undergone significant cooling,

which has led to shrinking (Watters and Nimmo 2010). Thermal and compositional models of the planet provide a wide range of estimated shrinking; the planet could have shrunk by between 0.6 and 10 km radially (Solomon 1977, Grott *et al* 2011, Watters and Nimmo 2010).

Byrne *et al.* (2014) calculated Mercury's global contraction from a global inventory of contractional features combined with estimates of fault displacement associated with each type of surface expression. The amount of horizontal movement across a thrust fault can be determined from the measured displacement of features on either side, most usefully offset crater rims (Galluzzi *et al* 2015). The steeper the average fault dip, the less horizontal movement is accommodated by each fault for a given horizontal offset, and so the lower the amount of global contraction necessary to account for it. The derived reduction in global radius recorded by Mercury's crust is 7.1 km if the average fault dip is 25°, but as little as 4.7 km if the average fault dip is 35° (Byrne *et al* 2014). An understanding of the average dip of the faults on Mercury is therefore vital to constrain contraction estimates and, therefore, to understand Mercury's thermal history. Estimates made using the shortening and vertical offset of craters that straddle faults on lobate scarps to calculate fault dip range between 6 ° and 57° with an average of 25° (Table 6.1, Galluzzi *et al*., 2019, 2015). Table 1.1 includes three estimates on Enterprise Rupes, ranging from 15° to 57°, with the steepest being in the west. Until now, no-fault dip on Mercury has been measured by direct means.

Table 6.1 Dips of Faults on Mercury measured indirectly using crater offset; ID refers to crater measurement in the source, '' notes craters on Enterprise Rupes.*

Source	ID	Dip
Galluzzi *et al*., 2015	01-A	31°
Galluzzi *et al*., 2015	02-A	53°
Galluzzi *et al*., 2015	03-A	42°
Galluzzi *et al*., 2015	04-B	14°
Galluzzi *et al*., 2015	05-C	20°
Galluzzi *et al*., 2015	06-D	29°
Galluzzi *et al*., 2015	07-E	9°
Galluzzi *et al*., 2015	08-F*	57°
Galluzzi *et al*., 2015	09-F*	30°
Galluzzi *et al*., 2015	10-F*	15°
Galluzzi *et al*., 2015	11-G	26°
Galluzzi *et al*., 2015	12-H	7°
Galluzzi *et al*., 2015	13-I	12°
Galluzzi *et al*., 2015	14-J	45°
Galluzzi *et al*., 2015	15-K	10°
Galluzzi *et al*., 2019	ER/Unnamed	6°
	Mean	**25°**
	Median	**23°**
	Min	**6°**
	Max	**57°**

6.3 A Fault's Geometry Revealed

Here I describe the first reported example on Mercury where the local topography exposes a fault trace sufficiently well that its dip can be measured (as opposed to being inferred). My example comes from the inner wall of a pit interpreted as an explosive volcanic vent.

As described in chapter 5, explosive volcanism is manifest on Mercury through endogenic pits (vents) that are up to tens of kilometres across and several kilometres deep. Faculae often surround vents: these are high albedo, spectrally red features that are probably explosive ejecta from the eruptions (Chapters 2.6.2 and 5, Goudge *et al*., 2014; Head *et al*., 2008). Unlike impact craters, these vents are non-circular and lack a raised rim, and hence I refer to the break of slope at the edge of a pit as the 'brink' to avoid confusion with the rim of an impact crater. High-resolution studies of these vents suggest that they did not form through caldera collapse (Rothery, Thomas and Kerber, 2014; Thomas *et al.*, 2014b), where the emptying of a magma chamber leads to subsidence creating a large volcanic crater. Instead, the vents are interpreted to be excavated by an explosive eruption, perhaps analogous to kimberlite pipes on Earth (White and Ross 2011).

During the process of reviewing volcanic vents on Mercury (Chapter 5), I identified several vents that occur directly on a tectonic fault (Figure 6.3). The fault scarp is not usually visible within these vents. Many factors could contribute to this, such as the vent post-dating the fault movement, space weathering, volcanic activity covering the scarp, poor illumination, or low image resolution. All of these would be excellent targets for BepiColombo imaging, especially the example in Figure 6.3a which is my second-best candidate. However, the only clear example that I have identified is one vent within Vazov crater (147.6°E, -65.6° N) that shows a small fault visible to the north wall of the vent as a ridge expressed as a trace on the internal vent wall (Figure 6.4). This is, therefore, a fault surface that is exposed in three dimensions.

Outside of the vent is a contractional ridge 3 km wide, 30 km long, which strikes NW-SW. It is most visible on the crater floor but continues as a ridge NW of the crater. The facing direction of the fault would be unclear if the vent did not expose the fault, showing the north-east trending within the vent. The section revealed in the vent wall shows that the main fault dips north. The fault trace is visible on the west wall of the vent but is hidden by the vent-wall shadow in the bottom and east of the vent (Figure 6.4 a, c).

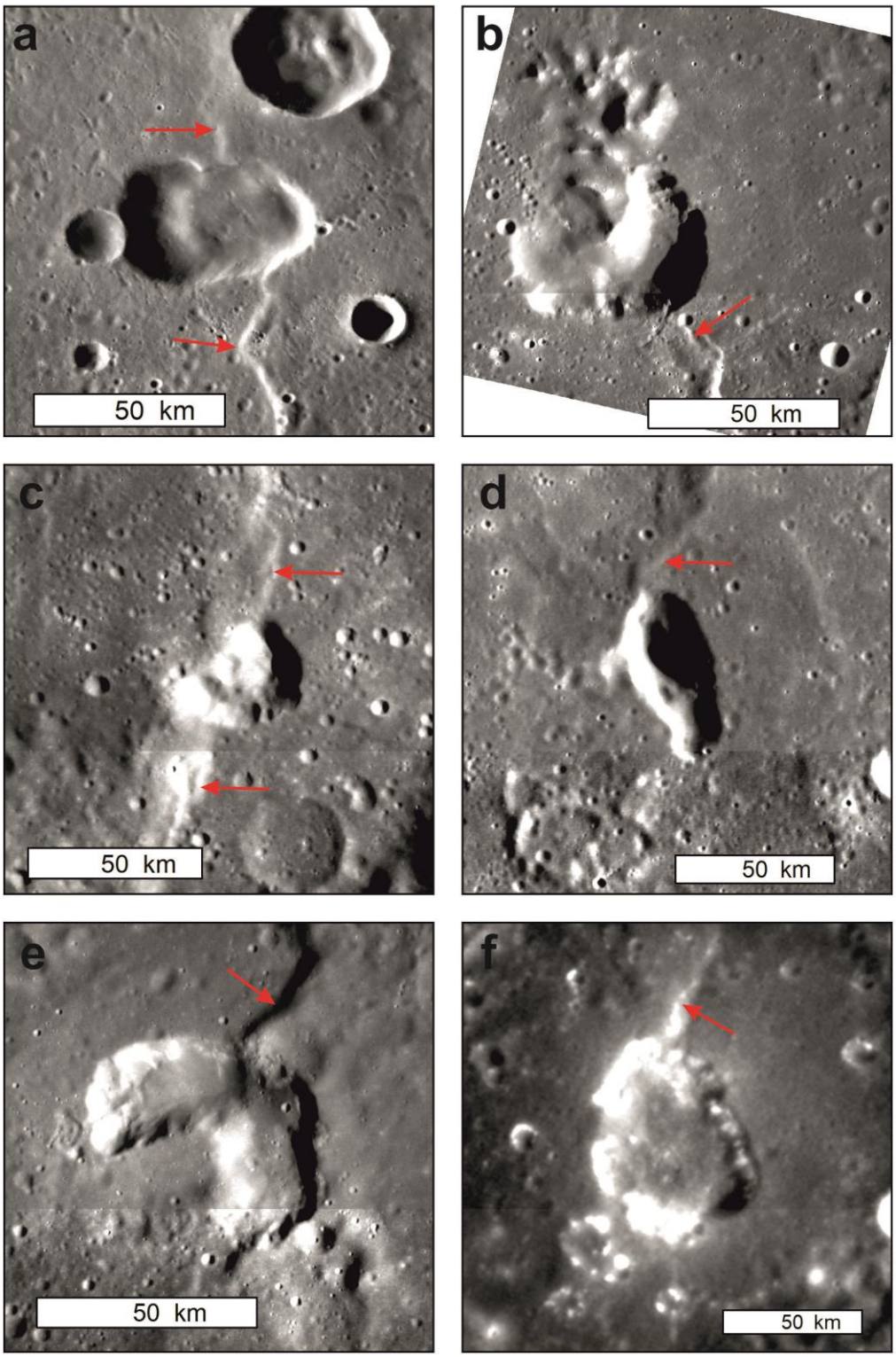

Figure 6.3 Selection of volcanic vents which are coincident with contractional structures, but which do not adequately reveal the fault surface in three dimensions. Red arrows point to scarps. a: image: EN1014936140M, centre: 148°E, 24°N. b: image: EN1048654092M centre: 67°W, 21°N. c: image: EN1021068336M centre: 105°W, 24°N. d: image: EN0258310462M centre: 162°W, 17°S. e: image: EN0257073440M centre: 112° W, 15°N. f: image: EN0131771793M centre: 30° E. 27°N.

6.4 Materials and Methods

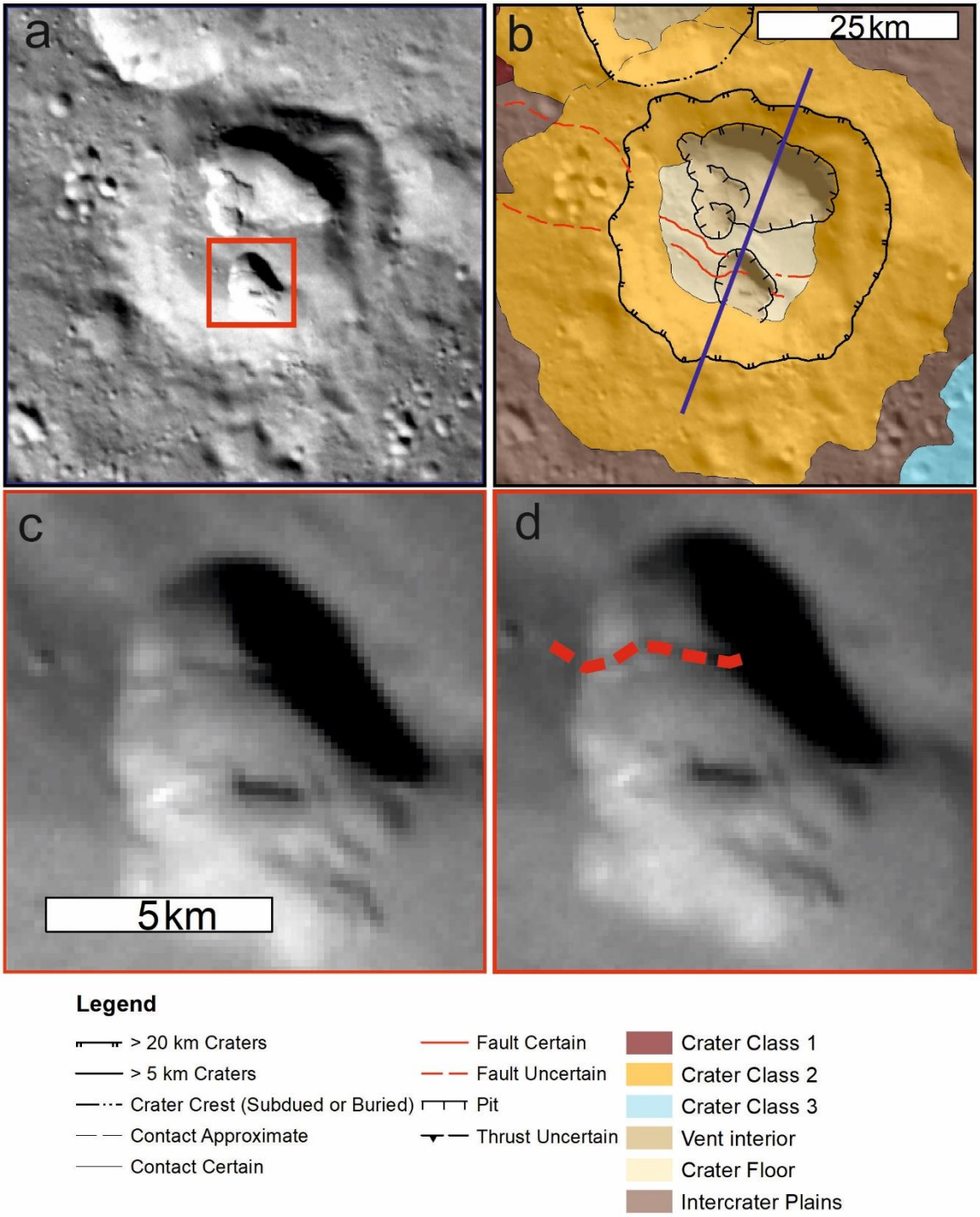

Figure 6.4 a. Image EN0261054374M, overview of the fault trace within Vazov crater as well as the location of c and d (red box). Image centre:147°E -65.5°N. b. interpreted geological map of the area in a, showing vents and fault location, the purple line shows the location of the section in Figure 6.6. c. Close up of vent within the vent site. d. the same area as c with the fault trace highlighted.

To study the fault, I used images from the Narrow-Angle Camera (NAC) onboard MErcury Surface, Space ENvironment, GEochemistry, and Ranging (MESSENGER) spacecraft (Solomon *et al* 2001). The vent's location in the southern hemisphere means no laser altimeter data are available. I processed the image data using the USGS's Integrated Software for Imagers and Spectrometers (v 3.5.1.7995, chapter 3.3). I produced a geologic map of the vent site based on image EN0231657081M (resolution of 163 m/pixel) using ESRI's ArcGIS software. I chose a sinusoidal projection centred on the vent. I used the mapping methods and units outlined by (Galluzzi *et al* 2016) following USGS (Tanaka *et al* 2011) and Planmap (Rothery and Balme 2018) guidelines (Chapter 3.5) and classified crater degradation state using the 5-class crater system (Chapter 2.5.1, 3.7.1,4.2.1, Kinczyk *et al*., 2020). I produced a digital terrain model (DTM) for the vent site using the AMES stereo pipeline (Broxton and Edwards 2008) using images: EN0231657081M and EN0231356027M. I could not provide vertical control for this DTM due to the lack of laser altimeter data, so I could not eliminate the possibility that systematic tilts related to uncertainties in the spacecraft pointing remained in these data. Thus, I did not use these data to perform dip measurements. Instead, I used shadow measurements on images EN0246250635M (176 m /pixel) and EN0261431434M (197 m / pixel). These are the highest resolution close to nadir images of this feature. Although I examined off-nadir images as well, I elected not to attempt to use these via the method of Barnouin *et al*. (2012) as I would have to correct both the shadow and horizontal measures and this would likely compound any errors from any uncertainty in satellite pointing.

I constructed a line propagating the fault strike from the NW crater floor over the vent. Then produced a second line (x) orthogonal to the strike to where the shadow from the vent intersects the fault trace. Finally, to enable me to calculate the depth of the scarp from the brink at the point the shadow intersected the fault trace, I constructed a line to record the length of the shadow from the intersection of the fault trace with the vent shadow to the brink of the vent. This line was drawn orthogonal to the shadow to get the shadow length (Figure 6.5).

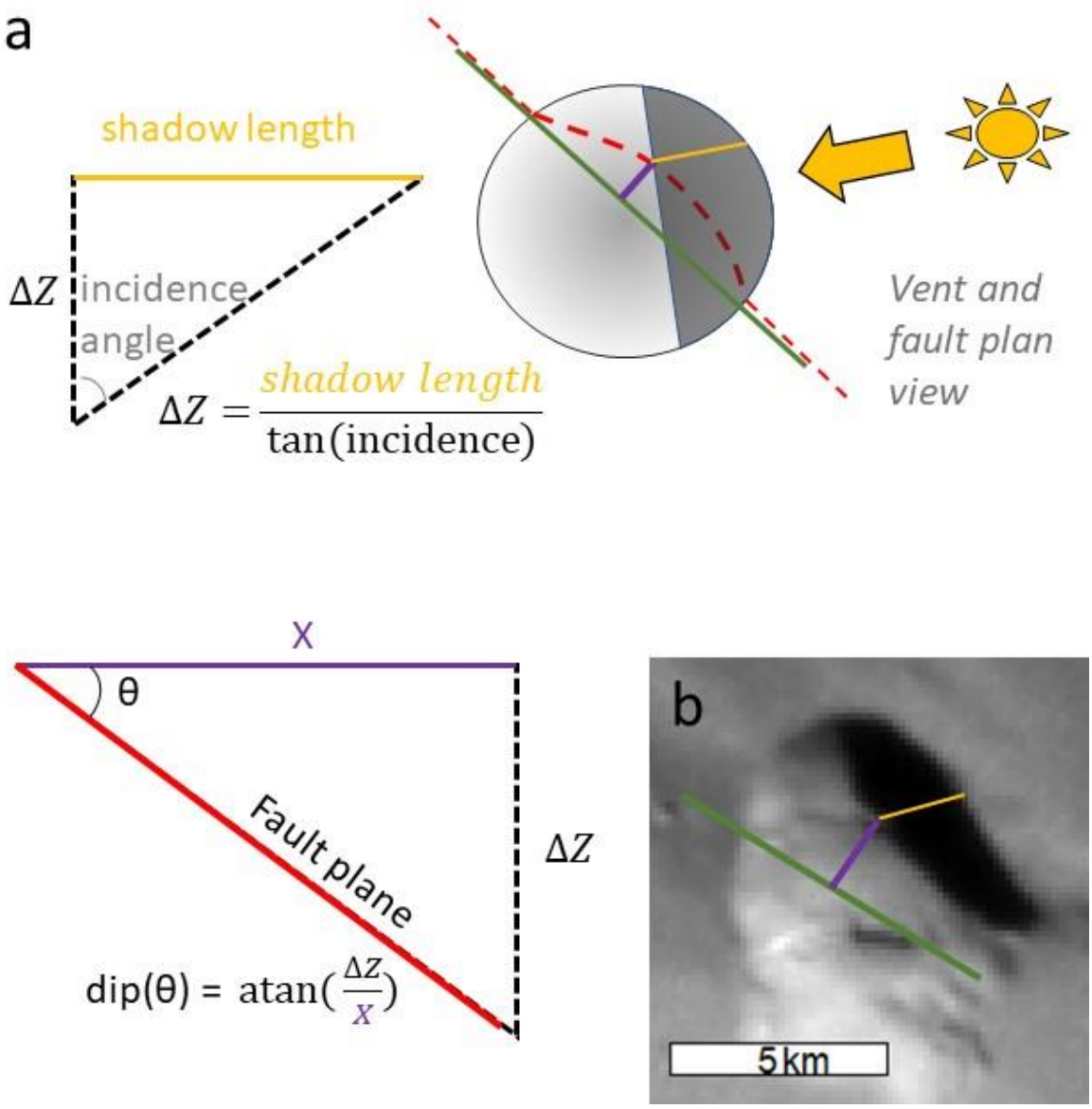

Figure 6.5 a. Method for calculating dip of fault. Redline: fault trace, Greenline: propagated strike, Purple line: horizontal distance between strike and intersection of fault with shadow, yellow line shadow-length measurement, b. Image EN0261054374M, showing how the method is applied to the fault scarp within the vent. Image centre: 147°E -65.6°N.

For each image, I repeated the measurements ten times to reduce measurement uncertainty from digitisation. I calculated the depth of vent at the intersection of the fault and the shadow using basic shadow measurement techniques (Pike 1974, Chappelow and Sharpton 2002) and then calculated the dip using this depth and the horizontal measurement (Figure 6.5). Unfortunately, there are no markers that enable us to estimate the amount of displacement on the fault.

6.5 Results

The geological map and image data show that the faulted vent is one of several vents within and around a degraded impact crater about 30 km in diameter. Beyond the vent, on the crater floor, the fault is clearly marked by the SW side of a 4 km wide ridge. The ridge suggests that this is a small scale version of the high relief ridges (with ridges up to 100 km wide). If so, I would expect opposite of the main fault an antithetic fault on the hanging wall (Figure 6.6). Within the vent itself, while there is an apparent change in slope where this antithetic fault ought to occur, there is no discrete shadow that can be measured. The main fault is clearly visible as a fault trace that cuts obliquely down the western internal wall of the vent and across its floor. In the east of the vent, the location of the fault rupture is in shadow and cannot be discerned, even by increasing the image 'stretch', but it does appear to emerge onto the impact crater floor east of the vent. The fault structure appears to continue beyond the vent-hosting impact crater to the northeast but is less apparent there than within the crater.

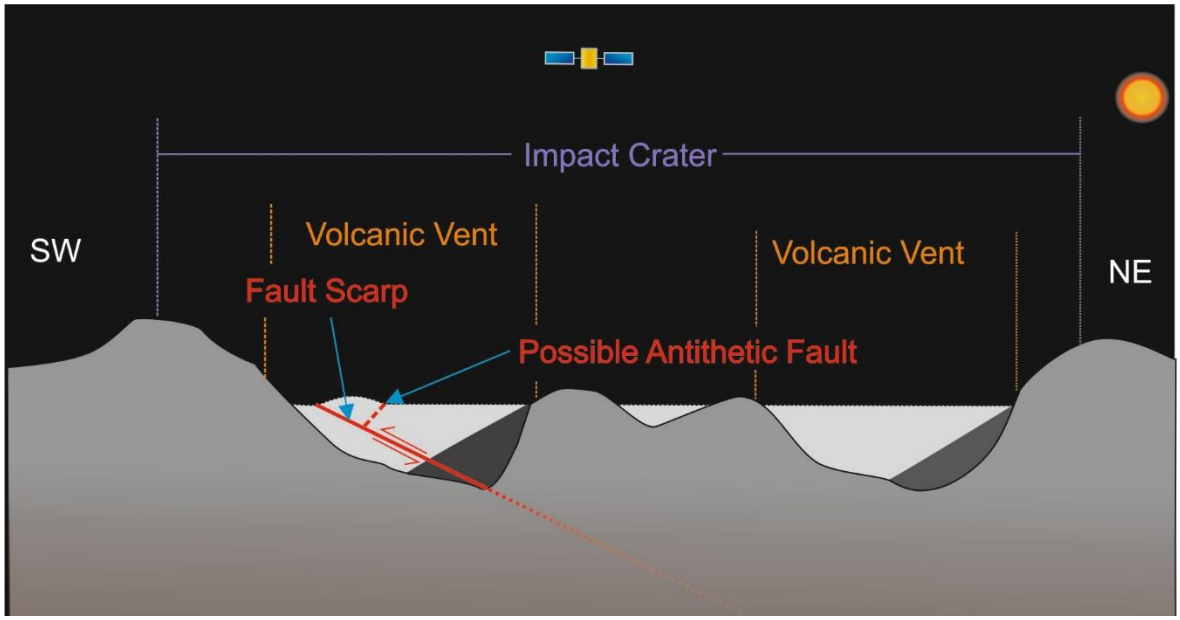

Figure 6.6 Illustrative cross-section of faulted vent site, not to scale.

I show my estimates for the fault surface dip from the two images in a box and whisker plot (Figure 6.7), and the means for the two images suggests a mean dip of 28° ±5°. Authors own schematic.

Uncertainties associated with this method arise from (i) issues with pointing, (ii) measurement error, and (iii) image resolution limits. To reduce the pointing issues, I used two nadir images to make measurements, the comparison between two images acquired at different times, allowing us to test whether there was a pointing error offset. The dip measured in EN0246250635M has a mean of 27.8°, and a median of 27.4°. The dip measured in EN0261431434M has a mean of 27.7° and a median of 27.5°. The similarity of the two measurements provides confidence in the technique. By making multiple repeat measurements, I tested the

repeatability of human operators to make the measurement and interpret the location of the strike and shadow intersection. This provides a measurement of the measurement error. Also, I assume that no line can be drawn more accurately than a 1-pixel width. A 1-pixel error resulted in the equivalent of +5.0/-4.7° error in the dip for image EN0246250635M and +5.4/-5.0 ° error in the dip for EN0261431434M (Figure 6.7).

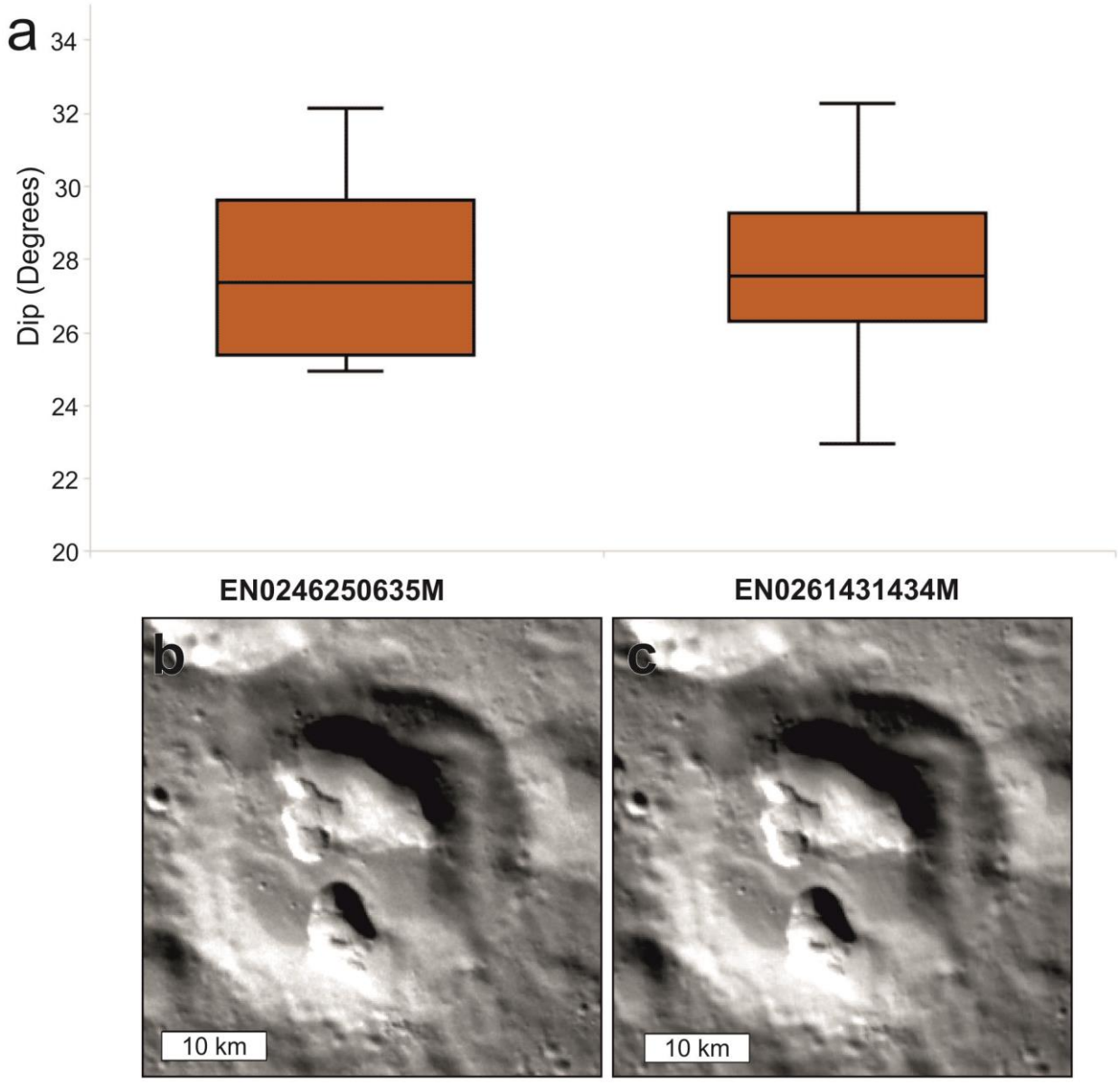

Figure 6.7 a) Box and whisker plot of dip measurements on each image, each image has 10 data point, the vertical lines show the range of data, the box encapsulates the first and third quartile with the central horizontal line the median. b) Image EN0246250635M (c) Image EN0261431434M .

6.6 Discussion

The presence of the vent within the impact crater shows that the vent postdates the formation of the impact crater. The crater degradation state corresponds to the 'partly degraded c2 class of Kinczyk *et al.* (2020), suggesting that it formed during the Tolstojan period (~3.9-4.0 Ga); however, I could not perform a reliable crater size-frequency analysis due to the small area involved. The tectonic fault cuts across the floor of the crater, showing that it was active after the crater formed, and so it was active more recently (though it could have existed before).

The timing of activity on the fault relative to the vent is also unclear. The along-strike continuity of the fault on either side of the vent suggests the fault formed before the vent. The vent-forming eruption could then have exploited the fault structure as a weakness to reach the surface, though the presence of other vents in the same crater shows this is not necessary. The presence of shading that allows me to measure the fault surface is a result of its present-day topographic expression inside the vent wall. This scarp could have formed during the excavation of the vent, with the excavation occurring preferentially within the fractured rock in the fault surface, leaving some of the hanging wall behind and forming a slight step. Other possible interpretations are that there has been post-eruption movement on a pre-existing fault to produce the step, or that the fault could have initiated entirely after the vent formation.

This fault, with a strike length of 30 km, is shorter than most lobate scarps on Mercury, which tend to be hundreds of kilometres long. The cross-profile of the three-kilometre-wide ridge associated with this fault suggests an antithetic fault on the northeast side of the ridge (see Figure 6.4), as is common in reverse faulting, and indeed is possibly the case with high relief ridges on Mercury (Strom *et al* 1975). However, an antithetic fault trace is not evident within the vent, though a change of slope may occur where I would expect it; a DEM or lidar profile is needed to check this.

With a dip of 28° ± 5°, this fault is slightly steeper than the mean value used by Galluzzi *et al.* (2019, 2015), but within the range of measured dips in their database and also matches with the slightly lower angles needed to account for the amount of vertical displacement observed at some points (Crane 2020), though the dip measurement I have is within error of the 30° predicted by the Anderson faulting model for a standard thrust fault (Anderson 1951) and so more data is needed. The fault is much smaller scale than most of Mercury's lobate scarps. Its surface expression is similar to high relief ridges end members of lobate scarp – high relief ridge structures. However, its dip is much shallower than that of Enterprise Rupes' 57° where morphologically a high relief ridge. Its dip suggests that it is a similar compressive feature. Its presence in the crater discourages the use of the measurement to apply directly to interpret rock rheology as the host rock is likely to have been pre-fractured by the impact event (e.g. Soderblom et al., 2015). On the other hand, almost all of Mercury's crust is likely to be highly fractured by a long history of impact cratering (Klimczak *et al* 2018).

While a single fault measurement is not conclusive, my data adds to the evidence that, on Mercury, shallowly dipping faults are more typical than steeper ones. Additionally, this work demonstrates that measurements such as these are possible and can be made even in the absence of DEM data. The image resolution does not

allow measurement of fault displacement, which would enable quantification of how much strain the fault has accommodated. Still, higher-resolution imaging data from BepiColombo (Rothery *et al.*, 2020) may allow this. BepiColombo should provide sufficient data to make more measurements like this, generating a database of the fault geometries in locations across Mercury and allowing a more detailed assessment of global tectonic and thermal models. If measurements of other faults prove possible and are in line with this example, applying such a result to the model of Byrne *et al.* (2014) would suggest that global contraction is more likely to be at the higher end of the estimated range (5.7 – 7.1 km).

6.7 Conclusions

The first direct measurement of a fault geometry exposed on Mercury results in an estimate of fault dip of ~28° ±5. This is within the range of fault dips calculated indirectly through measurements of crater displacement and for classical thrust fault models. Although only a single example, this dip estimate suggests that the higher-end estimates of radial shrinking by global contraction are more representative than lower estimates. BepiColombo will provide an opportunity to gain better data on this site and identify other locations where the volcanic vents offer a similar 3D insight into planetary tectonics.

7 Synthesis

The research I have conducted has to led to several new findings concerning the geological processes that have shaped Mercury. Here I draw together my research and place it into a global context before outlining further questions to be answered and suggesting specific locations that BepiColombo should target to answer some of these questions.

7.1 Geomorphologic Map: Summary of Mapping

I have produced a Geomorphic map of Mercury's H-14 "the Debussy" quadrangle, which I have split into plains units and materials related to impact cratering; I have classified craters using both a 3-class and 5-class system and used it to infer a geological history.

7.1.1 Assessment of Three and Five Class Crater Classification System

Impact craters dominate Mercury's surface and shape much of the planet and include examples from ancient impact basins to smaller, recent craters. Impact basins also contain the few extensional structures on Mercury. There are two systems used to show the relative degradation state of craters: a more detailed 5-class (Kinczyk *et al* 2020a) system and a 3-class system that offers less temporal resolution (Galluzzi *et al* 2016). I have mapped using both systems and found examples of conflicts between morphological classification and the formation order of the craters (based on superposition) in both systems (one in the 3-class and two in the 5-class). This is due to the use of multiple morphological features that degrade at different rates to classify craters into discrete bins. Whilst the 5-class system is more prone to this conflict, overall, I find that the benefit achieved by additional granularity in the 5-class system and the ability to link features approximately to the five chronostratigraphic units (Figure 4.51), as well as its compatibility with studies outside the 1:3 million mapping project, outweighs the disadvantage of rare conflicts.

7.1.2 Crater Structures

Rembrandt, as the second-largest intact impact basin on Mercury, offers a comparison with Caloris (the largest). Two key features that make Rembrandt distinctive is that it has no equivalent of Caloris's Odin Formation and only has a partly lava-covered floor. Despite the absence of an equivalent to the Odin Formation at Rembrandt, I have identified units similar to some of the other Caloris units: Van Eyke Formation, Nervo Formation (both forms of ejecta), and Caloris Montes units (a unit at the basin rim). Knobs characterise the Odin formation around Caloris. These have been identified as volatile-rich and potentially from the mantle (Wright *et al* 2020), but there are few blocks of ejecta at Rembrandt, and those that are present are mostly around the rim and without the distinctive knob morphology. I postulate that this might be linked to Rembrandt's smaller size (Rembrandt is only 50% the radius of Caloris). For example, if the knobs

originated as volatile-rich mantle-sourced ejecta blocks, then maybe Rembrandt didn't eject blocks of the mantle (or of such volatile-rich mantle), so the blocks of ejecta did not degrade into knobs in the same way.

The partial infilling of Rembrandt by Smooth Plains (compared to the floor of Caloris, which is completely covered) reveals a complicated history. The volcanic history must be related to the response of the impact basin (and underlying lithosphere) to strain. It is possible that multiple phases of effusive lava emplacement (potentially, some of the most recent effusive lavas on the planet; Semenzato *et al.*, 2020), as well as multiple phases of tectonic deformation (both compressional and extensional) caused by loading, isostatic rebound, upwelling or lateral movement of the mantle, have shaped the Rembrandt basin. However, the reason for the partial lava cover of the floor does not seem clear; is it due to melt generation, melt supply, or interior basin topography?

7.1.3 Plains Units

Plains cover the rest of the map away from impact sites. I found three units that I could consistently identify: Intercrater Plains, Intermediate Plains, and Smooth Plains. The Intercrater Plains and Smooth Plains are relatively uncontroversial units and have been mapped by all previous regional morphological mapping (e.g. Galluzzi *et al*., 2016; Kinczyk *et al*., 2018; Trask and Guest, 1975). These units are all interpreted to be lava plains of different ages (though heavily reworked and modified by cratering in the case of Intercrater Plains). The Intermediate Plains, although only making up a small area of my quadrangle map (4%), were not identified in the global 1:15 million scale mapping (Kinczyk *et al* 2018) of this region.

There is an ongoing debate over the existence of the unit at all (Whitten *et al* 2014a, 2020). The presence (or absence) of Intermediate Plains on maps comes down to two factors: the scale of the map and whether the authors think this is a mappable unit. The global map does not include Intermediate Plains anywhere (Kinczyk *et al* 2018), however, it is at a scale of 1:15 million, and, as Wright (2019) points out, many of the patches would be too small to map discretely at this scale. The other possibility is that Intermediate Plains do not exist and are an artefact of low image quality and or local modification by impact craters (Whitten *et al* 2014a, 2020).

As the map scale decreases, the amount of detail a map can depict decreases also, as it must cover more area. In the case of the 1:15 million scale, for example, only craters >90 km are outlined (Kinczyk *et al* 2018). This creates a generalisation while providing global context but necessitates the loss of detail (Wright 2019). The most expansive Intermediate Plains I have mapped in H-14 are only 190 km across, and many patches are <90 km across. As the differentiation of Intermediate Plains from other plains is more subtle than impact crater rims, they would not stand out during mapping at such a scale; this is why regional mapping is essential to identify key features of Mercury's complex history.

As to the question of whether Intermediate Plains exist, or instead are artefacts of localised ageing or poor image availability, I find Intermediate Plains away from relatively young impact craters (as outlined in Chapter 4), so I discount the explanation that they are all merely localised modification of Smooth Plains as suggested by Whitten *et al.* (2014). The authors of the same paper followed on this study by mapping the plains within the Derrain Quadrangle (Whitten *et al* 2020) and did identify possible Intermediate Plains,

though they speculate they could be a result of poor image quality. Both Galluzzi *et al.* (2016) and Wright *et al.* (2019) identified Intermediate Plains in their 1:3 million scale quadrangle maps, and so has Malliband (2020) in his thesis mapping of the Derain quadrangle, which borders Debussy to the north. I have also identified and mapped this category of plains, and while image quality is an issue, I think their presence reflects areas of plains that have undergone an intermediate amount of modification (and so are probably intermediate in age).

The relatively small (4%) area of Intermediate Plains in my map could be due to either a short window of formation or being covered by subsequent Smooth Plains. I have shown that Smooth Plains are more often found in ancient impact basins, confirming the results of Padovan, Tosi and Plesa (2016) and Padovan *et al*, (2017). If this is due to impact basins providing more conduits for magma to get to the surface, then in a contracting world, where magma ascent is probably inhibited (Solomon 1977), the conduits that do exist may be long-lasting (sections 4.3.1.2, 5.5.3 and 7.2). So in many areas, Smooth Plains may overprint Intermediate Plains. Another possibility for the Intermediate Plains, particularly around the edge of Smooth Plains, is that they are only partly mantled with a thin layer of lava; this would explain the flat bottomed craters but not the Intermediate level of cratering observed nor the undulating topography.

It has been suggested that widescale effusive volcanism on Mercury occurred in pulses over 500 Ma ending by 3.5 Ga (Byrne 2020). Emplacement of the Northern Smooth Plains, Caloris interior plains (see section 2.5.1.1), most of Rembrandt's interior plains, and many other small patches all occurred within the statistical error of 3.8 – 3.7 Ga (Hauck *et al* 2018, Byrne 2020). Thus, the Intermediate Plains may have formed during a discrete period in the Calorian. Supposing this pulsing of intensity is the case; the Intermediate Plains could have formed either in a relatively short period, towards the end of the late heavy bombardment, or during a phase of relatively low volume effusive volcanism. As Intercrater Plains date from the Pre-Tolstojan and the Tolstojan (Whitten *et al* 2014a), Intermediate Plains are likely to date to the late Tolstojan or early Calorian, I have placed it in the narrow window of the Tolstojan in my geological history (Figure 4.51). A global map of Intermediate Plains will make it possible to check if Intermediate Plains cover only a small portion of the global map or whether instead there is a bias within the quadrangle. A better understanding of the impact crater formation rate and impact crater size-frequency statistics will help to date these features. This should be possible with BepiColombo data.

7.1.4 Tectonic structures

Tectonic structures are the other significant morphologies within the quadrangle. The structures can be split into basin dependent features (wrinkle ridges and grabens) and lobate scarps, which do not always follow basin alignments. It should be noted that illumination effects can skew observations, and as wrinkle ridges are more subtle than lobate scarps, the mapping of these features will be more affected by illumination bias. For example, there is a lack of east-west and north-south wrinkle ridges in Borobudur Fossae within the Rembrandt impact. This structure is radial, and illumination conditions are probably causing this bias in recorded structures (east-west structures might not generate shadows because MESSENGER only imaged parts of the north of the basin during local solar noon). As both Pantheon and

Borobudur Fossae host radial grabens and wrinkle ridges, they are excellent locations to understand illumination bias in future with better image data from BepiColombo.

Global contraction dominates the global tectonics of Mercury. However, its fabric may be controlled by deep crustal structures generated during tidal despining (Klimczak *et al* 2015, Watters and Nimmo 2010, King 2008, Melosh and Dzurisin 1978). The Debussy Quadrangle shows a strong east-west bias in the large contractional structures (lobate scarps). An East-West bias is unexpected on Mercury: global tidal despining should cause either North-South bias and NW-SE/NE-SW bias around the mid-latitudes, or no orientation bias in these large structures (Klimczak *et al* 2015). The East-West direction that dominates the lobate scarps of H-14 is likely due to the Enterprise-Belgica Valley (EBV), a broad depression 460 km wide and 1500 km long in the quadrangle. The EBV is evident morphologically only by two scarps, but it dominates the topography of the map and also the structural orientations within the quadrangle. Other regional biases in structural orientations are reflected in the H-03 Victoria quadrangle, where some structures are controlled by a local high-magnesium geological terrain (Galluzzi *et al* 2019). Both H-14 and H-03 shows that even $1/15^{th}$ of the planet's structures can be biased by local geology and that global maps are needed to better understand global structural models.

So far, global maps have shown that faults between 60°N and 60°S have preferred north-south orientations. In contrast, thrust faults closer to the poles have a random orientation (Klimczak *et al* 2015, Byrne *et al* 2014). However, global studies have not yet addressed possible illumination bias (Preusker *et al* 2011, Klimczak *et al* 2015).

7.1.5 Geological History

I have been able to deduce a geological history of the quadrangle based on the geomorphic map; the use of the 5-class crater system enabled me to link together features and units to the chronostratigraphic history (Figure 4.51, Kinczyk *et al.*, 2020b).

Within the quadrangle, effusive volcanism forming plains in the Pre-Tolstojan through to the Calorian, tectonic activity is known to have occurred during the Tolstojan and Calorian and likely also occurred both before and subsequently. Explosive volcanic activity has likely occurred in the Mansurian, and probably also before. However, most endogenic activity (tectonic and volcanic) has waned since the Calorian (Byrne 2020, Banks *et al.,* 2015). Although some tectonic and explosive volcanic activity may have occurred within the quadrangle during the Kuiperian, this period was dominated by exogenic processes, including impact cratering and localised hollow formation.

7.2 Insights into Mercury's Geology from its Volcanoes

My work on Mercury's explosive vent sites has shown that the majority are compound, likely formed through multiple eruptions. Terrestrial volcanos classified as compound have this morphology because they erupted multiple times, such as Volcán Aucanquilcha in Chile; this comprises 20 individual vents that have been active over 11 Ma (Klemetti & Grunder, 2008).

In my study, the vent within Picasso has an asymmetrical facula, this could be caused by intervals in eruption, leading to facula fading on some parts and not in others (knowing that compound vent structures are seen in vents that do not have a facula), or this difference in facula intensity could be due to different eruption intensities at different parts of the vent. At Agwo Facula, the vent site shows different intensities of impact cratering and textural roughness (Rothery *et al* 2014), suggesting multiple separate eruptions (though this could be cratering caused by the eruptive process migrating).

The vent site within Nathair Facula is offset from the facula centre (Rothery *et al* 2020a), though this could be caused by the northern part of the vent being most recently emplaced or erupted from the most intensely active part of the vent. However, the offset is so severe that it may also require additional explanation, such as an off-vertical orientation for some of the conduits (Rothery *et al* 2020a). The Nathair Facula vent site also shows variable internal cratering, small pits and mantled interior, which is strong evidence for multiple phases of activity. At another vent site, I identified a tentative constructive edifice (Chapter 5.4.2.4). This feature has to have been built after the vent was excavated, which suggests a switch away from explosive volcanism towards more viscous effusive volcanism. All these observations suggest that multiple eruption events occur at least on some compound vent sites.

Repeated eruption requires the recharge of magma or volatiles. It is not possible to observe Mercury's crust below the surface, but it is likely to be layered due to the emplacement of multiple lava flows, overlapping ejecta blankets, and (at greatest depth) the source material for the volatile-rich low reflectance material (Thomas *et al* 2016, Murchie *et al* 2015, Denevi *et al* 2009, Weider *et al* 2015, Nittler *et al* 2011). Dykes are the most likely feeders to Mercury's volcanoes (Jozwiak *et al* 2018, Thomas *et al* 2015), and dykes cutting through the crust this would have a limited surface area (relative to sills) in contact with volatile-rich layers. If the dyke had stalled, then assimilation might still have occurred with ceiling/wall collapse or volatile migration aiding this. Volatile migration in the shallow crust is necessary for hollow formation (Wang *et al* 2020) and assimilation is strongly suspected of having increased the explosivity at least one eruption site on Mercury (Weider *et al* 2016).

Alternatively, if the volatile recharge was not occurring within the crust, then it must have been from the melt source. Global compression has usually been cited as an obstacle to this process (Solomon 1978, Wilson and Head 2008), however, it should be noted that stresses will not be uniform, and local crustal weaknesses such as craters or faults (Klimczak *et al* 2018), or stress differences such as those around the edges of crustal blocks, may enable melts to rise even when the crust is under horizontal compression. For repeated batches of magma ascent, these opportunities could arise from long-lived structural differences in the crust that enable multiple eruptions.

There are two main implications from my study of compound vents: (i) The multi-eruptive history with multiple separate eruptive centres at vent sites must be taken into account when studying the extent of the pyroclastic deposits that constitute faculae. Faculae are often modelled as a single central vent source (Brož *et al*., 2018; Kerber *et al*., 2009), but the dynamic histories shown by our examples suggest that these sites migrate over time and that eruptions built up their faculae from multiple centres. (ii) The proportion of vents without facula is likely underestimated (as seen in the comparison between H-14 and the global study

section 4.6), and further study of these sites would be valuable. Either a systematic global study or examining other spectral/geochemical data to identify other chemical signatures that may identify them is needed.

In addition to identifying compound vents, I also identified a small mound within one vent which is away from the walls and so unlikely to be a mass wasting deposit. Instead, I have interpreted it to be a constructive feature within the vent. However, it is partly covered by shadow, and so more data is needed to analyse comprehensively.

Finally, my measurement of a single fault dip of 28° ± 5° within a volcanic vent is only of a single, relatively small fault. It fits within the range of dips measured for other faults by indirect means. The fault is slightly steeper than the mean value of 25° suggested by Galluzzi *et al*. (2019, 2015) and, while suggestive of a shallower dip than the 30° expected from a thrust fault (Anderson 1951), the error bars overlap with this value. If further examples and measurements confirm this shallow dip, then it would fit with the higher ends (5.7 – 7.1 km) of global contraction estimates (Byrne *et al* 2014). Further work using BepiColombo data may be able to identify the amount of fault displacement as well as identify any additionally exposed scarps at other vents.

7.3 Other work and Future Targets

Here I highlight questions that arose during my study but which I could not pursue in detail and suggest some specific targets for BepiColombo (Chapter 2.1.4). In addition, a key near term future work goal is the integration of my map with the Derrain and Neruda quadrangles (plus other quadrangles when mapped). This has begun but awaits the completion of adjacent maps.

7.3.1 Plains units

The plains of H-14 need imaging with consistent lighting, preferably with multiple incidence angles, to help to settle the debate about whether Intermediate Plains are unit distinct from Smooth or Intercrater Plains. In addition to this, data from the BepiColombo Laser Altimeter (BELA) may also provide compositional and morphological data that may explain the origin of these sporadic blocks within the highlands (chapter 4.3.1.3) and provide another measure of roughness and cratering over the plains to help distinguish them. More Illumination directions will also help understand illumination bais in structural mapping.

The lack of correlation between morphological units and geochemical terrains shows that there are still gaps in our understanding of plains formation. Higher-resolution geochemical data from the Mercury Radiometer and Thermal Infrared Spectrometer (MERTIS) and the Mercury Imaging X-ray Spectrometer (MIXS) onboard BepiColombo will provide compositional data about the planet's surface with a spatial resolution of better than ~10 km/sample (Fraser *et al* 2010) to enable the study of the composition of plains and match them to morphology. This may also help pick out separate units within the same morphological units to build a better understanding of the formation of Smooth Plains. Spectrometer and Imagers for MPO BepiColombo-Integrated Observatory SYStem (SIMBIO-SYS) will provide images at <110 m resolution of the entire globe under different illumination conditions.

7.3.2 Impact Basins

At Rembrandt, a study of the continuity of the interior and exterior plains needs better images to understand the origins of the Smooth Plains and how they link with the impact ejecta. This study could also be linked to gravity data to understand the evolution of the Smooth Plains. Image data from SIMBIO-SYS would also allow us to build a better tectonic history and study the cross-cutting relationships of the grabens and faults around Borobudur Fossae. I do not doubt that better images of Borobudur Fossae will reveal even more tectonic complexity and reduce some of the bias seen in structural orientations in areas hitherto imaged only during solar-noon.

Compositional data from MERTIS (chapter 2.1.4) may help identify if there are multiple generations of Smooth Plains at the centre of Rembrandt. Modelling of the Rembrandt vs Caloris impact process and the generation of ejecta blocks may explain the lack of knobs at Rembrandt. Gravity data can also be used to understand whether the mantle holds up the structures beneath the Enterprise – Belgical Valley.

Further studies of large impact basins on Mercury and the distribution of Smooth Plains could be undertaken by combining better topographic and gravity data from BepiColombo. This will help us better understand whether crustal weaknesses in impact basins or the thinning of the crust there (or a combination of the two) enabled the emplacement of the plains.

7.3.3 Volcanic Vents

The current stereo imaged data is insufficient to make DEMs of the interior of the vents, and shape from shading could be used as an alternative route to make these DEMs to understand the internal structures of these vents better. In the future, BepiColombo could collect laser altimeter profiles of the volcanic vent sites and detailed stereo images for the construction of DEMs by photogrammetry. SIMBIO-SYS will image 10% of the planet's surface at 5 m per pixel; this enhanced resolution will allow better study of their internal morphology and could be used to detect any crater floor displacement associated with shallow sills. MERTIS and MIXS data of faculae (and potentially the floor within Nathair Facula) may help pick up chemical/mineralogical signs of changes in volcanism that may also indicate (or not) multiple eruptions at vent sites.

The rates of surface degradation, regolith mixing and weathering on the surface of Mercury need to be better quantified to understand the sizes of faculae and how quickly they are lost. Understanding the rates that morphological features are 'smoothed out' or obliterated by cratering and space weathering will help us to understand both the modification of plains and how compound vents evolve after volcanic activity stops, particularly those small pits in the vent at Nathair Facula (chapter 5.4.2.3). The rate at which landforms are lost on the planet would help us to understand these and other presumably transitory features such as hollows.

A global study of pits without a clear facula is needed, including using the global basemaps to identify other vents without facula. In addition, any related chemical signatures around these vents should be identified. However, this may require higher resolution data from MERTIS and MIXS.

Pitted ground (mentioned in Chapters 2.6.2, 5.3.2) is a variety of facula that does not have a vent site but instead shows a highly disturbed surface. Little work has been undertaken since the initial study (Thomas *et al* 2014a), and it warrants further analysis to understand the origins of the terrain type and to check that the current theory of the formation of lavas over volatile-enriched ground is confirmed by data collected by MESSENGER after the study.

Klimczak *et al.* (2018) show that Mercury is too densely fractured to distinguish whether the location of volcanic vents are related to lobate scarps or instead is random. However, they did not investigate which side of the lobate scarp vents are found. If these faults are acting as conduits, then hanging wall magmatism is more likely to form on the upthrown block rather than the downthrown block. Several vents sites in H-14 occur where craters overlap, and this could be a further avenue for study given that the impact cratering process is likely to increase porosity and connectivity within the crust.

Dark spots are discrete albedo features on Mercury's surface. They may be LRM exposed by impact cratering, generating a macula, but this needs to be more firmly established. They are rare, with a global survey in 2013 identifying only 34 examples (Xiao *et al* 2013). No work has been completed on them since then, and the higher resolution data collected later in MESSENGER's mission could provide more insight.

7.3.4 Specific Targets for BepiColombo

In addition to the areas for further study listed above, several locations which require specific data became apparent during my thesis. In addition to the faulted vents (chapter 6) and the vent sites identified (Appendix 3), I list in Table 7.1 some of the most intriguing features on the planet's surface for future examination with data from BepiColombo.

Table 7.1 Coordinates of features of interest.

LAT (°)	LON (°)	COMMENT
-38.6	78.2	A possible connection between Rembrandt interior and exterior plains (chapter 4.3.2.3)
48.6	139.4	Potential constructive edifice within vent (Chapter 5.4.2.4)
-3.0	17.5	Intense blue pit within a crater
64.0	35.9	Pits on the floor of vent the within Nathair Facula, nearby the vent floor appears mantled
-64.5	45.5	Flat facula with no exact vent site. It looks like a small patch of smooth lava
16.6	156.8	very low albedo blue patch
-24.9	145.0	very dark LRM exposed by a crater
-60.5	26.0	Pitted ground that may transition into vent site
-58.9	27.0	More pitted ground close to a vent
-59.1	27.5	Pitted ground interacting with hollows close to a crater peak ring
-49.1	15.5	Possible peak ring element exposed by a volcanic vent

48.8	156.9	Small facula on or next to an ejecta block inside Caloris
-65.5	147	Faulted vent in Vazov crater
24°	148	Faulted vent
21	67	Faulted vent
24	105	Faulted vent
-17	162	Faulted vent
15	112	Faulted vent
27	30	Faulted vent

8 Conclusion

8.1 Summary

I have produced the first geological map of the H-14 (Debussy) quadrangle on Mercury as part of a Europe-led process of mapping the planet Mercury at a scale of 1:3M. The production of a geological map of H-14 has led me to explore the volcanic and tectonic processes that have shaped Mercury. The volcanic vent sites within my quadrangle inspired me to study those elsewhere on the planet, and I measured the proportion that are or are not morphologically compound. In this process, I discovered a volcanic vent that had exposed a tectonic fault, and I have managed to make the first direct measurement of fault geometry on the planet.

8.2 Conclusions

- I used both 3- and 5-class systems to classify craters. The 5-class system, while flawed, provides a better reference to other work. In contrast, the 3-class system losses the ability to compare to a stratigraphic system that is mostly based on degradation. Overall I favour the five-class system.
- My map includes three different types of plains on Mercury, representing multiple stages of effusive volcanism, the low volumes of Intermediate Plains suggest that they formed in either a short time interval or during a period of low activity.
- Global mapping may not be sufficient for identifying the nuanced volcanic history; quadrangle-scale maps provide a greater understanding of the processes of plains emplacement.
- Multiple levels of mapping are needed to build an understanding. You cannot use a regional map to understand global tectonics, even on a one-plate world. Multiple scales of mapping are needed because, at the regional (quadrangle) scale, tectonic structures are dominated by local geological features caused by the interactions between impact basins. This signal is superposed on top of structures caused by tectonic stresses from global contraction. Illumination bias hampers studying structures on Mercury; this is understood but not yet quantified.
- The majority of explosive volcanic vents on Mercury are compound. I conclude that many vents underwent multiple eruptions. This is supported by evidence from faculae and internal cratering/mantling that there was a time gap between eruptions, although it is not clear if this is the case for all compound vents.
- Repeated eruptions require either a continued supply of volatile-rich magma or storage and recharge of magma. The most likely mechanism is resupply from source or deeper plumbing, but assimilation of volatiles from the crust or regolith may also contribute.

- I have identified a tentative constructional edifice within one volcanic vent. This feature requires further exploration to understand, but its form suggests a less explosive style of volcanism may have occurred towards the end of eruptive activity at this site. However, BepiColombo will have to collect further image data to understand this feature better, as well as collect data on the small pits within the vent in Nathair facula.
- I found one vent within an impact crater that reveals a fault scarp. I was able to measure the dip as 28° ± 5°. This fault may be an end member of a high relief ridge as it is associated with a ridge. The dip of this fault plane fits well with the other fault measurements measured by indirect methods. If confirmed and supported by other examples, this would be evidence for the higher end of the range of estimates of global contraction caused by cooling.
- There are multiple locations where vents intersect fault scarps, though often these are either poorly resolved or covered by regolith and could be better imaged by BepiColombo.

9 References

Allum J A E 2013 *Photogeology and regional mapping* (Elsevier)

Anderson E M 1951 The dynamics of faulting *Trans. Edinburgh Geol. Soc.* **8** 387–402 Online: http://trned.lyellcollection.org/cgi/doi/10.1144/transed.8.3.387

Antoniadi E M 1933 The Markings and Rotation of Mercury *J. R. Astron. Soc. Canada* **27** 403–10

Archinal B A, Acton C H, A'Hearn M F, Conrad A, Consolmagno G J, Duxbury T, Hestroffer D, Hilton J L, Kirk R L, Klioner S A, McCarthy D, Meech K, Oberst J, Ping J, Seidelmann P K, Tholen D J, Thomas P C and Williams I P 2018 Report of the IAU Working Group on Cartographic Coordinates and Rotational Elements: 2015 *Celest. Mech. Dyn. Astron.* **130** 1–46 Online: https://doi.org/10.1007/s10569-017-9805-5

Ash M E, Shapiro I I and Smith W B 1971 The System of Planetary Masses *Science (80-.).* **174** 551–6 Online: http://www.sciencemag.org/cgi/doi/10.1126/science.174.4009.551

Asphaug E and Reufer A 2014 Mercury and other iron-rich planetary bodies as relics of inefficient accretion *Nat. Geosci.* **7** 564–8

Baker D M H, Head J W, Schon S C, Ernst C M, Prockter L M, Murchie S L, Denevi B W, Solomon S C and Strom R G 2011 The transition from complex crater to peak-ring basin on Mercury: New observations from MESSENGER flyby data and constraints on basin formation models *Planet. Space Sci.* **59** 1932–48 Online: http://dx.doi.org/10.1016/j.pss.2011.05.010

Banks M E, Xiao Z, Braden S E, Barlow N G, Chapman C R, Fassett C I and Marchi S S 2017 Revised constraints on absolute age limits for Mercury's Kuiperian and Mansurian stratigraphic systems *J. Geophys. Res. Planets* **122** 1010–20

Banks M E, Xiao Z, Watters T R, Strom R G, Braden S E, Chapman C R, Solomon S C, Klimczak C and Byrne P K 2015 Duration of activity on lobate-scarp thrust faults on Mercury *J. Geophys. Res. Planets* **120** 1751–62 Online: http://doi.wiley.com/10.1002/2015JE004828

Barnouin O S, Zuber M T, Smith D E, Neumann G A, Herrick R R, Chappelow J E, Murchie S L and Prockter L M 2012 The morphology of craters on Mercury: Results from MESSENGER flybys *Icarus* **219** 414–27 Online: http://dx.doi.org/10.1016/j.icarus.2012.02.029

Baumgardner J, Wilson J and Mendillo M 2008 Imaging the sources and full extent of the sodium tail of the planet Mercury *Geophys. Res. Lett.* **35** 1–5

Becker K and Becker T 2015 MESSENGER MDIS Data Users ' Workshop *46th LPSC* (Houston) Online: https://messenger.jhuapl.edu/Resources/Workshops-and-Meetings/MESSENGER_MDIS_WorkShop_LPSC2015_Final.pdf

Becker K J, Robinson M S, Becker T L, Weller L A, Edmundson K L, Neumann G A, Perry M E and Solomon S C 2016 First Global Digital Elevation Model of Mercury *Lunar and Planetary Science Conference* vol 47 p 2959

Benkhoff J, van Casteren J, Hayakawa H, Fujimoto M, Laakso H, Novara M, Ferri P, Middleton H R and Ziethe R 2010 BepiColombo-Comprehensive exploration of Mercury: Mission overview and science goals *Planet. Space Sci.* **58** 2–20 Online: http://dx.doi.org/10.1016/j.pss.2009.09.020

Besse S, Doressoundiram A, Barraud O, Griton L, Cornet T, Muñoz C, Varatharajan I and Helbert J 2020 Spectral Properties and Physical Extent of Pyroclastic Deposits on Mercury: Variability Within Selected Deposits and Implications for Explosive Volcanism *J. Geophys. Res. Planets* **125** 1–13

Blair D M, Freed A M, Byrne P K, Klimczak C, Prockter L M, Ernst C M, Solomon S C, Melosh H J and Zuber M T 2013 The origin of graben and ridges in Rachmaninoff, Raditladi, and Mozart basins, Mercury *J. Geophys. Res. E Planets* **118** 47–58

Blewett D T, Chabot N L, Denevi B W, Ernst C M, Head J W, Izenberg N R, Murchie S L, Solomon S C, Nittler L R, McCoy T J, Xiao Z, Baker D M H, Fassett C I, Braden S E, Oberst J, Scholten F, Preusker F and Hurwitz D M 2011 Hollows on Mercury: MESSENGER evidence for geologically recent volatile-related activity *Science (80-.).* **333** 1856–9

Blewett D T, Robinson M S, Denevi B W, Gillis-Davis J J, Head J W, Solomon S C, Holsclaw G M and McClintock W E 2009 Multispectral images of Mercury from the first MESSENGER flyby: Analysis of global and regional color trends *Earth Planet. Sci. Lett.* **285** 272–82 Online: http://dx.doi.org/10.1016/j.epsl.2009.02.021

Blewett D T, Stadermann A C, Susorney H C, Ernst C M, Xiao Z, Chabot N L, Denevi B W, Murchie S L, McCubbin F M, Kinczyk M J, Gillis-Davis J J and Solomon S C 2016 Analysis of MESSENGER high-resolution images of Mercury's hollows and implications for hollow formation *J. Geophys. Res. Planets* **121** 1798–813

Blewett D T, Vaughan W M, Xiao Z, Chabot N L, Denevi B W, Ernst C M, Helbert J, D'Amore M, Maturilli A, Head J W and Solomon S C 2013 Mercury's hollows: Constraints on formation and composition from analysis of geological setting and spectral reflectance *J. Geophys. Res. E Planets* **118** 1013–32 Online: http://doi.wiley.com/10.1029/2012JE004174

Borin P, Cremonese G, Marzari F, Bruno M and Marchi S 2009 Statistical analysis of micrometeoroids flux on Mercury *Astron. Astrophys.* **503** 259–64

Braden S E and Robinson M S 2013 Relative rates of optical maturation of regolith on Mercury and the Moon *J. Geophys. Res. Planets* **118** 1903–14

Breuer D, Hauck S A, Buske M, Pauer M and Spohn T 2007 Interior Evolution of Mercury *Space Sci. Rev.* **132** 229–60 Online: http://link.springer.com/10.1007/s11214-007-9228-9

Broxton M J and Edwards L J 2008 The Ames Stereo Pipeline: Automated 3D Surface Reconstruction from Orbital Imagery *Lunar and Planetary Science Conference 39* p #2419

Brož P, Čadek O, Wright J and Rothery D A 2018 The Apparent Absence of Kilometer-Sized Pyroclastic

Volcanoes on Mercury: Are We Looking Right? *Geophys. Res. Lett.* **45** 12,171-12,179

Brunetti M T, Xiao Z, Komatsu G, Peruccacci S and Guzzetti F 2015 Large rock slides in impact craters on the Moon and Mercury *Icarus* **260** 289–300 Online: http://dx.doi.org/10.1016/j.icarus.2015.07.014

Bryan W B 1973 Wrinkle-ridges as deformed crust on ponded mare lava *Fourth Lunar Science Conference* vol 1 pp 93–106

Buczkowski D L, Goosmann E, Denevi B W, Ernst C M, Fassett C I and Byrne P K 2017 A Geologic Map of the Caloris Basin, Mercury *Planetary Mappers Meeting* (Flagstaff, Arizona)

Burns J A 1976 Consequences of the tidal slowing of Mercury *Icarus* **28** 453–8 Online: http://linkinghub.elsevier.com/retrieve/pii/0019103576901184

Byrne P K 2020 A Comparison of Inner Solar System Volcanism *Nat. Astron.* **4** 321–7 Online: http://dx.doi.org/10.1038/s41550-019-0944-3

Byrne P K, Klimczak C, Celâl Şengör A M, Solomon S C, Watters T R and Hauck, II S A 2014 Mercury's global contraction much greater than earlier estimates *Nat. Geosci.* **7** 301–7 Online: http://www.nature.com/doifinder/10.1038/ngeo2097

Byrne P K, Klimczak C and Sengör A M C 2018a The Tectonic Character of Mercury *Mercury: The View after Messenger* pp 249–87

Byrne P K, Klimczak C, Williams D A, Hurwitz D M, Solomon S C, Head J W, Preusker F and Oberst J 2013 An assemblage of lava flow features on Mercury *J. Geophys. Res. E Planets* **118** 1303–22

Byrne P K, Ostrach L R, Fassett C I, Chapman C R, Denevi B W, Evans A J, Klimczak C, Banks M E, Head J W and Solomon S C 2016 Widespread effusive volcanism on Mercury likely ended by about 3.5 Ga *Geophys. Res. Lett.* **43** 7408–16

Byrne P K, Ostrach L R, Fassett C I, Chapman C R, Evans A J, Klimczak C, Banks M E, Head J W and Solomon S C 2015 Widespread Plains Volcanism on Mercury Ended by 3.6 Ga *2015 AGU Fall Meet.* 7408–16

Byrne P K, Whitten J L, Klimczak C, McCubbin F M and Ostrach L R 2018b The Volcanic Character of Mercury *Mercury: The view after MESSENGER* (Cambridge: Cambridge University Press) pp 287–323

Chabot N L, Denevi B W, Solomon S C, Xiao Z, Ernst C M, Oberst J, Blewett D T, Nittler L R, Preusker F, Braden S E, Murchie S L, Head J W, Fassett C I, McCoy T J, Scholten F, Hurwitz D M, Baker D M H and Izenberg N R 2011 Hollows on Mercury: MESSENGER Evidence for Geologically Recent Volatile-Related Activity *Science (80-.).* **333** 1856–9

Chabot N L, Ernst C M, Harmon J K, Murchie S L, Solomon S C, Blewett D T and Denevi B W 2013 Craters hosting radar-bright deposits in Mercury's north polar region: Areas of persistent shadow determined from MESSENGER images *J. Geophys. Res. E Planets* **118** 26–36

Chabot N L, Ernst C M, Paige D A, Nair H, Denevi B W, Blewett D T, Murchie S L, Deutsch A N, Head J W and Solomon S C 2016 Imaging Mercury's polar deposits during MESSENGER's low-altitude campaign

Geophys. Res. Lett. **43** 9461–8

Chabot N L, Shread E E and Harmon J K 2018 Investigating Mercury's South Polar Deposits: Arecibo Radar Observations and High-Resolution Determination of Illumination Conditions *J. Geophys. Res. Planets* **123** 666–81

Chapman C R, Mosher J A and Simmons G 1970 Lunar cratering and erosion from Orbiter 5 photographs *J. Geophys. Res.* **75** 1445–66 Online: http://doi.wiley.com/10.1029/JB075i008p01445

Chappelow J E and Sharpton V L 2002 An improved shadow measurement technique for constraining the morphometry of simple impact craters *Meteorit. Planet. Sci.* **37** 479–86

Charlier B, Grove T L and Zuber M T 2013 Phase equilibria of ultramafic compositions on Mercury and the origin of the compositional dichotomy *Earth Planet. Sci. Lett.* **363** 50–60 Online: http://dx.doi.org/10.1016/j.epsl.2012.12.021

Christensen U R and Wicht J 2008 Models of magnetic field generation in partly stable planetary cores: Applications to Mercury and Saturn *Icarus* **196** 16–34

Cintala M J 1992 Impact-induced thermal effects in the lunar and mercurian regoliths *J. Geophys. Res.* **97** 947–73

Cohen K, Finney S, Gibbard P and Fan J 2013 The ICS International Chronostratigraphic Chart *Episodes* **36**

Crane K 2020 Structural interpretation of thrust fault-related landforms on Mercury using Earth analogue fault models *Geomorphology* **369** 107366 Online: https://doi.org/10.1016/j.geomorph.2020.107366

Crane K T and Klimczak C 2019 Tectonic patterns of shortening landforms in Mercury's northern smooth plains *Icarus* **317** 66–80 Online: https://doi.org/10.1016/j.icarus.2018.05.034

Crane K T and Klimczak C 2017 Timing and rate of global contraction on Mercury *Geophys. Res. Lett.* **44** 3082–9

Crider D H and Vondrak R R 2003 Space weathering effects on lunar cold trap deposits *J. Geophys. Res. E Planets* **108** 1–11

Cruikshank D P, Hartmann W K and Wood C A 1973 Moon: Ghost Craters formed during Mare Filling *Moon* **7** 440–52

Davidson J and De Silva S 2000 Composite Volcanoes *Encyclopeida of volcanoes 1* pp 663–81

Davies M E, Gault D E, Dwomik S W and Strom R G 1978 *Atlas of Mercury* (Washington: U.S. Government Printing Office)

Denevi B W, Chabot N L, Murchie S L, Becker K J, Blewett D T, Domingue D L, Ernst C M, Hash C D, Hawkins S E, Keller M R, Laslo N R, Nair H, Robinson M S, Seelos F P, Stephens G K, Turner F S and Solomon S C 2018a Calibration, Projection, and Final Image Products of MESSENGER's Mercury Dual Imaging System *Space Sci. Rev.* **214** 2 Online: http://dx.doi.org/10.1007/s11214-017-0440-y

Denevi B W, Ernst C M, Meyer H M, Robinson M S, Murchie S L, Whitten J L, Head J W, Watters T R, Solomon S C, Ostrach L R, Chapman C R, Byrne P K, Klimczak C and Peplowski P N 2013 The distribution and origin of smooth plains on Mercury *J. Geophys. Res. Planets* **118** 891–907 Online: http://doi.wiley.com/10.1002/jgre.20075

Denevi B W, Ernst C M, Prockter L M and Robinson M S 2018b The Geological History of Mercury *Mercury: The View after Messenger* pp 144–75

Denevi B W, Robinson M S, Solomon S C, Murchie S L, Blewett D T, Domingue D L, McCoy T J, Ernst C M, Head J W, Watters T R and Chabot N L 2009 The evolution of Mercury's crust: A global perspective from MESSENGER *Science (80-.).* **324** 613–8

Denevi B W, Seelos F P, Ernst C M, Keller M R, Chabot N L, Murchie S L, Domingue D L, Hash C D and Blewett D T 2016 Final Calibration and Multispectral Map Products from the Mercury Dual Imaging System Wide-Angle Camera *Lunar and Planetary Science Conference* vol 47 p 1264

Dollfus A, Chapman C R, Davies M E, Gingerich O, Goldstein R, Guest J, Morrison D and Smith B A 1978 IAU Nomenclature for albedo features on the planet mercury *Icarus* **34** 210–4

Domingue D L, Chapman C R, Killen R M, Zurbuchen T H, Gilbert J A, Sarantos M, Benna M, Slavin J A, Schriver D, Trávníček P M, Orlando T M, Sprague A L, Blewett D T, Gillis-Davis J J, Feldman W C, Lawrence D J, Ho G C, Ebel D S, Nittler L R, Vilas F, Pieters C M, Solomon S C, Johnson C L, Winslow R M, Helbert J, Peplowski P N, Weider S Z, Mouawad N, Izenberg N R and McClintock W E 2014 Mercury's Weather-Beaten Surface: Understanding Mercury in the Context of Lunar and Asteroidal Space Weathering Studies *Space Sci. Rev.* **181** 121–214 Online: http://link.springer.com/10.1007/s11214-014-0039-5

Domingue D L, Hash C D, Denevi B W and Murchie S L 2017 Extending MESSENGER's Mercury dual imager's eight-color photometric standardization to cover all eleven filters *Icarus* **297** 83–9 Online: http://dx.doi.org/10.1016/j.icarus.2017.06.023

Dzurisin D 1977 Mercurian bright patches: Evidence for physio-chemical alteration of surface material? *Geophys. Res. Lett.* **4** 383–6 Online: http://doi.wiley.com/10.1029/GL004i010p00383

Dzurisin D 1978 The tectonic and volcanic history of mercury as inferred from studies of scarps, ridges, troughs, and other lineaments *J. Geophys. Res. Solid Earth* **83** 4883–906 Online: http://doi.wiley.com/10.1029/JB083iB10p04883

Ebel D S and Alexander C M O 2011 Equilibrium condensation from chondritic porous IDP enriched vapor: Implications for Mercury and enstatite chondrite origins *Planet. Space Sci.* **59** 1888–94 Online: http://dx.doi.org/10.1016/j.pss.2011.07.017

Ebel D S and Stewart S T 2018 The Elusive Origin of Mercury *Mercury: The view after MESSENGER* ed S C Solomon, L R Nittler and B J Anderson (Cambridge, UK: Cambridge University Press) pp 516–43

Einstein A 1915 Erklarung der Perihelionbewegung der Merkur aus der allgemeinen Relativitatstheorie *Sitzungsber Preuss* **47** 831–9

Ernst C M, Chabot N L and Barnouin O S 2018 Examining the Potential Contribution of the Hokusai Impact to Water Ice on Mercury *J. Geophys. Res. Planets* **123** 2628–46

Ernst C M, Denevi B W, Barnouin O S, Klimczak C, Chabot N L, Head J W, Murchie S L, Neumann G A, Prockter L M, Robinson M S, Solomon S C and Watters T R 2015 Stratigraphy of the Caloris basin, Mercury: Implications for volcanic history and basin impact melt *Icarus* **250** 413–29 Online: http://dx.doi.org/10.1016/j.icarus.2014.11.003

Fassett C I, Crowley M C, Leight C, Dyar M D, Minton D A, Hirabayashi M, Thomson B J and Watters W A 2017 Evidence for rapid topographic evolution and crater degradation on Mercury from simple crater morphometry *Geophys. Res. Lett.* **44** 5326–35

Fassett C I, Head J W, Baker D M H, Zuber M T, Smith D E, Neumann G A, Solomon S C, Klimczak C, Strom R G, Chapman C R, Prockter L M, Phillips R J, Oberst J and Preusker F 2012 Large impact basins on Mercury: Global distribution, characteristics, and modification history from MESSENGER orbital data *J. Geophys. Res. E Planets* **117** 2–3 Online: http://doi.wiley.com/10.1029/2012JE004154

Fassett C I, Head J W, Blewett D T, Chapman C R, Dickson J L, Murchie S L, Solomon S C and Watters T R 2009 Caloris impact basin: Exterior geomorphology, stratigraphy, morphometry, radial sculpture, and smooth plains deposits *Earth Planet. Sci. Lett.* **285** 297–308 Online: http://dx.doi.org/10.1016/j.epsl.2009.05.022

Fassett C I, Kadish S J, Head J W, Solomon S C and Strom R G 2011 The global population of large craters on Mercury and comparison with the Moon *Geophys. Res. Lett.* **38** 1–6

Fegan E R, Rothery D A, Marchi S, Massironi M, Conway S J and Anand M 2017 Late movement of basin-edge lobate scarps on Mercury *Icarus* **288** 226–34 Online: http://dx.doi.org/10.1016/j.icarus.2017.01.005

Ferrari S, Massironi M, Marchi S, Byrne P K, Klimczak C, Martellato E and Cremonese G 2015 Age relationships of the Rembrandt basin and Enterprise Rupes, Mercury *Geol. Soc. London, Spec. Publ.* **401** 159–72 Online: http://sp.lyellcollection.org/lookup/doi/10.1144/SP401.20

Fraser G W, Carpenter J D, Rothery D A, Pearson J F, Martindale A, Huovelin J, Treis J, Anand M, Anttila M, Ashcroft M, Benkoff J, Bland P, Bowyer A, Bradley A, Bridges J, Brown C, Bulloch C, Bunce E J, Christensen U, Evans M, Fairbend R, Feasey M, Giannini F, Hermann S, Hesse M, Hilchenbach M, Jorden T, Joy K, Kaipiainen M, Kitchingman I, Lechner P, Lutz G, Malkki A, Muinonen K, Näränen J, Portin P, Prydderch M, Juan J S, Sclater E, Schyns E, Stevenson T J, Strüder L, Syrjasuo M, Talboys D, Thomas P, Whitford C and Whitehead S 2010 The Mercury Imaging X-ray Spectrometer (MIXS) on BepiColombo *Planet. Space Sci.* **58** 79–95 Online: https://linkinghub.elsevier.com/retrieve/pii/S0032063309001482

Freed A M, Solomon S C, Watters T R, Phillips R J and Zuber M T 2009 Could Pantheon Fossae be the result of the Apollodorus crater-forming impact within the Caloris basin, Mercury? *Earth Planet. Sci. Lett.* **285** 320–7 Online: http://dx.doi.org/10.1016/j.epsl.2009.02.038

Fulop A and Kurszlaukis S 2017 Monogenetic v. polygenetic kimberlite volcanism: In-depth examination of

the Tango Extension Super Structure, Attawapiskat kimberlite field, Ontario, Canada *Geol. Soc. Spec. Publ.* **446** 205–24

Galluzzi V 2015 *Structural Analysis of the Victoria Quadrangle (H2) of Mercury Based on NASA MESSENGER Data* (Università degli Studi di Napoli "Federico II")

Galluzzi V, Achille G D I, Ferranti L, Popa C, Palumbo P, Ii F, Di Achille G, Ferranti L, Popa C and Palumbo P 2015 Faulted craters as indicators for thrust motions on Mercury *Geol. Soc. London, Spec. Publ.* **401** 313–25 Online: http://sp.lyellcollection.org/cgi/doi/10.1144/SP401.17

Galluzzi V and BepiColombo Geological Mapping Team 2017 Status update on Mercury geological mapping and the Intermediate Plains controversy *BepiColombo SWT Meeting, 29 May – 1 June 2017,*

Galluzzi V, Ferranti L, Massironi M, Giacomini L, Guzzetta L and Palumbo P 2019 *Structural analysis of the Victoria quadrangle fault systems on Mercury: timing, geometries, kinematics and relationship with the high-Mg region*

Galluzzi V, Guzzetta L, Ferranti L, Di Achille G, Rothery D A and Palumbo P 2016 Geology of the Victoria quadrangle (H02), Mercury *J. Maps* **12** 227–38 Online: https://www.tandfonline.com/doi/full/10.1080/17445647.2016.1193777

Gault D E, Guest J E, Murray J B, Dzurisin D and Malin M C 1975 Some comparisons of impact craters on Mercury and the Moon *J. Geophys. Res.* **80** 2444–60 Online: http://doi.wiley.com/10.1029/JB080i017p02444

Genova A, Goossens S, Mazarico E, Lemoine F G, Neumann G A, Kuang W, Sabaka T J, Hauck S A, Smith D E, Solomon S C and Zuber M T 2019 Geodetic Evidence That Mercury Has A Solid Inner Core *Geophys. Res. Lett.* **46** 3625–33

Giacomini L, Massironi M, Galluzzi V, Ferrari S and Palumbo P 2020 Dating long thrust systems on Mercury: New clues on the thermal evolution of the planet *Geosci. Front.* **11** 855–70 Online: https://doi.org/10.1016/j.gsf.2019.09.005

Giacomini L, Massironi M, Marchi S, Fassett C I, Di Achille G and Cremonese G 2015 Age dating of an extensive thrust system on Mercury: Implications for the planet's thermal evolution *Volcanism Tectonism Across Inn. Sol. Syst.* 291–311

Gillis-Davis J J, Blewett D T, Gaskell R W, Denevi B W, Robinson M S, Strom R G, Solomon S C and Sprague A L 2009 Pit-floor craters on Mercury: Evidence of near-surface igneous activity *Earth Planet. Sci. Lett.* **285** 243–50 Online: http://dx.doi.org/10.1016/j.epsl.2009.05.023

Goosmann E, Buczkowski D L, Ernst C M, Denevi B W and Kinczyk M J 2016 Geologic Map of The Caloris Basin, Mercury *Lunar and Planetary Science Conference* vol 47 p 1254

Goudge T A, Head J W, Kerber L, Blewett D T, Denevi B W, Domingue D L, Gillis-Davis J J, Gwinner K, Helbert J, Holsclaw G M, Izenberg N R, Klima R L, McClintock W E, Murchie S L, Neumann G A, Smith D E, Strom

R G, Xiao Z, Zuber M T and Solomon S C 2014 Global inventory and characterization of pyroclastic deposits on Mercury: New insights into pyroclastic activity from MESSENGER orbital data *J. Geophys. Res. Planets* **119** 635–58 Online: http://doi.wiley.com/10.1002/2013JE004480

Greeley R and Spudis P D 1981 Volcanism on Mars *Rev. Geophys. Sp. Phys.* **19** 13–41

Grolier M J and Boyce J M 1984 Geologic map of the Borealis region (H-1) of Mercury *United States Geol. Surv. Misc. Investig. Ser. Map I-1660*

Grott M, Breuer D and Laneuville M 2011 Thermo-chemical evolution and global contraction of mercury *Earth Planet. Sci. Lett.* **307** 135–46 Online: http://dx.doi.org/10.1016/j.epsl.2011.04.040

Guest J E and Greeley R 1983 Geologic map of the Shakespeare quadrangle of Mercury *United States Geol. Surv.* **I–1408**

Guzzetta L, Galluzzi V, Ferranti L and Palumbo P 2017 Geology of the Shakespeare quadrangle (H03), Mercury *J. Maps* **13** 227–38 Online: https://www.tandfonline.com/doi/full/10.1080/17445647.2017.1290556

Hapke B 1977 Interpretations of optical observations of Mercury and the moon *Phys. Earth Planet. Inter.* **15** 264–74

Hapke B 2001 Space weathering from Mercury to the asteroid belt *J. Geophys. Res. Planets* **106** 10039–73 Online: http://doi.wiley.com/10.1029/2000JE001338

Hauck S A, Grott M, Byrne P K, Denevi B W, Stanley S and McCoy T J 2018 Mercury's Global Evolution *Mercury: The view after MESSENGER* (Cambridge: Cambridge University Press) pp 516–43

Hauck S A, Margot J L, Solomon S C, Phillips R J, Johnson C L, Lemoine F G, Mazarico E, McCoy T J, Padovan S, Peale S J, Perry M E, Smith D E and Zuber M T 2013 The curious case of Mercury's internal structure *J. Geophys. Res. E Planets* **118** 1204–20

Hawkins S E, Boldt J D, Darlington E H, Espiritu R, Gold R E, Gotwols B, Grey M P, Hash C D, Hayes J R, Jaskulek S E, Kardian C J, Keller M R, Malaret E R, Murchie S L, Murphy P K, Peacock K, Prockter L M, Reiter R A, Robinson M S, Schaefer E D, Shelton R G, Sterner R E, Taylor H W, Watters T R and Williams B D 2007 The mercury dual imaging system on the MESSENGER spacecraft *Space Sci. Rev.* **131** 247–338

Head J W, Murchie S L, Prockter L M, Robinson M S, Solomon S C, Strom R G, Chapman C R, Watters T R, McClintock W E, Blewett D T and Gillis-Davis J J 2008 Volcanism on Mercury: Evidence from the First MESSENGER Flyby *Science (80-.).* **321** 69–72 Online: http://www.sciencemag.org/cgi/doi/10.1126/science.1159256

Head J W, Murchie S L, Prockter L M, Solomon S C, Chapman C R, Strom R G, Watters T R, Blewett D T, Gillis-Davis J J, Fassett C I, Dickson J L, Morgan G A and Kerber L 2009 Volcanism on Mercury: Evidence from the first MESSENGER flyby for extrusive and explosive activity and the volcanic origin of plains *Earth Planet. Sci. Lett.* **285** 227–42 Online: http://dx.doi.org/10.1016/j.epsl.2009.03.007

Head J W and Wilson L 2017 Generation, ascent and eruption of magma on the Moon: New insights into

source depths, magma supply, intrusions and effusive/explosive eruptions (Part 2: Predicted emplacement processes and observations) *Icarus* **283** 176–223 Online: http://dx.doi.org/10.1016/j.icarus.2016.05.031

Head J W and Wilson L 1992 Lunar mare volcanism: Stratigraphy, eruption conditions, and the evolution of secondary crusts *Geochim. Cosmochim. Acta* **56** 2155–75

Hill R E T, Barnes S J, Gole M J and Dowling S E 1995 The volcanology of komatiites as deduced from field relationships in the Norseman-Wiluna greenstone belt, Western Australia *Lithos* **34** 159–88

De Hon R A and Scott D H 1981 Geologic map of the Kuiper Quadrangel of Mercury

Howard H T, Tyler G L, Esposito P B, Anderson J D, Reasenberg R D, Shapiro I I, Fjeldbo G, Kliore A J, Levy G S, Brunn D L, Dickinson R, Edelson R E, Martin W L, Postal R B, Seidel B, Sesplaukis T T, Shirley D L, Stelzried C T, Sweetnam D N, Wood G E and Zygielbaum A I 1974 Mercury: Results on mass, radius, ionosphere, and atmosphere from Mariner 10 dual-frequency radio signals *Science (80-.).* **185** 179–80

Hynek B ., Robbins S J, Mueller K, Gemperline J, Osterloo M K and Thomas R 2016a Unlocking Mercury's Geological History with detailed mapping of Rembrandt Basin: year 2 *Annual Planetary Geologic Mappers Meeting 2016* p 7023

Hynek B ., Robbins S J, Muller K, Gemperline J and Osterloo M K 2017 Unlocking Mercury's Geological History with detailed mapping of Rembrandt Basin: year 3 *3rd Planetary Data Workshop 2017* vol 3 p 7089

Hynek B ., Robbins S J, Osterloo M K, Mueller K, Gemperline J and Thomas R 2016b Unlocking Mercury's Geological History with detailed mapping of Rembrandt Basin *47th Lunar and Planetary Science Conference (2016)* p 2312

International Astronomical Union 2006 The IAU draft definiiton of a "planet" and "plutons" *Int. Astron. Union* Online: https://www.iau.org/news/pressreleases/detail/iau0

International Astronomical Union Working Group for Planetary System Nomenclature 2010 Planetary Names: Crater, craters: Debussy on Mercury *Gazet. Planet. Nomencl.* Online: https://planetarynames.wr.usgs.gov/Feature/14647

Jackson J A and Bates R L 1997 *Glossary of geology* (American Geological Institute)

James P B, Zuber M T, Phillips R J and Solomon S C 2015 Support of long-wavelength topography on Mercury inferred from MESSENGER measurements of gravity and topography *J. Geophys. Res. Planets* **120** 287–310 Online: http://doi.wiley.com/10.1002/2014JE004713

Jozwiak L M, Head J W and Wilson L 2018 Explosive volcanism on Mercury: Analysis of vent and deposit morphology and modes of eruption *Icarus* **302** 191–212 Online: https://doi.org/10.1016/j.icarus.2017.11.011

Vander Kaaden K E and McCubbin F M 2015 Exotic crust formation on Mercury: Consequences of a shallow, FeO-poor mantle *J. Geophys. Res. Planets* **120** 195–209 Online:

http://doi.wiley.com/10.1002/2014JE004733

Vander Kaaden K E and McCubbin F M 2016 The origin of boninites on Mercury: An experimental study of the northern volcanic plains lavas *Geochim. Cosmochim. Acta* **173** 246–63 Online: http://dx.doi.org/10.1016/j.gca.2015.10.016

Vander Kaaden K E, McCubbin F M, Nittler L R, Peplowski P, Weider S, Frank E and McCoy T J 2017 Geochemistry, mineralogy, and petrology of boninitic and komatiitic rocks on the mercurian surface: Insights into the mercurian mantle *Icarus* **285** 155–68 Online: http://dx.doi.org/10.1016/j.icarus.2016.11.041

Kay J P and Dombard A J 2019 Long-wavelength topography on Mercury is not from folding of the lithosphere *Icarus* **319** 724–8 Online: https://doi.org/10.1016/j.icarus.2018.09.040

Keil K 1968 Mineralogical and Chemical Relationships Among Enstatite Chondrites *J. Geophys. Res.* **73** 6945–76

Kennedy P J, Freed A M and Solomon S C 2008 Mechanisms of faulting in and around Caloris basin, Mercury *J. Geophys. Res. E Planets* **113** 1–12

Kerber L, Head J W, Blewett D T, Solomon S C, Wilson L, Murchie S L, Robinson M S, Denevi B W and Domingue D L 2011 The global distribution of pyroclastic deposits on Mercury: The view from MESSENGER flybys 13 *Planet. Space Sci.* **59** 1895–909 Online: http://dx.doi.org/10.1016/j.pss.2011.03.020

Kerber L, Head J W, Solomon S C, Murchie S L, Blewett D T and Wilson L 2009 Explosive volcanic eruptions on Mercury: Eruption conditions, magma volatile content, and implications for interior volatile abundances *Earth Planet. Sci. Lett.* **285** 263–71 Online: http://dx.doi.org/10.1016/j.epsl.2009.04.037

Kinczyk M J, Prockter L M, Byrne P K, Denevi B W, Ostrach L R and Skinner J A 2018 A Global Geological Map of Mercury *Mercury: Current and Futrure Science* p 6123

Kinczyk M J, Prockter L M, Byrne P K, Susorney H C M and Chapman C R 2020a A morphological evaluation of crater degradation on Mercury: Revisiting crater classification with MESSENGER data *Icarus* **341** 113637 Online: https://doi.org/10.1016/j.icarus.2020.113637

Kinczyk M J, Prockter L M, Byrne P K, Susorney H C M and Chapman C R 2020b A morphological evaluation of crater degradation on Mercury: Revisiting crater classification with MESSENGER data *Icarus* **341** 113637 Online: https://doi.org/10.1016/j.icarus.2020.113637

Kinczyk M J, Prockter L M, Chapman C R and Susorney H C M 2016 A morphological evaluation of crater degradation on Mercury: Revisiting crater classification with MESSENGER data *47th Lunar Planet. Sci. Conf.* 1573

King J S and Scott D H 1990 *Geologic map of the Beethoven quadrangle of Mercury*

King S D 2008 Pattern of lobate scarps on Mercury's surface reproduced by a model of mantle convection *Nat. Geosci.* **1** 229–32

Klemetti E W and Grunder A L 2008 Volcanic evolution of Volcán Aucanquilcha: A long-lived dacite volcano in the Central Andes of northern Chile *Bull. Volcanol.* **70** 633–50

Klima R L, Denevi B W, Ernst C M, Murchie S L and Peplowski P N 2018 Global Distribution and Spectral Properties of Low-Reflectance Material on Mercury *Geophys. Res. Lett.* **45** 2945–53

Klimczak C, Byrne P K and Solomon S C 2015 A rock-mechanical assessment of Mercury's global tectonic fabric *Earth Planet. Sci. Lett.* **416** 82–90 Online: http://dx.doi.org/10.1016/j.epsl.2015.02.003

Klimczak C, Crane K T, Habermann M A and Byrne P K 2018 The spatial distribution of Mercury's pyroclastic activity and the relation to lithospheric weaknesses *Icarus* **315** 115–23 Online: https://doi.org/10.1016/j.icarus.2018.06.020

Klimczak C, Ernst C M, Byrne P K, Solomon S C, Watters T R, Murchie S L, Preusker F and Balcerski J A 2013 Insights into the subsurface structure of the Caloris basin, Mercury, from assessments of mechanical layering and changes in long-wavelength topography *J. Geophys. Res. E Planets* **118** 2030–44

Klimczak C, Schultz R A and Nahm A L 2010 Evaluation of the origin hypotheses of Pantheon Fossae, central Caloris basin, Mercury *Icarus* **209** 262–70 Online: http://dx.doi.org/10.1016/j.icarus.2010.04.014

Klimczak C, Watters T R, Ernst C M, Freed A M, Byrne P K, Solomon S C, Blair D M and Head J W 2012 Deformation associated with ghost craters and basins in volcanic smooth plains on Mercury: Strain analysis and implications for plains evolution *J. Geophys. Res. E Planets* **117** 1–15

Kreslavsky M A and Head J W 2015 A Thicker Regolith on Mercury *Lunar and Planetary Science Conference* (Houston: Lunar and Planetary Institute) p 1246

Lambert J H 1772 *Anmerkungen und Zusätze zur Entwerfung der Land-und Himmelscharten* (Berlin)

López V, Ruiz J and Vázquez A 2015 Evidence for two stages of compressive deformation in a buried basin of Mercury *Icarus* **254** 18–23

Lucchetti A, Pajola M, Galluzzi V, Giacomini L, Carli C, Cremonese G, Marzo G A, Ferrari S, Massironi M and Palumbo P 2018 Mercury Hollows as Remnants of Original Bedrock Materials and Devolatilization Processes: A Spectral Clustering and Geomorphological Analysis *J. Geophys. Res. Planets* **123** 2365–79

Lucchitta B K and Schmitt H H 1974 Orange material in the Sulpicius Gallus formation at the southwestern edge of Mare Serenitatis *Proc. Fifth Lunar Conf.* **1** 223–34

Lyell C 1853 *Principles of Geology* (London: Spottswoodes and Shaw.)

Malin M C 1976 Observations of intercrater plains on Mercury *Geophys. Res. Lett.* **3** 581–4 Online: http://doi.wiley.com/10.1029/GL003i010p00581

Malliband C C 2020 *Geological Processes on Mercury and the Mapping of the Derain (H-10) Quadrangle* (The Open University)

Malliband C C, Conway S J, Rothery D A and Balme M R 2019 Potential Identification of Downslope Mass

Movements on Mercury Driven by Volatile-Loss *Lunar and Planetary Science Conference 2019* vol 50 p 1804

Malliband C C, Rothery D A, Balme M R and Conway S J 2020 1:3M Geological Mapping of the Derain (H-10) Quadrangle of Mercury *British Planetary Science Conference* p 79

Malliband C C, Rothery D A, Balme M R and Conway S J 2018 Small Smooth Units ("Young" Lavas?) Abutting Lobate Scarps On Mercury *Mercury: Current and Future Science* p 6092

Man B, Rothery D A, Balme M R, Conway S J and Wright J 2020 Geological Mapping of the Neruda Quadrange (H13) of Mercury *Planet. Geol. Mappers* 7028 Online: https://doi.org/10.1016/j.tmaid.2020.101607

Mancinelli P, Minelli F, Pauselli C and Federico C 2016 Geology of the Raditladi quadrangle, Mercury (H04) *J. Maps* **12** 190–202 Online: http://dx.doi.org/10.1080/17445647.2016.1191384

Manglik A, Wicht J and Christensen U R 2010 A dynamo model with double diffusive convection for Mercury's core *Earth Planet. Sci. Lett.* **289** 619–28 Online: http://dx.doi.org/10.1016/j.epsl.2009.12.007

Marchi S, Chapman C R, Fassett C I, Head J W, Bottke W F and Strom R G 2013 Global resurfacing of Mercury 4.0–4.1 billion years ago by heavy bombardment and volcanism *Nature* **499** 59–61 Online: http://www.nature.com/articles/nature12280

Matsuyama I and Nimmo F 2009 Gravity and tectonic patterns of Mercury: Effect of tidal deformation, spin-orbit resonance, nonzero eccentricity, despinning, and reorientation *J. Geophys. Res. E Planets* **114** 1–23

Mccauley J F, Guest J E, Schaber G G, Trask N J and Greeley R 1981 Stratigraphy of the Caloris basin, Mercury *Icarus* **47** 184–202

McClintock W E, Cassidy T A, Merkel A W, Killen R M, Burger M H and Vervack R J 2018 Observations of Mercury's Exosphere: Composition and Structure *Mercury* (Cambridge University Press) pp 371–406 Online: https://www.cambridge.org/core/product/identifier/9781316650684%23c14/type/book_part

McClintock W E, Izenberg N R, Holsclaw G M, Blewett D T, Domingue D L, Head J W, Helbert J, McCoy T J, Murchie S L, Robinson M S, Solomon S C, Sprague A L and Vilas F 2008 Spectroscopic observations of mercury's surface reflectance during MESSENGER's first mercury flyby *Science (80-.).* **321** 62–5

McClintock W E and Lankton M R 2007 The Mercury Atmospheric and Surface Composition Spectrometer for the MESSENGER Mission *Space Sci. Rev.* **131** 481–521 Online: http://link.springer.com/10.1007/s11214-007-9264-5

McCoy T J, Peplowski P N, McCubbin F M and Weider S Z 2018 The geochemical and mineralogical diversity of Mercury *Mercur. View after MESSENGER* 176–90

McCubbin F M, Vander Kaaden K E, Peplowski P N, Bell A S, Nittler L R, Boyce J W, Evans L G, Keller L P, Elardo S M and McCoy T J 2017 A Low O/Si Ratio on the Surface of Mercury: Evidence for Silicon Smelting? *J. Geophys. Res. Planets* **122** 2053–76

McGill G E and King E A 1983 Geologic map of the Victoria (H-2) quadrangle of Mercury *United States Geol.*

Surv. Misc. Investig. Ser. Map I-1409

McGrath M A, Johnson R E and Lanzerotti L J 1986 Sputtering of sodium on the planet Mercury *Nature* **323** 694–6 Online: http://www.nature.com/articles/323694a0

Melosh H J 2011 *Planetary surface processes* vol 13 (Cambridge University Press)

Melosh H J and Dzurisin D 1978 Mercurian global tectonics: A consequence of tidal despinning? *Icarus* **35** 227–36

Michel N C, Hauck S A, Solomon S C, Phillips R J, Roberts J H and Zuber M T 2013 Thermal evolution of Mercury as constrained by MESSENGER observations *J. Geophys. Res. E Planets* **118** 1033–44

Murchie S L, Klima R L, Denevi B W, Ernst C M, Keller M R, Domingue D L, Blewett D T, Chabot N L, Hash C D, Malaret E, Izenberg N R, Vilas F, Nittler L R, Gillis-Davis J J, Head J W and Solomon S C 2015 Orbital multispectral mapping of Mercury with the MESSENGER Mercury Dual Imaging System: Evidence for the origins of plains units and low-reflectance material *Icarus* **254** 287–305 Online: http://dx.doi.org/10.1016/j.icarus.2015.03.027

Murchie S L, Watters T R, Robinson M S, Head J W, Strom R G, Chapman C R, Solomon S C, McClintock W E, Prockter L M, Domingue D L and Blewett D T 2008 Geology of the caloris basin, mercury: A view from MESSENGER *Science (80-.).* **321** 73–6

Murchie S, Mick A, Prockter L, Rivkin A, Guinness E and Ward J 2016 MDIS CDR/RDR software interface specification

Murray B C, Strom R G, Trask N J and Gault D E 1975 Surface history of Mercury: Implications for terrestrial planets *J. Geophys. Res.* **80** 2508–14 Online: http://doi.wiley.com/10.1029/JB080i017p02508

Namur O, Collinet M, Charlier B, Grove T L, Holtz F and McCammon C 2016 Melting processes and mantle sources of lavas on Mercury *Earth Planet. Sci. Lett.* **439** 117–28 Online: http://dx.doi.org/10.1016/j.epsl.2016.01.030

Ness N F, Behannon K W, Lepping R P and Whang Y C 1975 Magnetic field of mercury confirmed *Nature* **255** 204–5

Ness N F, Behannon K W, Lepping R P, Whang Y C and Schatten K H 1974 Magnetic Field Observations near Mercury: Preliminary Results from Mariner 10 *Science (80-.).* **185** 151–60 Online: https://www.sciencemag.org/lookup/doi/10.1126/science.185.4146.151

Neuendorf K K E, Mehl J P and Jackson J A 2005 *Glossary of geology* (Alexandria, Va: American Geological Institute)

Nittler L R, Frank E A, Weider S Z, Crapster-Pregont E, Vorburger A, Starr R D and Solomon S C 2020 Global major-element maps of Mercury from four years of MESSENGER X-Ray Spectrometer observations *Icarus* **345** 113716 Online: https://doi.org/10.1016/j.icarus.2020.113716

Nittler L R, Starr R D, Weider S Z, McCoy T J, Boynton W V., Ebel D S, Ernst C M, Evans L G, Goldsten J O,

Hamara D K, Lawrence D J, McNutt R L, Schlemm C E, Solomon S C and Sprague A L 2011 The Major-Element Composition of Mercury's Surface from MESSENGER X-ray Spectrometry *Science (80-.).* **333** 1847–50 Online: http://www.sciencemag.org/cgi/doi/10.1126/science.1211567

Noyelles B, Frouard J, Makarov V V. and Efroimsky M 2014 Spin–orbit evolution of Mercury revisited *Icarus* **241** 26–44 Online: http://linkinghub.elsevier.com/retrieve/pii/S0019103514003078

Oberbeck V R 1975 The role of ballistic erosion and sedimentation in lunar stratigraphy *Rev. Geophys.* **13** 337–62

Oberst J, Preusker F, Phillips R J, Watters T R, Head J W, Zuber M T and Solomon S C 2010 The morphology of Mercury's Caloris basin as seen in MESSENGER stereo topographic models *Icarus* **209** 230–8

Orgel C, Fassett C I, Michael G, Riedel C, Bogert C H, Hiesinger H, van der Bogert C H and Hiesinger H 2020 Re-examination of the Population, Stratigraphy, and Sequence of Mercurian Basins: Implications for Mercury's Early Impact History and Comparison With the Moon *J. Geophys. Res. Planets* **125**

Ostrach L R, Robinson M S, Whitten J L, Fassett C I, Strom R G, Head J W and Solomon S C 2015 Extent, age, and resurfacing history of the northern smooth plains on Mercury from MESSENGER observations *Icarus* **250** 602–22 Online: http://dx.doi.org/10.1016/j.icarus.2014.11.010

Padovan S, Tosi N and Plesa A C 2016 Basin-Forming impact events on Mercury: effects on melt production and the depth of the source region *79th Annual Meeting of the Meteoritical Society* p 6256

Padovan S, Tosi N, Plesa A C and Ruedas T 2017 Impact-induced changes in source depth and volume of magmatism on Mercury and their observational signatures *Nat. Commun.* **8** 1–9 Online: http://dx.doi.org/10.1038/s41467-017-01692-0

Padovan S, Wieczorek M A, Margot J L, Tosi N and Solomon S C 2015 Thickness of the crust of Mercury from geoid-to-topography ratios *Geophys. Res. Lett.* **42** 1029–38

Pegg D L, Rothery D A, Balme M R and Conway S J 2021a Explosive Vent Sites on Mercury: Commonplace Multiple Eruptions and their Implications *Icarus* 114510 Online: https://linkinghub.elsevier.com/retrieve/pii/S0019103521001858

Pegg D L, Rothery D A, Conway S J and Balme M R 2021b A Fault Surface Exposed on Mercury *Planet. Space Sci.* 105223 Online: https://linkinghub.elsevier.com/retrieve/pii/S0032063321000623

Peplowski P N, Evans L G, Hauck S A, McCoy T J, Boynton W V, Gillis-Davis J J, Ebel D S, Goldsten J O, Hamara D K, Lawrence D J, McNutt R L, Nittler L R, Solomon S C, Rhodes E A, Sprague A L, Starr R D and Stockstill-Cahill K R 2011 Radioactive Elements on Mercury's Surface from MESSENGER: Implications for the Planet's Formation and Evolution *Science (80-.).* **333** 1850–2 Online: https://www.sciencemag.org/lookup/doi/10.1126/science.1211576

Peplowski P N, Klima R L, Lawrence D J, Ernst C M, Denevi B W, Frank E A, Goldsten J O, Murchie S L, Nittler L R and Solomon S C 2016 Remote sensing evidence for an ancient carbon-bearing crust on Mercury *Nat. Geosci.* **9** 273–6 Online: http://www.scopus.com/inward/record.url?eid=2-s2.0-

84963527493&partnerID=tZOtx3y1

Peplowski P N, Lawrence D J, Rhodes E A, Sprague A L, McCoy T J, Denevi B W, Evans L G, Head J W, Nittler L R, Solomon S C, Stockstill-Cahill K R and Weider S Z 2012 Variations in the abundances of potassium and thorium on the surface of Mercury: Results from the MESSENGER Gamma-Ray Spectrometer *J. Geophys. Res. E Planets* **117** 1–27

Peplowski P N and Stockstill-Cahill K 2019 Analytical Identification and Characterization of the Major Geochemical Terranes of Mercury's Northern Hemisphere *J. Geophys. Res. Planets* **124** 2414–29

Perry M E, Neumann G A, Phillips R J, Barnouin O S, Ernst C M, Kahan D S, Solomon S C, Zuber M T, Smith D E, Hauck S A, Peale S J, Margot J L, Mazarico E, Johnson C L, Gaskell R W, Roberts J H, McNutt R L and Oberst J 2015 The low-degree shape of Mercury *Geophys. Res. Lett.* **42** 6951–8

Peterson G A, Johnson C L, Byrne P K and Phillips R J 2019 Distribution of Areal Strain on Mercury: Insights Into the Interaction of Volcanism and Global Contraction *Geophys. Res. Lett.* **46** 608–15

Peterson G A, Johnson C L, Byrne P K and Phillips R J 2018 Distribution of Areal Strain On Mercury: Insights into the Interaction of Volcanism and Global Contraction *Geophys. Res. Lett.* 1–8 Online: http://doi.wiley.com/10.1029/2018GL080749

Pettengill G H and Dyce R B 1965 A Radar Determination of the Rotation of the Planet Mercury *Nature* **206** 1240–1240 Online: http://www.nature.com/articles/2061240a0

Pike R J 1974 Depth/diameter relations of fresh lunar craters: Revision from spacecraft data *Geophys. Res. Lett.* **1** 291–4 Online: http://doi.wiley.com/10.1029/GL001i007p00291

Pokorný P, Sarantos M and Janches D 2017 Reconciling the Dawn–Dusk Asymmetry in Mercury's Exosphere with the Micrometeoroid Impact Directionality *Astrophys. J.* **842** L17 Online: http://stacks.iop.org/2041-8205/842/i=2/a=L17?key=crossref.374bdb4062aca95aa01fcc500610b1da

Potter A E, Killen R M and Morgan T H 1999 Rapid changes in the sodium exosphere of Mercury *Planet. Space Sci.* **47** 1441–8

Preusker F, Oberst J, Head J W, Watters T R, Robinson M S, Zuber M T and Solomon S C 2011 Stereo topographic models of Mercury after three MESSENGER flybys *Planet. Space Sci.* **59** 1910–7

Prockter L M 2010 Evidence for Young Volcanism *Appl. Phys.* **668** 668–71

Prockter L M, Kinczyk M J, Byrne P K, Denevi B W, Head J W, Fassett C I, Whitten J L, Thomas R J, Buczkowski D L, Hynek B M, Ostrach L R, Blewett D T, Ernst C M and Group M M 2016 The First Global Geological Map of Mercury *47th Lunar and Planetary Science Confrence* p 1245

Rava B and Hapke B 1987 An analysis of the Mariner 10 color ratio map of mercury *Icarus* **71** 397–429

Roberts W A 1964 Secondary craters *Icarus* **3** 348–64

Robinson M S and Lucey P G 1997 Recalibrated mariner 10 color mosaics: Implications for mercurian

volcanism *Science (80-.).* **275** 197–200

Robinson M S, Murchie S L, Blewett D T, Domingue D L, Hawkins S E, Head J W, Holsclaw G M, McClintock W E, McCoy T J, McNutt R L, Prockter L M, Solomon S C and Watters T R 2008 Reflectance and Color Variations on Mercury: Regolith Processes and Compositional Heterogeneity *Science (80-.).* **321** 66–9 Online: http://www.sciencemag.org/cgi/doi/10.1126/science.1160080

Rothery D A and Balme M R 2018 Planmap Mapping Standards Document *Plan Map* Online: Mapping Standards Document

Rothery D A, Barraud O, Besse S, Carli C, Pegg D L, Wright J and Zambon F 2020a On the asymmetry of Nathair Facula, Mercury *Icarus* 114180 Online: https://doi.org/10.1016/j.scitotenv.2019.135938

Rothery D A, Mancinelli P, Guzzetta L and Wright J 2017 Mercury's Caloris basin: Continuity between the interior and exterior plains *J. Geophys. Res. Planets* **122** 560–76 Online: http://doi.wiley.com/10.1002/2017JE005282

Rothery D A and Massironi M 2010 Beagle Rupes - Evidence for a basal decollement of regional extent in Mercury's lithosphere *Icarus* **209** 256–61

Rothery D A, Massironi M, Alemanno G, Barraud O, Besse S, Bott N, Brunetto R, Bunce E, Byrne P, Capaccioni F, Capria M T, Carli C, Charlier B, Cornet T, Cremonese G, D'Amore M, De Sanctis M C, Doressoundiram A, Ferranti L, Filacchione G, Galluzzi V, Giacomini L, Grande M, Guzzetta L G, Helbert J, Heyner D, Hiesinger H, Hussmann H, Hyodo R, Kohout T, Kozyrev A, Litvak M, Lucchetti A, Malakhov A, Malliband C, Mancinelli P, Martikainen J, Martindale A, Maturilli A, Milillo A, Mitrofanov I, Mokrousov M, Morlok A, Muinonen K, Namur O, Owens A, Nittler L R, Oliveira J S, Palumbo P, Pajola M, Pegg D L, Penttilä A, Politi R, Quarati F, Re C, Sanin A, Schulz R, Stangarone C, Stojic A, Tretiyakov V, Väisänen T, Varatharajan I, Weber I, Wright J, Wurz P and Zambon F 2020b Rationale for BepiColombo Studies of Mercury's Surface and Composition *Space Sci. Rev.* **216** 66 Online: http://link.springer.com/10.1007/s11214-020-00694-7

Rothery D A, Thomas R J and Kerber L 2014 Prolonged eruptive history of a compound volcano on Mercury: Volcanic and tectonic implications *Earth Planet. Sci. Lett.* **385** 59–67 Online: http://dx.doi.org/10.1016/j.epsl.2013.10.023

Ruiz J, López V, Dohm J M and Fernández C 2012 Structural control of scarps in the Rembrandt region of Mercury *Icarus* **219** 511–4 Online: http://dx.doi.org/10.1016/j.icarus.2012.03.030

Schaber G G and McCauley J F 1980 *Geologic Map of the Tolstoj Quadrangle of Mercury* (USGS)

Schultz P H 1977 Endogenic modification of impact craters on Mercury *Phys. Earth Planet. Inter.* **15** 202–19

Semenzato A, Massironi M, Ferrari S, Galluzzi V, Rothery D A, Pegg D L, Pozzobon R and Marchi S 2020 An Integrated Geologic Map of the Rembrandt Basin, on Mercury, as a Starting Point for Stratigraphic Analysis *Remote Sens.* **12** 3213

Slade M A, Butler B J and Muhleman D O 1992 Mercury Radar Imaging: Evidence for Polar Ice *Science (80-.).*

258 635–40 Online: https://www.sciencemag.org/lookup/doi/10.1126/science.258.5082.635

Slavin J A, Middleton H R, Raines J M, Jia X, Zhong J, Sun W J, Livi S, Imber S M, Poh G K, Akhavan-Tafti M, Jasinski J M, DiBraccio G A, Dong C, Dewey R M and Mays M L 2019 MESSENGER Observations of Disappearing Dayside Magnetosphere Events at Mercury *J. Geophys. Res. Sp. Phys.* **124** 6613–35

Smith D E, Zuber M T, Phillips R J, Solomon S C, Hauck S A, Lemoine F G, Mazarico E, Neumann G A, Peale S J, Margot J L, Johnson C L, Torrence M H, Perry M E, Rowlands D D, Goossens S, Head J W and Taylor A H 2012 Gravity Field and Internal Structure of Mercury from MESSENGER *Science (80-.).* **336** 214–7

Smith M J, Paron P and Griffiths J S 2011 *Geomorphological Mapping: Methods and Applications* (Oxford: Elsevier)

Snyder J P 1982 *Map projections used by the U.S. Geological Survey* Online: https://pubs.er.usgs.gov/publication/b1532

Soderblom J M, Evans A J, Johnson B C, Melosh H J, Miljkovi K, Phillips R J, Andrews-hanna J C, Bierson C J, Iii J W H, Milbury C, Neumann G A, Nimmo F, Smith D E, Solomon S C and Sori M M 2015 Porosity From Impact Cratering 6939–44

Solomon S C 1978 On volcanism and thermal tectonics on one-plate planets *Geophys. Res. Lett.* **5** 461–4

Solomon S C 1976 Some aspects of core formation in Mercury *Icarus* **28** 509–21 Online: http://linkinghub.elsevier.com/retrieve/pii/001910357690124X

Solomon S C 1977 The relationship between crustal tectonics and internal evolution in the moon and Mercury *Phys. Earth Planet. Inter.* **15** 135–45

Solomon S C, McNutt Jr. R L, Gold R E, Acuña M H, Baker D N, Boynton W V., Chapman C R, Cheng A F, Gloeckler G, Head III J W, Krimigis S M, Mcclintock W E, Murchie S L, Peale S J, Phillips R J, Robinson M S, Slavin J a., Smith D E, Strom R G, Trombka J I and Zuber M T 2001 The MESSENGER mission to Mercury : scientiÿc objectives and implementation *Planet. Space Sci.* **49** 1445–65

Solomon S C, McNutt R L, Gold R E and Domingue D L 2007 MESSENGER Mission Overview *Space Sci. Rev.* **131** 3–39 Online: http://link.springer.com/10.1007/s11214-007-9247-6

Solomon S C, McNutt R L, Watters T R, Lawrence D J, Feldman W C, Head J W, Krimigis S M, Murchie S L, Phillips R J, Slavin J A and Zuber M T 2008 Return to Mercury: A Global Perspective on MESSENGER's First Mercury Flyby *Science (80-.).* **321** 59–62 Online: http://www.sciencemag.org/cgi/doi/10.1126/science.1159706

Sori M M 2018 A thin, dense crust for Mercury *Earth Planet. Sci. Lett.* **489** 92–9 Online: https://doi.org/10.1016/j.epsl.2018.02.033

Spudis P D and Guest J E 1988 Stratigraphy and geologic history of Mercury *Mercury* 118–164 Online: http://adsabs.harvard.edu/abs/1988merc.book..118S

Spudis P D and Prosser J G 1984 Geologic map of the Michelangelo quadrangle of Mercury *USGS Misc. Investig. Ser. Map I--2048*

Stark A, Oberst J, Preusker F, Burmeister S, Steinbrügge G and Hussmann H 2018 The reference frames of Mercury after the MESSENGER mission *J. Geod.* **92** 949–61 Online: https://doi.org/10.1007/s00190-018-1157-8

Stockstill-Cahill K R, McCoy T J, Nittler L R, Weider S Z and Hauck S A 2012 Magnesium-rich crustal compositions on Mercury: Implications for magmatism from petrologic modeling *J. Geophys. Res. E Planets* **117**

Stoffler D and Ryderm G 2001 Stratigraphy and Isotope Ages of Lunar Geologic Units *Space Sci. Rev.* **96** 9–54

Strom R G, Banks M E, Chapman C R, Fassett C I, Forde J A, Head J W, Merline W J, Prockter L M and Solomon S C 2011 Mercury crater statistics from MESSENGER flybys: Implications for stratigraphy and resurfacing history *Planet. Space Sci.* **59** 1960–7 Online: http://dx.doi.org/10.1016/j.pss.2011.03.018

Strom R G, Chapman C R, Merline W J, Solomon S C and Head J W 2008 Mercury Cratering Record Viewed from MESSENGER's First Flyby *Science (80-.).* **321** 79–81 Online: http://www.sciencemag.org/cgi/doi/10.1126/science.1159317

Strom R G, Malin M C and Leake M A 1990 *Geologic map of the Bach region of Mercury* Online: http://pubs.er.usgs.gov/publication/i2015

Strom R G, Trask N J and Guest J E 1975 Tectonism and volcanism on Mercury *J. Geophys. Res.* **80** 2478–507

Suzuki Y, Yoshioka K, Murakami G and Yoshikawa I 2020 Seasonal Variability of Mercury's Sodium Exosphere Deduced From MESSENGER Data and Numerical Simulation *J. Geophys. Res. Planets* **125** 1–13

Tanaka K L, Skinner J A and Hare T M 2011 Planetary Geologic Mapping Handbook – 2011 *Abstr. Annu. Meet. Planet. Geol. Mappers* 21 p. Online: https://ntrs.nasa.gov/archive/nasa/casi.ntrs.nasa.gov/20100017213.pdf

Tavani S, Storti F, Lacombe O, Corradetti A, Muñoz J A and Mazzoli S 2015 A review of deformation pattern templates in foreland basin systems and fold-and-thrust belts: Implications for the state of stress in the frontal regions of thrust wedges *Earth-Science Rev.* **141** 82–104 Online: http://dx.doi.org/10.1016/j.earscirev.2014.11.013

Thomas R J, Hynek B M, Rothery D A and Conway S J 2016 Mercury's low-reflectance material: Constraints from hollows *Icarus* **277** 455–65 Online: http://dx.doi.org/10.1016/j.icarus.2016.05.036

Thomas R J, Rothery D A, Conway S J and Anand M 2015 Explosive volcanism in complex impact craters on Mercury and the Moon: Influence of tectonic regime on depth of magmatic intrusion *Earth Planet. Sci. Lett.* **431** 164–72

Thomas R J, Rothery D A, Conway S J and Anand M 2014a Hollows on Mercury: Materials and mechanisms involved in their formation *Icarus* **229** 221–35 Online: http://linkinghub.elsevier.com/retrieve/pii/S0019103513004909

Thomas R J, Rothery D A, Conway S J and Anand M 2014b Long-lived explosive volcanism on Mercury *Geophys.*

Res. Lett. **41** 6084–92

Thomas R J, Rothery D A, Conway S J and Anand M 2014c Mechanisms of explosive volcanism on Mercury: Implications from its global distribution and morphology *J. Geophys. Res. E Planets* **119** 2239–54

Tissot M A 1880 SUR LA REPRESENTATION DES SURFACES ET LES PROJECION DES CARTES GEOGRAPHIQUES *J. des candidats aux écoles Polytech. Norm.* **19** S1–40

Tobler W 1987 Measuring spatial resolution. *Proceedings of the land resource information systems conference* pp 12–6

Tosi N, Grott M, Plesa A C and Breuer D 2013 Thermochemical evolution of Mercury's interior *J. Geophys. Res. E Planets* **118** 2474–87

Trask N J and Dzurisin D 1984 *Geologic map of the Discovery Quadrangle of Mercury*

Trask N J and Guest J E 1975 Preliminary geologic terrain map of Mercury *J. Geophys. Res.* **80** 2461–77 Online: http://doi.wiley.com/10.1029/JB080i017p02461

Udry A, Wilbur Z E, Rahib R R, McCubbin F M, Vander Kaaden K E, McCoy T J, Ziegler K, Gross J, DeFelice C, Combs L and Turrin B D 2019 Reclassification of four aubrites as enstatite chondrite impact melts: Potential geochemical analogs for Mercury *Meteorit. Planet. Sci.* **26** Online: http://doi.wiley.com/10.1111/maps.13252

Vervack R J, Killen R M, McClintock W E, Merkel A W, Burger M H, Cassidy T A and Sarantos M 2016 New discoveries from MESSENGER and insights into Mercury's exosphere *Geophys. Res. Lett.* **43** 11,545-11,551

Walker D and Hays J F 1977 Plagioclase flotation and lunar crust formation *Geology* **5** 425 Online: https://pubs.geoscienceworld.org/geology/article/5/7/425-428/195394

Wang Y, Xiao Z, Chang Y and Cui J 2020 Lost Volatiles During the Formation of Hollows on Mercury *J. Geophys. Res. Planets* **125** 1–19

Watters T R, Daud K, Banks M E, Selvans M M, Chapman C R and Ernst C M 2016a Recent tectonic activity on Mercury revealed by small thrust fault scarps *Nat. Geosci.* **9** 743–7 Online: http://dx.doi.org/10.1038/ngeo2814%0Ahttp://10.1038/ngeo2814%0Ahttp://www.nature.com/ngeo/journal/v9/n10/abs/ngeo2814.html#supplementary-information

Watters T R, Head J W, Solomon S C, Robinson M S, Chapman C R, Denevi B W, Fassett C I, Murchie S L and Strom R G 2009a Evolution of the Rembrandt impact basin on Mercury. *Science* **324** 618–21 Online: http://www.ncbi.nlm.nih.gov/pubmed/19407197

Watters T R, Montési L G J, Oberst J and Preusker F 2016b Fault-bound valley associated with the Rembrandt basin on Mercury *Geophys. Res. Lett.* **43** 11,536-11,544

Watters T R, Murchie S L, Robinson M S, Solomon S C, Denevi B W, André S L and Head J W 2009b Emplacement and tectonic deformation of smooth plains in the Caloris basin, Mercury *Earth Planet. Sci. Lett.* **285** 309–19 Online: http://dx.doi.org/10.1016/j.epsl.2009.03.040

Watters T R and Nimmo F 2010 The Tectonics of Mercury *Planetary Tectonics* pp 15–80

Watters T R, Robinson M S and Cook A C 1998 Topography of lobate scarps on Mercury: New constraints on the planet's contraction *Geology* **26** 991–4

Watters T R, Selvans M M, Banks M E, Hauck S A, Becker K J and Robinson M S 2015 Distribution of large-scale contractional tectonic landforms on Mercury: Implications for the origin of global stresses *Geophys. Res. Lett.* **42** 3755–63 Online: http://doi.wiley.com/10.1002/2015GL063570

Watters T R, Solomon S C, Klimczak C, Freed A M, Head J W, Ernst C M, Blair D M, Goudge T A and Byrne P K 2012 Extension and contraction within volcanically buried impact craters and basins on Mercury *Geology* **40** 1123–6

Watters T R, Solomon S C, Robinson M S, Head J W, André S L, Hauck S A and Murchie S L 2009c The tectonics of Mercury: The view after MESSENGER's first flyby *Earth Planet. Sci. Lett.* **285** 283–96

Watters W A 2006 Structure of polygonal impact crates at Meridiani Planum, Mars, and a model relating target structure to crater shape *Lpsc* **02139** 2163

Weider S Z, Nittler L R, Murchie S L, Peplowski P N, McCoy T J, Kerber L, Klimczak C, Ernst C M, Goudge T A, Starr R D, Izenberg N R, Klima R L and Solomon S C 2016 Evidence from MESSENGER for sulfur- and carbon-driven explosive volcanism on Mercury *Geophys. Res. Lett.* **43** 3653–61 Online: http://doi.wiley.com/10.1002/2016GL068325

Weider S Z, Nittler L R, Starr R D, Crapster-Pregont E J, Peplowski P N, Denevi B W, Head J W, Byrne P K, Hauck S A, Ebel D S and Solomon S C 2015 Evidence for geochemical terranes on Mercury: Global mapping of major elements with MESSENGER's X-Ray Spectrometer *Earth Planet. Sci. Lett.* **416** 109–20 Online: http://dx.doi.org/10.1016/j.epsl.2015.01.023

Weider S Z, Nittler L R, Starr R D, McCoy T J, Stockstill-Cahill K R, Byrne P K, Denevi B W, Head J W and Solomon S C 2012 Chemical heterogeneity on Mercury's surface revealed by the MESSENGER X-Ray Spectrometer *J. Geophys. Res. E Planets* **117** 1–15

White J D L and Ross P 2011 Maar-diatreme volcanoes : A review *J. Volcanol. Geotherm. Res.* **201** 1–29 Online: http://dx.doi.org/10.1016/j.jvolgeores.2011.01.010

Whitten J L, Fassett C I and Ostrach L R 2020 The Derain (H-10) Quadrangle on Mercury *Planetary Geological Mappers* p 7049

Whitten J L and Head J W 2015 Rembrandt impact basin: Distinguishing between volcanic and impact-produced plains on Mercury *Icarus* **258** 350–65 Online: http://dx.doi.org/10.1016/j.icarus.2015.06.022

Whitten J L, Head J W, Denevi B W and Solomon S C 2014a Intercrater plains on Mercury: Insights into unit definition, characterization, and origin from MESSENGER datasets *Icarus* **241** 97–113 Online: http://dx.doi.org/10.1016/j.icarus.2014.06.013

Whitten J L, Head J W and Solomon C 2014b Rembrandt basin: distinguishing between volcanic and impact-

produced smooth plains deposits on Mercury *Lunar Planet. Sci. Conf.* **45** 1289

Wilhelms D E 1976 Mercurian volcanism questioned *Icarus* **28** 551–8

Wilhelms D E and McCauley J F 1971 *Geologic Map Of The Near Side Of The Moon* (Flagstaff, AZ: USGS for NASA)

Williams J P, Ruiz J, Rosenburg M A, Aharonson O and Phillips R J 2011 Insolation driven variations of Mercury's lithospheric strength *J. Geophys. Res. E Planets* **116** 1–13

Wilson L 2009 Volcanism in the Solar System. *Nat. Publ. Gr.* **2** 389–97 Online: http://www.nature.com/ngeo/journal/v2/n6/abs/ngeo529.html

Wilson L, Hawke B R, Giguere T A and Petrycki E R 2011 An igneous origin for Rima Hyginus and Hyginus crater on the Moon *Icarus* **215** 584–95 Online: http://dx.doi.org/10.1016/j.icarus.2011.07.003

Wilson L and Head J W 1983 A comparison of volcanic eruption processes on Earth, Moon, Mars, Io and Venus *Nature* **302** 663–9

Wilson L and Head J W 2017 Generation, ascent and eruption of magma on the Moon: New insights into source depths, magma supply, intrusions and effusive/explosive eruptions (Part 2: Theory) *Icarus* **283** 146–75 Online: http://dx.doi.org/10.1016/j.icarus.2016.05.031

Wilson L and Head J W 2008 Volcanism on Mercury: A new model for the history of magma ascent and eruption *Geophys. Res. Lett.* **35** 1–5

Wood C A, Head III J W and Cintala M J 1977 Crater degradation on Mercury and the Moon: Clues to surface evolution *Proc. Lunar Sci. Conf. 8th* pp 3503–20

Wood C A and Radebaugh J 2020 Morphologic Evidence for Volcanic Craters near Titan ' s North Polar Region 0–3

Wright J 2019 *MESSENGER Observations of Volcanism on Mercury: From Hokusai Quadrangle Down to Small Cones* (The Open University) Online: https://doi.org/10.21954/ou.ro.0000f075

Wright J, Conway S J, Morino C, Rothery D A, Balme M R and Fassett C I 2020 Modification of Caloris ejecta blocks by long-lived mass-wasting: A volatile-driven process? *Earth Planet. Sci. Lett.* **549** 116519 Online: https://doi.org/10.1016/j.epsl.2020.116519

Wright J, Rothery D A, Balme M R and Conway S J 2018 Constructional Volcanic Edifices on Mercury: Candidates and Hypotheses of Formation 1–20

Wright J, Rothery D A, Balme M R and Conway S J 2019 Geology of the hokusai quadrangle (H05), Mercury *J. Maps* **15** 509–20

Xiao Z, Prieur N C and Werner S C 2016 The self-secondary crater population of the Hokusai crater on Mercury *Geophys. Res. Lett.* **43** 7424–32

Xiao Z, Strom R G, Blewett D T, Byrne P K, Solomon S C, Murchie S L, Sprague A L, Domingue D L and Helbert J 2013 Dark spots on Mercury: A distinctive low-reflectance material and its relation to hollows *J.*

Geophys. Res. Planets **118** 1752–65 Online: http://doi.wiley.com/10.1002/jgre.20115

Zuber M T, Montési L G J, Farmer G T, Hauck S A, Andreas Ritzer J, Phillips R J, Solomon S C, Smith D E, Talpe M J, Head J W, Neumann G A, Watters T R and Johnson C L 2010 Accommodation of lithospheric shortening on Mercury from altimetric profiles of ridges and lobate scarps measured during MESSENGER flybys 1 and 2 *Icarus* **209** 247–55 Online: http://dx.doi.org/10.1016/j.icarus.2010.02.026